

SAPIENZA
UNIVERSITÀ DI ROMA

Sapienza University of Rome

Department Chemical Engineering Materials Environment
PhD in Chemical Processes for Industry and Environment

Thesis For The Degree Of Doctor Of Philosophy

Polymeric Cryogels: An Experimental and Modeling Integrated Approach for Biomedical and Chromatographic Applications

Thesis Advisor
Prof. Alessandra Adrover

Thesis Co-Advisors
Prof. Patrizia Paolicelli
(Dept. of Drug Chemistry and Technologies)
Prof. Paola Nardinocchi
(Dept. of Structural and Geotechnical Engineering)

Candidate
Carolina Lauriola
1741892

XXXVIII cycle

Abstract

This thesis reports an integrated experimental and theoretical study on porous polymeric systems, concerning optimization for biomedical applications and modeling as possible stationary phases in chromatographic processes. The research covers two main areas: the first encompasses synthesis, characterization, and modeling of dextran-based cryogels for controlled drug delivery and tissue engineering, while the second is devoted to computational modeling of triply periodic geometries aimed at the design of effective chromatographic columns. The methacrylic derivatives of dextran were synthesized and systematically studied in the experimental section in order to define the window of formation of cryogel-like systems. The influence of polymer concentration, reagent ratio, and the presence of oxygen was investigated, highlighting the key role played by these parameters in determining crosslinking kinetics, porosity, and mechanical properties. By physical, structural and morphological analyses, the ranges of parameters allowing attainment of stable, highly interconnected macroporous networks were identified. Afterwards, the study was extended to the assessment of the effects exerted by polymer molecular weight and spacer length on swelling behavior, degradation rate, and mechanical response. Dextran-based cryogels were also tested as drug delivery systems employing vitamin B_{12} as model drug molecule: it has been proven that the loading method drastically affects the release mechanism. A mechanistic two-phase model was developed, able to successfully describe the transition between Fickian and non-Fickian release behaviors. To enhance biological performances, blended cryogels containing methacryol gelatin were prepared. The preparation method effectively combines structural robustness due to dextran derivatives with bioactivity from gelatin. Preliminary cellular adhesion and proliferation tests confirmed the potential of these systems as biocompatible scaffolds. On the theoretical side, a modified Mechano-Diffusion model was formulated to describe the swelling mechanics of cryogels, introducing porosity and polymer volume fraction to better represent the macroporous nature of the material. Finally, a computational study was carried out on chromatographic stationary phases modeled as triply periodic minimal surface (TPMS) structures. By employing the Two-Zone Moment Analysis, the hydrodynamic dispersion and kinetic performance of different geometries were analyzed, identifying gyroid- and diamond-type structures as the most promising for high-efficiency separations and feasible for advanced 3D printing fabrication. Overall, the approach presented here covers everything from material design to experimental characterization and theoretical modeling, thereby contributing to the further development of cryogel-based systems for bioapplications and providing significant insight into the principles of developing novel chromatographic media.

2025 Carolina Lauriola, all rights reserved.

Contents

1 Introduction and Structure of the Thesis **1**
1.1 Background of the research . . . 1
1.2 Polymer gels: from hydrogels to cryogels . . . 2
1.3 Preparation of cryogels and hydrogels: the mechanism of cryoconcentration and the influence of experimental parameters . . . 3
1.4 Cryogels as Drug Delivery Systems for Controlled release . . . 6
1.4.1 Modeling controlled release in polymer systems . . . 7
1.5 Cryogels as Tissue engineering Scaffolds . . . 8
1.6 Swelling processes in polymer systems . . . 9
1.6.1 Standard modeling of swelling processes: Mechano-Diffusion, Mixture Theory and Poromechanics . . . 10
1.7 Cryogels in Chromatography . . . 15
1.8 Structure of the Thesis . . . 16
1.9 Overview of the Experimental and Theoretical Work . . . 17

I Dextran-based cryogels for biomedical purposes **21**

2 Materials and methods **23**
2.1 Materials . . . 23
2.2 Polymer synthesis . . . 23
2.2.1 Synthesis of dextran methacrylate . . . 23
2.2.2 Synthesis of dextran derivatives . . . 25
2.2.3 Single-phase synthesis of Methacryloyl gelatin . . . 26
2.3 Preparation of Dextran-based gel systems . . . 27
2.3.1 Preparation of DEX_{40}HEMA cryogels and hydrogels for the formation window. . . . 28
2.3.2 Preparation of dextran-based cryogels . . . 35
2.3.3 Preparation of DEX-GelMA cryogels . . . 37
2.3.4 Preparation of Dextran methacrylate cryogels and hydrogels . . . 37
2.4 Estimation of the gel fraction . . . 38
2.5 Absorption, swelling and degradation studies . . . 38
2.6 Morphological characterization . . . 39
2.7 Compression studies . . . 39
2.8 Release of vitamin B_{12} . . . 40
2.9 Rheological analysis of methacrylic derivatives of dextran-GelMA blended systems . . . 41
2.10 Cell culture . . . 42
2.10.1 Adhesion and proliferation studies . . . 42

3 Characterization and synthesis of DEX_{40}HEMA cryogels: effect of experimental parameters 43
3.1 Determination of the formation window of the DEX_{40}HEMA cryogels . . . 43
3.1.1 Identification of the lower limits . . . 45
3.1.2 Identification of the upper limits . . . 48
3.2 Mechanical characterization and SEM analysis . . . 53
3.3 Side observations: preliminary analysis on the effect of the presence of oxygen during the gelation . . . 56
3.3.1 Swelling study . . . 57
3.3.2 Mechanical characterization and SEM analysis . . . 57

4 Cryogels from methacrylic derivatives of dextran as drug delivery systems: effect of the dextran chain length and of the spacer 63
4.1 Swelling studies of dextran-derivatives samples . . . 64
4.2 FE-SEM analysis and mechanical properties of dextran-derivatives samples . 66
4.3 Release studies . . . 70
4.4 Theoretical model of drug release in the pre-loading case . . . 73
4.4.1 Estimation of the diffusion coefficient $D_{B_{12}}$ . . . 77

5 Cryogels as cell scaffolds: Dextran-based polymers and Methacryloyl gelatin hybrid systems 79
5.1 Swelling and degradation studies . . . 80
5.2 Rheological studies . . . 82
5.3 FE-SEM analysis and mechanical characterization . . . 83
5.4 Adhesion and proliferation studies . . . 88

6 Mechanics of Swelling of cryogel-like structures 91
6.1 Experimental section: swelling of DEX_{40}MA cryogels . . . 91
6.2 The Mechano–Diffusion Model . . . 93
6.2.1 Review of the basic model: the case of cryogels . . . 98
6.3 Analysis of the experimental data . . . 105

7 Cryogels as promising stationary phases for liquid chromatography: a literature review 111
7.1 Monolithic structures in LC . . . 112
7.2 Cryogels as stationary phases and transport principles . . . 112
7.3 Applications of cryogels as monolithic columns . . . 113
7.3.1 Ion-Exchange Chromatography . . . 113
7.3.2 Affinity Chromatography . . . 115
7.3.3 Hydrophobic Interaction Chromatography . . . 119
7.4 Modeling approaches for Cryogel Stationary Phases . . . 120
7.5 Towards new highly ordered stationary phases: 3D-Printed Structures . . . 121
7.6 Surface Properties and Fluid-Solid Interactions . . . 122

II Computational modeling of liquid chromatography: Dispersion properties of triply periodic minimal surface stationary phases

8 Dispersion properties of triply periodic minimal surface stationary phases for Liquid Chromatography **127**
8.1 The exact moment analysis: overview 128
8.2 The case of Superficial Adsorption 133
8.2.1 Theoretical framework 134
8.2.2 Geometries 136
8.2.3 Fluid dynamic properties 139
8.2.4 Hydrodynamic dispersion (no retention $k'' = 0$) 141
8.2.5 Dispersion with superficial retention 148
8.2.6 Kinetic performance of TPMS structures 152
8.3 The mesoporous case 157
8.3.1 Theoretical framework 158
8.3.2 Geometries 160
8.3.3 Dispersion analysis 161
8.3.4 Kinetic performance of TPMS structures 168

9 Conclusions and Future developments **173**
9.1 Summary of the research work 173
9.2 Future developments 177

Chapter 1

Introduction and Structure of the Thesis

1.1 Background of the research

Recent years have seen an exponential increase in the field of biomaterials in the biomedical and pharmaceutical sectors, which is mainly due to the increase in population and average age [1, 2]. Materials exhibiting biocompatibility and biodegradability properties have become essential in regenerative medicine, controlled therapeutic delivery systems and the field of diagnostics [3]. In particular, the gel category represents a valuable class of materials, which has garnered significant attention due to the exceptional properties of versatility, flexibility, response to stimuli and mechanical resistance, as well as biodegradability and biocompatibility. A three-dimensional network is formed by the arrangement of polymer chains, allowing molecules, drugs, or cells to be trapped [4]. The properties of gel matrices are determined by the polymer used to make them: hydrophilic or hydrophobic crosslinked structures, or a combination of both. A key desired property is the ability to absorb large amounts of water and biological fluids, resulting in swelling [5]. Gel matrix type is chosen based on the specific application and desired properties. Gels are materials that can incorporate different types of drugs and release them in a controlled manner, facilitating drug administration. At the same time, they have the potential to serve as wound healing systems and scaffolds for tissue engineering.
Hydrogel systems, three-dimensional matrices, obtained by chemical or physical crosslinking of highly hydrophilic polymers, are part of this class of materials and are therefore capable of absorbing large quantities of water and biological fluids [6]. For the preparation of hydrogels it is necessary to choose materials based on a number of essential properties, including porosity, swelling capacity and mechanical properties [7]. The specific composition, together with the physical properties, in fact, make hydrogels highly attractive for a wide range of biomedical applications, proving highly promising, such as systems for the delivery and modified release of drugs, scaffolds for tissue regeneration and for wound dressing [8]. However, while they are widely usable in many biomedical fields, there are some limitations on the other hand. For example, poor mechanical properties restrict the set of possible applications. In fact, they often have low resistance, poor elasticity, poor ability to recover

the initial structure. They are therefore classified as mechanically weak systems [9]. Their morphological structure, characterized by pores with diameters in the order of nanometers, is appreciated, for example, for controlled drug release applications. However, in the case of biologically active molecules with high dimensions, release may be excessively slow. In such circumstances matrices with larger sized or erodible pores are more appropriate. Even in other fields, such as tissue engineering, matrices equipped with macropores are more suitable for application, promoting cell adhesion and proliferation [10]. For this reason, it is common to employ porogenic agents, which are added to the polymer solution before crosslinking. Nevertheless, there are two negative implications. First of all, it is not always possible to completely remove the porogenic agent and, if not biocompatible, this can negatively affect the properties of the matrix. Furthermore, a non-biocompatible and non-biodegradable porogenic agent generates equally non-biodegradable waste substances. In recent years, several alternatives of porogenic systems have been investigated with the intention of finding a less invasive solution with fewer consequences. The porogen with the fewest implications is represented by water in the solid state. In fact, if the crosslinking process is carried out at temperatures below the freezing temperature of the solvent, a phase separation occurs with the formation of solid domains - i.e. ice crystals - and liquid domains - i.e. the polymer solution. During this process, as the crystals grow, the liquid phase becomes increasingly concentrated: we speak of cryoconcentration. At the end of the synthesis process of this peculiar type of hydrogel, the matrices are freeze-dried and the place previously occupied by the ice crystals is replaced by air. The solvent crystals served as templates for the macroporous and highly interconnected network. This category of hydrogel is called cryogel. This approach leads to the formation of a particular class of hydrogels superporous, which are called cryogels [11].
The research work of this thesis is set within this context.

The following sections introduce in more detail the concept, preparation, and properties of cryogels, forming the core of the first part of this thesis.

1.2 Polymer gels: from hydrogels to cryogels

Among them, hydrogels are widely used because of their capability of absorbing large quantities of water and biological fluids [6]. The choice of the material to use for the preparation of a hydrogel strongly influences the final properties of the sample and, thus, its application field [7]. In fact, hydrogels are highly attractive for a wide range of biomedical applications, proving highly promising, such as systems for the delivery and modified release of drugs, scaffolds for tissue regeneration and for wound dressing [8]. Nevertheless, they have some structural and mechanical limitations - low resistance, poor elasticity, poor ability to recover the initial structure - which reduce their range of applications [9]. On the one hand this characteristic may be a valuable asset, as evidenced by controlled drug release. However, in the case of big molecules, the release could be too slow, thus negatively impacting. In this

situation, matrices with larger sized or erodible pores are more appropriate. Even in other fields, such as tissue engineering, matrices equipped with macropores are more useful. To overcome these limitations, it is common to use porogenic agents to be added to the polymer solution prior to crosslinking. Regardless, this practice has two negative aspects. The first is linked to the disposal of used substances. The second is that it is not always possible to have the complete removal of the porogenic agent after crosslinking. This can negatively affect the properties of the solid matrix. In recent years, several alternatives of porogenic systems have been investigated with the intention of finding a less invasive solution with fewer consequences. In this regard, the use of the cryo-gelling technique has been proposed. It involves the use of ice crystals as porogenic agents.This approach leads to the formation of a particular class of superporous hydrogels, which are called cryogels [11].
This old technology, which dates back to five decades ago, has been rediscovered due to its precious and unique properties. Cryogels share some features, such as a porous structure and superabsorbency, with hydrogels [33–36]. Nevertheless, from multiple perspectives, cryogels represent an improved version. Specifically, they are characterized by an open interconnected macroporous structure, and consequently a higher surface area, and display optimal liquid absorption capacities and greater mechanical performance. On the contrary, hydrogels show smaller pore size and low elasticity, which are not suitable for several applications [37, 38].

1.3 Preparation of cryogels and hydrogels: the mechanism of cryoconcentration and the influence of experimental parameters

The morphological and mechanical differences between hydrogels and cryogels arise from a distinct procedure of formation of the aforementioned scaffolds. As far as it concerns hydrogels, the polymerization and crosslinking process occur at room temperature. Cryogels, instead, are formed at a temperature below the freezing point of the solvent, therefore polymerization and crosslinking occur in the interstitial spaces between the ice crystals, which are subsequently removed by freeze-drying or thawing processes. In this way, the space previously occupied by the ice crystals, which play the role of porogens, is replaced by the corresponding interconnected porous network. Although low temperatures reduce the kinetics of the polymerization and crosslinking reactions according to Arrhenius' law, the partial freezing of the solvent determines the concentration of the polymer solution - referred to as cryoconcentration - in liquid microvolumes to the advantage of the gelation process. Thus, ice crystals act as a structural model for the pore walls. Cryoconcentration is considered to have a large impact in initiating a chemical reaction between microphases that are in a frozen state. In fact, the freezing process removes solvent molecules from the liquid microphase, increasing the concentration of the polymer solution and crosslinking agents. The existence of the liquid microphase also causes a depression of the freezing point, which further pro-

motes supercooling and enhances the cryogelation process. From a technical standpoint, achieving a well-defined cryogel structure requires that ice crystal nucleation occurs slightly before polymer crosslinking, ensuring proper cryoconcentration and phase separation. If the crosslinking kinetics are faster than crystallization, polymerization takes place without ice formation, yielding a hydrogel instead of a cryogel. Conversely, if crosslinking is too

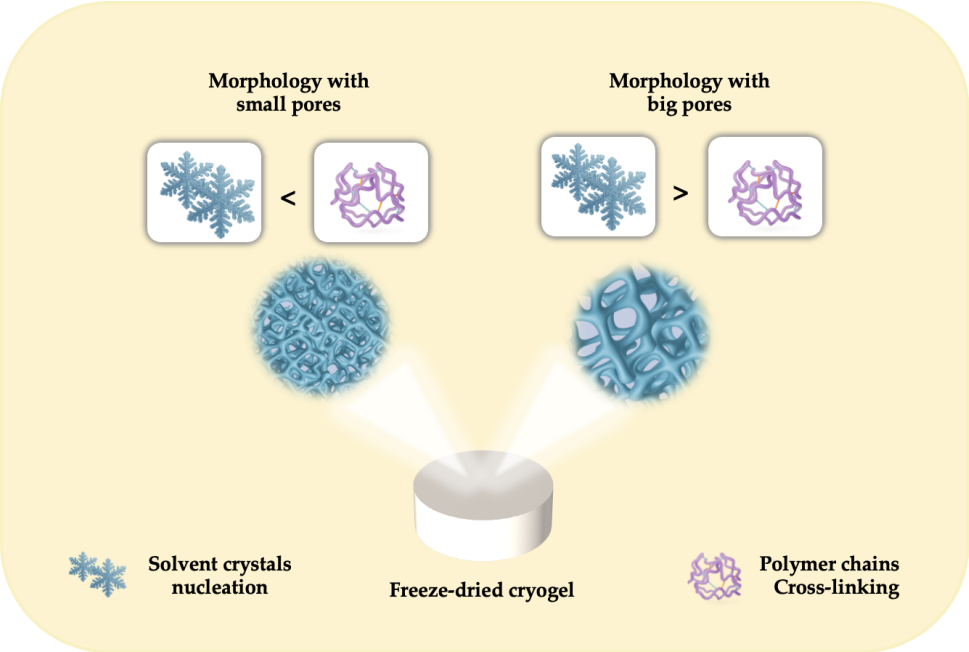


Figure 1.1: Pictorial representation of the effect of the balance between the freezing and the reticulation kinetics on the morphology of cryogel samples. When the crosslinking process prevails during the cryoconcentration, pores are small and have a low degree of interconnection. On the contrary, when the freezing process is dominant, scaffolds have large, highly interconnected pores.

slow, large ice crystals develop, resulting in a material with few but very large pores and a weakly cross-linked network. Therefore, the cryotropic gelation process represents a delicate balance between solvent crystallization and polymer crosslinking. This balance is fundamental in determining the architecture, morphology, and mechanical properties of the final cryogel. For a graphical representation see fig. 1.1. The physical properties and morphology of cryogels are governed by several parameters that must be carefully controlled during preparation. In particular, the final structure—namely the shape, size, and architecture of the pores—is strongly influenced by experimental conditions such as temperature, freezing rate, reaction time, crosslinking kinetics, and the concentrations of both the polymer and the crosslinking agent. For instance, increasing the concentration of reactive species accelerates crosslinking, while lower freezing temperatures enhance the freezing rate. Numerous studies have demonstrated a linear correlation between freezing rate and pore size: faster freezing leads to the formation of a greater number of smaller ice crystals, resulting in finer pores. A similar effect is observed with higher polymer concentrations, likely due to an in-

creased availability of reactive groups for crosslinking and a reduction in free water content, which becomes more involved in solubilizing macromolecules. By tuning these parameters, the properties of cryogels can be precisely tailored to suit specific applications. Both hydrogels and cryogels exhibit a porous internal network; however, cryogels, owing to their sponge-like macroporous structure, display superior and faster swelling behavior. Their interconnected pores also provide ample space for cell seeding and proliferation, as well as for the diffusion of nutrients and metabolic waste products. Moreover, cryogels exhibit enhanced mechanical performance compared with conventional hydrogels, including higher elasticity, resilience, and structural stability. They can withstand substantial deformation without rupture, demonstrating notable shape-memory properties, which make them suitable as injectable systems capable of retaining integrity and functionality post-injection. Mechanical properties, like internal morphology, are strongly affected by the experimental setup. An increase in polymer concentration typically results in greater rigidity and thicker pore walls. Due to the cryoconcentration phenomenon, the pore walls of cryogels are inherently thicker and denser than those of hydrogels, conferring excellent mechanical strength that is further modulated by the degree of crosslinking. Ultimately, the unique combination of tunable porosity, mechanical robustness, and high interconnectivity makes cryogels highly attractive materials for biomedical and biopharmaceutical applications. Fig. 1.2 gives an overview of the fields in which the macroporous structure of cryogels is exploited.

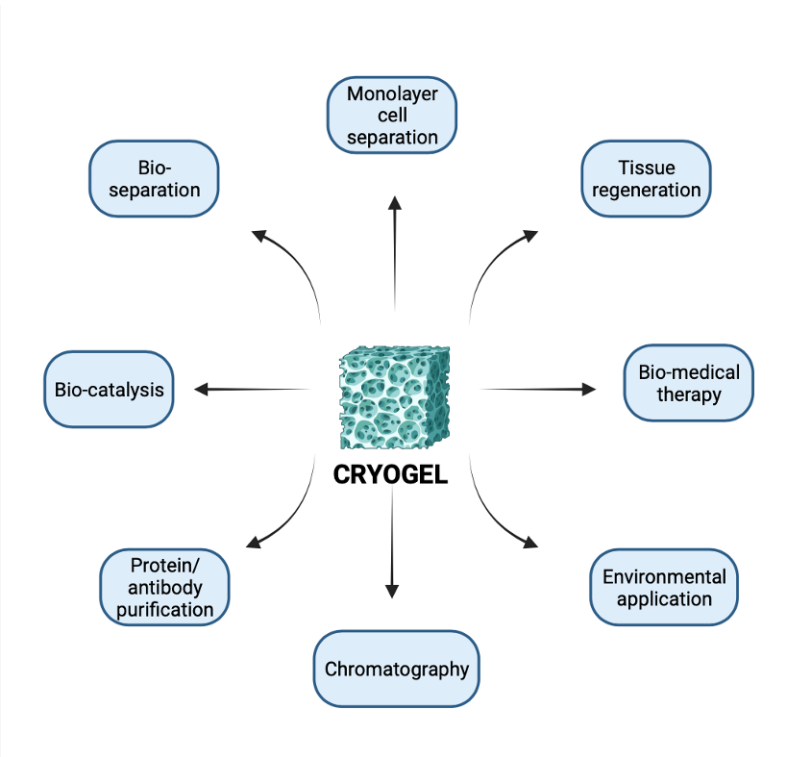


Figure 1.2: Graphical representation of the areas where cryogel matrices can be utilized.

1.4 Cryogels as Drug Delivery Systems for Controlled release

Modified-release pharmaceutical formulations are designed to deliver a constant amount of active pharmaceutical ingredient (API) over a defined period, enabling control over the rate, duration, and site of drug release. This approach improves patient compliance while minimizing adverse effects commonly associated with high therapeutic doses or frequent administrations [39]. Polymeric cryogels have been identified as promising materials for the development of *drug delivery systems* (DDSs). Their unique and highly tunable structural and physicochemical properties make them suitable for meeting specific therapeutic requirements [40]. For instance, cryogels enable the controlled release of active compounds, which can be modulated by varying the polymer composition, crosslinking density, or the physicochemical conditions of release. When designing a *carrier* for a specific API, both the loading capacity and the release kinetics of the system must be carefully considered. Hydrophilic drugs, bioactive peptides, and proteins can be incorporated either directly or indirectly—before or after the cryotropic gelation process [41]. In such cases, diffusivity is influenced by the degree of swelling and the crosslinking density of the polymeric network. In general, drug release from porous matrices occurs through either *diffusion* or *degradation* mechanisms [42]. In the former case, diffusion of the active ingredient through the polymeric matrix is strongly dependent on pore size and overall porosity. Specifically, the pores must be larger than the molecular diameter of the drug to allow its transport, and their dimensions can be tuned by modifying the physical characteristics of the system [41]. Alternatively, when the pore size of the network is smaller than the drug molecules, diffusion can still occur through processes such as *swelling*, *deformation*, or *degradation*, as schematically represented in Figure 1.3 [43, 44]. However, theoretical prediction of the drug release profile from cryogel matrices remains complex, due to the multiple chemical and physical interactions influencing the process [43]. It is reasonable to assume that the higher porosity and greater swelling capacity of cryogels allow for higher drug loading and a typically faster and more immediate release compared to hydrogels. Consequently, they may appear less suitable for prolonged or controlled release. Nevertheless, drug molecules can become temporarily entrapped within the pore walls of the cryogel, which may influence the overall release kinetics [43]. The slower release profile occasionally observed can be attributed to the *cryoconcentration effect* of the polymer–drug solution. The formation of ice crystals during cryogelation increases the concentration of the polymer solution, which then undergoes crosslinking and entraps the drug within the network [41]. A deeper understanding of the release mechanisms from cryogel systems could be instrumental in optimizing their performance, thereby enhancing both the safety and efficacy of the delivered therapeutic agents. However, while numerous studies have modeled the release behavior of hydrogel-based systems [45], relatively few have explored the corresponding mechanisms in cryogel matrices.

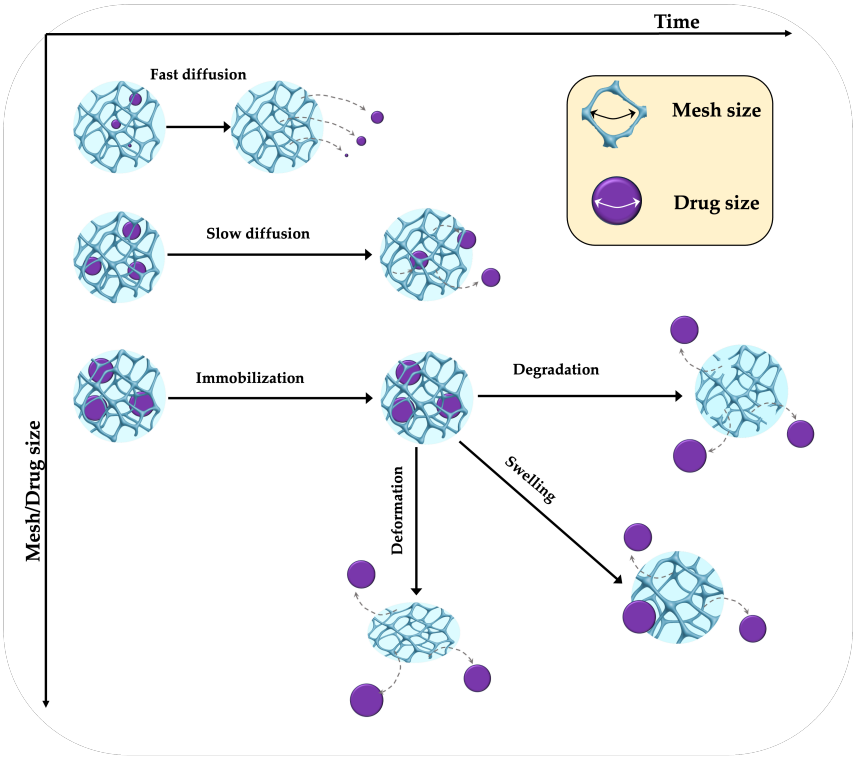


Figure 1.3: Graphical representation of the release mechanisms based on the ratio between the mesh size of the polymer mesh and the size of the drug molecule.

1.4.1 Modeling controlled release in polymer systems

Although numerous studies have attempted to model the release from polymeric matrices, including hydrogels [46–50], few articles have developed models that accurately describe the behavior of drug diffusion from cryogels [51–56].

From a theoretical standpoint, diffusion-controlled release from polymeric matrices is commonly described by Fick's second law:

$$\frac{\partial C}{\partial t} = D\nabla^2 C \tag{1.1}$$

where C is the concentration of the diffusing species and D is the effective diffusion coefficient.

Most applied models include the semi-empirical Higuchi and Korsmeyer-Peppas' equations [57–60], which do not fit properly some experimental findings [15]. Under simplifying assumptions, analytical solutions of Fick's law lead to the Higuchi model, which predicts a square-root dependence of the released mass on time:

$$M_t = k_H\, t^{1/2} \tag{1.2}$$

where M_t is the cumulative amount of drug released at time t and k_H is the Higuchi constant. Moreover, previous studies have reported important differences in the release profiles from dextran-based cryogels and hydrogels, that were attributed to a cryoconcentration phe-

nomenon affecting the drug during the criogelation process [61]. Despite this effect, cryogels are not highly efficient for the sustained release of small molecules [62, 63]. For this reason, different strategies have been proposed to better control the release behaviour of drugs from cryogels, including dextran-based cryogels [64]. Specifically, dextran has been combined with poly(N-isopropyl acrylamide) to develop thermoresponsive cryogels[65], with cyclodextrins [66] or with mesoporous bioactive glass [67]. Although these strategies proved to extend the drug release rate from dextran-based cryogels, better results would be achieved once the behavior of drug diffusion from cryogels could be accurately described. In this thesis, a mechanistic model is proposed to explain the anomalous non-Fickian trend of release curves of Vitamin B_{12} (cobalamin) from Dextran-based cryogels. The non-Fickian behavior observed cannot be attributed to a Case II diffusion process [59, 60], because the swelling process in cryogels is extremely fast and the release process occurs from a fully swollen sample. Depending on the drug loading procedures adopted, we observed two different release behaviours: a fast Fickian release when freeze-dried samples are infused with the drug after cryogel formation, or a retarded highly non-Fickian behavior, when the drug is loaded before the cryogelation process. The non-Fickian release, due to cryoconcentration phenomenon, has been modeled with a two-step release process, that accurately predicts experimental release curves characterized by a long lag time and a slower release, suggesting the opportunity to exploit this attribute with a view to the controlled release of the drug. This aspect represents a determining factor for numerous therapies and several models have been proposed in the literature [68–70], but none of them referring explicitly to cryogels.

1.5 Cryogels as Tissue engineering Scaffolds

Tissue engineering is a branch of biomedical engineering that studies the possibility of regenerating damaged organs and tissues without running into organ transplant problems, such as rejection reactions [71]. It allows the regeneration and replacement of the original tissues thanks to three-dimensional scaffolds, which promote cell adhesion, differentiation and proliferation. The ideal scaffold must be integrated into the tissues without inducing immune and inflammatory reactions, therefore it must be biocompatible and biodegradable; furthermore the degradation must be similar at tissue regeneration times [72–74]. Hydrogels have been widely used as polymer scaffolds due to their high water content and soft tissue-like physical properties. However, the small pore sizes (usually in the nanometer range) of conventional hydrogels have hindered their effective application in the field of tissue engineering due to limited cell penetration capacity and poor molecular diffusion of proteins, oxygen, nutrients and waste products [75]. The tissue engineering sector has undergone a major breakthrough thanks to the introduction of cryogels. The literature is increasingly extensive and detailed it shows how good they are and the advantages they offer: use of biocompatible monomers and solvents makes them suitable for vivo applications, both from the point of view of the absence of immunogenicity and cytotoxicity, both regarding cell growth. The highly inter-

connected macroporous structure allows these systems to retain large amounts of solvent, but also a large number of macromolecules and cells, so as to assure a stable environment for cell adhesion and migration. Furthermore, from a purely mechanical point of view, cryogels demonstrate high strength when subjected to compressive forces and traction, keeping their internal sponge-like structure intact [74]. Hwang *et al.* investigated the use of cryogels of only polyethylene glycol dimethacrylate in oligomeric form, as potential cellular scaffolds [76]. Specifically, the effect of polymerization conditions (varying based on the ratios of APS and TEMED reagents used and based on freezing temperatures) on the properties and internal microstructure of the systems was studied. Such systems have demonstrated, as expected, poor adhesion capacity to bovine chondrocytes (bCCs) and human mesenchymal cells (hMSCs). Therefore, in order to allow their use as cellular scaffolds, cryogels were subjected to coating with type I collagen. Systems with an exclusively cryogel structure were excellent supports for the adhesion of chondrocytes, with a cell viability of most of the cells up to 36 hours after culture, in addition to having a homogeneous distribution in structure and showing increasing proliferation as a function of time, thanks to the high available surface area due to pores. Similar response was found with human mesenchymal cells. In the systems that were instead synthesized in a heterogeneous way, that is, having partly a cryogel structure and partly a hydrogel structure, it was observed that the cells concentrated more in the area having cryogel structure, as well as showing less vitality once 36 hours had passed since culture, confirming that porosity and interconnection are characteristics of fundamental relevance in these scaffolds to promote their application in tissue engineering [76]. This work of thesis explored the potential use of hybrid dextran-gelatin systems as cellular scaffolds. As it happend in [76], the introduction of gelatin was fundamental in order to allow cell growth.

1.6 Swelling processes in polymer systems

When a dry polymeric gel is placed in a solvent, the solvent molecules penetrate into the 3D cross-linked network as a result of the chemical potential gradients that have been established. In consequence to uptake of solvent, the volume of the gel increases. This phenomenon is referred to as swelling process [77]. In the pharmaceutical and biomedical fields, swelling phenomena are fundamental. In fact, swelling can be exploited as a mechanism to control the drug release (the case of hydrogels, for instance) [78, 79]. Moreover, it permits the scaffold to absorb body fluids, deliver nutrients, and facilitate cell infiltration [80, 81]. Thus, being able to predict the swelling behaviour of soft materials is crucial since it affects cell viability and proliferation. There are several parameters that influence the entity of the swelling. For instance, the affinity among the polymer chains and the solvent molecules is one of them. The greater the affinity, the higher the amount of absorbed solvent. The amount of solvent absorbed by the gel depends not only on the polymer solvent interaction. In fact, the crosslinking density and the architecture of network affect the deformation, too. To better

understand this statement, a more detailed description of the phenomenon on a molecular scale is required. When solvent molecules diffuse through the 3D-network, polymer chains deform and stretch, consistently with the macroscopic deformation. As far as it concerns

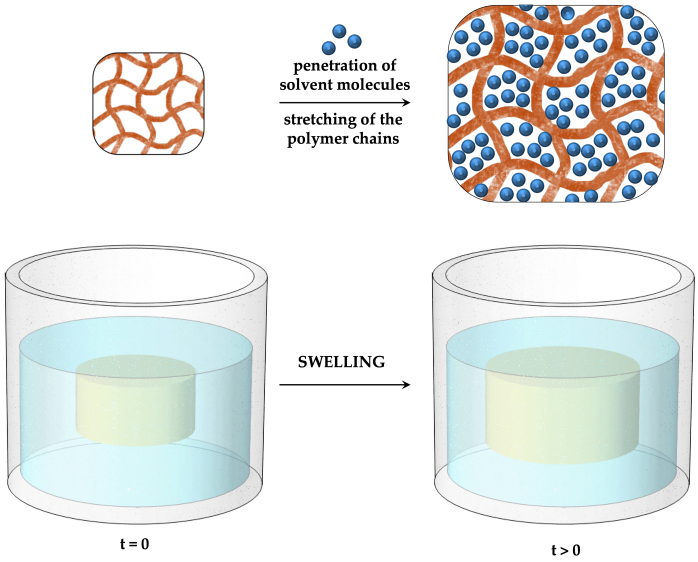


Figure 1.4: Representation of the swelling process on the macroscopic scale (the sample volume increases) and on the microscopic scale (polymer chains stretch and deform).

the equilibrium configuration, it is reached when there is a balance between the osmotic pressure arising from the interaction solvent-polymer and the elastic pressure resulting from the deformation of the reticulated polymer network. Figure 1.4 represents a pictorial description of the swelling phenomenon of a gel, both on a microscopic and macroscopic point of view. The swelling behavior can be characterized through the swelling ratio J_d, which is the ratio between the volume of the swollen sample V_{sw} and the volume of the dry sample V_{dry}, and the swelling capability Q, which can be expressed as the ratio between the mass of the swollen sample m_{sw} and the one of dry sample m_{dry}. Frequently, the solvent uptake Q_{ads} - i.e. the mass of absorbed solvent referred to the dry sample mass - is considered.

$$J_d = \frac{V_{sw}}{v_{dry}}, \qquad Q = \frac{m_{sw}}{m_{dry}}, \qquad Q_{ads} = \frac{m_{sw} - m_{dry}}{m_{dry}} \tag{1.3}$$

In the next paragraph, an overview about the models used for describing the mechanics of swelling, will be given.

1.6.1 Standard modeling of swelling processes: Mechano-Diffusion, Mixture Theory and Poromechanics

Swelling is an inherently coupled phenomenon, wherein the uptake or transport of a solvent (e.g., water, solute) induces significant mechanical deformation in the solid matrix (e.g., hydrogel, cryogel). Accurate predictive modeling of this process requires a framework that can self-consistently account for the interaction between mass transport and mechanical

equilibrium. This section provides an overview of the primary continuum-based theories used to describe swelling kinetics and equilibrium: Mixture Theory (formalizing multi- constituent interactions), Poromechanics (describing the hydro-mechanical coupling in porous media), and Mechano-Diffusion. To be precise, the main purpose of this short review is to explain the reasons that led to the adoption of the Mechano-Diffusion theory, adequately modified, in order to describe the swelling phenomena of cryogels, highly porous polymer systems. The main aspects of the Theory of the Mixtures and Poromechanics will be highlighted below, subsequently their critical issues will be discussed. The study object is a deformable porous solid media saturated with a fluid. Within the framework of gel mechanics and biomechanics, both phases are typically regarded as incompressible, since their bulk modulus greatly exceeds the magnitudes of the fluid pressures and the stresses generated in the body by swelling-induced deformation. Large-deformation analyses are often conducted in a Lagrangian system. Hence, in the following mechanical description a Lagrangian framework will be adopted, thus the reference frame is fixed to the solid skeleton. In this context, it is fundamental to introduce some aspects. Each point of the solid skeleton in the reference framework denoted with $\mathbf{X}$, while in the current configuration it is indicated as $\mathbf{x}$. The deformation gradient is $\mathbf{F} = \nabla\mathbf{x}$ and the corresponding determinant is the Jacobian $J = \det\mathbf{F}$. Mixture theory provides a rigorous continuum framework to model deformable porous media

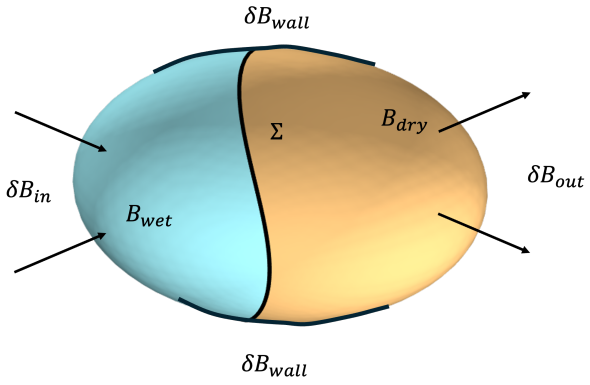


Figure 1.5: Graphical representation of the hydration problem.

permeated by fluids and describes the swelling phenomenon as a coupled chemomechanical process. According to this approach, the saturated porous system is treated as a binary mixture of an incompressible solid phase and an incompressible liquid phase (see fig. 1.5). From a mathematical perspective, the problem is modeled through the introduction of two moving boundaries, one referred to the solid skeleton and the other to the penetrating fluid. The central assumption is that, at any instant of time, each material point is simultaneously occupied by both phases (solid and fluid). Each constituent is continuous and satisfies its own mass and momentum balance equations. The key variables are the solid and liquid volume fractions- ϕ_s and ϕ_l - and the velocities of the solid and liquid components - i.e. $\mathbf{v}_s$ and $\mathbf{v}_l$. Following the rigorous formulation provided by Ambrosi [82], the system of equations

that describe the swelling of the porous body is listed below

$$\frac{\partial}{\partial t}\big[J(1-\phi_s)\big] + \nabla\cdot\big((1-\phi_s)(\mathbf{v}_l-\mathbf{v}_s)J\mathbf{F}^{-T}\big) = 0, \tag{1.4}$$

$$\nabla\cdot\big((\phi_s\mathbf{v}_s + (1-\phi_s)\mathbf{v}_l)J\mathbf{F}^{-T}\big) = 0, \tag{1.5}$$

$$\nabla\cdot\big((\mathbf{T}_s - \phi_s p\mathbf{I})J\mathbf{F}^{-T}\big) = \mathbf{0}, \tag{1.6}$$

$$(1-\phi_s)(\mathbf{v}_l-\mathbf{v}_s)J = -\frac{\mathbf{K}}{\mu}\nabla(pJ\mathbf{F}^{-T}). \tag{1.7}$$

At the boundary of the domain, suitable conditions guarantee mechanical and hydraulic consistency. Denoting by $\hat{\mathbf{n}}$ the outward normal in the reference configuration, the standard boundary conditions are:

$$(\mathbf{T}_s - p\mathbf{I})\mathbf{F}^{-T}\cdot\hat{\mathbf{n}} = \mathbf{t}_0 \qquad p = P_{\text{ext}}, \qquad \mathbf{v}_l\mathbf{F}^{-T}\cdot\hat{\mathbf{n}} = q_n \quad \text{at } \partial B_{in} \tag{1.8}$$

$$\big[\!\big[J\rho_s\boldsymbol{v}_s\otimes\boldsymbol{v} - J\mathbf{T}(e+1)\mathbf{F}^{-T}\big]\!\big] = 0 \quad \text{across } \Sigma_0 \tag{1.9}$$

$$\boldsymbol{v} = \mathbf{F}^{-1}(\boldsymbol{v}_l - \boldsymbol{v}_s). \tag{1.10}$$

where $\mathbf{t}_0$ is the external traction, P_{ext} the imposed pressure, and q_n the prescribed normal flux. For impermeable or rigid boundaries, the following conditions hold:

$$\mathbf{v}_s = \mathbf{0}, \quad \text{at } \partial B_{out} \tag{1.11}$$

$$(\mathbf{v}_l - \mathbf{v}_s)\mathbf{F}^{-T}\cdot\hat{\mathbf{n}} = 0 \quad \text{at } \partial B_{wall} \tag{1.12}$$

These relations express the continuity of total tractions and mass fluxes across the boundary and are consistent with the thermodynamic structure of the mixture theory. The tensor $\mathbf{T}_s$, which represents the Cauchy effective stress in the solid skeleton, must be specified through a constitutive equations. For instance, in the case of small deformation, $\mathbf{T}_s = \mathbb{C} : \mathbf{E}_s$, where $\mathbb{C}$ and $\mathbf{E}_s = (\nabla\mathbf{u}_s + \nabla\mathbf{u}_s^{\top})/2$ are respectively the elasticity tensor and the infinitesimal strain. For large deformations of a hyperelastic body, $\mathbf{T}_s$ must be derived form strain-energy relations depending on the deformation gradient

$$\mathbf{T}_s = \frac{1}{J}\,\mathbf{F}\,\frac{\partial W^{\top}}{\partial \mathbf{F}}\,, \tag{1.13}$$

According to the poromechanical approach [83],[84], the deformable solid matrix and the fluid saturating porous space are treated as the superimposition of two continua (see fig. 1.6). Traditional linear poroelasticity assumes infinitesimal strains and constant permeability, which is often inadequate for soft materials (e.g., gels, tissues) where finite volumetric changes and nonlinear effects dominate. In this case, the key state variables are the solid displacement $\mathbf{u}_s(\mathbf{X},t)$ and the pore pressure $p(\mathbf{X},t)$. The porosity $\phi_f = 1-\phi_s$ follows from the solid deformation through the Jacobian J, according to $J = (1-\Phi_{f,0})/(1-\phi_f)$, where

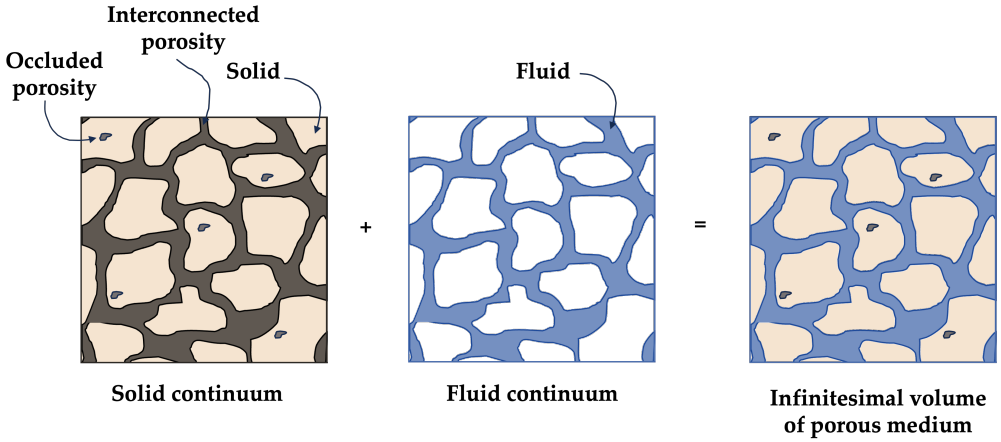


Figure 1.6: The porous elementary volume as the superimposition of the solid skeleton and the fluid continuum.

$\Phi_{f,0}$ is the reference porosity. The governing equations in the Lagrangian configuration then read

$$\nabla \cdot \left[J(\boldsymbol{\sigma}' - p\mathbf{I})\mathbf{F}^{-T} \right] = \mathbf{0} \tag{1.14}$$

$$\frac{\partial (J\phi_f)}{\partial t} + J\nabla \cdot \left[\phi_f (\mathbf{v}_f - \mathbf{v}_s)\mathbf{F}^{-1} \right] = 0 \tag{1.15}$$

$$\phi_f (\mathbf{v}_f - \mathbf{v}_s) = -\frac{k(\phi_f)}{\mu} \mathbf{F}^{-T} \nabla_0 p \tag{1.16}$$

The first equation enforces mechanical equilibrium of the solid–fluid mixture, the second represents fluid mass balance, and the third expresses Darcy's law in the solid reference frame. The total Cauchy stress $\boldsymbol{\sigma}$ is decomposed according to Terzaghi's effective stress principle,

$$\boldsymbol{\sigma} = \boldsymbol{\sigma}' - p\mathbf{I} \tag{1.17}$$

where $\boldsymbol{\sigma}'$ denotes the effective stress supported by the solid skeleton. The constitutive relation between effective stress and deformation derives from the hyperelastic potential $W(\mathbf{F})$,

$$\boldsymbol{\sigma}' = \frac{1}{J}\mathbf{F} \left(\frac{\partial W}{\partial \mathbf{F}} \right)^T \tag{1.18}$$

For isotropic materials undergoing large strains, a logarithmic Hencky-type elasticity is often adopted,

$$\mathbf{H} = \tfrac{1}{2} \ln\left(\mathbf{F}^T \mathbf{F}\right) \tag{1.19}$$

$$J\boldsymbol{\sigma}' = \Lambda \operatorname{tr}(\mathbf{H})\mathbf{I} + (M - \Lambda)\mathbf{H} \tag{1.20}$$

where $\Lambda = K - \frac{2}{3}G$ and $M = K + \frac{4}{3}G$, with K and G the drained bulk and shear moduli, respectively. The permeability $k(\phi_f)$ typically depends on the porosity and is described by

a Kozeny–Carman relation,

$$k(\phi_f) = k_0 \frac{(1-\Phi_{f,0})^2}{\Phi_{f,0}^3} \frac{\phi_f^3}{(1-\phi_f)^2} \tag{1.21}$$

The corresponding boundary conditions in this formulation are the following

$$\mathbf{u}_s = \bar{\mathbf{u}}_s \tag{1.22}$$

$$J(\boldsymbol{\sigma}' - p\mathbf{I})\mathbf{F}^{-T}\mathbf{N} = \bar{\mathbf{t}} \tag{1.23}$$

$$p = \bar{p} \tag{1.24}$$

$$\phi_f(\mathbf{v}_f - \mathbf{v}_s)\mathbf{F}^{-T}\mathbf{N} = \bar{q} \tag{1.25}$$

This nonlinear poromechanical formulation captures the strong coupling between the solid deformation and the pore pressure evolution that arises in soft or highly deformable materials. In the limit of infinitesimal strains and constant permeability, this formulation reduces to Biot's linear poroelasticity, where deformation and pressure are weakly coupled through diffusion-like processes. In contrast, the fully nonlinear theory captures the finite-strain kinematics, evolving permeability, and the strong two-way interaction between solid and fluid phases. On the ground of the previous outlines, it can be concluded that both the approaches present drawbacks, which are particularly evident when a computation analysis is required. This situation is related the basic assumption that the deformable porous body and the permeating fluid are two distinct interacting domains. The Lagrangian formulation is preferred because it simplifies the mathematical and computational formulation of the problem. In fact, the reference configuration is fixed to the solid skeleton. So, the computational domain is kept constant and there is no need to update it during the evolution of the deformation. However, the type of systems that are studied in this thesis work, cryogels, are supermacroporous polymeric gels with a high level of heterogeneity. Thus, a big portion of the body volume (around 70-80 %) is occupied by the liquid phase. In this context, the Lagrangian description fails because it describes the swelling phenomenon by tracking material point belonging to the solid matrix, while fluid motion is dominating and the deformation mechanisms occurring in the pore space is not properly captured. On the contrary, the Mechano-Diffusion theory [85] consider the hydrated body as a homogenized continuum, without directly discerning between the solid and liquid phases. This approach is founded on the statistical mechanics of polymer networks developed by Flory and Rehner [16, 17], which provides a thermodynamically consistent description of swelling by combining the elastic response of the polymer network with the thermodynamic contribution of solvent polymer mixing. Differently from the Mixture and the Poromechanical theories, in which the molecular-level mixing contribution is totally neglected, Mechano-Diffusion approach captures both the elastic deformation of the solid skeleton and the chemical potential of mixing that drives solvent absorption. Since it relies on a single homogenized body, the Mechano-

Diffusion model is more robust from a computational standpoint, and it does not involve tracking of individual domains or interfaces and is stable for large deformations and inhomogeneous swelling. Therefore, this model establishes a solid physical basis and computational efficiency for analyzing the swelling dynamics, thus it overcomes the strong limitations of mixture theory and poromechanics without losing the essential coupling. Furthermore, with proper modifications, it could be remain a valid model even in the presence of large fluid-filled regions, a situation that reflects the case of cryogel-like systems.

1.7 Cryogels in Chromatography

Monolithic structures (MS) have been getting more attention as stationary phases for liquid chromatography (LC) because of their permeability, mechanical integrity, and ease of fabrication. In this context, cryopolymerized systems matrices embody the perfect example of monolithic structure. Indeed, the distinctive microarchitecture of cryogel allows unhindered flow and low backpressures even at high flowrates [86, 87]. Over the past two decades, research in liquid chromatography (LC) has increasingly focused on developing new column designs to improve packing uniformity beyond that achievable with conventional packed-bed or monolithic silica columns. One promising approach involves the fabrication of highly ordered columns through in situ etching of micromachined pillar arrays using lithographic masks or using 3D-printing [27, 28]. Such advanced LC columns represent hierarchical porous media, combining large inter-pillar macropores with small intra-pillar micropores. This configuration provides both a regular flow path for efficient solute transport and a high surface area for adsorption–desorption processes. Because of their ordered periodic structure, the column can be modeled by analyzing a single unit cell, from which effective transport parameters can be derived using homogenization techniques. Several methodologies have been employed for this purpose, including multiple-scale expansion [88, 89], volume averaging [90, 91], and moment analysis([92]), which serve as alternative homogenization strategies to more computationally intensive methods such as stochastic Lagrangian simulations [93, 94], Computational Fluid Dynamics (CFD) / Direct Numerical Simulations (DNS and Lattice Boltzmann models [95, 96]. These techniques aim to estimate large-scale, or asymptotic, dispersion properties of solute transport. Recently, growing attention has been given to the transient behavior of dispersion, which becomes increasingly relevant with the miniaturization of analytical devices. As experimental time and length scales decrease, accurately describing transient transport becomes essential for interpreting chromatographic performance. The homogenization method proposed in this work enables the analysis of both the time evolution and asymptotic behavior of the effective velocity and dispersion tensor governing solute transport in hierarchical porous media with diffusion and adsorption–desorption in the microporous stationary phase. A careful bibliographic study has shown that the use of cryogels as stationary phases in chromatographic columns is very widespread [18–20]. In fact, these matrices are characterized by an internal morphology with large interconnected

channels and good mechanical properties, which can be modulated both through the used polymers and through the crosslinking conditions. For these reasons, cryogels allow separations with low diffusion resistances, low pressure drops and flowrates similar to those used in the case of High Performance Liquid Chromatography. On the other hand, macropores allow the passage of not only small molecules but also large cells and without the need for a previous feed purification treatment. Finally, the possibility of functionalizing the polymeric matrix makes it suitable for many chromatographic separation modes. The monolithic structure, compared to traditional packed beds, allows for better performance. A growing body of computational studies has demonstrated that ordered stationary phases can significantly reduce band broadening compared to random packings by minimizing eddy dispersion and mass transfer resistance [21–26]. By standardizing the internal channel architecture of the porous medium, ordered geometries in the stationary phase effectively mitigate these limitations. Prior investigations have shown that ordered arrays of pillars [27, 28], spheres, and other regular polygons [23, 29–32] can theoretically outperform randomly packed beds.

1.8 Structure of the Thesis

This thesis is organized to accompany the reader from the general framework of biomaterials to the specific design and optimization of cryogels based on dextran, and finally to their technological application. This study encompasses both experimental and theoretical studies, including computational modeling. The experimental aspect revolves around the preparation and characterization of methacrylated dextran cryogels as well as the influence of polymer concentration, initiator ratio, and other process parameters on the final structure and swelling behavior. The theoretical aspect of this thesis aims to simulate the transport and swelling processes occurring in such porous polymeric systems and investigate the ordered geometries that can be used as stationary phases in chromatography.

Chapter 2 discusses the present state-of-the-art development of hydrogel and cryogel materials, their preparation methods, and their uses in biomedicine, emphasizing the dominant theoretical approaches to describe the swelling and diffusion processes.
Chapter 3 presents the materials, reagents, and procedures used for polymer synthesis, cryogel preparation, and the characterization techniques.
Chapter 4 details the optimization of the dextran-based cryogel (dextran 40,000 units functionalized with 2-Hydroxyethyl methacrylate), in which the cryogel formation window is determined as a function of reagent concentration and methacrylic group concentration.
Chapter 5 introduces other dextran derivatives with varying molecular weights and spacer chain lengths and provides degradation studies and mechanical property analyses as well as a two-phase diffusion model for vitamin B_{12} release.
Chapter 6 examines blended systems involving Dextran (DEX) and Methacryloyl Gelatin (GelMA) to enhance biocompatibility, including preliminary cell adhesion and proliferation studies.

Chapter 7 proposes a modified Mechano–diffusion model to describe the swelling behavior of cryogel systems.
Finally, Chapter 8 analyzes triply periodic minimal surface geometries as ordered structures for 3D-printed chromatographic stationary phases.
The conclusions present the results obtained and outline the future directions.

1.9 Overview of the Experimental and Theoretical Work

In essence, this work is divided into an experimental investigation (the methodologies adopted, including the synthesis of polymers and cross-linked systems and the study of physical properties, are reported in Chapter 2) with related modeling of pharmaceutical release phenomena and, preliminarily, of the swelling dynamics, and in a purely computational part, to explore possible new geometries to be adopted in the 3D printing of stationary phases in the chromatographic field.
A significant part of the work focused on the optimization of cryogel-type matrices based on methacrylic derivatives of dextran (DEX), an exopolysaccharide synthesized by lactic acid bacteria. As a non-toxic, biocompatible, biodegradable and strongly hydrophilic biopolymer, DEX is highly appreciated in the industrial and biomedical fields [12]. To proceed with the optimization of cryogel systems with biomedical applications, it was necessary to analyze how different parameters that intervene in the formation process of this matrix influence its morphological and mechanical properties. For this reason, a methacrylic derivative of dextran with good biodegradability and biocompatibility characteristics was first selected: dextran (40,000 units) functionalized with 2-hydroxyethylmethacrylate (HEMA) - i.e. DEX_{40}HEMA. The presence of a carbonate bond from the methacrylic group and the dextran chain makes this polymer advantageous for regenerative medicine and drug delivery system applications, despite having less chemical stability than dextran methacrylate (DEX_{40}MA) in which among the methacrylic group dextran there is only one ester bond. The optimization analysis was carried out keeping the volume of polymer solution (2 mL) and the temperature of the cryostatic bath constant (-12 ± 0.5 °C). Furthermore, the molar ratio between the two reagents used, ammonium peroxydisulfate/N,N,N',N'-tetramethylethylenediamine, APS/TEMED was kept fixed at 0.9. Therefore, the parameters to be investigated were reduced to the polymer concentration, i.e. the mmoles of methacrylic groups (MGs) in the starting solution, and to the concentration of reagents, in terms of the APS/MG molar ratio. Therefore, it was decided to act directly on the crosslinking kinetics and, indirectly, on the freezing kinetics. The temperature was not varied, but polymer solutions with different concentrations of the components lead to different cryoscopic lowering effects. Regarding the concentration ranges, it was observed that no cross-linked polymer structure is formed below 2.5 % w/v (0.015 $mmoles_{MG}$), while above 9.4 % w/v (0.055 $mmoles_{MG}$) matrices are obtained that are too massive for the desired purposes. Subsequent analysis involved systems at the following concentrations: 2.5 % w/v, 4.2 % w/v, 6.0 % w/v, 7.6 % w/v, and 9.4 %

w/v, corresponding, respectively, to 0.015 mmoles_{MG}, 0.025 mmoles_{MG}, 0.035 mmoles_{MG}, 0.045 mmoles_{MG}, and 0.055 mmoles_{MG}. For each system, the $\text{mmoles}_{APS}/0.015\ \text{mmoles}_{MG}$ ratios were varied to locate its lower and upper bounds. Both were characterized through swelling tests and, as regards the lower limit, by evaluating the fraction of cross-linked polymer (gel fraction GF). Among systems with a low concentration of reagents, systems with GF greater than 0.75–0.80 have been classified as cryogels. Although the upper limit is concerned, the swelling behavior was analyzed both in terms of trend—how quickly equilibrium is reached—and considering the quantity of solvent absorbed at equilibrium—i.e. the degree of Q swelling expressed as weight ratio between the masses of the hydrated system and the dry one. Unlike a hydrogel, the swelling dynamics of a cryogel is characterized by high solvent uptakes and rapid achievement of the equilibrium condition (from a few seconds to a few minutes). This situation is determined by the particular microarchitecture of the cryogel system. In addition, a preliminary evaluation was made on the effect of oxygen as a quencher of the radical reaction. The adopted synthesis protocol requires the polymer solutions to be in contact with air for the entire duration of the procedure. It follows that oxygen, present in dissolved form within the solution, can interfere with the radical reaction. To investigate the extent of this situation, the following methodology was adopted. Inert nitrogen was blown into the solution—eliminating the oxygen—and keeping this inert atmosphere until the end of the cryoreticulation.

In Chapter 4 is described the following step of the optimization of dextran-based matrices. It was decided to investigate other methacrylic derivatives of dextran. In particular, the effects of the molecular weight of the DEX chain (DEX_{40} and DEX_{500}, respectively if composed of 40,000 or 500,000 units) and the spacer length (2-HEMA, or polyethylene glycol with average molecular weight 360 or 500, PEG_{360}MMA and PEG_{500}MMA). On the basis of the information obtained from the formation window, cryogels were prepared from polymer solutions containing 0.035 mmoles_{MG} and with a ratio $\text{mmoles}_{APS}/\text{mmoles}_{MG} = 0.6$ that would guarantee a GF close to unity. These systems were compared in terms of degree of swelling, biodegradation times and mechanical properties. In addition, release studies involving loading of the model molecule, cobalamin, were carried out according to two different procedures. In the first, vitamin B_{12} is dissolved in the starting polymer solution before the addition of the reagents and has therefore actively participated in the crosslinking process. The second methodology involved, however, variation by infusion on lyophilic samples, subsequently frozen and re-dried before being subjected to release tests. Preliminary analysis showed a highly non-Fickian trend in the case of pre-loading. In contrast, after-loading leads to release kinetics more similar to Fickian ones. It was therefore hypothesized that this behavior was due to an involvement of vitamin B_{12} in cryoconcentration, which would have determined its entrapment in the microporous domain (the polymeric network). In conformity with these assumptions, it was built a model which involves the presence of two phases: a microphase (polymeric network) and a macrophase (porous network). During release, the drug trapped in the microphase is irreversibly released into the macroporous phase from which it can diffuse into the liquid reservoir. Since the model predicts that at the boundary

the concentration of drug is equal to the homogeneous concentration of the liquid reservoir at any moment, there is no need to assure that the perfect sink conditions are respected. The evaluation of diffusivities was carried out on the basis of asymptotic data.
The mechanical and morphological properties of cryogels make such structures very attractive for regenerative medicine application. In fact, the large, highly interconnected pores allow the exchange of nutrients and waste with the surrounding environment, while the thick and resistant walls promote adhesion. However, such characteristics are not sufficient when cells come into play. In fact, the chemical properties of the starting polymer matrix must be considered. For example, dextran, as a polysaccharide, does not contain the essential amino acids that the cell needs [13, 14]. In order to overcome this obstacle it was decided to use a blended system by introducing gelatin methacrylate (GelMA), a polymer obtained by denaturing porcine collagen, and which contains the amino acids necessary for both cellular metabolism and proliferation. In this way, these characteristics of GelMA were exploited, and the mechanical properties of dextran-based systems were simultaneously exploited. Therefore, as set out in Chapter 5, blended systems based on methacrylic derivatives of dextran and methacrylated gelatin were prepared, starting from polymer solutions containing 0.050 $mmol_{MG}$ and with APS/MG molar ratios of 0.45. These systems were selected starting from the previous work [15] in which samples based on GelMA and $DEX_{40}MA$ were analyzed, a less biocompatible alternative to the polymers investigated in this thesis. The matrices were characterized physically, morphologically and mechanically. In addition, preliminary tests of cell adhesion and proliferation were carried out by seeding aneuploid immortal human keratinocytes (HaCat).
Swelling, which has been analyzed for all the studies previously described, represents a fundamental phenomenon in the biomedical field, which deserves in-depth modeling. Indeed, the swelling behavior of polymers governs their mechanical integrity, transport properties, and environmental responsiveness. Modeling this process is essential to predict material performance, enable rational design, and control functionality across diverse polymer-based applications. In Chapter 6 a strategy to approach the modeling of cryogel systems is given. In the literature there are several theories that describe the swelling mechanics of hydrogels, for example Mechano-Diffusion, or of porous systems, such as mixture theory and poromechanics. While the first does not consider systems with macroporosity and in fact the analyzed hydrogels only have pores in the order of nanometers, the description of the hydration of the porous systems in the other two theories occurs through a Lagrangian framework (i.e. the deformation follows the solid skeleton), not suitable for situations in which a large volume is occupied by liquid, and does not consider the interaction between polymer and solvent. Therefore, the theory of Mixture and Poromechanics are not suitable for modeling swelling phenomena in cryogels. As part of this thesis, it was therefore chosen to modify the theory of Mechano-Diffusion, a rigorous homogenization approach which considers the polymer-solvent system as a single continuous body. Moreover, it is based on the statistical mechanics of polymers by Flory and Rehner [16, 17], thus the effect of the interaction between the two constituents on the swelling capability is taken into consideration. To have experimental

data as far as it concerns both the swelling degree Q and the volumetric ratio J_d, swelling tests on samples prepared from Dextran methacrylate, a very chemically stable system, were performed. As a starting point, the basic model was modified by introducing the porosity and a preliminary analysis of it was carried out.
A careful bibliographic study has shown that the use of cryogels as stationary phases in chromatographic columns is very widespread [18–20]. In fact, these matrices are characterized by an internal morphology with large interconnected channels and good mechanical properties, which can be modulated both through the used polymers and through the crosslinking conditions. For these reasons, cryogels allow separations with low diffusion resistances, low pressure drops and flowrates similar to those used in the case of High Performance Liquid Chromatography. On the other hand, macropores allow the passage of not only small molecules but also large cells and without the need for a previous feed purification treatment. Finally, the possibility of functionalizing the polymeric matrix makes it suitable for many chromatographic separation modes. The monolithic structure, compared to traditional packed beds, allows for better performance. A growing body of computational studies has demonstrated that ordered stationary phases can significantly reduce band broadening compared to random packings by minimizing eddy dispersion and mass transfer resistance [21–26]. By standardizing the internal channel architecture of the porous medium, ordered geometries in the stationary phase effectively mitigate these limitations. Prior investigations have shown that ordered arrays of pillars [27, 28], spheres, and other regular polygons [23, 29–32] can theoretically outperform randomly packed beds. Based on these statements, a purely theoretical and computational analysis of ordered structure serving as stationary phases was conducted in Chapter 8, developed in Section II. More in detail, the exact moment method for the determination of the dispersion tensor in retentive porous media has been adopted to compute the dispersion coefficients, the plate height curves and the kinetic performance factors of eight different 3D printable stationary phases based on triply periodic minimal surfaces (TPMS). The three cases in which the stationary phase is impermeable (hydrodynamic dispersion) or superficially retentive or fully porous have been analyzed in detail.

Part I

Dextran-based cryogels for biomedical purposes

Chapter 2

Materials and methods

2.1 Materials

All used reagents were of analytical grade. Type A gelatin from porcine skin (∼300 Bloom), dextran (DEX) from *Leuconostoc mesenteroides* (Mn 40,000, DEX_{40}; Mn 500,000, DEX_{500}), methacrylic anhydride (MAA), hydroquinone mono-methyl ether, N,N′-carbonyldiimidazole (CDI), N-methyl-2-pyrrolidone, 4-dimethylaminopyridine (4-DMAP), anhydrous dimethylsulfoxide (DMSO), anhydrous tetrahydrofuran (THF), nicotinamide (NIC), ammonium persulfate (APS), N,N, N′, N′-tetramethylethylenediamine (TEMED), glycidyl methacrylate (MGA), hydroxyethyl methacrylate (HEMA), polyethylene glycol mono-methacrylate (Mn 360 and 500; PEG_{360}MMA and PEG_{500}MMA), deuterated water D_2O, dialysis membranes (cut-off 12–14 kDa), the vitamin B12 (98% in cyanocobalamin), L-glutamine and methanol for HPLC (MeOH) were purchased from Sigma - Aldrich (Merck KGaA). Double distilled water, absolute ethanol (EtOH), 2-methoxyethanol, acetic acid (CH_3COOH), 37% w/w hydrochloric acid (HCl), monobasic potassium phosphate (KH_2PO_4) and sodium hydroxide in pellets (NaOH) were purchased from Carlo Erba. Fluorescent calcein (Invitrogen), fetal bovine serum (FBS), phosphate-buffered saline (PBS, 10X), and the penicillin/streptomycin antibiotic mixture (10,000 U/mL) were purchased from ThermoFisher Scientific. The culture medium DMEM-F12 was purchased from Lonza. All reagents were of analytical grade.

2.2 Polymer synthesis

2.2.1 Synthesis of dextran methacrylate

Synthesis of DEX_{40}MA was carried as reported in previous studies [15, 97]. DEX_{40} (2.5 g) was solubilized in anhydrous DMSO (20 mL) at room temperature under magnetic stirring for 24 hours. After complete dissolution, 4-DMAP (0.71 g) and MGA (0.26 mL) were added. The reaction mixture was maintained under magnetic stirring at room temperature for 24 hours. At the end of the reaction time, the solution was precipitated dropwise into 100 mL of absolute ethanol under continuous stirring. The precipitate underwent vacuum filtration

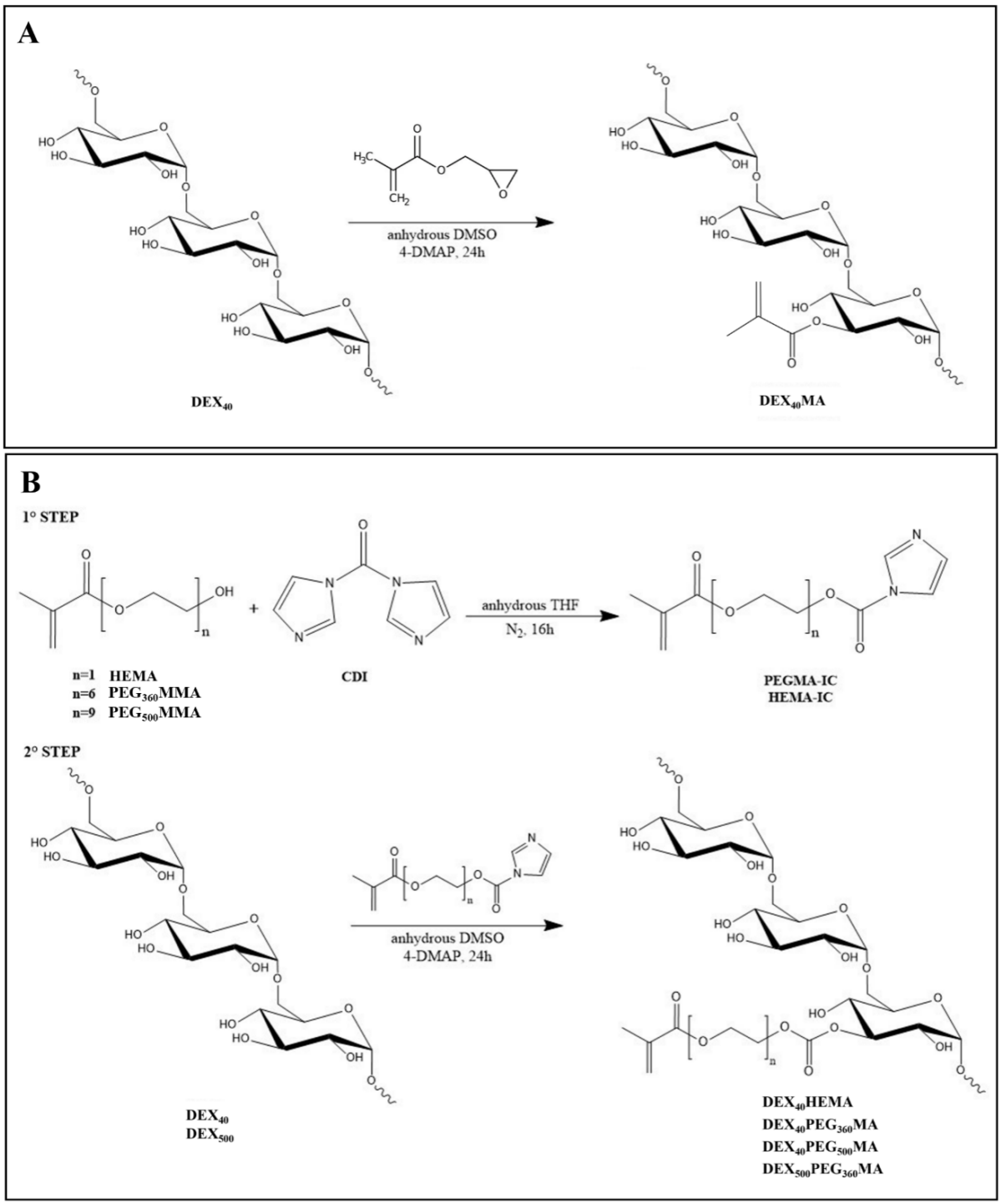


Figure 2.1: Scheme of the synthesis of $DEX_{40}MA$ (**A**) and the other dextran derivatives, i.e. DEX-HEMA and DEX-PEGMA (**B**).

and was redissolved in distilled water (30 mL). The solution was neutralized with HCl (1N). Subsequently, it was dialyzed against distilled water for three days and finally it was freeze-dried. To characterize the lyophilised polymer, ^{1}H-NMR analysis was performed with a Bruker Avance 400 spectrometer (Rheinstetten, Germany). The ^{1}H-NMR spectrum was recorded in D_2O and using NIC as internal standard. To this purpose, 10 mg of polymer were dissolved in 0.4 mL of D_2O and 0.2 mL of NIC solution in D_2O (1mg/mL). The obtained degree of methacrylation was 5% ±1%.

2.2.2 Synthesis of dextran derivatives

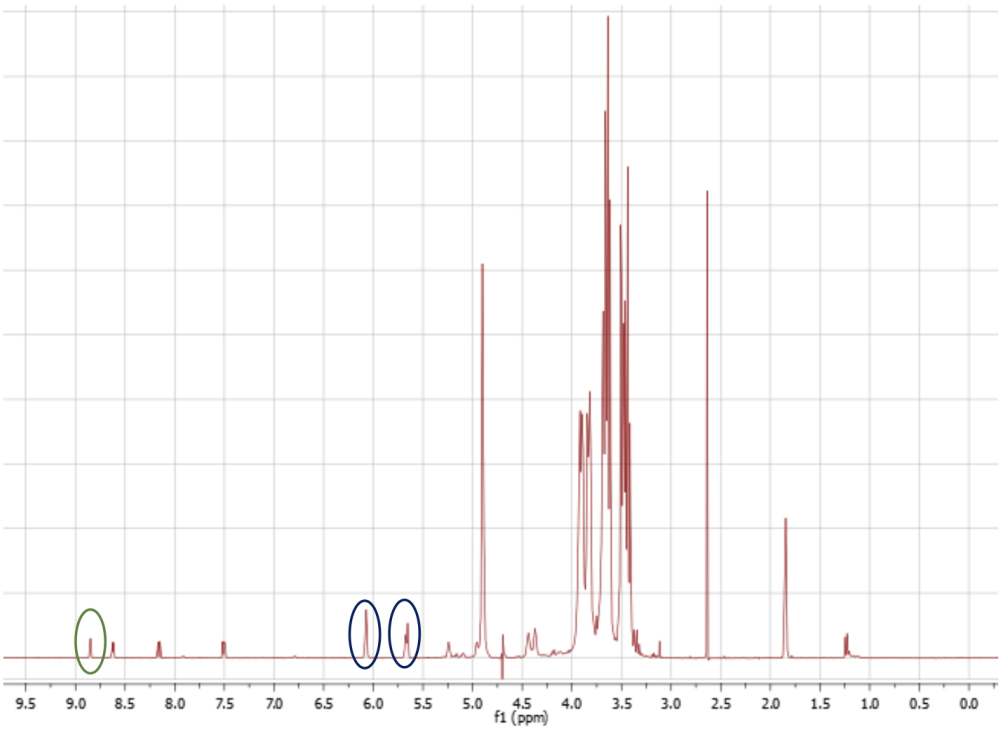


Figure 2.2: ^{1}H NMR spectrum of Dex40HEMA in D2O. The green-circled signal corresponds to the internal standard, whereas the blue-circled signals correspond to the methacrylic protons of the polymer.

The other methacrylic derivatives of dextran were synthesized as described in previous works [98, 99], with slight modifications. The synthesis procedure involved two steps. In the first one, 2-HEMA (0.29 g, 2.2 mmoles), $PEG_{360}MMA$ (0.80 g, 2.2 mmoles) or $PEG_{500}MMA$ (1.10 g, 2.2 mmoles) was dissolved in anhydrous THF (7 mL) and, following this, CDI (0.37 g, 2.2 mmoles) was added. The reaction was carried out under nitrogen atmosphere for 16 hours at room temperature. So, hydroquinone mono-methyl ether (0.12 g) was added to the intermediate and HEMA-IC (hydroxyethyl methacrylate N-imidazoylcarbamate) or PEMGA-IC (polyethylene glycol N-imidazoylcarbamate) was obtained after evaporating THF under reduced pressure conditions. In the second step, DEX (2.4 g, 14.8 mmoles of glucose repetitive unit) was dissolved in anhydrous DMSO (18 mL in the case of DEX_{40} and 25 mL in the

case of DEX_{500}) and the catalyst 4-DMAP (0.47 g, 3.85 mmoles) was introduced. HEMA-IC or PEMGA-IC were added to the mixture without purification and the system was left to react for 24 hours under magnetic stirring at room temperature. The reaction scheme of the synthesis of $DEX_{40}MA$ and dextran derivatives is reported in Figs. 2.1(**A**)-(**B**). The obtained mixture was precipitated dropwise in absolute ethanol (100 mL) for DEX_{40} and in methoxyethanol (150 mL) for DEX_{500}. The subsequent filtration allowed the separation of the solid phase which was dissolved in distilled water (20 mL for DEX_{40} and 40 mL for DEX_{500}) and it was neutralized with HCl (2 M) to avoid basic hydrolysis. The polymeric solution was dialyzed in distilled water, frozen and then lyophilized by using a LIO 5P freeze-dryer (5 Pascal, Milan, Italy). After the freeze-drying process, the polymers were characterized through ^{1}H-NMR analysis. The ^{1}H-NMR spectra were recorded in the presence of NIC used as internal standard. ^{1}H-NMR samples were prepared by solubilizing 10 mg of polymer in 0.4 mL of D_2O and 0.2 mL of NIC solution in D_2O (1 mg/mL). The degree of derivatization DD% was calculated basing on the peaks of the standard and of the methacrylic groups. The value of the achieved DD% was of 5%±1% for all the synthesized polymers. For an in-depth discussion of ^{1}H-NMR spectra of dextran derivatives see [98].

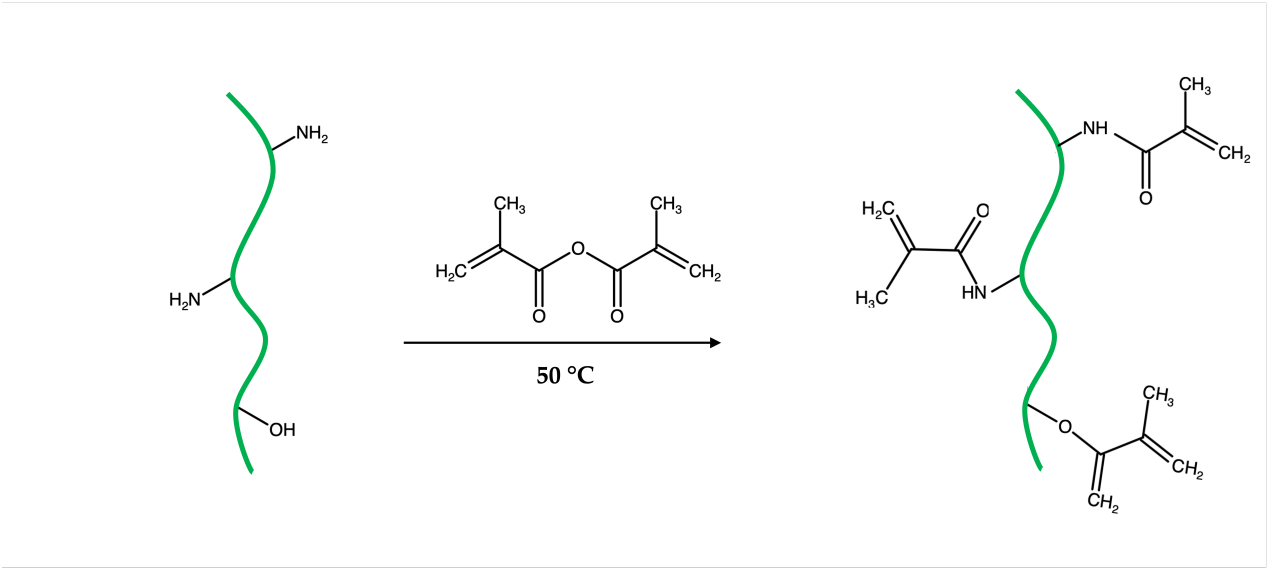


Figure 2.3: Scheme of the single-phase synthesis of GelMA.

2.2.3 Single-phase synthesis of Methacryloyl gelatin

The synthesis of methacryloyl gelatin (GelMA) was carried out according to the general scheme reported in fig 2.3 and performed following the single-step procedure previously optimized in our laboratories. Specifically, 1 g of gelatin was dissolved in 20 mL of anhydrous DMSO at 50 °C for 2 h under magnetic stirring. Subsequently, 0.3 mL of MAA/g Gel was added, and the solution was kept under stirring for 3 h at 50 °C. At the end of the reaction, the product was dialyzed against distilled water at 37 °C for 3 days. Finally, the polymer solution was frozen at –50 °C and lyophilized. After the freeze-drying process, the polymers

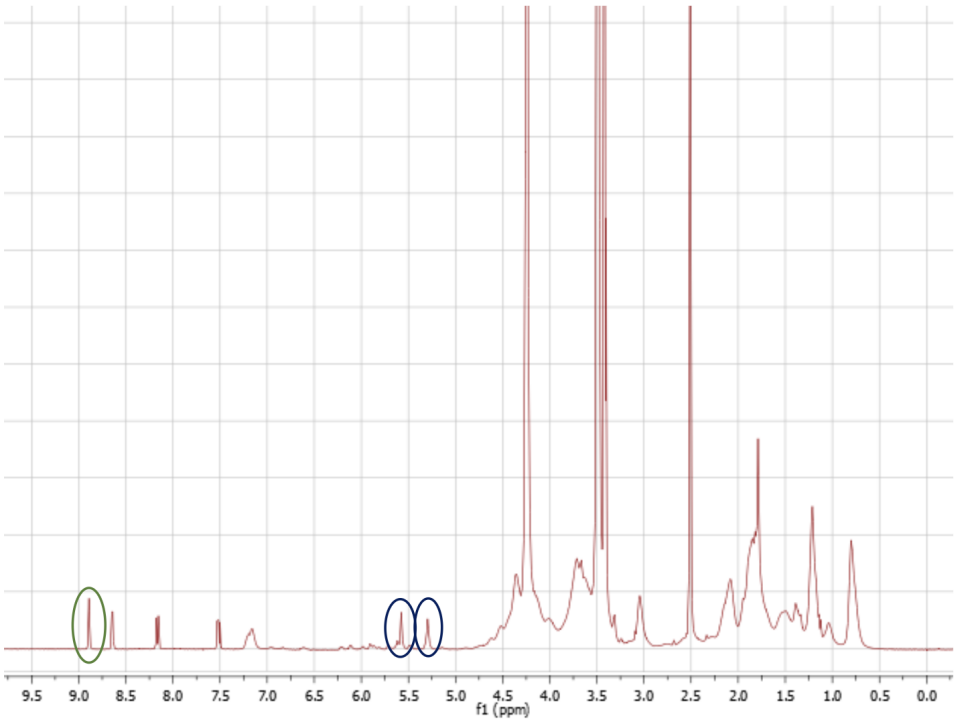


Figure 2.4: ^{1}H NMR spectrum of GelMA in DMSO-d_6. The green-circled signal corresponds to the internal standard, while the blue-circled signals correspond to the methacrylic protons of the polymer..

were characterized through ^{1}H-NMR analysis. The ^{1}H-NMR spectra were recorded in the presence of NIC used as internal standard. ^{1}H-NMR samples were prepared by solubilizing 10 mg of polymer in 0.4 mL of D_2O and 0.2 mL of NIC solution in D_2O (1 mg/mL). The degree of derivatization DD% was calculated basing on the peaks of the standard and of the methacrylic groups (see Fig. 2.4). The value of the achieved DD% was of 0.53 $\pm$ 0.02 mmol/g.

2.3 Preparation of Dextran-based gel systems

Dextran-based chemical gels were prepared by free radical crosslinking reaction, triggered by the presence of the two reagents APS and TEMED. Following a reaction with water, the peroxydisulfate anion initiates the radical process, releasing the free radials sulphate (HSO_4) and hydroxyl (OH). However, since the decomposition of APS occurs only at high temperatures (about 70 °C) or after long reaction times, it is necessary to employ a catalyst, as TEMED. This tertiary amine, following a complexation reaction with APS, accelerate the formation of the radicals which, reacting with the methacrylic groups of DEX, lead to the formation of chemical polymer networks. Fig. 2.5 gives a schematically representation of the redox reaction.

It must be underlined the potential toxicity of the APS/TEMED redox initiation system and the need of cytotoxicity studies on the proprosed cryogel systems. However, it should

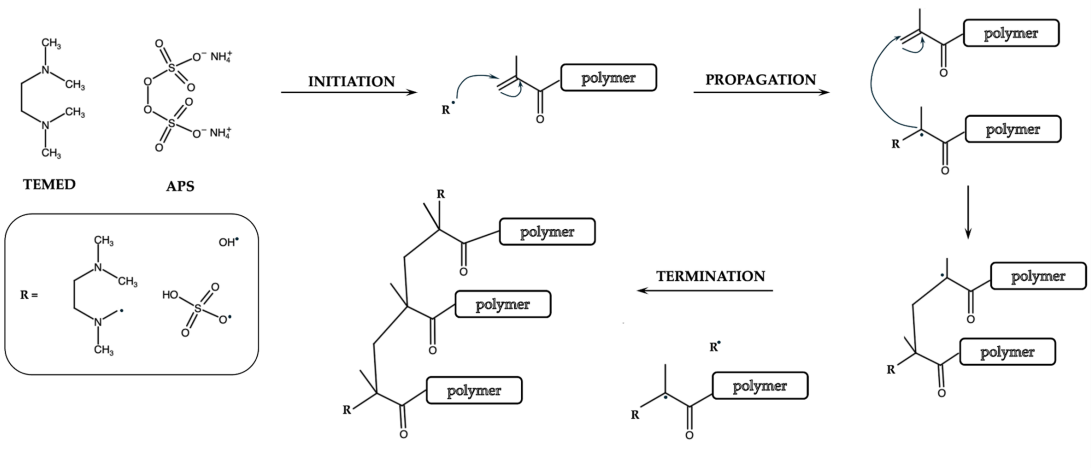


Figure 2.5: Mechanism of radical crosslinking initiated by APS and TEMED.

be considered that one of the advantages of cryogels over the corresponding hydrogels is the need for smaller amounts of crosslinking reagents for network formation due to the cryoconcentration process. In light of this consideration, cryogels might be safer than the corresponding hydrogel systems. In any case, other biocompatible crosslinking methods can be applied to develop cryogel networks, such as those recently reviewed by Maiti et al. and Alavarse et al. [100, 101] or safer alternatives to TEMED, such as those proposed by Pumford et al. [102]. We have not yet performed cytocompatiblity studies on these cryogels, although they are obviously possible as sterile cryogels can be obtained by fabrication under aseptic conditions, with a standard procedure that requires that all the components of the pregel solution are sterilized separately, and then aseptically blended. This procedure, aimed at obtaining sterile cryogels, is usually adopted in all cases where final sterilization may cause substantial modification or degradation of the drug. All cryogels have been prepared with a freezing procedure that lasted 2 hours. It was verified that the crosslinking reaction is completed after this interval of time. Indeed, it was observed no differences between samples obtained by prolonging the cryogelation up to four and six hours [15].

2.3.1 Preparation of DEX_{40}HEMA cryogels and hydrogels for the formation window.

Cryogels were prepared by free radical crosslinking of DEX_{40}HEMA in distilled water, using the redox initiation system APS/TEMED. The crosslinking reaction was carried out in the presence of oxygen or after its removal, following the procedures described in subsections 2.3.1 and 2.3.1, respectively.

Air

A certain amount of Dex_{40}HEMA was dissolved in distilled water at room temperature, through magnetic stirring for 15 minutes. Following the complete solubilization of the polymer, appropriate volumes of APS and TEMED taken from 5% w/v solutions were added,

while making sure to maintain the final volume of the polymer solution constant and equal to 2 mL. The mixtures were allowed to homogenize for 30 seconds, transferred rapidly to a cryostat at the temperature of -12°C ± 0.5°C and mantained in such conditions for 2 hours, before undergoing the freeze-drying step.

As already mentioned, Dex_{40}HEMA was selected to outline the formation window of cryogel-like networks. To this end, the concentration of APS and methacrylic groups (MG) was opportunely varied with the scope of identifying the limiting conditions that allow the formation of cryogel-like networks. This procedure was repeated for several numbers of mmoles of methacrylic groups (0,015, 0.025, 0.035, 0.045, 0.055 $mmoles_{MG}$), which means different concentrations of the systems (2.5, 4.2, 6.0, 7.6 and 9.4 % w/v). The ratio $mmoles_{APS}/mmoles_{TEMED}$ was fixed equal to 0.9 in any analyzed case.

As far as it concerns hydrogels, the procedure of preparation was similar to the one of cryogels. However, after APS and TEMED were added, the systems were left at room temperature for 24 hours and frozen at -12°C ± 0.5°C for 20 minutes. Finally, they were lyophilized and the macroporous scaffolds were obtained.

It should be pointed out that crosslinking of the polymer at room temperature was only possible with Dex_{40}HEMA concentrations of 7.6% and 9.4% w/v and employing a $mmoles_{APS}/mmoles_{MG}$ ratio of 3.00 and 2.00, respectively.

Detailed information about the investigated polymer concentrations and $mmoles_{APS}/mmoles_{MG}$ ratios for cryogel systems can be found in Table 2.1. Regarding the hydrogel systems, several attempts were carried out to achieve gel formation. On account of this, the concentrations of the reagents were increased while maintaining the total solution volume constant at 2 mL. The compositions of the corresponding polymer solutions are reported in Table 2.2.

Table 2.1: Composition of all DEX_{40}HEMA solutions used for the preparation of cryogels samples to build the formation window

Polymer concentration (% w/v)	$mmoles_{MG}$	$mmoles_{APS}$ / $mmoles_{MG}$	**APS (μL)**	**TEMED (μL)**	**Sample**
2.5	0.015	0.60	41	23	0.015–0.60
		0.65	45	25	0.015–0.65
		0.70	48	27	0.015–0.70
		0.75	51	29	-
		0.80	55	31	-
		0.85	58	33	-
		0.90	61	35	0.015–0.90
		0.95	65	37	0.015–0.95
		1.00	68	39	-
		1.10	75	43	-
		1.20	82	47	-
		1.30	89	50	-

Polymer concentration (% w/v)	$mmoles_{MG}$	$mmoles_{APS}$ / $mmoles_{MG}$	**APS (μL)**	**TEMED (μL)**	**Sample**
		1.35	92	52	-
		1.40	96	54	-
		1.45	99	56	-
		1.50	103	58	-
		1.55	106	60	-
		1.60	110	62	-
		1.65	113	64	-
		1.70	116	66	-
		1.80	123	70	-
		1.90	130	74	-
		1.95	133	76	0.015–1.95
		2.00	137	78	-
		2.10	144	81	-
		2.20	151	85	-
		2.30	158	89	-
		2.40	164	93	-
		2.50	171	97	0.015–2.50
		2.60	178	101	-
		2.70	185	105	-
		2.80	192	109	-
		2.90	198	113	-
		3.00	205	116	0.015–3.00
4.2	0.025	0.45	51	29	0.025–0.45
		0.50	57	32	0.025–0.50
		0.55	63	35	0.025–0.55
		0.60	68	39	0.025–0.60
		0.65	74	42	0.025–0.65
		0.70	80	45	-
		0.75	86	48	-
		0.80	91	52	-
		0.85	97	55	-
		0.90	103	58	-
		0.95	108	61	-
		1.00	114	65	-
		1.10	126	71	-
		1.20	137	78	-
		1.30	148	84	-

Polymer concentration (% w/v)	$mmoles_{MG}$	$mmoles_{APS}$ / $mmoles_{MG}$	**APS (μL)**	**TEMED (μL)**	**Sample**
		1.40	160	90	-
		1.50	171	97	-
		1.55	177	100	-
		1.60	183	103	-
		1.70	194	110	-
		1.80	205	116	-
		1.90	217	123	-
		2.00	228	129	-
		2.10	240	136	-
		2.20	251	142	-
		2.30	262	149	-
		2.40	274	155	-
		2.50	285	161	-
		2.60	297	168	-
		2.80	319	181	-
		2.90	331	187	-
		3.00	342	194	-
		3.50	399	226	-
		4.05	462	262	0.025–4.05
		4.20	479	271	0.025–4.20
		4.35	496	281	0.025–4.35
		4.50	513	291	0.025–4.50
6.0	0.035	0.40	64	36	0.035–0.40
		0.45	72	41	0.035–0.45
		0.50	80	45	0.035–0.50
		0.55	88	50	-
		0.60	96	54	-
		0.65	104	59	-
		0.70	112	63	-
		0.75	120	68	-
		0.80	128	72	-
		0.85	136	77	-
		0.90	144	81	-
		0.95	152	86	-
		1.00	160	90	-
		1.10	176	99	-
		1.20	192	108	-

Polymer concentration (% w/v)	$mmoles_{MG}$	$mmoles_{APS}$ / $mmoles_{MG}$	**APS (μL)**	**TEMED (μL)**	**Sample**
		1.30	208	117	-
		1.35	216	122	-
		1.40	224	126	-
		1.45	232	131	-
		1.50	240	135	-
		1.55	248	140	-
		1.60	256	145	-
		1.70	272	154	-
		1.80	287	163	-
		1.90	304	172	-
		2.00	319	181	-
		2.10	335	190	-
		2.20	351	199	-
		2.30	367	208	-
		2.40	383	217	-
		2.50	399	226	-
		2.60	415	235	-
		2.80	447	253	-
		2.90	463	262	-
		3.10	495	280	0.035–3.10
		3.15	503	285	0.035–3.15
		3.20	511	289	0.035–3.20
		3.30	527	298	0.035–3.30
		3.65	583	330	0.035–3.65
		4.50	719	407	0.035–4.50
7.6	0.045	0.30	62	35	0.045–0.30
		0.35	72	41	0.045–0.35
		0.40	82	47	0.045–0.40
		0.45	92	52	-
		0.50	103	58	-
		0.55	113	64	-
		0.60	123	70	-
		0.65	134	76	-
		0.70	144	81	-
		0.75	154	87	-
		0.80	164	93	-
		0.85	175	99	-

Polymer concentration (% w/v)	$mmoles_{MG}$	$mmoles_{APS}$ / $mmoles_{MG}$	**APS (μL)**	**TEMED (μL)**	**Sample**
		0.90	185	105	-
		0.95	195	110	-
		1.00	205	116	-
		1.10	226	128	-
		1.20	247	140	-
		1.30	267	151	-
		1.35	277	160	-
		1.40	288	163	-
		1.45	298	168	0.045–1.45
		1.50	308	174	-
		1.55	318	180	0.045–1.55
		1.65	339	192	0.045–1.65
		1.75	359	203	0.045–1.75
		1.85	380	215	0.045–1.85
		1.95	400	227	0.045–1.95
		2.10	431	244	0.045–2.10
		2.25	462	262	0.045–2.25
		2.30	472	267	0.045–2.30
		2.50	513	291	0.045–2.50
9.4	0.055	0.30	75	43	0.055–0.30
		0.35	88	50	0.055–0.35
		0.40	100	57	0.055–0.40
		0.45	113	64	-
		0.50	126	71	-
		0.55	138	78	-
		0.60	151	85	-
		0.65	163	92	-
		0.70	176	99	-
		0.75	188	106	-
		0.80	201	114	-
		0.85	213	121	-
		0.90	226	128	-
		0.95	238	135	-
		1.00	251	142	-
		1.10	276	156	-
		1.20	201	170	-
		1.30	326	185	0.055–1.30

Polymer concentration (% w/v)	$mmoles_{MG}$	$mmoles_{APS}$ / $mmoles_{MG}$	**APS (μL)**	**TEMED (μL)**	**Sample**
		1.35	339	192	0.055–1.35
		1.40	351	199	0.055–1.40
		1.45	364	206	0.055–1.45

Table 2.2: Composition of all $DEX_{40}HEMA$ solutions used to prepare hydrogel systems.

Polymer concentration (% w/v)	$mmoles_{MG}$	$mmoles_{APS}$ / $mmoles_{MG}$	**APS (μL)**	**TEMED (μL)**	**Sample**
2.5	0.015	2.00	137	78	-
		2.50	171	97	-
		3.00	205	116	-
		3.50	240	135	-
		4.00	274	155	-
		7.00	479	271	-
		10.00	685	387	-
		15.00	1027	581	-
4.2	0.025	2.00	228	129	-
		3.00	342	194	-
		4.00	456	258	-
		5.00	571	323	-
		7.00	799	452	-
		11.00	1255	710	-
6.0	0.035	2.00	320	181	-
		3.00	479	271	-
		4.00	639	362	-
		4.50	719	407	-
7.6	0.045	2.00	411	232	-
		3.00	616	349	0.045–3.00
9.4		2.00	502	284	0.055–2.00

Nitrogen atmosphere

It was of practical interest to understand the role of oxygen in the crosslinking process and how it affects the internal structure of the scaffolds. As a consequence, cryogels were also prepared under nitrogen atmosphere with the aim of comparing them with the ones described in section . The polymer was preliminarily solubilized through magnetic stirring. Subsequently, the polymeric solution was put under nitrogen atmosphere, and it was kept for

20 minutes. Afterwards, the solution was sonicated maintaining the nitrogen atmosphere in order to remove the bubbles formed during the insufflation of N2 and APS and TEMED were added. The following steps were the same of the procedure that was previously described in section 2.3.1. Systems of $DEX_{40}HEMA$ (0.035 $mmoles_{MG}$) were prepared for APS/MG mola ratios equal to 0.6 and 0.8.

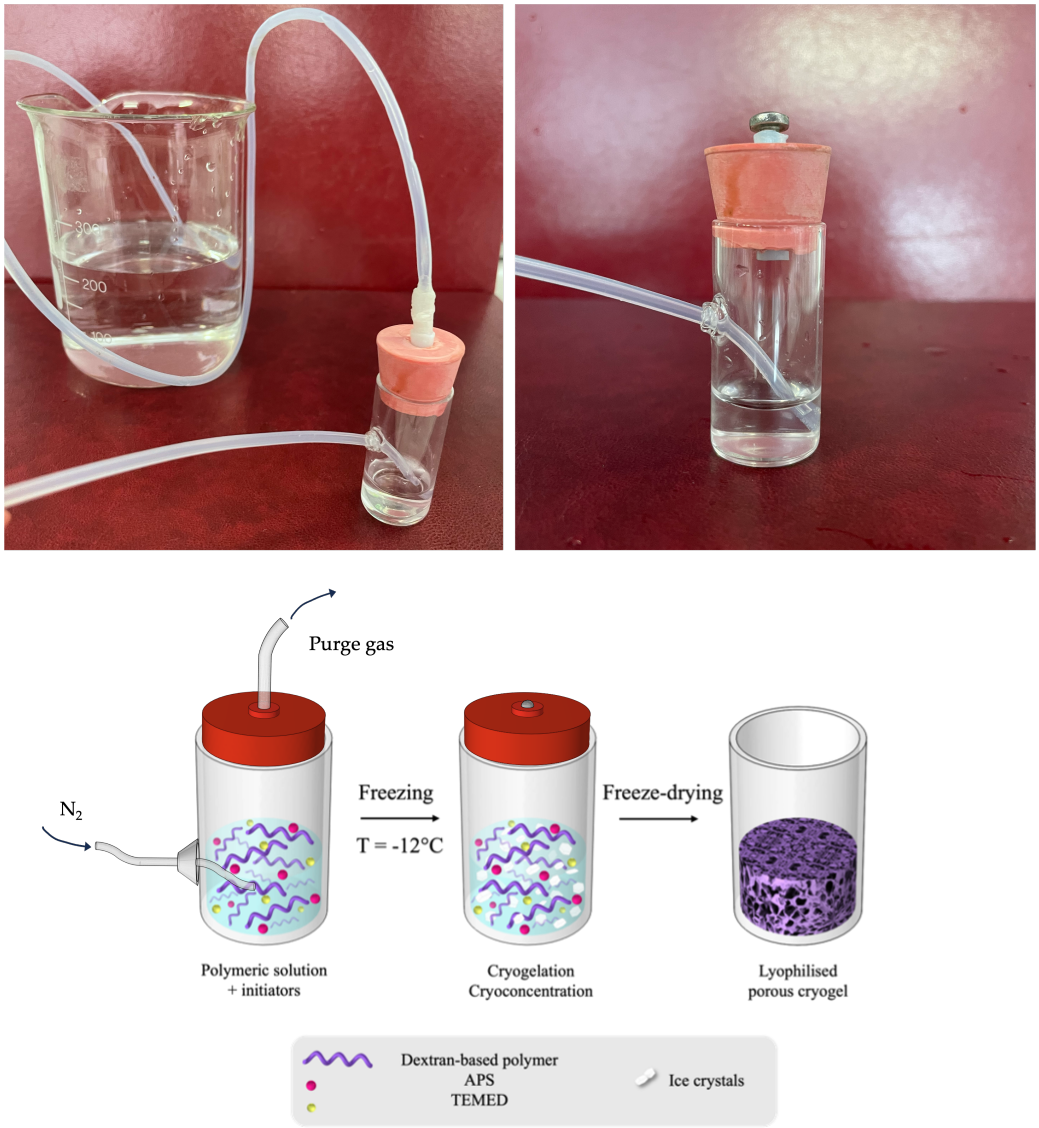


Figure 2.6: Pictorial representation of all the steps required for preparation od $DEX_{40}HEMA$ under nitrogen atmosphere (**a**). On the top, the utilized real apparatus is shown, both with the purge system (**b**) and without (**c**).

2.3.2 Preparation of dextran-based cryogels

Cryogels were prepared by free radical crosslinking reaction in distilled water, using the redox initiation system APS/TEMED. A certain amount of $DEX_{40}MA$, $DEX_{40}HEMA$, $DEX_{40}PEG_{360}MA$, $DEX_{40}PEG_{500}MA$, or $DEX_{500}PEG_{360}MA$ (for mg see table 2.3), corresponding to 0.035 mmoles of methacrylic groups, was dissolved in distilled water through magnetic stirring.

Following the complete solubilization of the polymer, APS (96 μL) and TEMED (54 μL) were added and after 30 seconds the systems were put into a cryostat (already set at the temperature of -12°C) for two hours, before undergoing the freeze-drying step. A pictorial representation of all the steps required for cryogel preparation is reported in Figure 2.7. The freeze-drying process was carried out with a LIO 5P bench freeze-dryer (5 Pascal, Italy) equipped with a vacuum pump Adixen (Alcatel, France). The polymer solutions were prepared in cylindrical glass molds (diameter 20 mm, height 40 mm) at room temperature. The final volume of the polymer solutions was 2 mL, which allowed us to obtain cylindrical lyophilized cryogel samples of 18.5 ± 0.5 mm diameter and 7.1 ± 0.2 mm height.

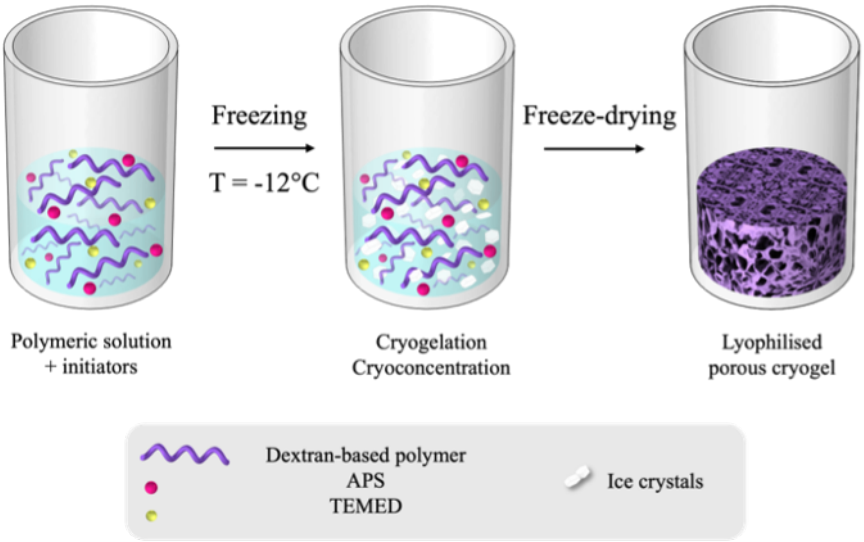


Figure 2.7: Pictorial representation of all the steps required for cryogel preparation.

Polymer	**DEXMA**	**DEXHEMA**	**DEXPEG$_{360}$**	**DEXPEG$_{500}$**
Polymer mass (mg)	116	120	130	135

Table 2.3: Amount of polymer used for the preparation of the different DEX-based formulations.

The method adopted for the preparation of cryogels is the result of an experimental campaign in which polymer concentration (6% w/v) and freezing temperature (-12 °C) were kept constant, whereas APS and TEMED concentrations were modified in order to vary the crosslinking rate of the polymer. We found out that we could obtain cryogel networks using APS concentrations in the range 1.5 – 13 mg/mL, and varying TEMED concentration according to APS, in order to keep the mmoles APS/mmoles TEMED ratio equal to 0.9 in all the cases. Based on these data, the cryogels systems investigated in this work were prepared selecting an APS concentration within this range, specifically 2.4 mg/mL, which correspond to a mmoles APS/mmoles methacrylic groups ratio of 0.6.

2.3.3 Preparation of DEX-GelMA cryogels

The preparation of dual-network cryogels composed of a methacrylic derivative of dextran and methacrylated gelatin was performed as an extension of the previous work [15], in which $DEX_{40}MA$ was employed. The objective was to investigate dextran-based variants exhibiting enhanced biodegradability and biocompatibility, thereby rendering them more suitable for applications in tissue engineering. As a preliminary study, it was decided to focus on one of the three systems that in study [15] was established to be optimal: $GelMA_3/DexMA_3$ - i.e. with bpth GelMA and $DEX_{40}MA$ at a concentration equal to 3% w/v and corresponding to 0.050 $mmoles_{MG}$. Consequently, the hybrid systems were formulated to contain 0.050 $mmoles_{MG}$, maintaining a constant amount of GelMA and varying the mass of the dextran-based polymer according to its molecular weight. The APS/MG and APS/TEMED molar ratios were fixed at 0.45 and 0.9, respectively. The total volume of the polymeric solution was kept constant at 2 mL. The specific quantities of polymers and reagents employed are reported in Table 2.4. The polymers were dissolved at 50 °C for 15 minutes under magnetic stirring. Upon completion of the solubilization process, the solution was allowed to cool to room temperature for 5 minutes, after which the APS and TEMED reagents, taken from 5% w/v stock solutions, were added. The resulting mixture was homogenized and rapidly transferred into a cryostat maintained at –12.0 °C, where it was allowed to freeze for 2 hours. Subsequently, the frozen samples were subjected to lyophilization.

Sample	GelMA (mg)	DEX-HEMA (mg)	DEX-PEGMA (mg)
DEX_{40}HEMA-GelMA	60	62	–
$DEX_{40}PEG_{360}$MA-GelMA	60	–	67
$DEX_{40}PEG_{500}$MA-GelMA	60	–	70
DEX_{500}HEMA-GelMA	60	62	–
$DEX_{500}PEG_{360}$MA-GelMA	60	–	67

Table 2.4: Composition of the dextran-gelatin hybrid cryogels containing 0.050 $mmoles_{MG}$.

2.3.4 Preparation of Dextran methacrylate cryogels and hydrogels

Cryogels were prepared by free radical crosslinking reaction in distilled water, using the redox initiation system APS/TEMED. A certain amount (116 mg) of $DEX_{40}MA$ corrisponding to 0.035 mmoles of methacrylic groups, was dissolved in distilled water through magnetic stirring. Four different systems were prepared with distinct APS7MG molar ratios, respectively 0.60, 3.00, 3.50 and 3.75. Following the complete solubilization of the polymer, APS and TEMED (see Table 2.5 for the exact quantities) were added and after 30 seconds the systems were put into a cryostat (already set at the temperature of -12°C) for two hours, before being freeze-dried. The freeze-drying process was carried out with a LIO 5P bench freeze-dryer (5 Pascal, Italy) equipped with a vacuum pump Adixen (Alcatel, France). The polymer

solutions were prepared in cylindrical glass molds (diameter 20 mm, height 40 mm) at room temperature. The final volume of the polymer solutions was 2 mL, which allowed us to obtain cylindrical lyophilized cryogel samples of 18.5 ± 0.5 mm diameter and 7.1 ± 0.2 mm height.. As far as it concerns the hydrogel system, it was prepared with a $\text{mmoles}_{APS}/\text{mmoles}_{MG} = 4.50$. The procedure is the same as described in 2.3.1.

Table 2.5: Composition of all $DEX_{40}MA$ solutions used for the preparation of cryogel and hydrogel samples for modeling swelling mechanics.

$\text{mmoles}_{\text{APS}}$ / $\text{mmoles}_{\text{MG}}$	**APS** (μ**L**)	**TEMED** (μ**L**)	**Comments**
0.60	96	54	
3.00	478	271	
3.50	559	316	
3.75	599	339	
4.50	719	407	Hydrogel

2.4 Estimation of the gel fraction

The gel fraction serves as a valuable qualitative indicator of the effectiveness of network formation in reticulated gels, since it provides information about the number of cross-links that take place between the polymer chains in the sample. The higher the gel fraction is, the greater the degree of covalent bonding is [103]. To assess the amount of cross-linked polymer during the cryogelation process, dry samples were weighed and thereafter they were subjected to a 7 wash cycles with an excess of distilled water. This allowed for the removal of residues of APS and TEMED, as well as any non-chemically cross-linked polymer. Upon completion of the washing process, the samples samples were frozen, freeze-dried, and again weighed. The gel fraction GF was then evaluated as:

$$GF = \frac{M_{\text{wash}}}{M_{\text{dry}}} \tag{2.1}$$

where M_{wash} stands for the mass of the sampled subjected to the 7-cycles wash, while M_{dry} is the mass of the initial dry sample, appropriately corrected considering the removal of APS and TEMED.

2.5 Absorption, swelling and degradation studies

Absorption studies were performed with the intention of evaluating the maximum liquid uptake of the samples and the time required for complete swelling. For this purpose, phosphate buffer (PBS, pH 7.4) was preheated to the temperature of 37 °C and added dropwise to the

surface of freeze-dried cryogels until a drop of PBS was observable at the bottom of the samples. The kinetics of swelling was determined by placing the samples in PBS (pH 7.4), kept in a thermostated water bath at the temperature of 37.0 ± 0.5 °C. The lyophilized specimens were left swelling until the swelling equilibrium was achieved. The water intake was tracked for 1 h. In the case of the systems prepared for the formation window, it was necessary to track the evolution for 300 minutes since not all samples achieved the equilibrium configuration quickly. Specifically, at regular time intervals, cryogels were removed from the swelling medium and the excess of liquid was whipped off by percolation at atmospheric pressure. In this way it was possible to weigh the samples. The swelling degree was evaluated as

$$Q(t) = \frac{M_{sw}(t)}{M_{dry}} \tag{2.2}$$

where $M_{sw}(t)$ is the weight (g) of the swollen sample at the time t and M_{dry} is the weight (g) of the dry sample. After the swelling studies, cryogels were left in PBS (pH 7.4) at 37.0 ± 0.5 °C and degradation rates were estimated. The samples were removed from the medium at variable intervals of time to measure their weights and to evaluate their weight variation. This procedure was repeated until the complete sample degradation. All tests were conducted in triplicate.

2.6 Morphological characterization

The internal architecture of freeze-dried cryogels was observed via field-emission scanning electron microscope (FE-SEM) MIRA 3 by Tescan. Since the samples were characterized by low electrical conductivity, they were coated with a thin layer of gold to prevent electronic charging and to improve image quality. The coating process was carried out in vacuum conditions (0.4 mbar) for 2 minutes by a sputter coater Edwards S150B applying a voltage of 1 kV and an electrical current of 40 mA to the gold electrode.

2.7 Compression studies

Mechanical tests were performed at room temperature with a universal testing machine Zwick/Roell Z010 (Ulm, Germany) equipped with a 10 kN load cell employing a test speed of 1 mm/min. The stress-strain curves derived from these tests were used to determine the values of the compression modulus, plateau stress, and densification stress. In fact, from the analysis of the aforementioned curves, it is possible to distinguish three main zones. In the first section, characterized by low stress values, the deformation of the system follows an increasing and linear trend.

2.8 Release of vitamin B_{12}

Release studies of vitamin B_{12} were conducted on $DEX_{40}PEG_{360}MA$, $DEX_{40}PEG_{500}MA$, $DEX_{40}MA$, $DEX_{40}HEMA$, $DEX_{500}PEG_{360}MA$. 2.5 mg of drug were loaded in cryogel samples prepared with 120 mg of polymer, giving approx. 50 (w/w) polymer/drug ratio which should ensure limited drug interference with the crosslinking process.

Two different loading procedures were implemented

1. Loading before cryogel formation (pre-loading)
   Cryogels were loaded with 2.5 mg of vitamin B_{12} by introducing a solution of vitamin B_{12} in distilled water (2.5 mg/mL) directly into the system before the low-temperature crosslinking step, which was carried out as reported in Section 2.3.2, leading to the cryogel formation.

2. Loading on preformed cryogel (after-loading)
   Freeze-dried cryogel samples were infused with a solution of vitamin B_{12}. The concentration of the solution was so that, on the base of absorption volumes, the amount of vitamin B_{12} in the cryogel was 2.5 mg. After loading, the specimens were lyophilized.

Each scaffold was placed in 20 mL of PBS (pH 7.4) under mild magnetic stirring. Temperature was maintained at 37.0 ± 0.5 °C by a water bath. At defined intervals of time, aliquots of 250 μL of the release medium were taken and immediately replaced with an identical volume of fresh PBS, so that the reservoir volume (20 mL) was maintained constant. Withdrawals were made every minute for the first 5 minutes, then every 5 minutes up to 20 minutes, every 10 minutes until the first hour passed, every 30 minutes up to 2 hours, and then every hour up to 8 hours. The last two aliquots were withdrawn after 24 and 48 hours.The concentration c_{res} of the released drug in the reservoir volume was evaluated by HPLC analysis.The HPLC consisted of a Perkin Elmer Series 200 LC pump, supplemented with a 235 Diode Array Detector and equipped of a Merck Hibar LiChrocart (250-4, 5 μm) RP-18 column. A 65:35 mixture of 0.01 M CH_3COOH/MeOH was used as eluent. The flow rate was set to 0.7 mL/min. Aliquots of 25 μL of every sample solution were injected into the HPLC system. A calibration curve c[mg/mL]=0.0465A[V×s], valid in the concentration range c ∈ [0.0005, 0.16] mg/mL and reported in Figure 2.8, was constructed to quantify the concentration of vitamin B_{12} in the reservoir at each withdrawal time instant (λ_{max} = 361 nm). All experiments were conducted in triplicate. Release profiles were reported as c_{res} vs t and M_t/M_∞ vs time t [min] (amount of drug released up to time t rescaled onto the total amount of drug released after an infinite time) with the corresponding standard deviations

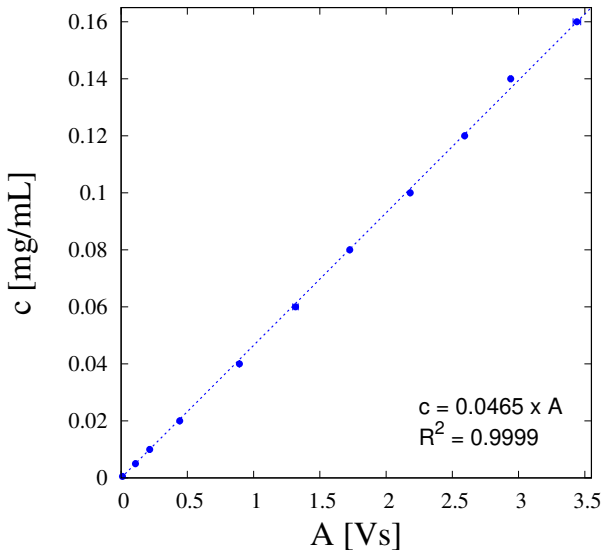


Figure 2.8: HPLC calibration curve of Vitamin B_{12}.

2.9 Rheological analysis of methacrylic derivatives of dextran-GelMA blended systems

The study of the crosslinking kinetics of polymer solutions was carried out by time sweep type rheological analysis on the solutions polymeric used for the formation of the various cryogel samples prepared as described in subsection 2.3.3. Specifically, the following polymer blends were analyzed: DEX_{40}-HEMA/GelMA, DEX_{500}-HEMA/GelMA, DEX_{40} $PEG_{360}MA$/GelMA, DEX_{40}-$PEG_{500}MA$/GelMA and DEX_{500}-$PEG_{360}MA$/GelMA. The analyzes were carried out using a TA HR1 stress-control rheometer, managed by TRIOS software. The geometry used was of the cone-flat type having a diameter of 40 mm, an angle of 1.005° and a gap of 0.027 mm. The polymers were solubilized for 15 minutes at 50°C, in a quantity of distilled water such as to reach a final volume of 0.5 mL including the volumes of the APS and TEMED solutions. Once the solubilization of the polymers is completed, the solutions are left at room temperature for 5 minutes before adding the required volumes of APS and TEMED, always taken from 5% w/solutionsV and, after 15 seconds of addition, quickly pour into the center of the rheometer plate, taking care to distribute them evenly between the two elements of the geometry. The study was conducted for 1 hour, working at a frequency of 1 Hz and imposing a deformation equal to 1% on the sample. These parameters were selected so as to fall within the linear visco-elasticity range of the polymer system, determined through strain sweep type experiments. Sweep analysis gives information about the storage and loss moduli G' and G"

2.10 Cell culture

Aneuploid human immortal keratinocytes (HaCats) were selected to investigate the biocompatibility and cell behavior of the cryogels. The HaCats were expanded in a T-75 flask and cultured at 37 ° C and 5% CO_2 in DMEM/F-12 enriched with 10% v/v fetal bovine serum (FBS), 1% v/v of L-glutamine and 1% v/v of an antibiotic solution consisting of penicillin and streptomycin.

2.10.1 Adhesion and proliferation studies

Cylindrical portions of each sample of hydrated cryogel (diameter 5 mm, thickness 3 mm) were steam sterilized at 121°C for 10 min and then freeze-dried under aseptic conditions. The lyophilized samples were placed in 96-well plates and loaded with 25 L of a HaCat cell suspension at a density of 2.5×10^6 cells/cryogel. The specimens were incubated for 1 h at 37 ° C to allow cell adhesion to the scaffolds. After the adhesion step, they were transferred into 48-well plates and supplemented with 1 mL of culture medium. At selected time points (2, 5, and 10 days), cell viability was assessed using a fluorescent live-cell staining method. Briefly, after removal of the culture medium, each sample was incubated with 10 μL of a calcein solution for 15 min at 37 ° C, followed by three washing steps with culture medium to remove excess dye. The investigated cryogels were then examined under a fluorescence microscope to evaluate the presence and distribution of viable cells within the scaffolds.

Chapter 3

Characterization and synthesis of $DEX_{40}HEMA$ cryogels: effect of experimental parameters

In order to determine if dextran-based cryogenic samples are suitable for biomedical and drug delivery applications, an accurate investigation of the effect of the experimental conditions which influence the characteristics of the scaffold was conducted. More in depth, it was decided to maintain the temperature of the cryostatic bath constant and to vary the concentrations of polymer and crosslinking agents. $Dex_{40}HEMA$ was selected as the reference polymer as it presents the biocompatibility and biodegradability properties required for the purposes of the previously mentioned applications. Section3.1 gives a deep discussion about the identification of the upper and lower limits for the formation of $DEX_{40}HEMA$ cryogels expressed in terms of swelling capability Q and gel fraction GF. The mechanical characterization of some of the samples analyzed in the previous section is presented in Section 3.2. As an early study, the impact of the presence of oxygen is discussed in Section 3.3.

3.1 Determination of the formation window of the $DEX_{40}HEMA$ cryogels

The aim of this part of the work was to evaluate the effect of some of the parameters that can influence the formation of cryogel-type polymer matrices produced from a methacrylic derivative of dextran, $DEX_{40}HEMA$, through a radical-type reaction, induced by the APS/TEMED redox system.

There are three factors that affect the cryogelation reaction: the concentration of methacrylic groups, the concentration of the radicalic initiators and the freezing temperature. With the intention of definying the formation window of $DEX_{40}HEMA$ cryoreticulated systems, it was decided to proceed as follows. The freezing temperature was kept constant at -12°C and the $mmoles_{APS}/mmoles_{TEMED}$ ratio was held at 0.9. On the contrary, the concentration of

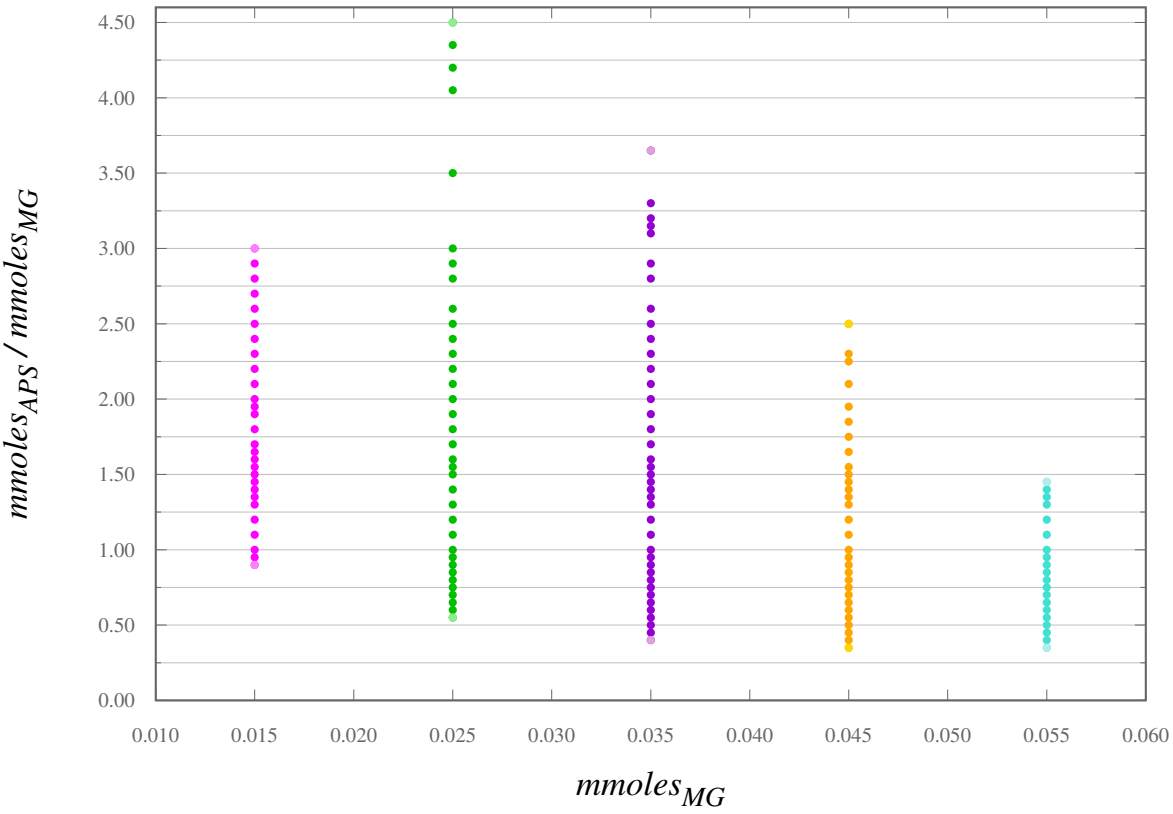


Figure 3.1: Cryogel formation diagram for $DEX_{40}HEMA$-based. Systems were obtained by varying the polymer concentration—hence the mmoles concentration of methacrylate groups—and the APS/MG molar ratio. Darker dots indicate successful formation of cryogel systems, whereas lighter symbols indicate incomplete cryogel (bottom dots) formation or the formation of a hydrogel-like matrix (top dots).

methacrylic groups and the $mmoles_{APS}/mmoles_{MG}$ ratio were varied according to the criteria illustrated below. The concentration of the MGs was modified by varying the amount of solubilized polymer, ensuring that the final volume of the polymer solution remained constant (2 mL), while the degree of derivatization of the $DEX_{40}HEMA$ was kept constant at the value of 5%±1%.
First, the range of polymer concentrations that can lead to samples suitable for biomedical applications was outlined. It was observed that quantities of MG less than 0.015 mmoles were insufficient to allow the formation of gel matrices, while quantities greater than 0.055 $mmoles_{MG}$ were not taken into consideration since they would determine the formation of matrices with a massive structure, not suitable for the desired purposes. As a consequence, the concentrations to be investigated were selected. In more detail, they were 2.5, 4.2, 6.0, 7.6 and 9.4% w/v, corresponding respectively to 0.015, 0.025, 0.035, 0.045, 0.055 $mmoles_{MG}$.
The next step was to determine the limit amounts of APS for every concentration of MG, and so limit values of the $mmoles_{APS}/mmoles_{MG}$ ratio, which permit the creation of polymeric structures that meet the definition of cryogel.

3.1.1 Identification of the lower limits

To identify the minimum quantity of reactants that permitted the formation of a cryogel-like structure, samples at different $mmoles_{APS}/mmoles_{MG}$ ratio were prepared, for each investigated polymer concentration. The parameters employed to establish whether or not the specimen was a cryogel were the gel fraction and the degree of swelling.
The starting point was the analysis of the gel fractions. The lowest $mmoles_{APS}/mmoles_{MG}$ ratios that were necessary to ensure unitary GFs were identified. For ratios below the minimum threshold, crosslinking is not complete prior to the freezing process. This is a direct consequence of a slow crosslinking kinetics and leads to a loss of mass of the system when hydrated, which leads to gel fraction values dropping below unity and progressively lower as one moves away from the limit value. Of note is that it was decided to classify as cryogels the samples for which the gel fraction was above 0.75-0.8. That is to say, systems in which 25-20 % of the polymer has not crosslinked have been identified as the lower limit. This fraction is not retained after washing.
Table 3.1 presents the impact of the $mmoles_{APS}/mmoles_{MG}$ ratio change on the GF value for each polymer concentration.

As it is possible to derive from the mean values reported in Table 3.1, for higher polymer concentrations, the complete reticulation of the polymer solution, i.e. unitary GF, is achieved with lower $mmoles_{APS}/mmoles_{MG}$ ratios. In order to justify this circumstance, it has been assumed that when the mass of the polymer is lower, and therefore the concentration of MG is lower, a greater concentration of crosslinking agent is required to guarantee adequate crosslinking kinetics and therefore the formation of a densely cross-linked three-dimensional network. As outlined in 3.1, a decrease in these ratios leads, at a constant concentration, to progressively lower GF values. In this context, it is very useful to compare lyophilized

Sample	*GF*	**Polymer concentration (% w/v)**	$\text{mmoles}_{\text{MG}}$	$\textbf{mmoles}_{\text{APS}}/\textbf{mmoles}_{\text{MG}}$
0.015–0.95	1.00±0.01	2.5	0.015	0.95
0.025–0.65	1.00±0.02	4.2	0.025	0.65
0.035–0.50	0.98±0.01	6.0	0.035	0.50
0.045–0.40	0.97±0.02	7.6	0.045	0.40
0.055–0.40	0.97±0.02	9.4	0.055	0.40
0.015–0.90	**0.74±0.01**	2.5	0.015	0.90
0.025–0.60	**0.79±0.03**	4.2	0.025	0.60
0.035–0.45	**0.77±0.01**	6.0	0.035	0.45
0.045–0.35	**0.78±0.01**	7.6	0.045	0.35
0.055–0.35	**0.80±0.02**	9.4	0.055	0.35
0.015–0.65	0.62±0.03	2.5	0.015	0.65
0.025–0.45	0.40±0.01	4.2	0.025	0.45
0.035–0.40	0.50±0.06	6.0	0.035	0.40
0.045–0.30	0.58±0.15	7.6	0.045	0.30
0.055–0.30	0.62±0.05	9.4	0.055	0.30

Table 3.1: Effect of varying the $\text{mmoles}_{\text{APS}}/\text{mmoles}_{\text{MG}}$ ratio on GF for each polymer concentration. **Bold** values indicate the lower limits of the formation window.

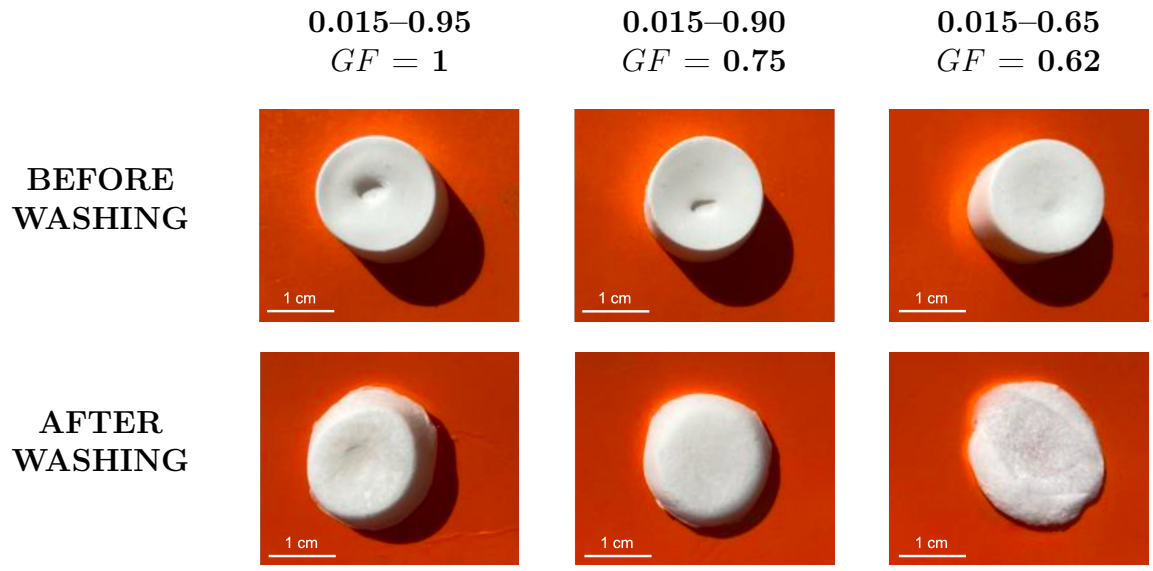


Figure 3.2: Freeze-dried samples, before and after washing, prepared from polymer solutions at the lower investigated concentration - i.e. 2.5% w/v (0.015 mmoles_{MG}). Effect of the amounts of the APS/TEMED redox system on the *GF* and on the macroscopic structure.

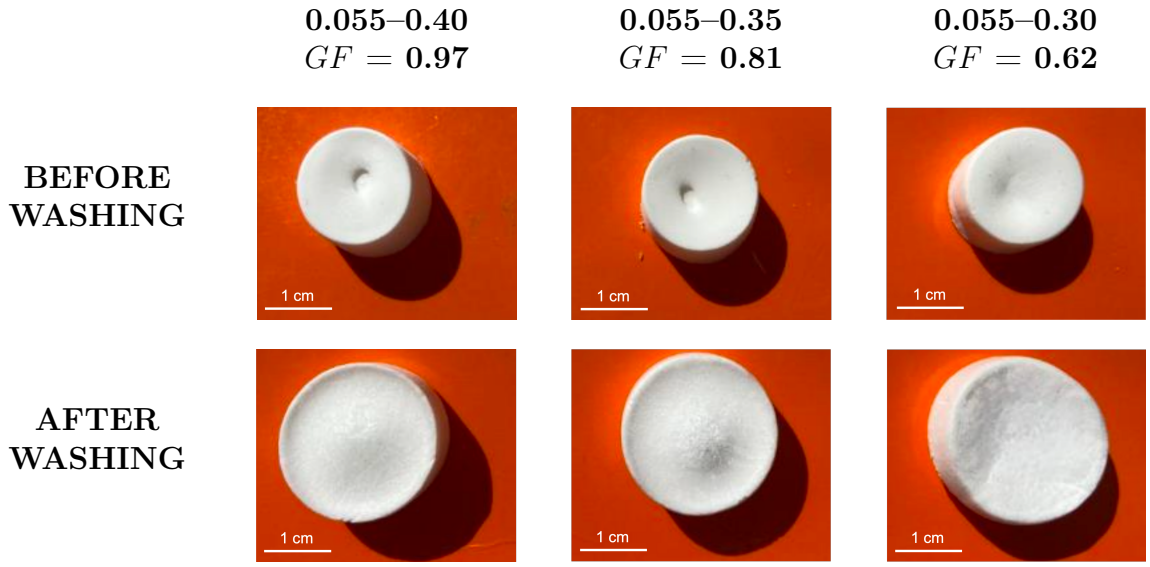


Figure 3.3: Freeze-dried samples, before and after washing, prepared from polymer solutions at the highest investigated concentration - i.e. 9.4% w/v (0.055 $mmoles_{MG}$). Effect of the amounts of the APS/TEMED redox system on the GF and on the macroscopic structure.

samples obtained from the same polymer concentration, but with different quantities of the APS/TEMED redox system. Regarding the specimens prepared from 2.5 % w/v polymer solutions, it can be observed that in decreasing the ratio $mmoles_{APS}/mmoles_{GM}$ from 0.95 to 0.90, up to 0.65, there is a progressive decrease in gel fraction values, which go from 1 to 0.75 and 0.62. Each corresponds to a different ability to keep the initial structure of the lyophile unchanged (3.2). As for cryogels prepared from 9.4% w/v polymer solutions, going from a $mmoles_{APS}/mmoles_{GM}$ ratio of 0.40 to 0.35, up to 0.30, the GF values were evaluated to be equal to 0.97, 0.81 and 0.62, respectively (3.3). Therefore, although the two cases - that of lower and higher concentrations of polymer - show similarities, however as can be concluded from the comparison of the two figures (figs. 3.2 and 3.3), the lyophiles obtained from the higher concentration polymer solution 3.3, show fewer structural changes as the gel fraction values vary. This effect can probably be traced back to the greater quantity of polymer present, which leads to less collapse of the structure.

As already anticipated, the characterization of the lower limit samples involved the study of the behavior of the systems when subjected to swelling tests. The aim of such studies wass to identify the degree of swelling (Q) of the system obtained. The degree of swelling (Q), expressed as the ratio of the swollen weight ($M_{sw}(t)$) to the initial dry weight (M_{dry}). In this way, it can be evaluated how many times the system increases its weight by incorporating the aqueous solution in which it is immersed.

What is more, the degree of swelling is also useful for obtaining information about the internal porosity of the system. In fact, since a cryogel-like matrix has a highly interconnected network of macropores, differently from a hydrogel-like matrix, its degree of swelling at equilibrium, intuitively, should be higher and reached more quickly, as the size of the pore favors the entry of a greater quantity of the solution in which it is immersed.

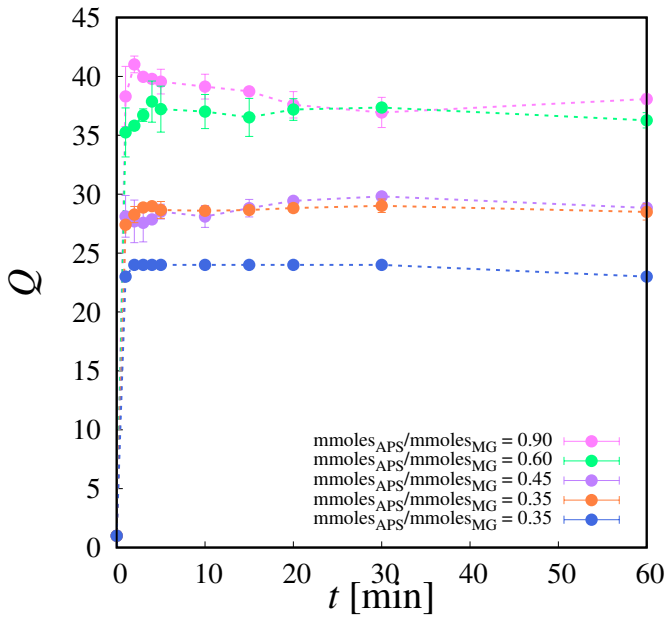


Figure 3.4: Swelling curves of the $DEX_{40}HEMA$ samples were taken as those of the systems formed with the minimum amount of reactants that still exhibited cryogel-like behavior.

Systems of $DEX_{40}HEMA$ with gel fraction values between 0.75 and 0.80 were selected (see Table 3.1).
Hydration tests were conducted in phosphate buffer (pH=7.4) at 37.0 ± 1.0 °C as explained in section 2.5. The analysis of the swelling data reported in 3.4, allows to conclude that all systems taken as the lower limit and therefore characterized by average gel fraction values between 0.75 and 0.80, have a cryogel-like behavior. The samples, on the other hand, quickly reach the equilibrium condition, which is typical of cryogels, and exhibit a significant swelling capacity that exceeds that of porous hydrogel system. The figure 3.4 suggests that systems with a higher polymer concentration are characterized by a lower value of Q, which decreases significantly from 0.015 to 0.055 $mmoles_{MG}$. This condition is due to a greater polymer mass and a greater crosslinking density: a greater concentration of MG brings the polymer chains closer together, limiting the ability to absorb solvent. The comparisons between each system taken as the lower limit and the corresponding system with $GF = 1$ are shown in the figures 3.5.

3.1.2 Identification of the upper limits

Prior explaining the criteria exploited to characterize the upper zone of the formation window, it is very useful to remember some concepts related to the formation process of a cryogel. As already mentioned, the microarchitecture of a cryogel is determined by a balance between the freezing kinetics and the crosslinking kinetics. When the reticulation velocity is much higher than the rate of crystal formation, the resulting sample will have a very dense structure, with a lower degree of interconnection between the pores. In the limits, it will resemble

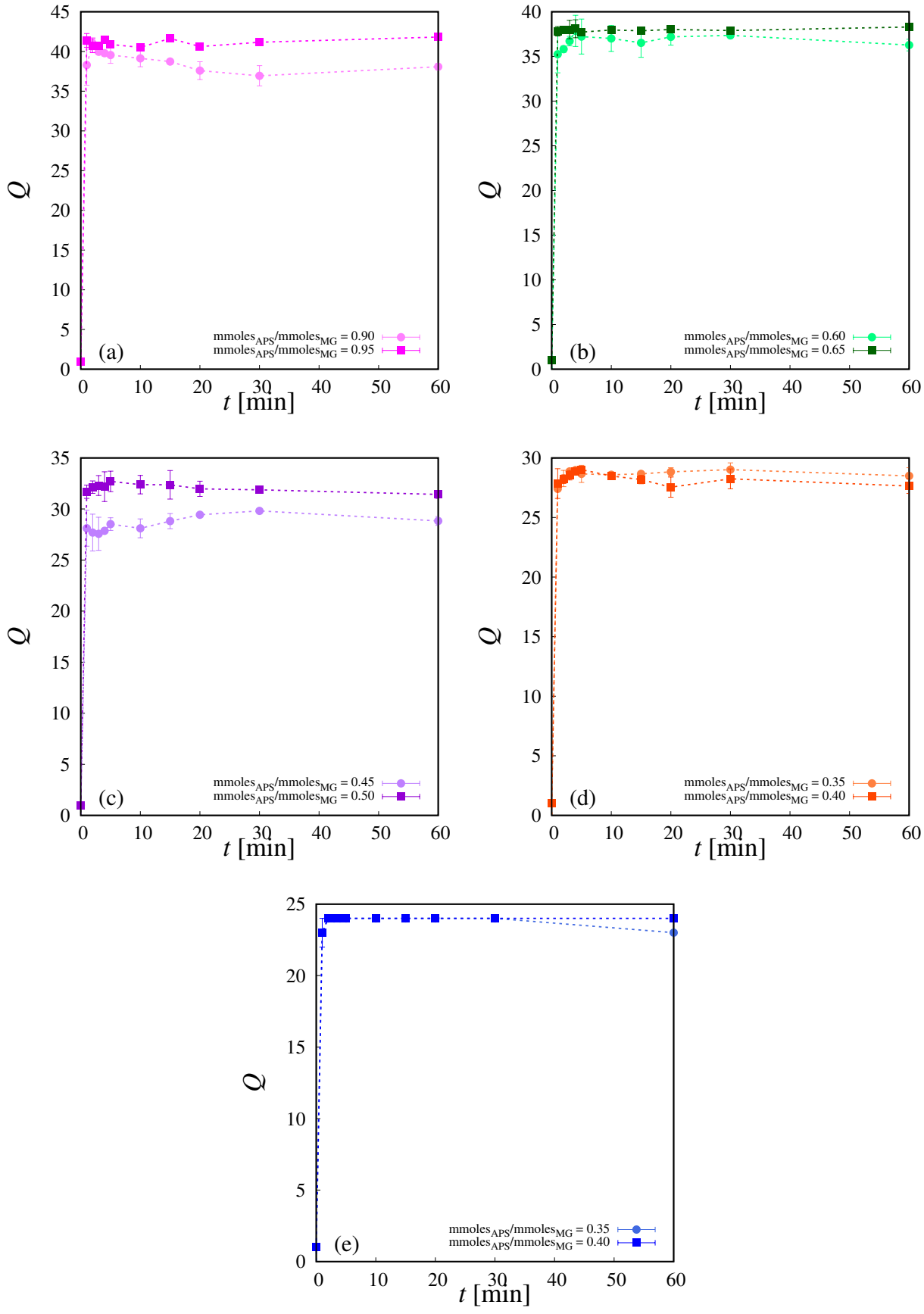


Figure 3.5: Swelling curves of $DEX_{40}HEMA$ samples prepared with an APS/MG molar ratio corresponding to the lower limit and to $GF \approx 1$. (**a**) 2.5 % w/v - 0.015 $mmoles_{MG}$. (**b**) 4.2 % w/v - 0.025 $mmoles_{MG}$. (**c**) 6 % p w/v - 0.035 $mmoles_{MG}$. (**d**) 7.6 % w/v - 0.045 $mmoles_{MG}$. (**e**) 9.4 % w/v - 0.055 $mmoles_{MG}$.

the structure of a porous hydrogel.
According to what was explained, to find the maximum $mmoles_{APS}/mmoles_{MG}$ ratios that ensured a cryogel-like structure, the following procedure was undertaken, as explained below. Precisely, swelling studies were performed for each polymer concentration and for different concentrations of the reactants. The swelling degree was then compared to the one of the corresponding hydrogel. Due to the difference in the morphology, one would expect the water uptake of the hydrogel to be lower than that of the corresponding cryogel. Thus, the limit value of the $mmoles_{APS}/mmoles_{MG}$ ratio was selected to match the swelling trends in a hydrogel sample.
Hydrogel samples were prepared as explained in 2.3.1. Several concentration of reactants were tested before finding the optimal combination, which allowed for the production of a strong and stable hydrogel structure. It is of utmost importance to put in evidence that these kinds of specimens formed only at the polymer concentrations 7.6% and 9.4% w/v, and at $mmoles_{APS}/mmoles_{MG}$ ratios of 3.00 and 2.00, respectively. This suggests the strong effect of the MG quantity on the formation of the samples. In fact, as the polymer concentration decreases, a greater amount of reagent is required. The limiting case is where there are no longer enough methacrylic groups available to create macroscopic hydrogel matrices. Below 7.6% w/v polymer concentrations did not allow hydrogel matrices to be obtained even when substantial excesses of APS/TEMED reagents were used.
The effect of the $mmoles_{APS}/mmoles_{MG}$ ratio on the internal structure of the samples was highlighted through the swelling studies.
The degree of swelling (Q), in fact, is strongly influenced by the ratio $mmoles_{APS}/mmoles_{MG}$ in relation to the freezing rate. If the polymer concentration is kept constant, it is possible to achieve the complete crosslinking of the polymer ($GF = 1.0$) by adding a higher amount of APS/TEMED reagents in the original polymer solution. However, under such circumstances, the crosslinking kinetics prevail over the freezing kinetics as it proceeds more rapidly. That implies a reduced growth of ice crystals, resulting in a lower degree of interconnection between the porous domains with a direct effect on the swelling capacity of the system. More precisely, under extremely high concentrations of the crosslinking agents, the resulting structures display morphological features resembling those of hydrogel systems.

The characterization of the upper limits of the formation window has, therefore, involved the preparation cryogel systems with high $mmoles_{APS}/mmoles_{MG}$ ratios and their corresponding hydrogel analogues. In this way it was possible to cryogel-like from hydrogel-like behavior through swelling analysis, thus assessing the upper formation limit. Below is a detailed explanation of the adopted procedures.
In the case of samples obtained from more concentrated polymer solutions - namely 9.4% w/v (0.055 $mmoles_{GM}$) and 7.6% w/v (0.045 $mmoles_{GM}$) - swelling tests were initially performed for the respective hydrogel samples. Subsequently, the obtained curves were compared with those of cryogel samples prepared by progressively decreasing the $mmoles_{APS}/mmoles_{MG}$ ratio, until the minimum amount of APS and TEMED reagents required to produce a matrix consistent with the definition of a cryogel were found. From this perspective, the hydrogel

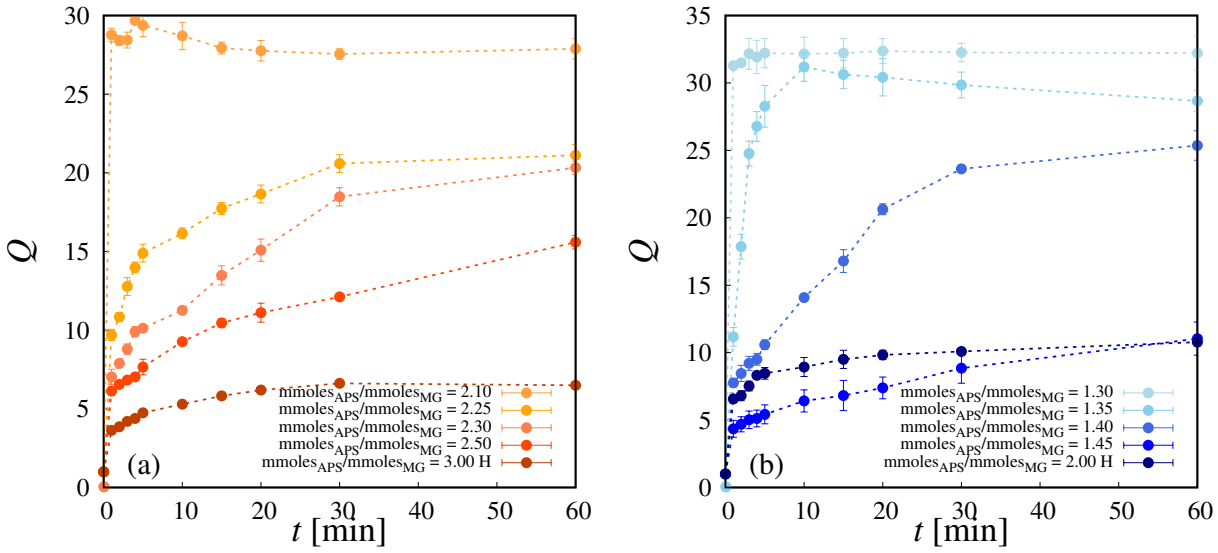


Figure 3.6: Swelling curves of DEX_{40}HEMA samples prepared with an APS/MG molar ratio corresponding to the upper limit (**a**) 7.6 % w/v - 0.045 $mmoles_{MG}$. (**b**) 9.4 % w/v - 0.055 $mmoles_{MG}$.

was employed as a positive control, serving to determine whether the resulting matrix behave as a hydrogel or a cryogel. For both polymer concentrations, a transition region can be identified, in which samples exhibit characteristics intermediate between those of hydrogels and cryogels Although their swelling proceeds gradually over time, as in hydrogels, the equilibrium swelling ratio (Q) attains values typical of cryogel systems (Fig. 3.6).
When it comes to systems at the lowest polymer concentrations, i.e. 6.0% w/v, 4.2% w/v and 2.5% w/v, respectively corresponding to 0.035, 0.025 and 0.015 $mmoles_{GM}$, only the trends in the swelling curves of the cryogel samples are reported, as the APS/MG molar ratio varies. Indeed, it was not possible to obtain the corresponding reference hydrogels according to the procedure described in 2.3.1. However, the curves confirm the effect of the reagent concentration on the Q value, and hence on the internal morphology of the system, as it was previously observed. To be underlined, as it is clear from the swelling curves of the examined samples that, again, the value of Q starts to progressively decrease, as the $mmoles_{APS}/mmoles_{MG}$ ratio increases (fig. 3.7).
Afterward, it is worth taking into account the impact of the polymer concentration change on the swelling process for the 4.2% w/v and 2.5% w/v systems. From Fig. 3.7, it can be clearly seen that a lower content of methacrylic groups in the initial polymer solution leads to the formation of systems exhibiting swelling behavior typical of cryogel matrices, despite the high concentration of the APS/TEMED redox pair. In fact, it can be observed that the equilibrium condition is reached rapidly. In the end, it is possible to confirm the close correlation between concentration of APS/TEMED reagents, polymer concentration and degree of swelling (Q).

Pictures 3.8 show the different structure of the swollen samples based on the polymer concentration and reactives cincentration.

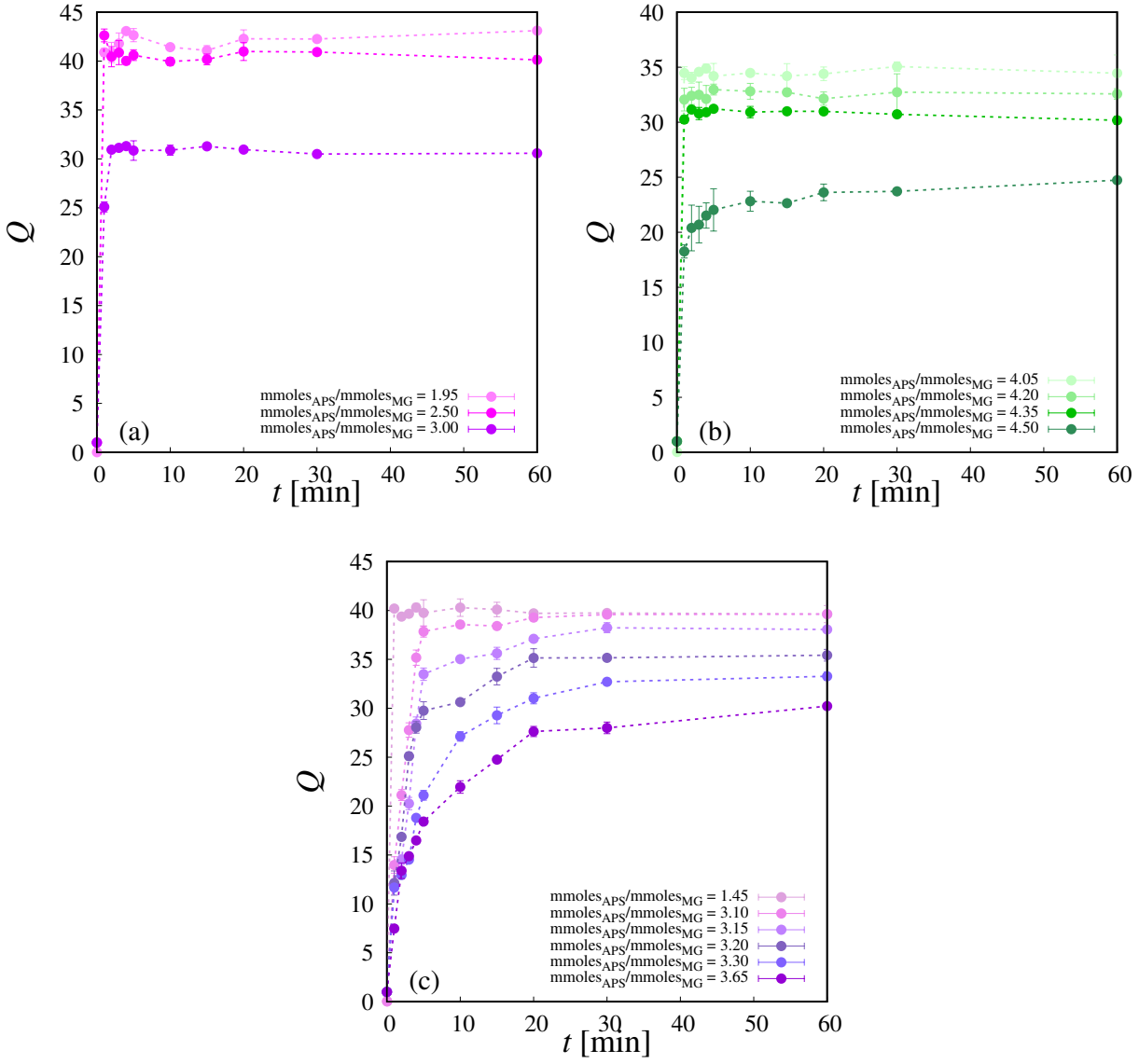


Figure 3.7: Swelling curves of DEX$_{40}$HEMA samples prepared with an APS/MG molar ratio corresponding to the upper limit and to $GF \approx 1$. (**a**) 2.5 % w/v - 0.015 mmoles$_{MG}$. (**b**) 4.2 % w/v - 0.025 mmoles$_{MG}$. (**c**) 6 % w/v - 0.035 mmoles$_{MG}$.

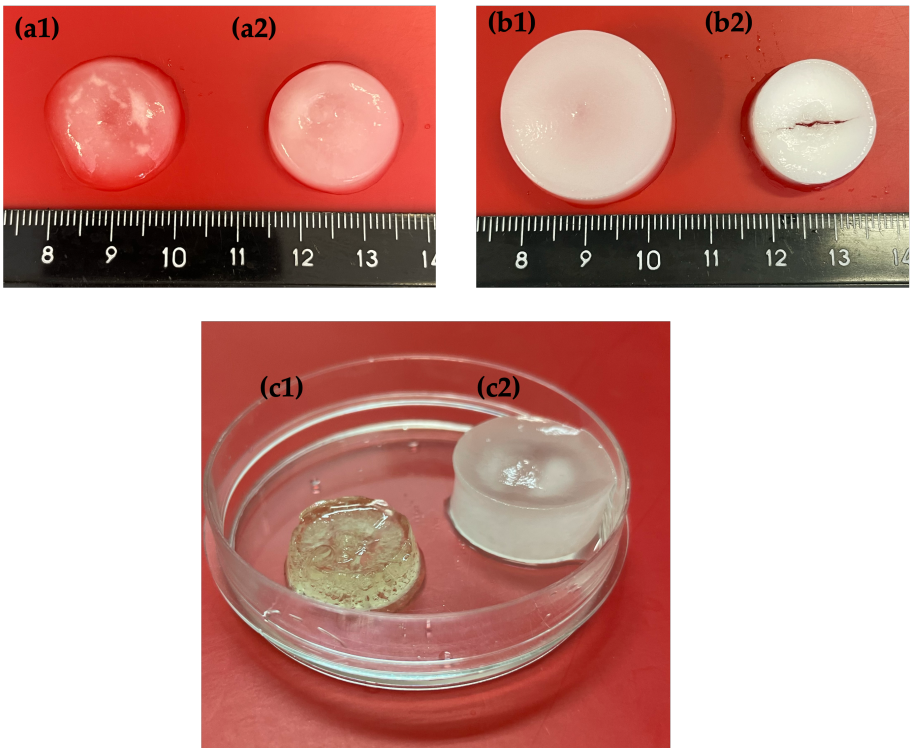


Figure 3.8: Comparison between samples prepare with the lower and higher limit of APS/MG molar ratio. (**a1**) and (**a2**) samples containing 0.015 mmoles_{MG}. (**b1**) and (**b2**) samples containing 0.055 mmoles_{MG}. Picture (**c1**) and (**c2**) show a hydrogel and a cryogel containing 0.045 mmoles_{MG}, case of upper limits.

3.2 Mechanical characterization and SEM analysis

To evaluate their microarchitecture, it was decided to subject certain samples to field emission scanning electron microscopy analysis. To this end, the systems obtained from polymer solutions with polymer concentration (9.4% w/v, corresponding to 0.055 mmoles_{MG}) and $\text{mmoles}_{APS}/\text{mmoles}_{MG}$ ratios of 1.30; 1.35; 1.40 and 1.45 and the reralized hydrogel system with ratio 2 were selected.
The observations of the FE-SEM images shown in figs. 3.9 (**a**)–(**e**) enabled to highlight that at higher concentrations of crosslinking agent, there corresponds a decrease in the average size of the pores, which are close to those of the pores of the analyzed hydrogel sample. A more homogeneous pore distribution should be observed in the case of systems made by cryoreticulation compared to hydrogel systems. This condition depends on the fact that the interconnected pore system is formed within the first systems mentioned precisely as a result of the formation process. Instead, in the case of hydrogel systems, the pores are formed only at a moment subsequent to that of formation of the polymer network, when they are subjected to freezing and freeze-drying processes which determine fractures within the three-dimensional structure, acting as porogens [104].

Mechanical compression tests were carried out to evaluate the effect of the concentration of crosslinking agent on the properties of the samples in the dry state. The selected systems are the same as in 3.2. The stress-strain trend in fig. 3.10 shows three different regions:

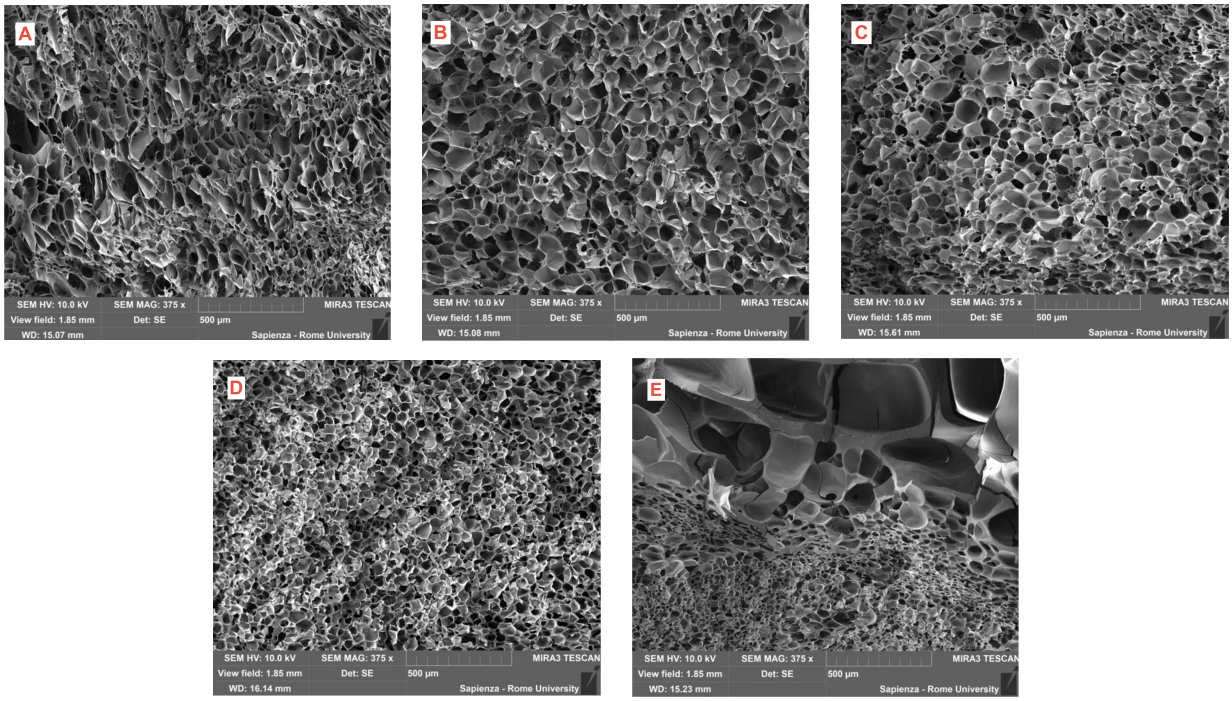


Figure 3.9: FE-SEM images of cryogel and hydrogel samples at 375x magnification. Systems obtained from polymer solutions containing 0.055 $mmoles_{MG}$ of cryogel type with with ratios $mmoles_{APS}/mmoles_{MG}$ equal to (**a**) 1.30, (**b**) 1.35, (**c**) 1.40, (**d**) 1.45 and of hydrogel type with a ratio $mmoles_{APS}/mmoles_{MG}$ equal to (**e**) 2.00.

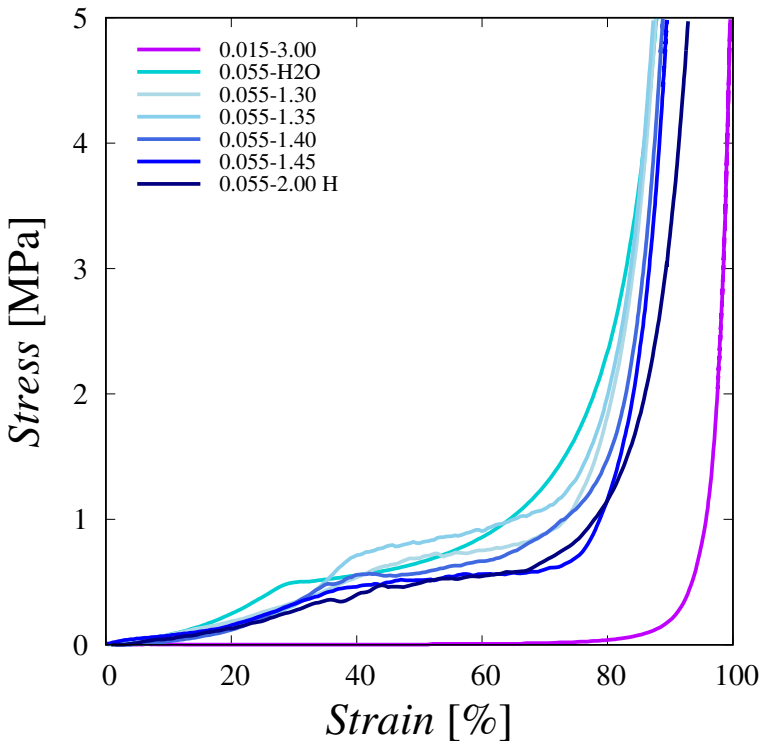


Figure 3.10: Stress-Strain curves obtained from the compression tests for all the types of dry samples analyzed in this chapter

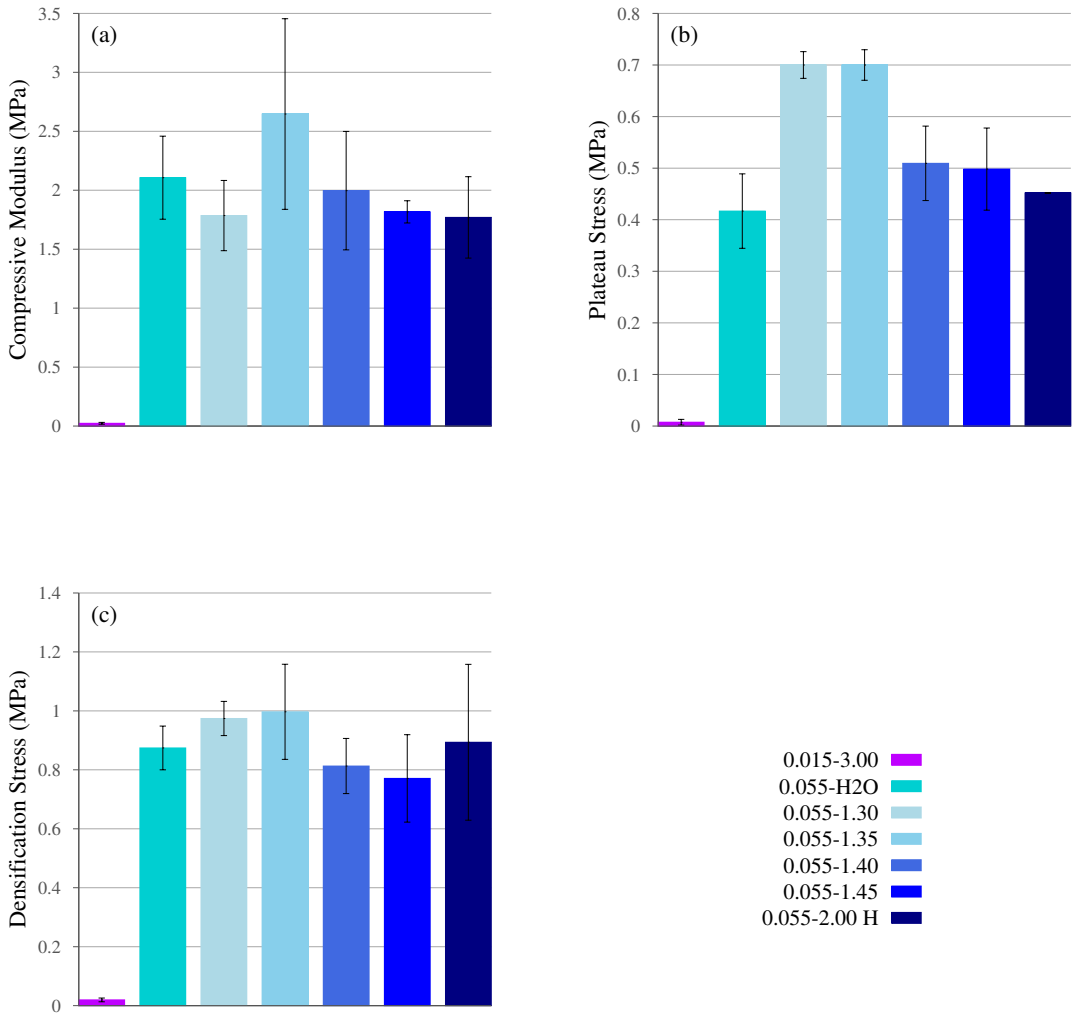


Figure 3.11: Compressive properties of freeze-dried cryogels and hydrogels. The analyzed systems derive from polymer solutions containing 0.015 mmoles_{MG} with $\text{mmoles}_{APS}/\text{mmoles}_{MG} = 3.00$ and 0.055 mmoles_{MG} with $\text{mmoles}_{APS}/\text{mmoles}_{MG} = 1.30$, 1.35, 1.40 and 1.45. (**a**) Compressive modulus, (**b**) plateau stress, (**c**) densification stress of the different freeze-dried hybrid cryogels

the compressive one, the plateau one and the densification one. In order to give a proper description of these three distinct zones, three parameters were extrapolated: the compressive modulus, the plateau stress, and the densification stress. The compressive modulus was evaluated as the slope of the straight line characterizing the first region of the curve. To evaluate the plateau stress, the elastic region and the plateau region were isolated, subsequently the interpolation lines to each region were fitted in order to identify their intersection point. As far as it regards the densification stress, following the procedure proposed in [105], was evaluated as the stress value at which the efficiency of the material, that is the ratio between the energy absorbed by the material up to a certain strain and the stress itself, reaches its maximum. Fig. 3.11 provides a short summary of these parameters. After careful consideration of the mechanical properties of the systems containing 0.055 $mmoles_{MG}$, it is possible to highlight that as the ratio $mmoles_{APS}/mmoles_{MG}$ increases the mechanical properties of the systems appear to be worse, despite the differences between the various systems examined not being very pronounced. Instead, the comparison between systems containing 0.015 $mmoles_{MG}$ and systems containing 0.055 $mmoles_{MG}$ reveals that in the case of systems created starting from polymer solutions at 2.5 % w/v the values of the compressive modulus, plateau stress and densification stress are significantly lower than those obtained for the systems produced at the highest polymer concentration under investigation. This is a clear confirmation of the correlation between polymer concentration, degree of crosslinking, and final mechanical properties.

3.3 Side observations: preliminary analysis on the effect of the presence of oxygen during the gelation

Since the analyzed matrices are formed through a radical polymerization process, one might wonder how the interaction with oxygen present in air can influence their morphological and mechanical properties. To this end, preliminary studies were carried out as follows. The study was limited to matrices from polymer solutions containing 0.035 $mmoles_{MG}$. Two $mmoles_{APS}/mmoles_{MG}$ ratios were explored: 0.6 and 0.8. For both concentrations of crosslinker, samples were prepared following two procedures, the conventional one in which the solutions are in contact with air, and the one involving the creation of an inert atmosphere. The latter was accomplished by blowing nitrogen into the polymer solution prior to the addition of APS and TEMED and the cryo-freezing process. Experimental evidence shows that, although oxygen can act as a radical quencher, cryogels obtained in its absence have greater inhomogeneity, lower mechanical strength and lower quality.

The matrix that is produced in the absence of oxygen exhibits more anisotropy during the swelling phase, especially in the axial direction, than those that are generated by maintaining oxygen within the polymer solution. From fig. 3.12 it is possible to appreciate the different configurations that are reached at equilibrium after a swelling test.

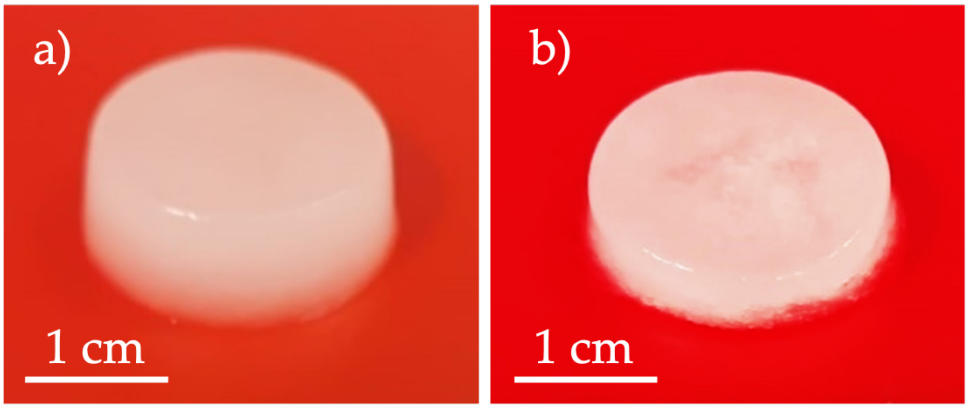


Figure 3.12: Cryogels of $DEX_{40}HEMA$ prepared with SI 0.035mmoles MG and an initiator ratio $mmoles_{APS}/mmoles_{MG} = 0.60$, formed under two conditions: (**a**) in presence of oxygen (air) (**b**) in absence of oxygen (nitrogen atmosphere).

.

3.3.1 Swelling study

Since the swelling capabiltiy reflects the structural properties of the specimens and so is related to the porosity of the sample, swelling studies in PBS at 37°C ± 0.5 °C were performed to compare the behavior of cryogel prepared in the presence and in the absence of oxygen. The hydration behavior as a function of time is given in figs. 3.13 (**a**)–(**d**). Swelling trends as a function of time confirm the difference between the cryogel systems studied. In particular, specimens prepared in an inert atmosphere show a higher swelling capacity than the corresponding systems prepared in the presence of oxygen (figs. 3.13 (**a**) and (**b**)) . Therefore, to obtain Q values comparable with those of samples made in a nitrogen atmosphere. In the case of systems made from polymer solutions in contact with air, it is necessary to use greater quantities of crosslinking agents used to induce radical crosslinking of the $DEX_{40}HEMA$.

3.3.2 Mechanical characterization and SEM analysis

The FE-SEM microscopy confirms the important role played by oxygen on the microarchitecture of cryogels, as it can be inferred from figs. 3.14 (**A**)–(**D**) . The obtained images highlight that, in general, systems created in an inert atmosphere are characterized by an inhomogeneous internal morphology, in which a poorly organized crosslinking is observed with pores of variable diameter. In particular, in each of the two cases, larger pores are observed in the case of the system with lower APS and TEMED content. As a confirmation of what was observed in the swelling tests, the systems with the most similar internal morphology are the one created in the presence of oxygen with a $mmoles_{APS}/mmoles_{MG}$ ratio equal to 0.6 and the one prepared in the absence of it with $mmoles_{APS}/mmoles_{MG}$ ratio equal to 0.8.

To study the mechanical properties of the systems, uniaxial compression tests were carried out. The typical stress-strain behaviors shown in fig. 3.15 . The values of compressive modulus, plateau stress and densification stress were evaluated as described in the section

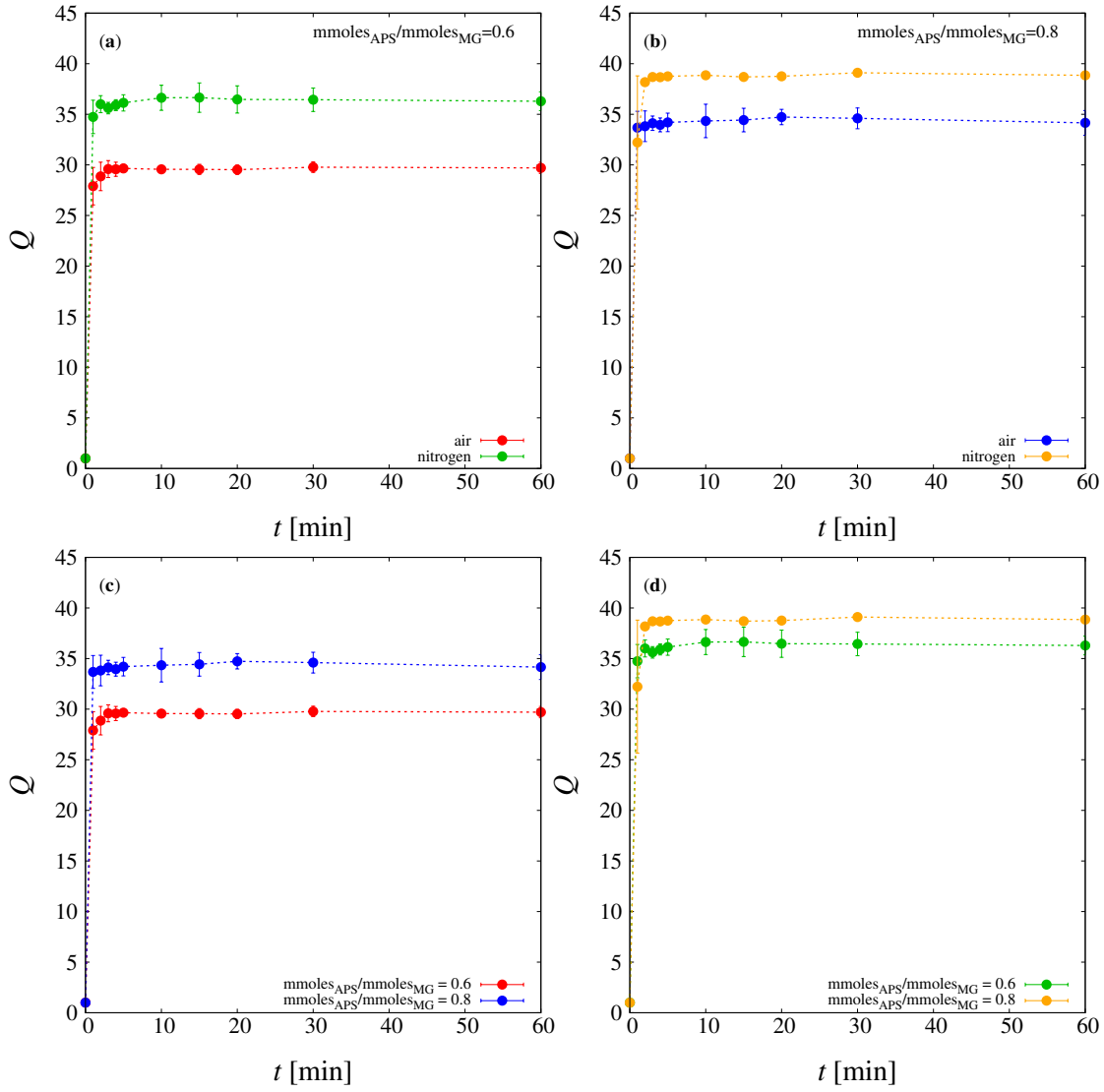


Figure 3.13: Swelling behavior of DEX$_{40}$HEMA cryogels. The analyzed systems containing 0.035 mmoles$_{MG}$ are prepared in the presence and in the absence of oxygen with mmoles$_{APS}$/mmoles$_{MG}$ ratios of 0.6 and 0.8. Comparison between systems with (**a**) mmoles$_{APS}$/mmoles$_{MG}$ = 0.6 and (**b**) mmoles$_{APS}$/mmoles$_{MG}$ = 0.8 prepared in the presence and in the absence of oxygen. Comparison between mmoles$_{APS}$/mmoles$_{MG}$ = 0.6 and 0.8 of systems prepared in contact with (**c**) air and (**d**)nitrogen atmosphere.

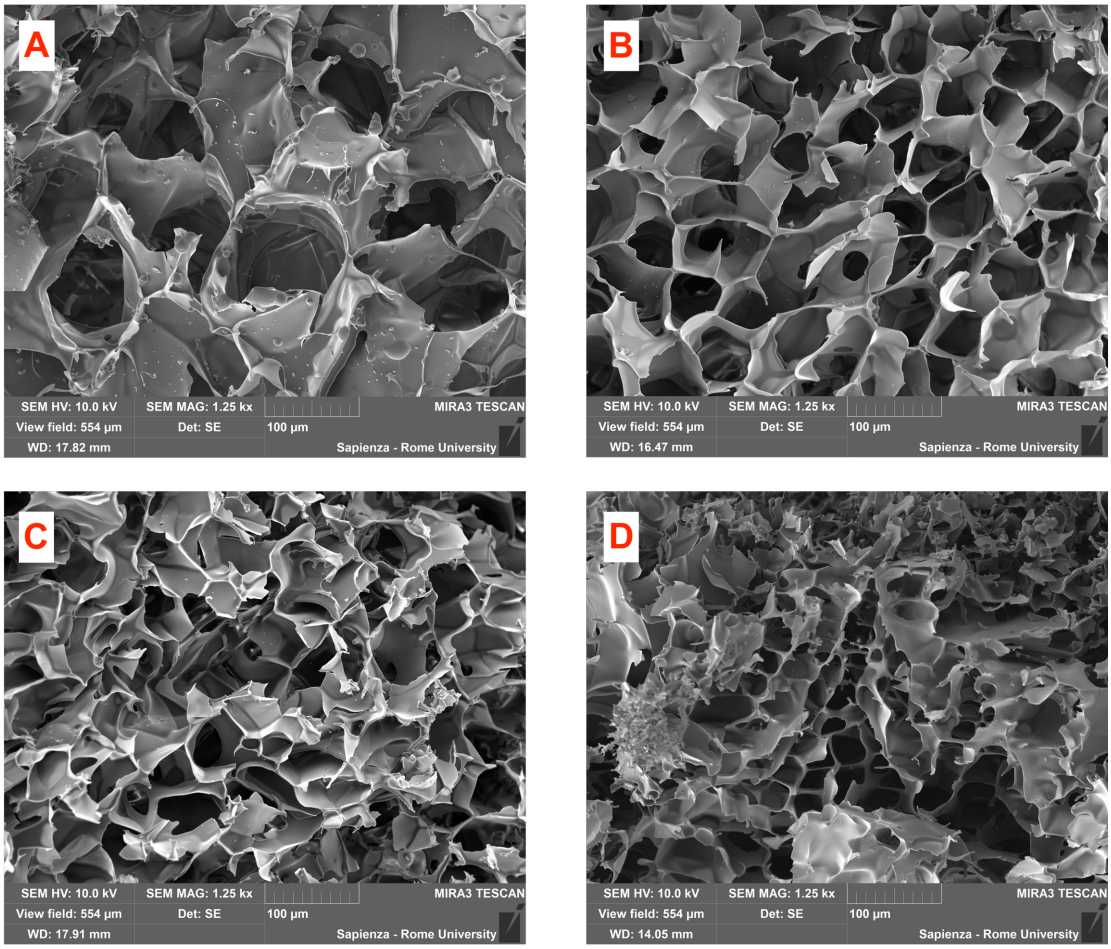


Figure 3.14: SEM images of dry $DEX_{40}HEMA$ cryogel samples obtained at 100x magnification. The analyzed systems containing 0.035 $mmoles_{MG}$ are made in the presence of oxygen with $mmoles_{APS}/mmoles_{MG}$ ratios of (**A**) 0.6 and (**B**) 0.8 and in the absence of oxygen with $mmoles_{APS}/mmoles_{MG}$ ratios of (**C**) 0.6 and (**D**) 0.8.

3.2.

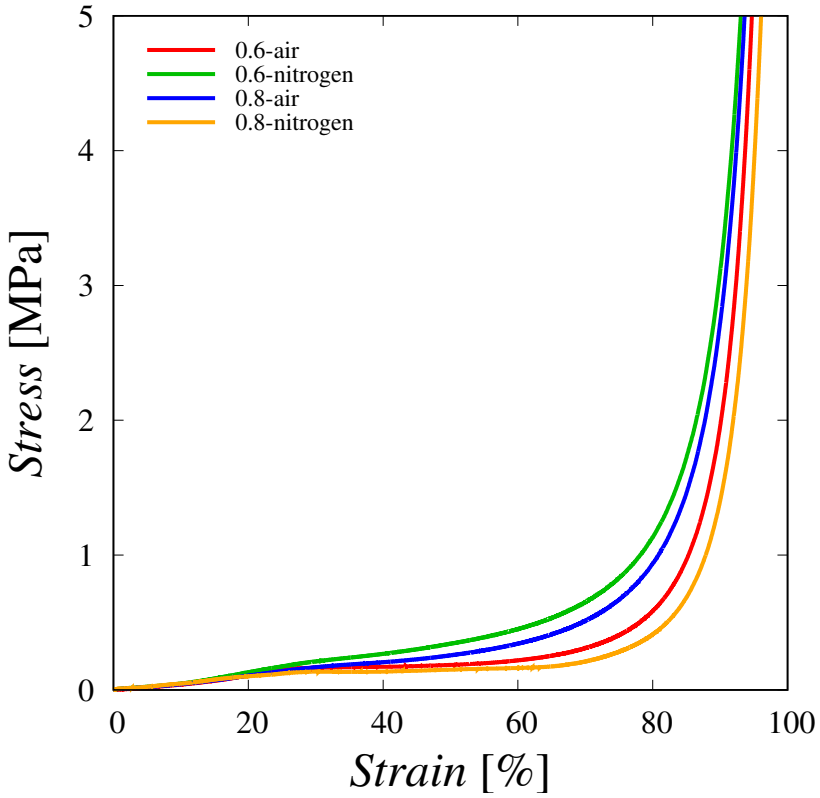


Figure 3.15: Stress-Strain curves obtained from the compression tests for all the types of dry samples analyzed in this chapter

The analysis of mechanical properties confirms the differences between systems made in nitrogen atmosphere and air, for both explored $\text{mmoles}_{APS}/\text{mmoles}_{MG}$ ratios. The observation of the compression curves and the analysis of the values reported in fig. 3.16 (**a**)–(**d**) lead to the conclusion that the system made of nitrogen with a ratio $\text{mmoles}_{APS}/\text{mmoles}_{MG}$ of 0.6 presents a slightly greater structural resistance and rigidity in the dry state. While, for the higher ratio, the observed response of the material suggests a more inhomogeneous internal structure, which densifies for lower stress values. These results could indicate the formation of a polymer network with characteristics more similar to those of a hydrogel system, in the sense that the structure is less homogeneous and with a lower degree of interconnectivity.

Even for systems built in the presence of oxygen, a difference is observed, albeit less marked, linked to the quantity of APS used. Specifically, increasing the $\text{mmoles}_{APS}/\text{mmoles}_{MG}$ ratio from 0.6 to 0.8 produces a polymer network characterized by higher densification stress values. This could be traced back to a different resistance of the matrix walls due to less radical quenching.

Following hydration of the matrices, a decrease in compression modulus values is observed as expected for all the systems analyzed. Furthermore, the increase in the $\text{mmoles}_{APS}/\text{mmoles}_{MG}$ ratio determines both in the presence and absence of oxygen a decrease in the value of this modulus which however can be attributed to different effects. In particular, in systems

generated in nitrogen this decrease could confirm the hydrogel-like nature of the polymer network, while in other systems it could be traced back to the different swelling capacity of the two matrices.

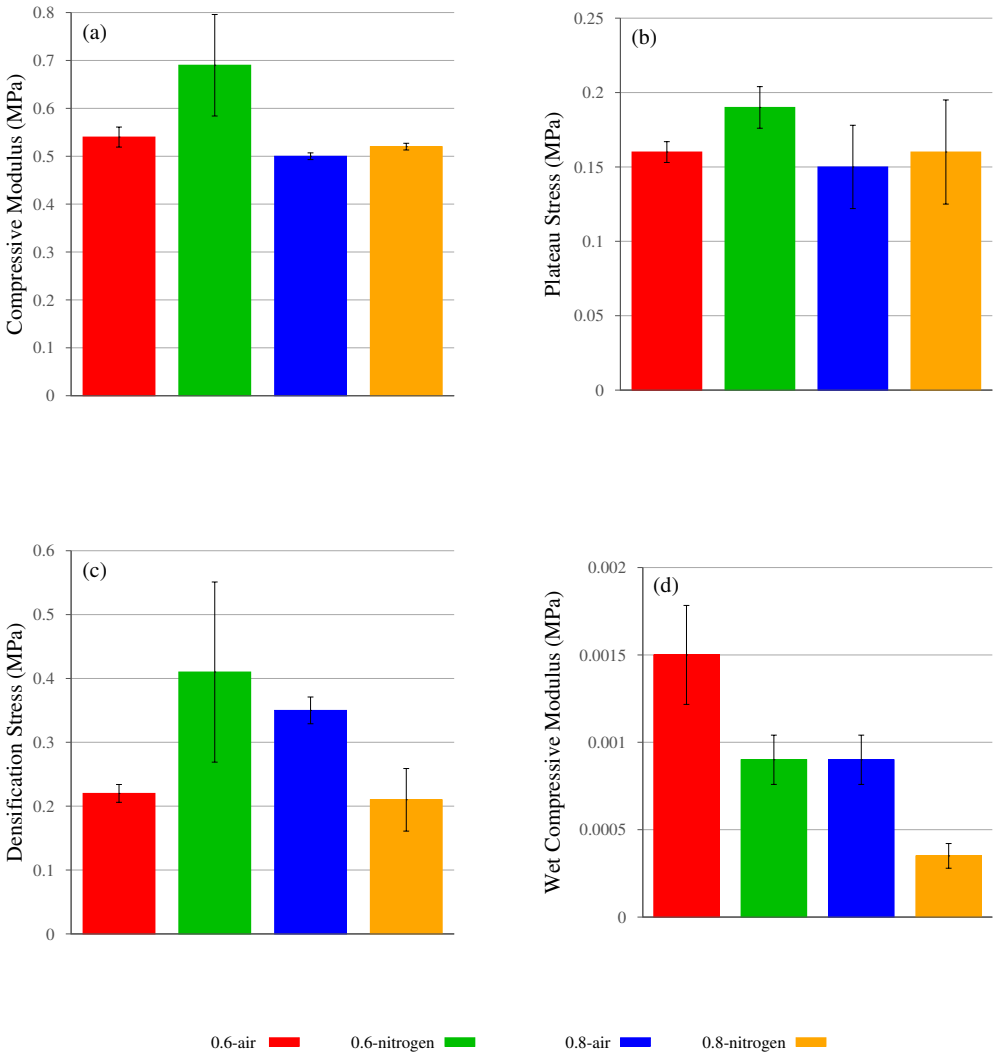


Figure 3.16: Mechanical properties of cryogel systems at a polymeric concentration of 6 % w/v with $\text{mmoles}_{APS}/\text{mmoles}_{MG}$ ratios = 0.6 and 0.8. The systems are reticulated in the presence or absence of oxygen. The compressive modulus (**a**), the plateau stress (**b**) and the densification stress (**c**) are shown for dry samples and the compressive modulus (**d**) is reported for wet samples too.

Chapter 4

Cryogels from methacrylic derivatives of dextran as drug delivery systems: effect of the dextran chain length and of the spacer

In this chapter, the systems obtained from dextran methacrylic derivatives are analyzed. Starting from the formation window developed and described in the Chapter 3, the work was oriented towards selecting formulations that guaranteed cryogel-like behavior. In detail, the examined systems were prepared with a polymer concentration of 6.0 % w/v - that is, containing 0.035 $mmoles_{MG}$ - with a ratio of $mmoles_{APS}/mmoles_{MG} = 0.6$. The synthesis of such polymers was conducted according to procedures previously optimized in these laboratories (see Section2.3.2). The investigated systems are distinguished first by the molecular weight of the dextran chain, 40,000 Da for the DEX_{40} and 500,000 for the DEX_{500}. Furthermore, they are differentiated by the type of spacer used for the polymer derivative. Specifically, since the reagents employed in the synthesis (2-HEMA, $PEG_{360}MMA$ and $PEG_{500}MMA$) influenced the corresponding polymer derivatives, which are therefore characterized by 1, 6 and 9 oxyethylene units. In order to establish a more comprehensive comparative analysis, systems of $DEX_{40}MA$ were also produced. This polymer, despite being chemically more stable, does not respond to the need to have properties that are highly requested today, especially in the biomedical field, such as biocompatibility and biodegradability, differently from other synthesized polymer derivatives. The aim of the study was to investigate the effect of dextran molecular weight and spacer length on scaffold lattice formation and its properties. Hence, the study sought to examine how dextran molecular weight and spacer length affect the formation and properties of scaffold lattices. To this end, swelling studies were carried out in order to identify the degree of swelling of the formed polymer network. The degree of swelling (Q) was expressed as the ratio of the weight of the swollen gel ($M_{sw}(t)$) to the initial (M_{dry}) of the dry sample (section 2.5). This value allows you to determine how many times the cryogel increases its weight, defining the overall quantity of solution it can

incorporate to increase its volume. The samples obtained were subjected to swelling and degradation studies in phosphate buffer (pH 7.4) and at a temperature of 37.0 ± 1.0 °C. Moreover, FE-SEM morphological analyses were performed on the samples to understand how the microarchitecture differs between cases, and uniaxial compression tests were performed to characterize the mechanical response of the samples. Finally, the dextran-based cryogels were investigated for controlled drug release purposes. In vitro release studies were conducted using vitamin B_{12} as model drug. Two different drug-loading procedures were adopted (see section 2.8), leading to very different drug release curves. The first method, which involves loading cobalamin before the cryoconcentration process, led to a slowed non-Fickian release behavior. On the contrary, samples in which the template molecule was loaded subsequent to cryoconcentration, showed a fast Fickian release. The non-Fickian drug release, observed for all the five different dextran-based cryogels investigated, is actually due to the cryoconcentration phenomenon, modeled with a two-step release process. The proposed transport model accurately predicts experimental release curves characterized by a long lag time, confirming that dextran-based cryogels are suitable for controlled release [106].

4.1 Swelling studies of dextran-derivatives samples

From the swelling studies, no marked differences emerged depending on the molecular weight of the dextran chain or the type of spacer. A comparison based on these variables is shown in Figures 4.1(**a**)–(**d**). As it can be observed, almost complete swelling is attained within 2 minutes for all investigated cryogels. The influence of the spacer on the swelling capability $Q(t)$ is illustrated in Figures 4.1(**a**) and (**b**), which respectively show the behaviour of all the samples prepared with DEX_{40} ($DEX_{40}MA$, $DEX_{40}HEMA$, $DEX_{40}PEG_{360}MA$, $DEX_{40}PEG_{500}MA$) and with DEX_{40} ($DEX_{500}HEMA$, $DEX_{500}PEG_{360}MA$). More specifically, it can be noted that $DEX_{40}MA$ absorbed less solvent than all other specimes, which can be ascribed to the lower hydrophilicity. In addition, it can be observed that a slightly lower equilibrium swelling degree is observable for $DEX_{40}PEG_{500}MA$. It can be attributed to the formation of clusters between the oxyethylene units, resulting in a greater degree of interaction between the polymer chains and the formation of conglomerates which, in turns, determine a smaller mesh of the polymer network and a lower capability of solvent penetration, as shown by SEM analysis in Figures 4.4(**C**)-(**D**). Indeed, during freeze concentration, the dextran/PEG concentrations might become high enough for phase separation to occur, thus forming dextran and PEG clusters, as observed by Heller et al. [107].
Figures 4.1(**c**) and (**d**) highlight the effect of the DEX molecular weight. The different molecular weights of the starting dextran do not cause dignificant variations in the swelling degree for cryogels based on $DEX_{40}PEG_{360}MA$ and $DEX_{500}PEG_{360}MA$. A different trend, however, is observed with the $DEX_{500}HEMA$ which swells much more than the corresponding system obtained from the lower molecular weight polymer analogue.

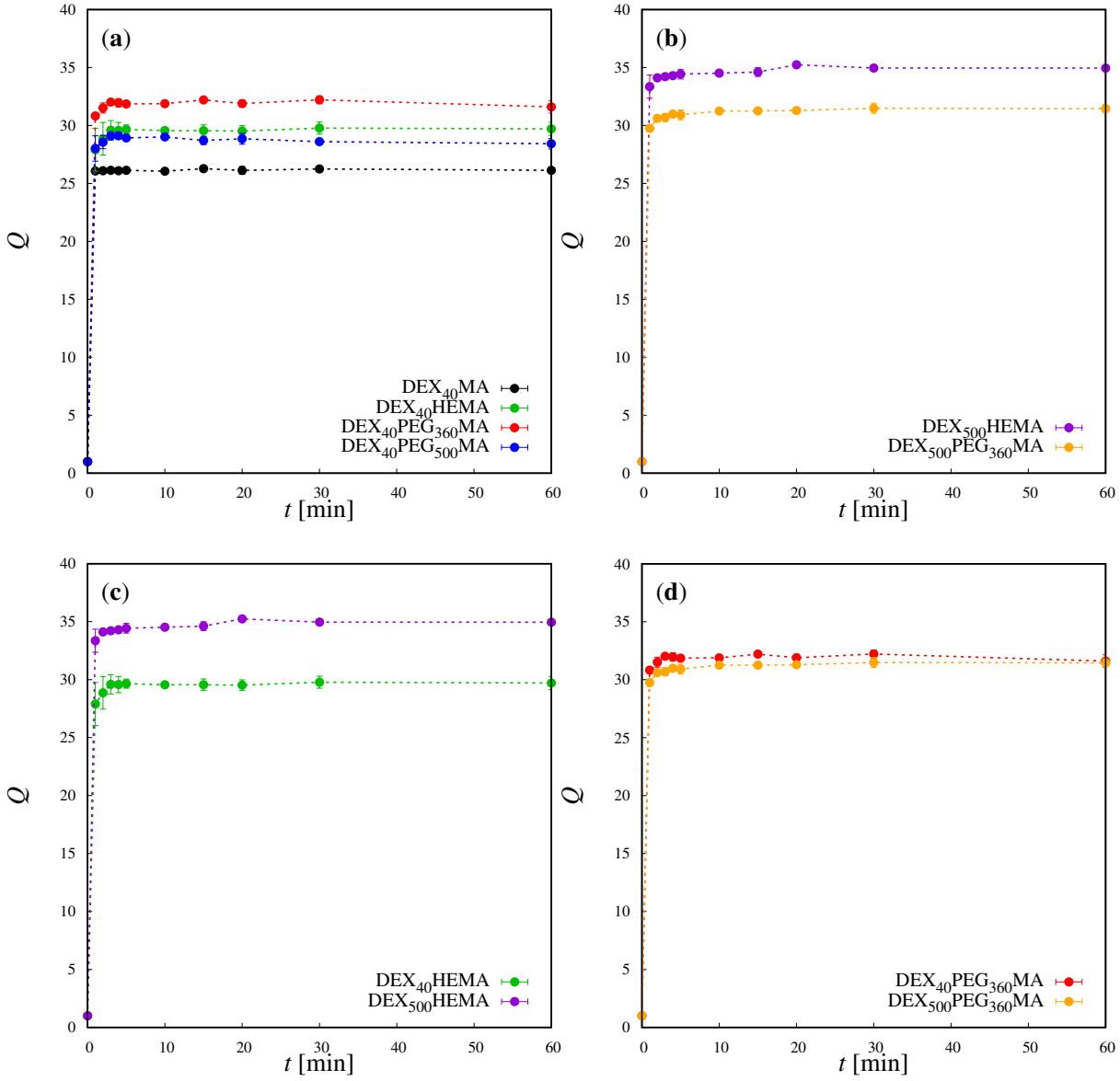


Figure 4.1: Swelling capability curves of dextran samples prepared from polymer solutions containing 0.035 mmoles_{MG} with $\text{mmoles}_{APS}/\text{mmoles}_{MG} = 0.6$. (**a**) comparison between DEX_{40} samples, (**b**) comparison between DEX_{500} samples, (**c**) comparison between samples with the same spacer HEMA and (**d**) comparison between samples with the same spacer $\text{PEG}_{360}\text{MA}$.

Figure 4.3 shows a picture of a $DEX_{40}PEG_{360}MA$ cryogel before (**a**) and after complete swelling (**b**).

The degradation process of the scaffolds was evaluated by monitoring the parameter Q over time until complete degradation of the matrices. From this analysis, the effect of the initial DEX molecular weight can be clearly observed. It must be underlined that $DEX_{40}MA$ sample mantained its structure even after 3 months, th the Q value remaining constant at around 26. This behavior can be explained as follows: $DEX_{40}MA$ contains methacrylic groups linked to the DEX chain through an ester bond, whereas in the other systems a carbonate group is present between the DEX and the spacer. Consequently, as expected, hydrolysis in phosphate buffer proceeds faster for all other systems except for the $DEX_{40}MA$.

The degradation data shown in Figure 4.2 have larger errors than swelling data (as highlighted by the error bars) intrinsically due to the experimental procedure, but show a well-defined decaying behaviour, with a total degradation time of 35 days for cryogels derived from DEX_{40} and 45 days for those derived from from DEX_{500} .

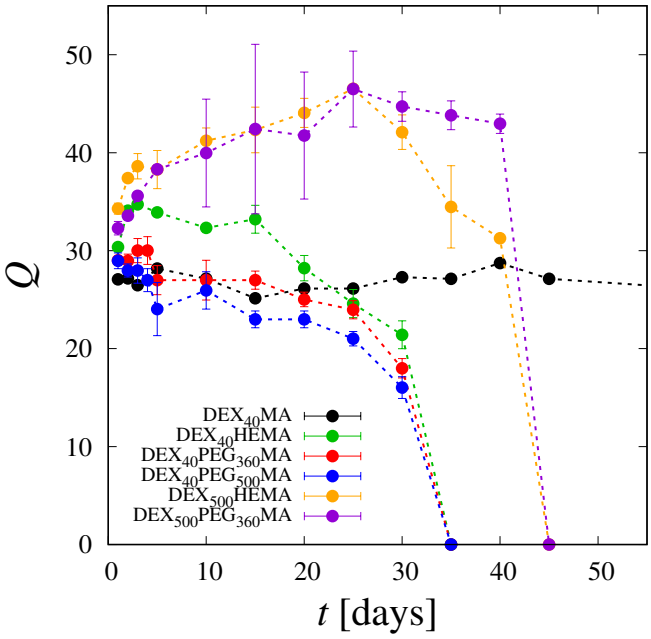


Figure 4.2: Swelling capability curves of dextran samples prepared from polymer solutions containing 0.035 $mmoles_{MG}$ with $mmoles_{APS}/mmoles_{MG} = 0.6$. (**a**) comparison between DEX_{40} samples, (**b**) comparison between DEX_{500} samples, (**c**) comparison between samples with the same spacer HEMA and (**d**) comparison between samples with the same spacer $PEG_{360}MA$.

4.2 FE-SEM analysis and mechanical properties of dextran-derivatives samples

The images 4.4**A** – **F** captured by FE-SEM microscopy validate the unique internal structure of the cryogel systems. The samples, before being subjected to SEM analysis, were prepared

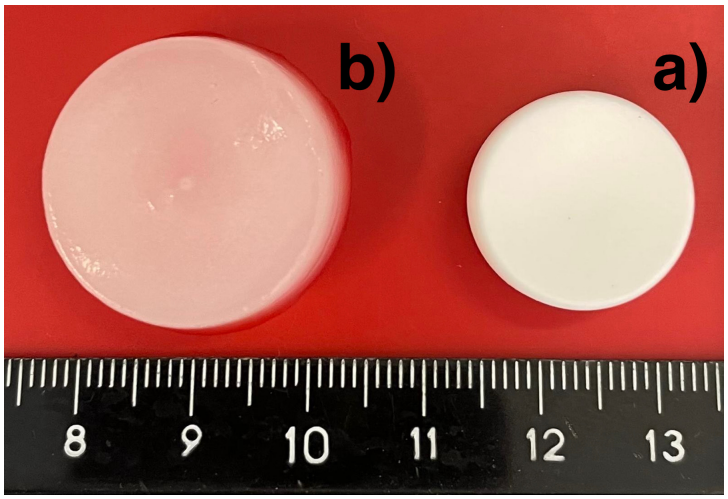


Figure 4.3: Freeze-dried $DEX_{40}PEG_{360}MA$ cryogel before (**a**) and after complete swelling (**b**).

as described in sect. **??**. The comparison of SEM images from all systems was performed to determine the effect of increasing the molecular weights of the dextran chain and spacer on system morphology.
First, the observed differences between systems are reported based on the type of spacer. Regarding the systems of $DEX_{40}MA$ and $DEX_{40}HEMA$, it is observed a much more organized internal structure for the former. However, the pores are found to be smaller in size and with a lower degree of interconnection. This turns out to be in line with the lower swelling capability of the $DEX_{40}MA$ observed in the tests described in paragraph **??**. The increase in the number of oxyethylene units, i.e. the increase in the molecular weight of the spacer, makes the internal structure much more complex. Namely, filamentous bridges that are connected to thicker walls can be seen in the image related to the $DEX_{40}PEG_{360}MA$ system, unlike the ones previously examined.The presence of filamentous structures is even more evident in the $DEX_{40}PEG_{500}MA$ samples. Such morphological differences are a consequence of the hydrophilic characteristics of HEMA and the hydrophobic behavior of PEG. In fact, the latter should tangle on itself, forming clusters in order to protect its hydrophobic nature. This influences the solubility of the corresponding polymer solution and everything is reflected in a distinct internal structure of the matrix produced.

To define the mechanical properties of the matrices obtained, mechanical compression tests were carried out so as to obtain the corresponding stress-strain graphs (fig.4.5), characterized by the three typical regions for these porous systems. As previously underlined in the chapter 3, in order to correctly describe these three distinct zones, three parameters shown in figs 4.6(**a**)–(**d**) were extrapolated: the compression module, the plateau effort and the densification effort. As it can be seen from fig. 4.6(**a**), the system based on $DEX_{40}MA$ has a lower compression modulus than all other methacrylic dextran derivatives. Furthermore, the analysis of the behavior of the other samples in the linear elastic deformation zone leads to affirm that, for the same molecular weight of the dextran chain, systems with spacers containing multiple oxyethylene units are characterized by greater stiffness. This difference

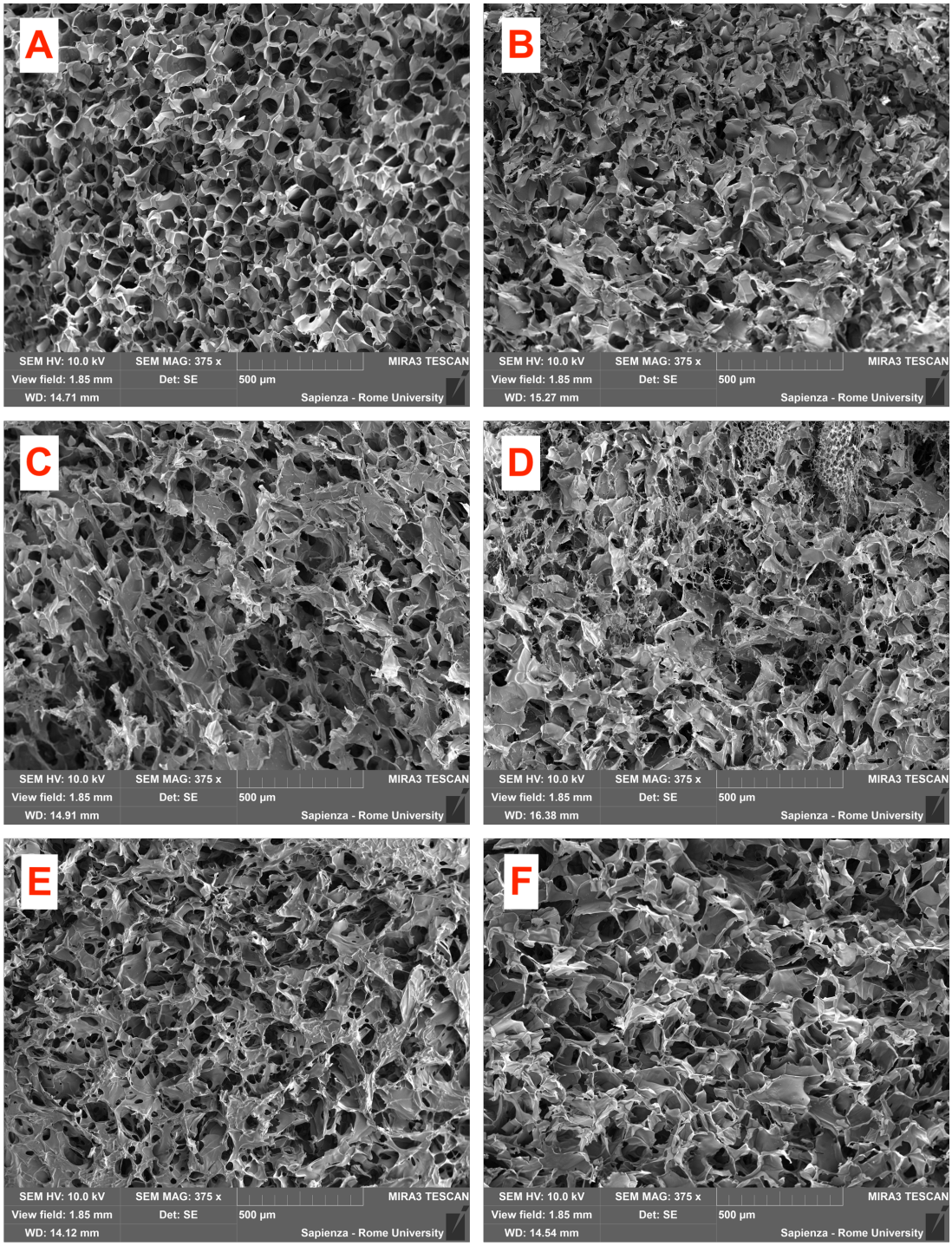


Figure 4.4: SEM images showing the morphology of cryogels. (**A**) $DEX_{40}MA$. (**B**) $DEX_{40}HEMA$. (**C**) $DEX_{40}PEG_{360}MA$. (**D**) $DEX_{40}PEG_{500}MA$. (**E**) $DEX_{500}HEMA$. (**F**) $DEX_{500}PEG_{360}MA$.

.

is marked by moving from HEMA-containing systems to PEG-containing systems, while it becomes less significant between samples with a higher number of oxyethylene units. Comparing the values of the compression modulus for the same molecular weight of spacer, the difference of these values is more accentuated in the case of HEMA as spacer. Of all the systems, the $DEX_{500}PEG_{360}MA$ densifies to higher strain values, therefore it is characterized by a homogeneous matrix that collapses much more quickly than other systems. In the

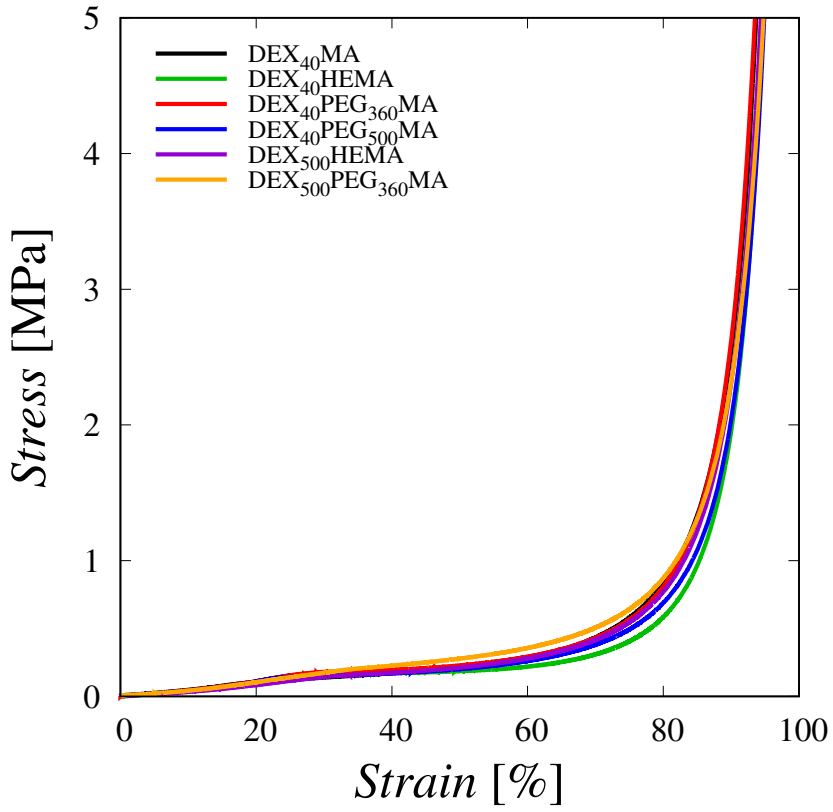


Figure 4.5: Stress-Strain curves obtained from the compression tests for all dextran-derivatives samples in the dry state. The samples are prepared from solutions containing 0.035 mmoles$_{MG}$ with an APS/MG molar ratio = 0.6.

hydrated state, samples of $DEX_{40}PEG_{500}MA$ have a higher rigidity.

4.3 Release studies

All the samples analyzed in this chapter were investigated as possible controlled drug delivery platforms. To this end, release studies were performed following the procedure described in Section 2.8. From a preliminary analysis of the experimental data, it can be concluded that for all dextran-based cryogels the related release curves exhibit a non-Fickian behavior when the drug is loaded before the cryogelation process.
Indeed, Figure 8.11 shows the release curves M_t/M_∞ vs t of pre-loaded B_{12} for $DEX_{40}MA$, $DEX_{40}HEMA$ and $DEX_{500}PEG_{360}MA$. The log-log plot permits to highlight the non-Fickian behaviour characterized by an exponent $n = 1.1$ for all these dextran-based cryogels. The B_{12} release is characterized by the same lag time for all the cryogels, and represents the fingerprint of drug trapping in the stationary phase induced by the cryoconcentration process.

With the aim of having a deep comprehension of what influenced the release, it was decided to utilize a different method of loading the model drug and, thus, to compare the results from the two release procedures. To this end, it was decided to conduct the analysis on systems exhibiting different diffusional exponent n. In doing so, $DEX_{40}PEG_{360}MA$ and $DEX_{40}PEG_{500}MA$ cryogels were selected. Release curves, shown in Figure 8.4**a** for $DEX_{40}PEG_{360}MA$ and in Figure 8.4**b** for $DEX_{40}PEG_{500}MA$, are highly sensitive to the drug-loading procedure. Specifically, for both cryogels analyzed, the release curve for the after-loaded drug is significantly faster than that obtained with the pre-loaded drug. Moreover, the after-loaded release curve exhibits, for both cryogels, a well defined power-law behavior $M_t/M_\infty \sim t^n$ at short-intermediate time-scale, characterized by an exponent $n = 0.55$ close to $n = 0.5$ characterizing the Fickian behaviour [59]. On the contrary, the pre-loaded release curves exhibit a markedly non-Fickian behaviour characterized by an exponent n significantly larger than 0.5. Specifically $n = 0.8$ for $DEX_{40}PEG_{360}MA$ and $n = 1.2$ for $DEX_{40}PEG_{500}MA$. The larger is the value of the n exponent, the longer is the lag time observed in the release curves [70].

A similar non-Fickian behavior was already observed for methacryloyl gelatin (GelMA) blended with dextran methacrylate ($DEX_{40}MA$) cryogels [15] and explained as a consequence of the cryoconcentration phenomenon. Indeed, the cryogel can be viewed as a hierarchical porous structure characterized by the coexistence of two phases, a microporous dense stationary one, in which the drug (in the pre-loaded case) gets trapped during the cryogelation process, and a macroporous "mobile" one. During the release process, the cryogel sample rapidly swells, and the drug, initially trapped in the microporous phase, is irreversibly released in the macroporous phase where is free to diffuse out of the sample. Therefore, the release process in the pre-loading case occurs in two steps characterized by two different time-scales: the time-scale t_t associated to the internal drug-transfer process from the stationary to the mobile phase (controlling the lag time) and the time-scale t_d associated with

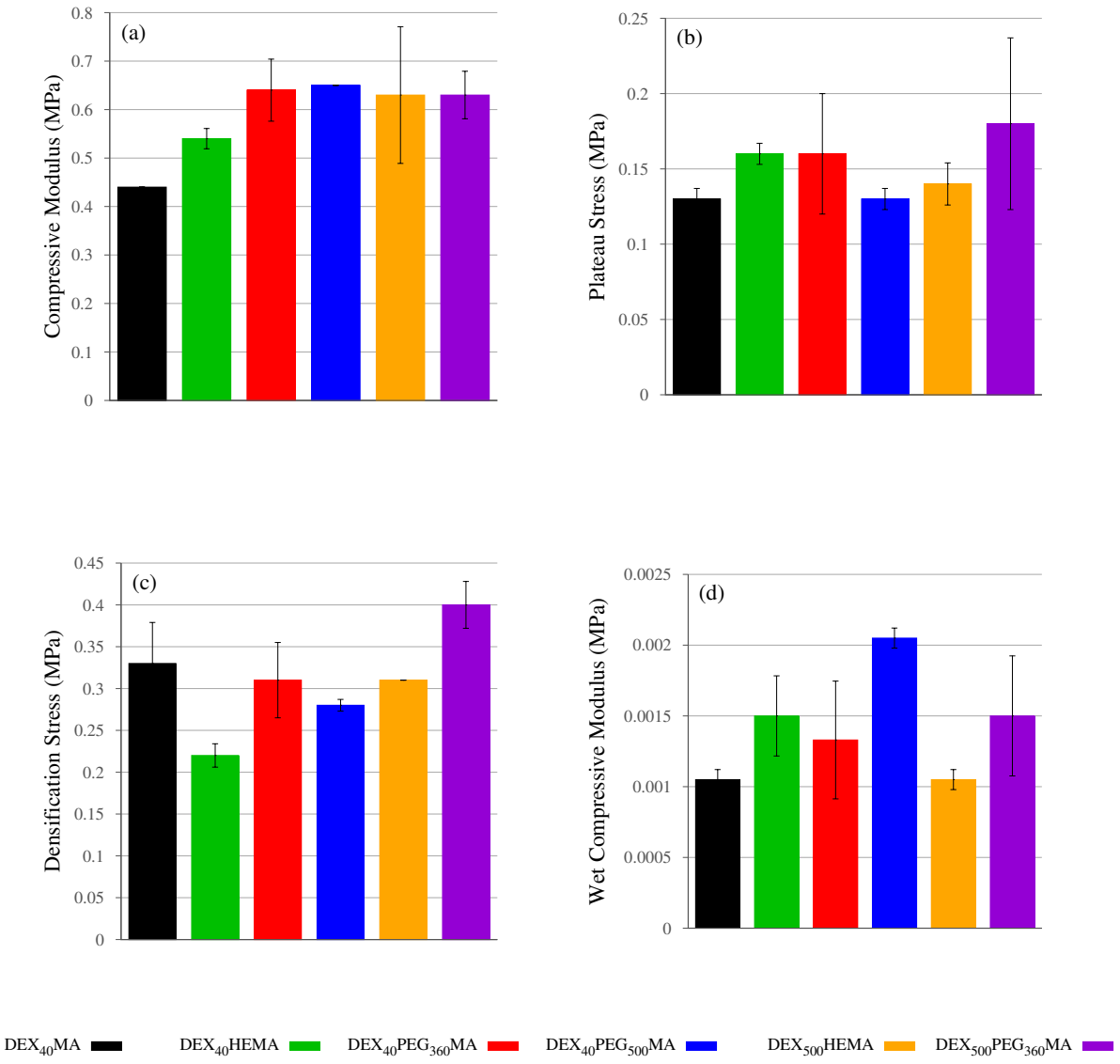


Figure 4.6: Mechanical properties of cryogel systems at a polymeric concentration of 6 % w/v with $\text{mmoles}_{APS}/\text{mmoles}_{MG}$ ratios = 0.6 and 0.8. The systems are reticulated in the presence or absence of oxygen. The compressive modulus (**a**), the plateau stress (**b**) and the densification stress (**c**) are shown for dry samples and the compressive modulus (**d**) is reported for wet samples too.

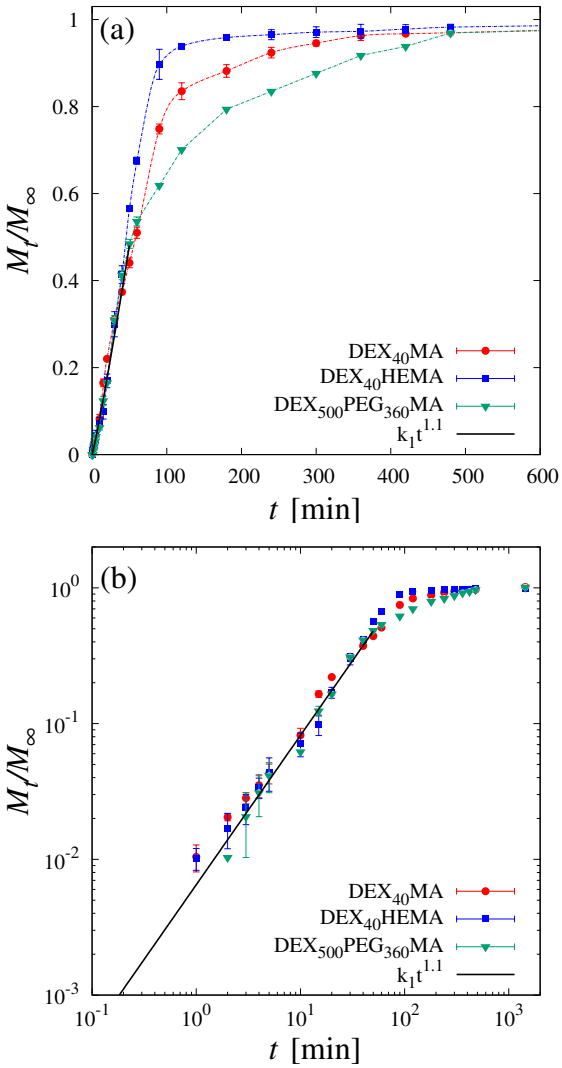


Figure 4.7: M_t/M_∞ vs t for pre-loaded B_{12} from $DEX_{40}MA$, $DEX_{40}HEMA$ and $DEX_{500}PEG_{360}MA$ cryogels. The continuous black line highlights the non-Fickian behaviour $M_t/M_\infty \sim t^n$ with $n = 1.1$.

the diffusive transport in the macroporous phase. The interplay between these two transport processes is responsible for the observed non-Fickian behavior of the release curves in case of the drug is pre-loaded. On the contrary, if the drug is infused in the lyophilized sample after the cryogel formation (after-loading procedure) there is no drug trapping in the microporous phase (absence of the cryoconcentration phenomenon) and drug release occurs exclusively by diffusive transport in the macroporous phase. By considering that the swelling process is extremely fast, compared to the diffusional time-scale, the release curves exhibit a typical Fickian behaviour, as experimentally observed.

In presence of cryoconcentration, the more pronounced non-Fickian behaviour of $DEX_{40}PEG_{500}MA$ with respect to $DEX_{40}PEG_{360}MA$ is due to a larger fraction of drug initially trapped in the microporous phase. This finding is in agreement with the reduced swelling capability of $DEX_{40}PEG_{500}MA$ due to the formation of clusters between the oxyethylene units, resulting in a greater degree of interaction between the polymer chains and the formation of conglom-

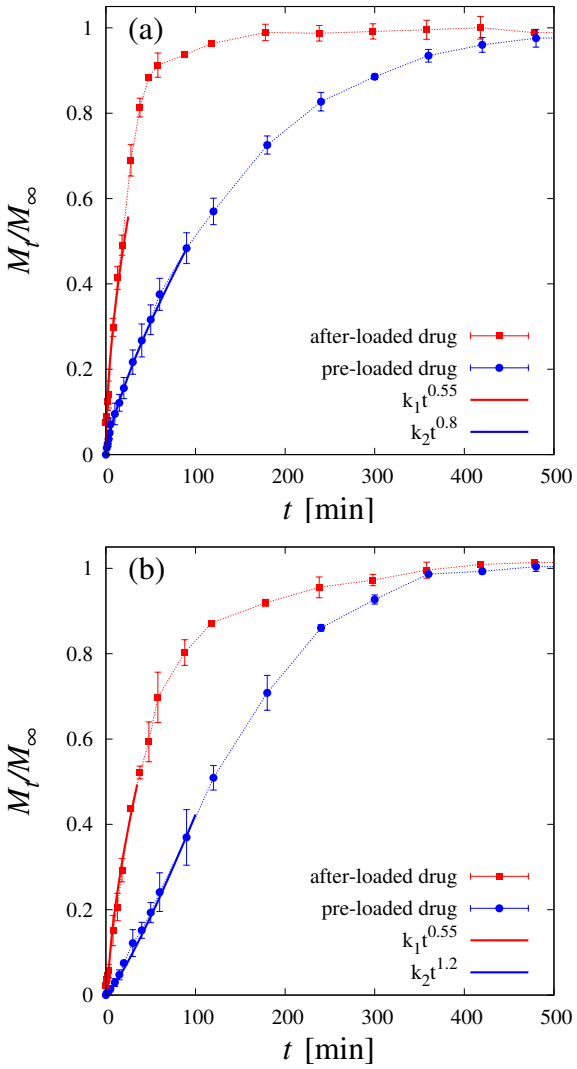


Figure 4.8: Release curves of vitamin B_{12} in the case of pre-loaded drug (blue curves) and after-loaded drug (red curves). (**a**) Release from $DEX_{40}PEG_{360}MA$ cryogel. (**b**) Release from $DEX_{40}PEG_{500}MA$ cryogel.

erates, as shown by SEM images.

4.4 Theoretical model of drug release in the pre-loading case

The transport model developed is based on the coexistence of two phases: a microporous stationary phase, in which the vitamin is initially concentrated due to the cryoconcentration phenomenon, and a macroporous mobile phase where drug transport occurs exclusively by diffusion. Indeed, the swelling process of the lyophilized sample is extremely fast (order of 2 minutes to reach equilibrium conditions) so that the cryogel is assumed fully swollen at the beginning of the release process. For this reason, the non-Fickian release observed cannot be attributed to a Case II transport process [59],[60], in which drug release and swelling

are two phenomena occurring simultaneously. Let $R_{sw} \simeq 13$ mm and $H_{sw} \simeq 10$ mm the dimensions (radius and height) of the swollen cylindrical sample (volume $V_{cyl} = \pi R_{sw}^2 H_{sw}$) and $m_0 \simeq 2.5 \pm 0.1$ mg the amount of drug loaded in the cryogel, so that the initial drug concentration in the specimen is $c_0 = m_0/V_{cyl} \simeq 0.47$ mg/mL.

The drug trapped in the microporous phase, with initial concentration $c_s(r, z, 0) = \varepsilon_0 c_0$, is irreversibly released in the macroporous mobile phase with a linear transfer rate $k_t c_s$, directly proportional to the local drug concentration $c_s(r, z, t)$. The fraction ε_0 of drug initially trapped in the microporous phase is one important parameter of the model as well as the transfer coefficient $k_t[s^{-1}]$ controlling the time-scale $t_t = 1/k_t$ associated with the internal drug-transfer process between phases. Once in the mobile phase, the drug is free to diffuse out of the sample into the liquid reservoir (volume V_{res}) where perfect mixing conditions are ensured by agitation.

Let $c_m(r, z, t)$ and $c_{res}(t)$ the drug concentration in the mobile phase and in the reservoir, respectively, with initial conditions $c_m(r, z, 0) = (1-\varepsilon_0)c_0$ and $c_{res} = 0$. The coupled balance equations for c_s, c_m and c_{res} read as

$$\frac{\partial c_s(r,z,t)}{\partial t} = -k_t c_s \tag{4.1}$$

$$\frac{\partial c_m(r,z,t)}{\partial t} = D_{B_{12}} \nabla^2 c_m + k_t c_s \tag{4.2}$$

$$c_m(r,z,t)\Big|_S = c_{res}(t), \quad \frac{\partial c_m}{\partial r}\Big|_{r=0} = 0 \tag{4.3}$$

$$V_{res} \frac{\mathrm{d}c_{res}(t)}{\mathrm{d}t} = D_{B_{12}} \int_S -\nabla c_m \cdot \mathbf{n}\, ds - \sum_{i=1}^{N_w^t} V_w c_{res} \delta(t - t_w^i) \tag{4.4}$$

where $\delta(t)$ is a Dirac delta function, $\nabla(\cdot) = (\frac{\partial \cdot}{\partial r}, \frac{\partial \cdot}{\partial z})$ and $\nabla^2(\cdot) = \frac{\partial^2 \cdot}{\partial z^2} + \frac{1}{r}\frac{\partial}{\partial r}\big(r\frac{\partial \cdot}{\partial r}\big)$ are the gradient and Laplacian operators in cylindrical coordinates, S is the lateral surface of the cylindrical specimen, $\mathbf{n}$ the outward unit normal vector of S and $D_{B_{12}}$ the diffusion coefficient of B_{12} in PBS in the macroporous phase.

Numerical results for the concentration fields were obtained by solving the transport scheme with a commercial software enforcing Finite-Element Method (Comsol 5.5). For the numerical integration of the coupled time-dependent transport equations of c_s and c_m, the Coefficient Form PDE package was adopted on the 2-d axial symmetric geometry (cylinder) and solved in transient conditions (time-dependent solver, fully-coupled method) together with the ODE for c_{res}. Lagrangian quadratic elements have been chosen. The MUMPS solver was adopted with relative tolerance 10^{-6}.

The time-dependent Dirichlet boundary condition, Eq. (4.3), replaces the generally adopted perfect sink condition ($c_m|_S = 0$) that is not appropriate for describing our experiments in which the ratio α

$$\alpha = V_{cyl}/V_{res} \tag{4.5}$$

is about 1/4 in our experiments and therefore is not small enough for the perfect sink

approximation to be valid ($\alpha \ll 1$). Increasing the volume of the reservoir is to be avoided as the concentration of the drug, at the first withdrawals, would be too low and also would worsen the mixing conditions in the reservoir.

The adoption of Eq. (4.3) for c_m at the boundary S requires the introduction of the balance equation (4.4) for c_{res}. Eq. (4.4) takes into account the finite volume of the reservoir and the N_w withdrawals (each with volume V_w) that are made at different time instants $\{t_w^i\}_{i=1}^{N_w}$ in order to measure, by HPLC, the drug concentration in the reservoir $c_{res}(t_i)$ at the withdrawal time t_i and build up the experimental $M_t(t_i)$ vs t_i release curve

$$M_t(t_i) = c_{res}(t_i)V_{res} + \sum_{j=1}^{N_w^t} c_{res}(t_j)V_w \tag{4.6}$$

where N_w^t denotes the number of withdrawals made from time $t = 0$ to time t (or equivalently t_i). Eq. (4.6) can be also adopted to evaluate the amount of drug $M_t(t)$ released up to time t from the transport model Eqs. (4.1)-(4.4), by simply replacing $c_{res}(t_i)$ with $c_{res}(t)$.

The finite value of α and the withdrawals influence the total amount of drug M_∞ that can be asymptotically released [108, 109]. Indeed, according to Eq. (4.6), M_∞ attains the form

$$M_\infty = c_{res}^\infty V_{res} + \sum_{j=1}^{N_w} c_{res}(t_j)V_w = \frac{c_0 V_{cyl}}{1+\alpha} + \frac{\alpha}{1+\alpha}\sum_{j=1}^{N_w} c_{res}(t_j)V_w \tag{4.7}$$

where $c_{res}^\infty = (c_0 V_{cyl} - \sum_{j=1}^{N_w^t} c_{res}(t_j)V_w)/(V_{cyl} + V_{res})$ is the asymptotic concentration in the reservoir, coinciding with the uniform drug concentration c_m^∞ that asymptotically sets in the mobile phase when all components of the concentration gradient nihilate ($\nabla c_m = \mathbf{0}$), and the drug release from the specimen to the reservoir stops. From Eq. (4.7) it can be readily observed that, the larger is the value of α, the more M_∞ deviates from (and is smaller than) $m_0 = c_0 V_{cyl}$. On the contrary, the effect of the withdrawals is to increase the amount of drug asymptotically released.

Given the large porosity of the cryogels and the relatively small molecular weight of the B_{12}, the diffusion coefficient $D_{B_{12}}$ can be assumed close to the bare diffusion coefficient of B_{12} in PBS. Specifically, we assumed $D_{B_{12}} = 7.2 \times 10^{-10}$ m^2/s for both $DEX_{40}PEG_{360}MA$ and $DEX_{40}PEG_{500}MA$ cryogels. See section 4.4.1 for a detailed analysis of the physical/-mathematical considerations supporting this choice.

The two parameters to tune in order to fit the experimental data are the fraction ε_0 of B_{12} initially trapped in the microporous phase and the transfer rate coefficient k_t. The best-fit value for k_t is $k_t = 2.6 \cdot 10^{-4}$ s^{-1} for both cryogels. The two cryogels differ in the amount of vitamin initially trapped in the microphase, namely $\varepsilon_0 = 0.80$ for $DEX_{40}PEG_{360}MA$ and $\varepsilon_0 = 0.95$ for $DEX_{40}PEG_{500}MA$. This difference, as in the case of the equilibrium swelling degree, could be explained by a larger amount of conglomerates in the $DEX_{40}PEG_{500}MA$ due to a stronger interaction between the chains. This results in a smaller mesh size of the polymer network, which then traps a larger fraction of the drug.

The excellent agreement between model predictions and experimental release curves for $DEX_{40}PEG_{360}MA$ and $DEX_{40}PEG_{500}MA$ in the pre-loaded case is shown in Figure 8.7. Figure 8.7 clearly shows how the model is capable of describing the lag time and the non-

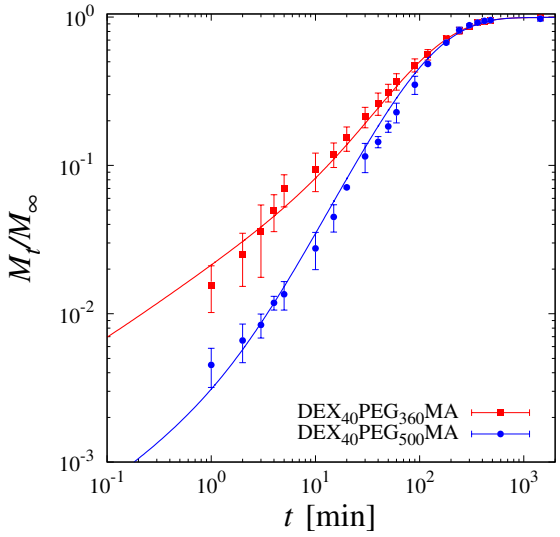


Figure 4.9: Log-log plot of release data of vitamin B_{12} (pre-loaded) from $DEX_{40}PEG_{360}MA$ and $DEX_{40}PEG_{500}MA$ cryogels. Continuous lines indicate model predictions.

Fickian behaviour of the release curves, as well as the long-term saturation towards the complete release. As a further confirmation, Figure 4.10 shows a quantitative comparison between the experimental values of c_{res} at different withdrawal time instants t_i and model predictions.

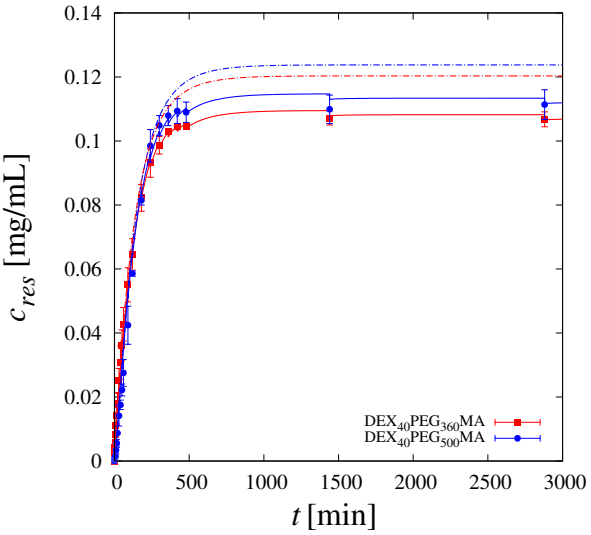


Figure 4.10: Comparison between experimental results for $c_{res}(t_i)$ (points) and model predictions. Continuous lines are numerical results accounting for the effect of withdrawals on release dynamics. Dashed lines are numerical results neglecting the effect of withdrawals on release dynamics.

Figure 4.10 allows us to appreciate the importance of taking into account the effect

of withdrawals on release dynamics [108, 109]. Indeed, each withdrawal (and subsequent replenishment of the same aliquot with fresh solution) results in an immediate decrease in the drug concentration in the reservoir, and this affects the release dynamics, especially in the case of frequent withdrawals on intermediate time-scales. Actually, Figure 8.8 shows the excellent agreement between experimental data and model predictions when withdrawals are properly accounted for (continuous lines). On the contrary, a significant deviation between experimental data and model predictions (dashed lines) can be observed if withdrawals are neglected in the dynamics of c_{res}. Neglecting withdrawals in modelling the release dynamics is possible, but this may lead to significant errors in the estimate of transport parameters, namely k_t and ε_0.

Finally, it is worth noting that the best-fit values of the transfer-rate coefficient k_t implies a value of the Damkölher number Da order of ten. Specifically,

$$Da = \frac{t_d}{t_t} = \frac{\frac{(H_{sw}/2)^2}{D_m}}{\frac{1}{k_t}} = \frac{k_t (H_{sw}/2)^2}{D_{B_{12}}} \simeq 9 \tag{4.8}$$

By considering that Da represents the ratio between the characteristic diffusion time t_d and the characteristic transfer time t_t, a value of Da significantly larger than unity implies that the internal drug transfer between the micro and the macro phase is a fast process, controlling the temporal evolution of the release curves at short/intermediate time-scales. On the contrary, the long-term behaviour is controlled by drug diffusion in the macroporous phase, and this allows us to estimate the value of the diffusion coefficient $D_{B_{12}}$, as discussed in detail in section 4.4.1.

The interplay between internal transfer and diffusion in the mobile phase, at short intermediate time-scales, is responsible for the non-Fickian behaviour, more pronounced for $DEX_{40}PEG_{500}MA$ because a larger fraction of drug is initially trapped in the stationary phase.

4.4.1 Estimation of the diffusion coefficient $D_{B_{12}}$

On long time-scale, when the release process is controlled solely by drug diffusion in the macroporous phase, the fraction of unreleased drug $1 - M_t/M_\infty$ in the cylindrical sample decays exponentially over time t as

$$1 - \frac{M_t}{M_\infty} \sim e^{-D_{B_{12}} t \lambda_0^2}, \quad \lambda_0^2 = \alpha_1^2 + \frac{\pi^2}{H_{sw}^2} \tag{4.9}$$

where λ_0^2 is the first (dominant) eigenvalue of the Laplacian operator ∇^2 in cylindrical coordinates with homogeneous Dirichlet boundary conditions and α_1 is the first positive root of the J_0 Bessel function $J_0(\alpha_1 R_{sw}) = 0$. For the dimensions R_{sw} and H_{sw} of the swollen samples under investigation, the dominant eigenvalue λ_0 is equal to $\lambda_0 = 13.571 \times 10^4$ [m^{-2}]. Figure 8.15 shows the decay of $1 - M_t/M_\infty$ vs t for both cryogels $DEX_{40}PEG_{360}MA$

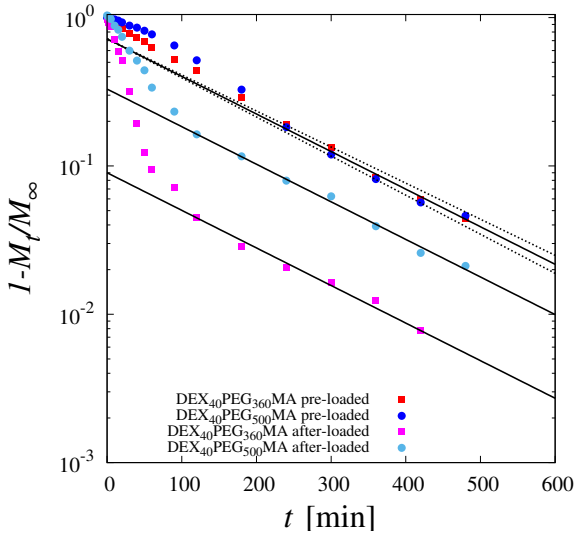


Figure 4.11: Log-normal plot of $1-\frac{M_t}{M_\infty}$ vs t for $DEX_{40}PEG_{360}MA$ and $DEX_{40}PEG_{500}MA$ for both drug loading conditions (pre and after cryogel formation). Continuous lines indicate the exponential decay, Eq. (4.9), with $D_{B_{12}} = (7.17 \pm 0.3) \times 10^{-10}$ m^2/s . Dashed lines highlight the confidence interval.

and $DEX_{40}PEG_{500}MA$ and for both loading conditions (pre and after cryogel formation). The log-normal scale adopted highlights that, on long time-scales, the trend is indeed an exponential decay over time, characterized by the same exponent for all the curves. By best-fitting the experimental exponential decay of $1 - M_t/M_\infty$ vs t with Eq. (4.9) it is possible to estimate the diffusion coefficient $D_{B_{12}}$ in the macroporous phase, thus obtaining $D_{B_{12}} = (7.17 \pm 0.3) \times 10^{-10}$ m^2/s. The long-term exponential decay is the same for all the curves, whether the drug was loaded before cryogel formation or after cryogel formation by infusion. This confirms that the lag effect observed in the release curves in the case of preloaded drug is due solely to the entrapment of the drug in the stationary phase by cryoconcentration.

Chapter 5

Cryogels as cell scaffolds: Dextran-based polymers and Methacryloyl gelatin hybrid systems

As anticipated in Chapter 1, cryogel systems are highly appreciated in the field of tissue engineering both for their morphology, characterized by highly interconnected macropores that allow cells to exchange nutrients and gases with the external environment, both for the excellent mechanical properties, which promote cell adhesion and growth. Although the dextran-based systems analyzed in the previous chapters show excellent mechanical properties, they are nevertheless systems that do not promote cell growth. In several studies, it has in fact been highlighted that systems based only on dextran are not suitable for cell cultures as they are not able to provide the required nutrients. However, blended systems are frequently created to exploit the characteristics of different polymers. In a previous study, [15], hybrid systems based on DEX_{40}HEMA and GelMA, showed better results. However, dextran methacrylate appears to be inadequate as it is highly stable from a chemical point of view, failing to meet the requirements for biocompatibility and biodegradability. This can be traced back to the fact that methacrylic groups are linked to the dextran chain through ester-type bonds, taking into account these considerations, it was decided to replace DEX_{40}MA with the methacryl derivatives of dextran analyzed in the previous chapters, as the carbonate bonds between spacer and polymer chain favor biodegradation and make the polymers more biocompatible. In particular, starting from the work developed in the article [15], one of the three best performing systems ($DexMA_3$-$GelMA_3$) was selected, containing 0.050 $mmoles_{MG}$. More precisely, in the creation of the samples analyzed below, the same quantity of GelMA (60mg) and the same volume of polymer solution (2 mL) were maintained, and the mass of dextran-based polymer was varied based on the molecular weight, in order to ensure that the final system contained 0.055 $mmoles_{MG}$. The samples obtained were characterized with mechanical tests and photon hemisison electron microscopy analyses, through swelling tests and through preliminary cell adhesion tests. This chapter is structured as follows. In Section 5.1 the results of the swelling tests are reported, highlighting the differences in behavior

resulting from the type of DEX or spacer used, and the biodegradability characteristics of the samples have been unsealed. In Section 2.9 the results from time sweep rheological analysis are displayed. Next, in Section 5.3, morphological and mechanical differences between samples were highlighted. Finally, the section 5.4 shows results of preliminary cell adhesion tests. Biocompatibility investigations are referred to subsequent studies.

5.1 Swelling and degradation studies

The dual network matrices were subjected to swelling and degradation tests in phosphate buffer (pH 7.4) at physiological temperature (37 °C) as described in Section 2.5. A comparative analysis, expressed in terms of swelling capacity, was conducted to assess the effect of both the dextran chain length and the effect of spacer length. Figs. 5.2(**a**)–(**d**) display the typical swelling dynamics of cryogels: all the samples achieve the equilibrium swelling capability within 3 minutes. Moreover, the values of Q asses to 25-30. The only exception is in the case of $DEX_{40}PEG_{500}MA$ scaffolds, which absorb a lower quantity of solvent. This may be explained as a consequence of the formationof clusters among the oxyethylene units of the PEG_{500} chain: as a consequence, there is a higher degree of interaction among the polymeric chains and so a lower Q. In fig. 5.1 it is reported the comparison between a freeze-dried and a complete swollen $DEX_{40}PEG_{360}MA$-GelMA cryogel. Even if the difference in the swelling dynamics is not that evident, the bioerosion process, tracked through the change in mass of the sample left in PBS at 37°C ± 1°C, puts in evidence the effect of the molecular weight of both the DEX chain and the spacer. As it can be observed in Fig. 5.3 , the higher the molecular weight of the dextran chain, the longer the time needed to completely degradate.

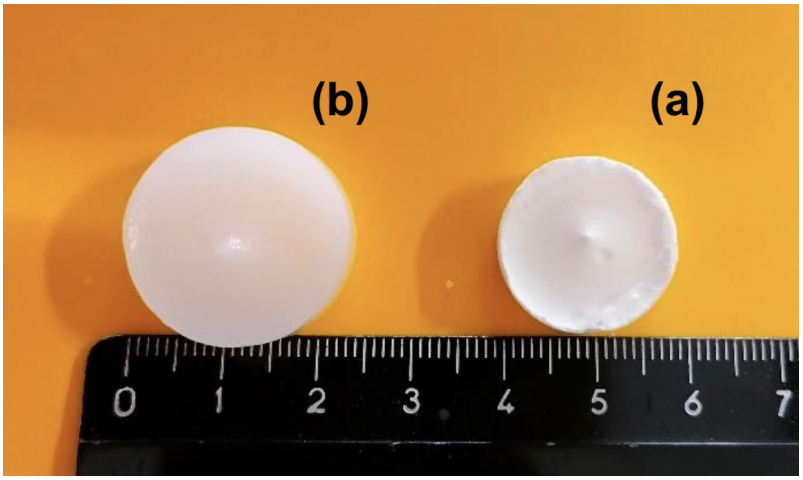


Figure 5.1: Freeze-dried DEX40PEG360MA-GelMA cryogel containing 0.050 $mmoles_{MG}$ with (**a**) $mmoles_{APS}/mmoles_{MG} = 0.45$ before (**a**) and after complete swelling (**b**).

.

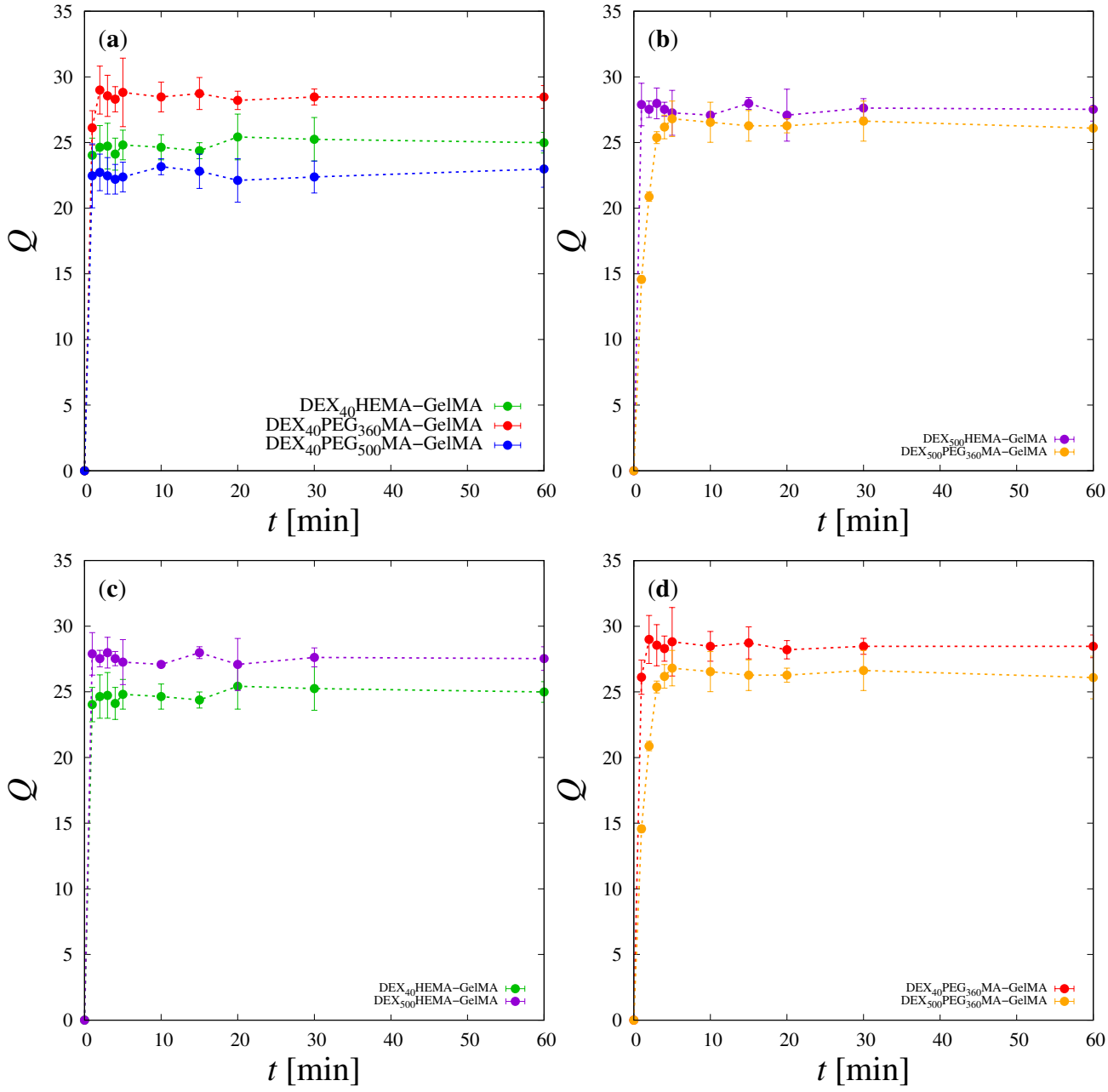


Figure 5.2: Swelling curves of cryogels made of Dextran derivative and GelMA containing 0.050 mmoles_{MG} with $\text{mmoles}_{APS}/\text{mmoles}_{MG} = 0.4$: (**a**) comparison between all the derivatives of DEX_{40} with different spacers (HEMA, PEG_{360}, PEG_{500}); (**b**) comparison between all the derivatives of DEX_{500} with different spacers (HEMA, PEG_{360}); (**c**) comparison between DEX_{40} and DEX_{500} with the same spacer HEMA; (**d**) comparison between DEX_{40} and DEX_{500} with the same spacer PEG_{360}.

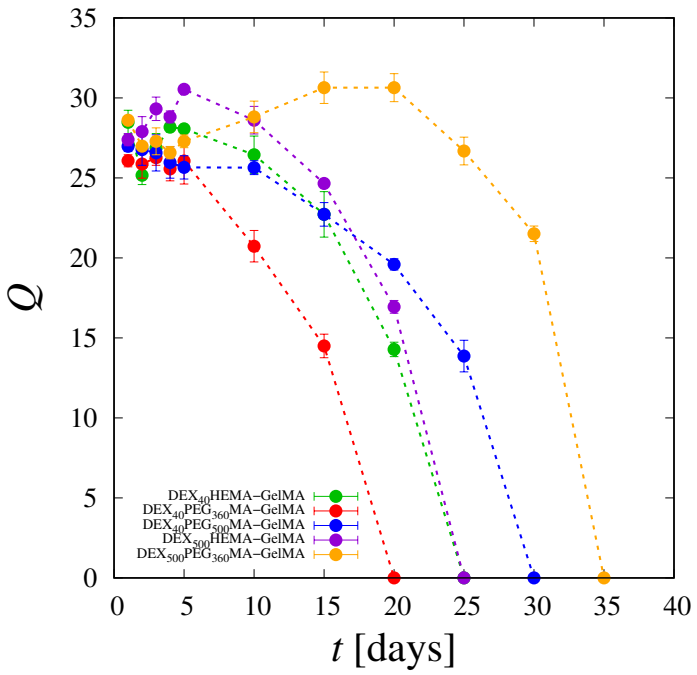


Figure 5.3: Degradation curves of all the analyzed systems prepared with GelMA and methacrylated derivatives of dextran. DEX_{500}-based samples take more time to undergo complete degradation.

5.2 Rheological studies

All the polymer solutions used for the preparation of the cryogels were subjected to rheological analysis, in order to determine their crosslinking kinetics. In fact, it is of crucial importance that the polymer crosslinking process begins after the nucleation of the ice crystals and ends before the complete freezing of the mass, otherwise if the gel cross-linked before the formation of the ice crystals there would be the formation of a system with the characteristics of a hydrogel, in which the sponge-like structure is not present. Considering that the various polymer solutions present the same concentration of methacrylic groups, the volumes of reagents (APS and TEMED) added to trigger the radical crosslinking process were the same for all systems. The polymer solutions of each sample, appropriately added with APS and TEMED, were subjected to rheological analysis to identify the cross-over point of the G' and G'' modules as a function of time and therefore study their kinetics of crosslinking. Time-sweep curves provide information about the point of gel formation, i.e. the moment in which G' becomes greater than G''. From the results obtained and reported in 5.4, a comparable trend can be observed for all the solutions analyzed. In fact, all samples show a crosslinking time within the range of 11.30 and 12.0 min. These results confirm that the crosslinking kinetics, under the conditions adopted, mainly depends on the concentration of the methacrylic groups present and is poorly influenced by the conformation and molecular weight of the methacrylic derivative of the Dex used. From the same curves it is also possible to identify when the reaction comes to an end, or when the plateau is reached: from the analyzes carried out, the formation of all the gels can be considered almost complete after

about 40 minutes. Based on the results obtained from the rheological analyses, all cryogel systems were prepared employing the same amount of the APS and TEMED reagents In fact, in all cases it should be possible to achieve ice crystal nucleation before the start of the crosslinking process.

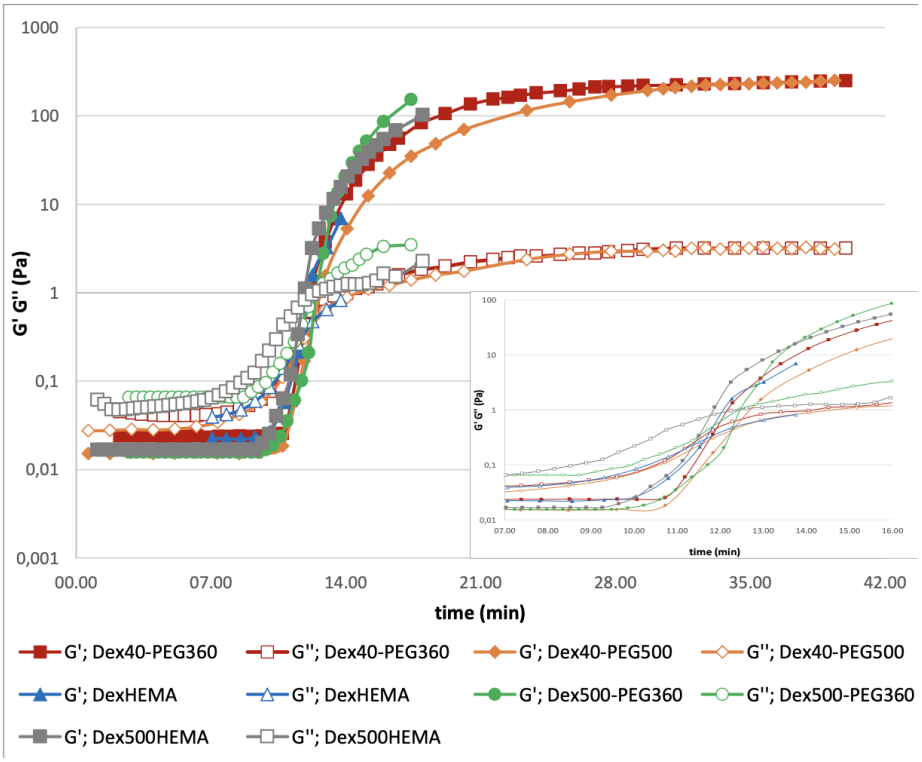


Figure 5.4: Time-sweep type rheological analyses of polymer solutions composed of GelMA and the various methacrylic dextran derivatives..

5.3 FE-SEM analysis and mechanical characterization

The FE-SEM analysis of the microarchitecture of the investigated systems was performed as described in Section 2.6. The micrographs presented in Fig. 5.5 confirm the presence of a highly interconnected macroporous network. Moreover, the pores appear regular and homogeneous, with an average diameter of approximately 50 μm and thin, well-defined walls. These structural features confer a high solvent uptake capacity to the cryogels, indicative of their intrinsic sponge-like morphology. In addition, the extensive pore interconnectivity is anticipated to support cell proliferation by facilitating efficient nutrient and gas diffusion throughout the scaffold.

All the five blended systems have been characterized by uniaxial compression mechanical test. According to the results, all the studied specimens have a similar behavior, as it can be seen in fig 5.7. A deeper look at the linear strain region reveals that systems obtained from higher molecular weight polymers are more resistant, meaning they better resist the strain imposed by the DEX_{500}HEMA/GelMA and $DEX_{40}PEG_{500}$MA/GelMA cryogels, followed by $DEX_{500}PEG_{360}$MA/

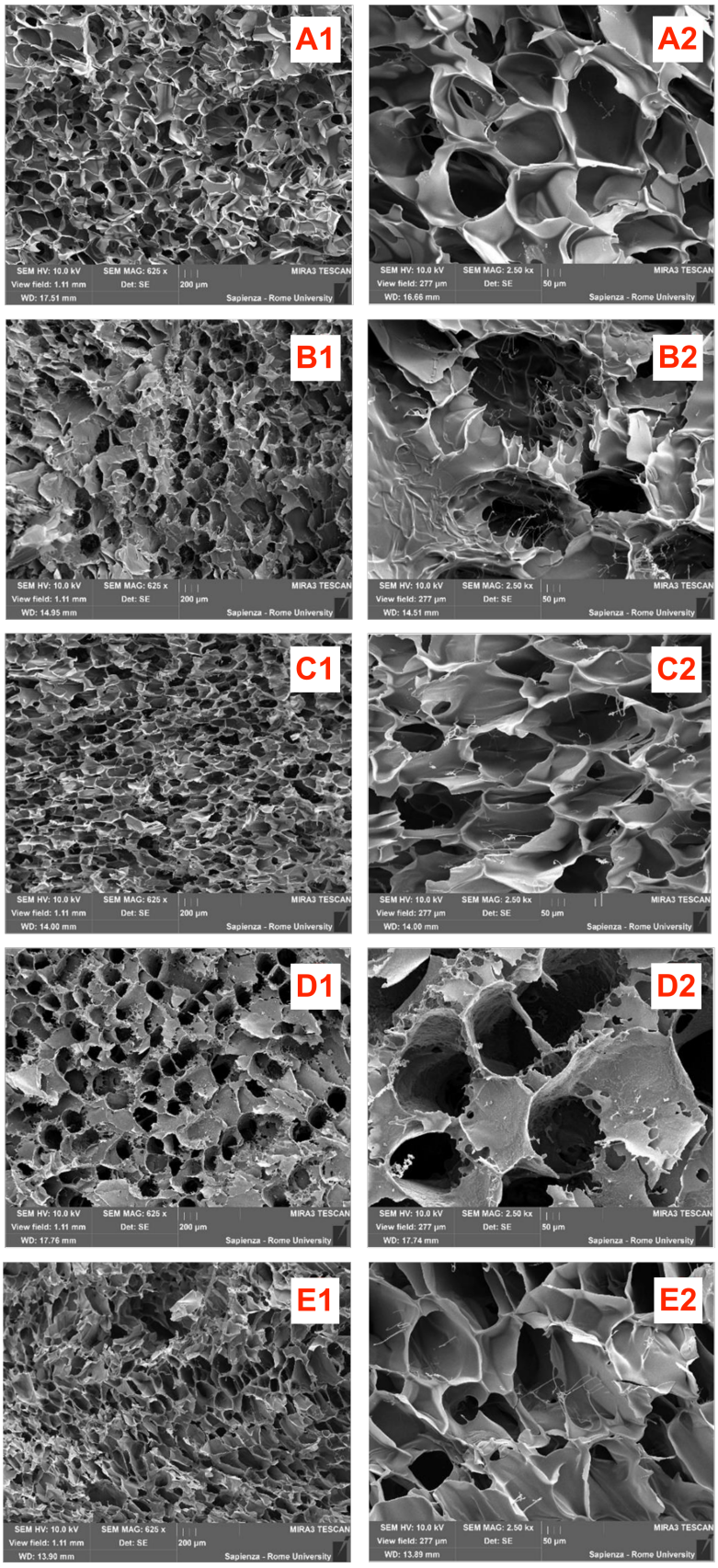


Figure 5.5: SEM images of dry cryogel samples obtained at 625x and 2.50kx magnifications. The analyzed systems were prepared from polymer solutions containing 0.050 mmoles$_{MG}$ and an APS/MG molar ratio = 0.45. (**A1**) and (**A2**) DEX_{40}HEMA-GelMA. (**B1**) and (**B2**) $DEX_{40}PEG_{360}$MA-GelMA. **C1**) and (**C2**) $DEX_{40}PEG_{500}$MA-GelMA. (**D1**) and (**D2**) DEX_{500}HEMA-GelMA. (**E1**) and (**E2**) $DEX_{500}PEG_{360}$MA-GelMA.

GelMA, $DEX_{40}PEG_{360}MA$/GelMA and finally $DEX_{40}HEMA$/GelMA. This behavior can be attributed to lower porosity caused by stronger inter-chain interactions, which reduce network interconnection. The analysis of the plateau regions confirms a coherent trend, while observing the densification region it is clear that systems characterized by smaller pores (i.e. systems with polymers at higher molecular weights) and fewer interconnections first reach the maximum degree of deformability. The overall analysis reveals that the $DEX_{40}HEMA$/GelMA systems are those which, with the same imposed load, are subject to greater deformation and this is linked both to the length of the spacer and to the molecular weight of the starting dextran chain.

Since implanted scaffolds are typically subjected to various mechanical stresses, it was of particular interest to analyze the effects of the compression testis on the internal architecture of the investigated samples. As a consequence, all specimens, after the mechanical tests, were rehydrated in distilled water, lyophilized, and subsequently examined by FE-SEM analysis. As shown in Fig. 5.8(**A1**)–(**E2**), both the rehydration process and the applied compressive stress markedly influenced the pore morphology. The most affected samples were those composed of $DEX_{40}HEMA$, $DEX_{500}HEMA$, and $DEX_{500}PEG_{360}MA$. In particular, the pore shapes were noticeably altered, their dimensions were modified due to increased wall thickness, and several filamentous structures appeared fractured. All the mechanical parameters were extrapolated from the stress-strain curves as explained in Section 3.2.

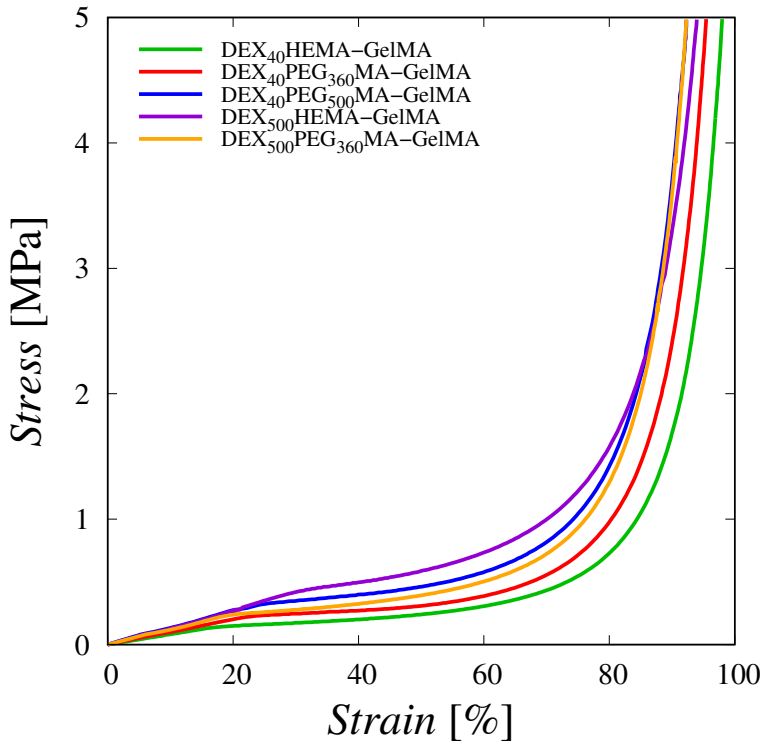


Figure 5.6: Stress-Strain curves obtained from the compression tests for all the types of dry samples prepared from polymer solutions containing 0.050 $mmoles_{MG}$ and $mmoles_{APS}$ /$mmoles_{MG}$ =0.45

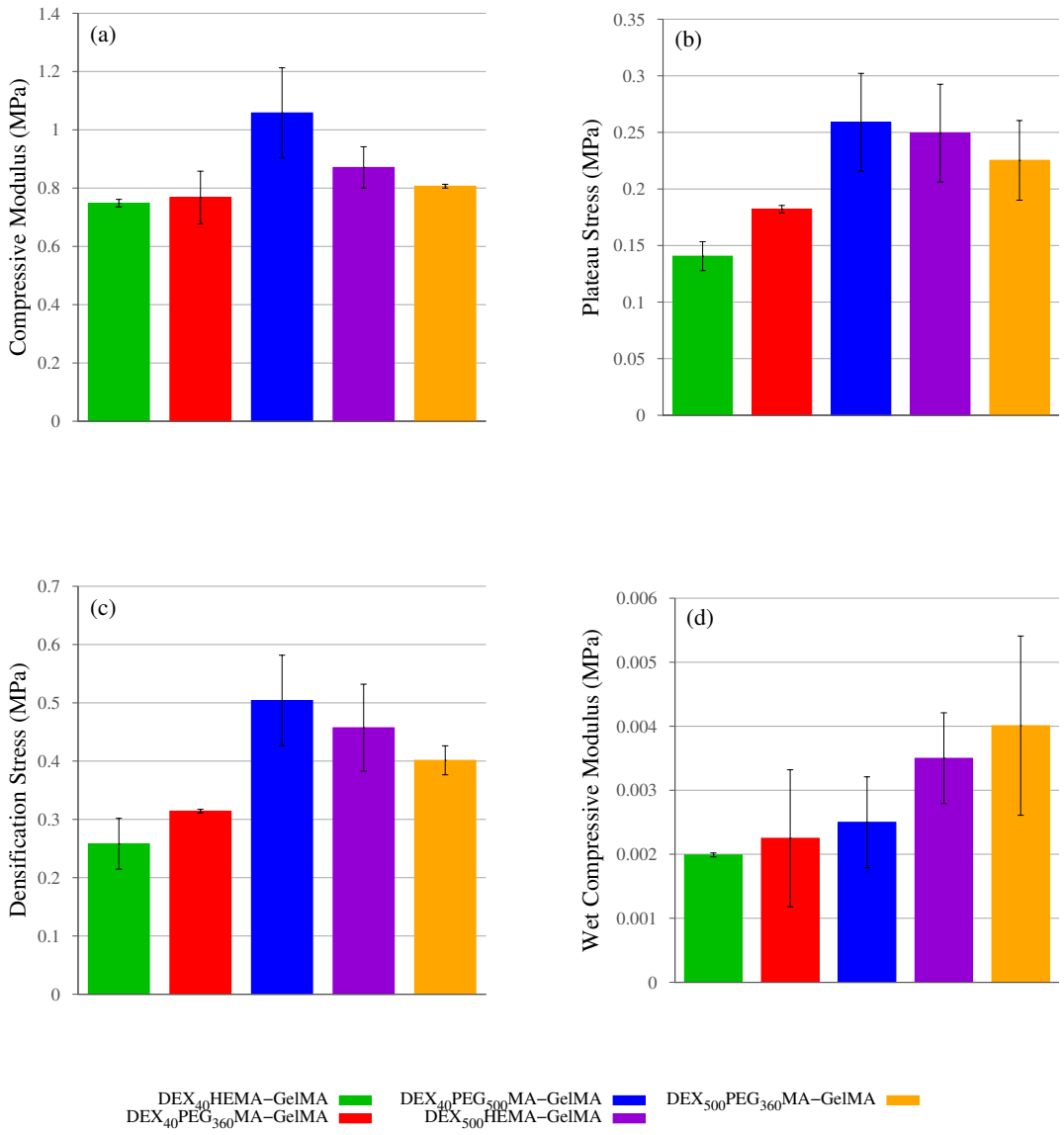


Figure 5.7: Compressive properties of freeze-dried cryogels prepared from dextran-GelMA blended solutions containing 0.050 mmoles$_{MG}$ and with an APS/MG molar ratio = 0.45. (**a**) Compressive modulus, (**b**) plateau stress, (**c**) densification stress of the different freeze-dried hybrid cryogels and (**d**) compressive modulus of hydrated cryogels.

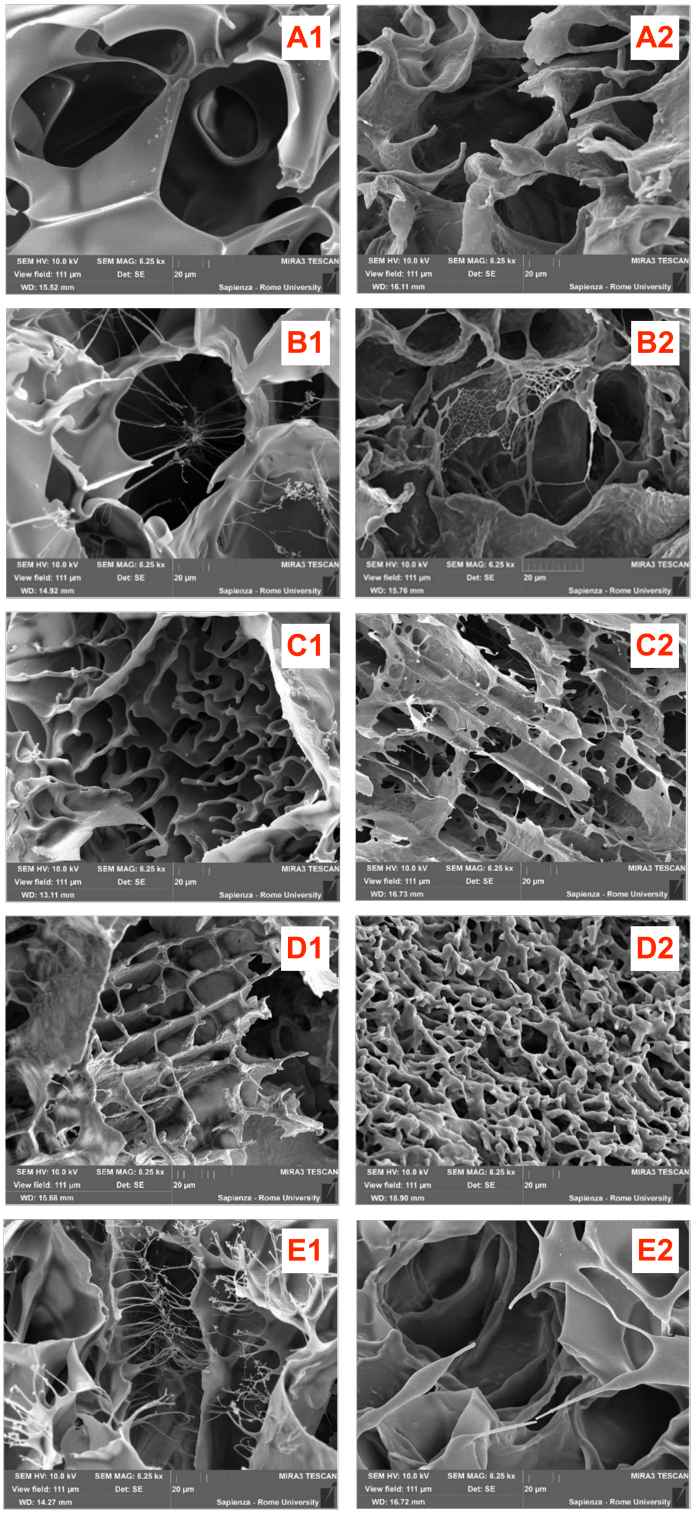
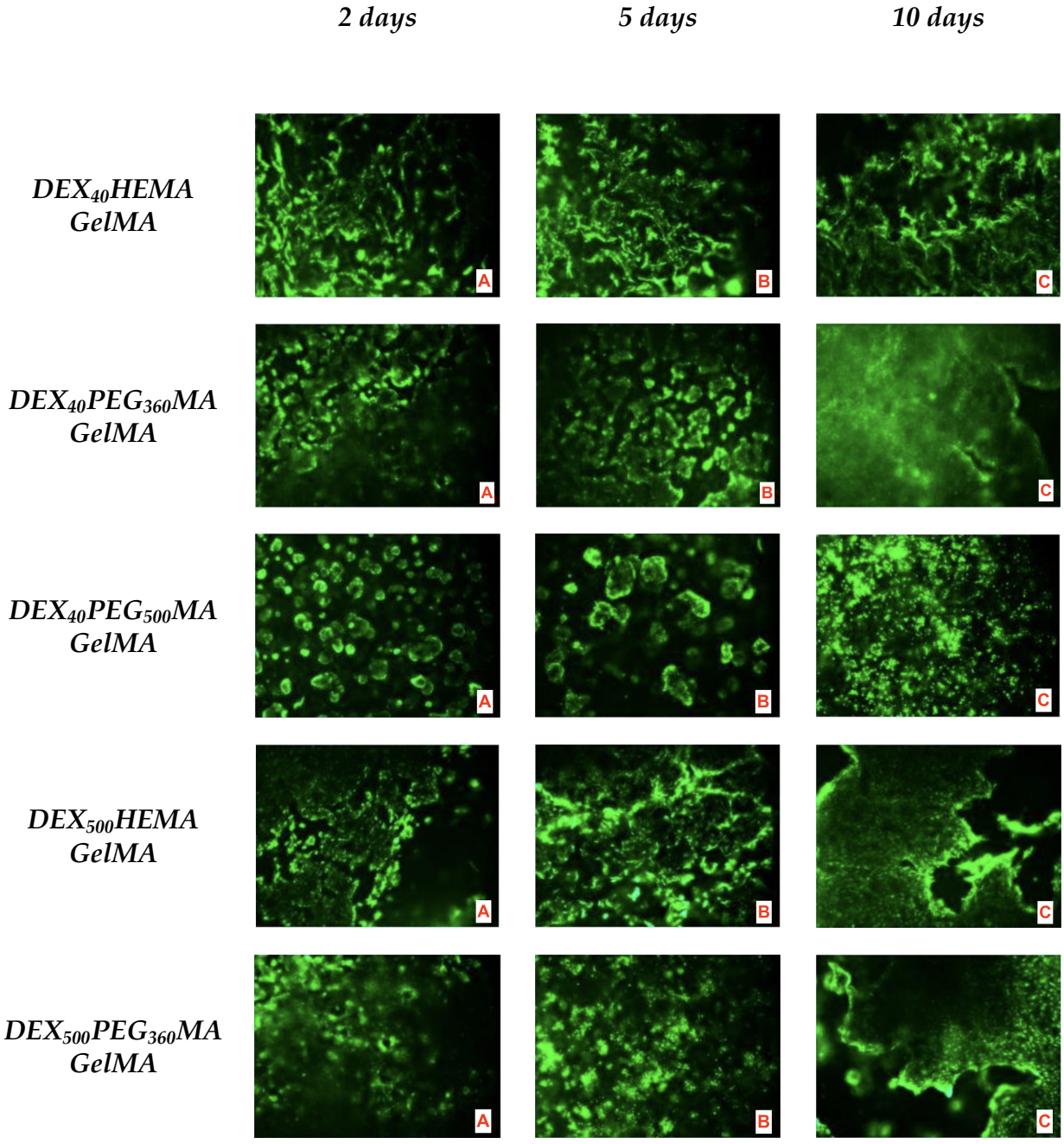


Figure 5.8: SEM images of dry cryogel samples after the compression tests obtained at 2.50kx magnification. The analyzed systems were prepared from polymer solutions containing 0.035 $mmoles_{MG}$ and an APS/MG molar ratio = 0.6. (**A1**) and (**A2**) DEX_{40}HEMA-GelMA. (**B1**) and (**B2**) $DEX_{40}PEG_{360}$MA-GelMA. **C1**) and (**C2**) $DEX_{40}PEG_{500}$MA-GelMA. (**D1**) and (**D2**) DEX_{500}HEMA-GelMA. (**E1**) and (**E2**) $DEX_{500}PEG_{360}$MA-GelMA.

5.4 Adhesion and proliferation studies

With the aim of gaining knowledge about their applicability in the field of tissue engineering, all the synthesized hybrid systems were tested for their ability to support the adhesion and growth of cells in vitro. A suspension containing 2.5×10^6 HaCat cells was seeded on the surface of sterilized specimens. The prepared systems were observed, on pre-established days, under a fluorescence microscope, after staining of the themselves. The structure of the scaffold must have characteristics that allow the engraftment of cells on the walls as well as an interconnection between the pores that allow cells to communicate and proliferate. These properties could actually be affected by the molecular weight of the selected polymer and by cryogelation conditions, as set forth previously. In fact these two parameters strongly affect the microarchitecture of the specimens. The images 5.9 reveal that each sample is suitable for cell growth and proliferation, with variations visible days later regarding the number of cells present within the scaffolds. Moreover, the adhesion to the walls makes it possible to glimpse the characteristic structure of the cryogel itself, highlighting the porosity and interconnection between the pores.

Figure 5.9: Fluorescence microscope images of cryogel systems observed at a distance of (A) 2 days, (B) 5 days and (C) 10 days after seeding the cells.



Chapter 6

Mechanics of Swelling of cryogel-like structures

Swelling phenomena play a critical role in the biomedical and pharmaceutical fields. For instance, they are exploited to control the release of drugs or to create advanced tissue engineering scaffods [110–118]. Thus modeling the swelling dynamics for predicting how material behave is crucial. Cryogels are a class of polymeric materials that exhibit exceptional hydration properties, which are derived from porous morphology. Although there are several models in the literature to model the swelling of porous systems, no one has yet found an approach capable of predicting the behavior of cryorticulated systems.
The scope of this chapter is to introduce the mechanics of swelling of cryogels, which is substantially different from the one of canonic hydrogels. In fact, cryogels systems and hydrogel systems which underwent the freezing and freeze-drying steps, are charaterized by the presence of a porous structure. Due to this, the dynamics of swelling must be treated differently from the traditional Mechano-Diffusion theory. The identification of such a model is useful for the purposes of the training window introduced in Chapter 3. In fact, the study of swelling trends can be used as an additional factor in determining whether or not a sample meets the definition of cryogel. In this perspective, in this preliminary phase, the swelling tests were repeated for systems at a concentration of 0.035 mmoles_{GM} and for various concentrations of crosslinker, using DEX_{40}MA, as it is more chemically stable than the other methacrylic derivatives of dextran. The aim is to use this model in the future to apply it also to the most biocompatible polymer forms, which find greater application in the biomedical field.

6.1 Experimental section: swelling of DEX_{40}MA cryogels

DEX_{40}MA cryogels and hydrogels were prepared according to the procedure described in 2.3.4 starting from polymer solution with a concentration of 6 % w/v (0.035 mmoles_{MG}). Different APS/MG molar ratios were explored: 0.6, 3.0, 3.5, 3.75 for cryogels and 4.5 for hydrogels.

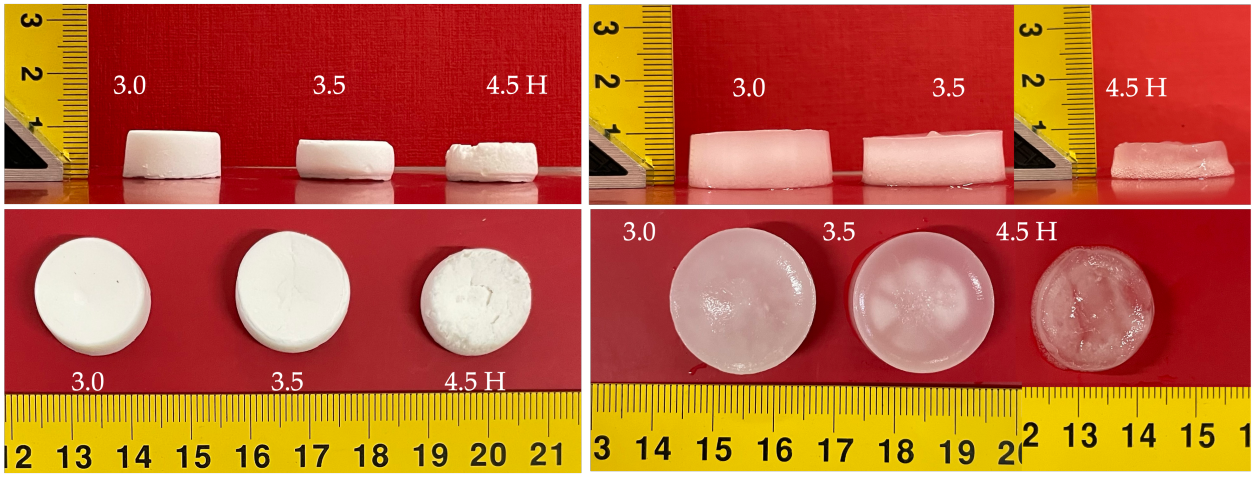


Figure 6.1: Effect of the concentration of reactives on the morphology of dried and swollen samples.

All the systems were immersed in 50 mL of PBS at 37 °C ± 1°C to track the evolution of the solvent uptake and the resulting deformation. Fig. 6.2(**a**) reports the temporal evolution of the swelling capability Q of the samples, while fig. 6.2(**b**) shows the temporal variation of the volumetric ratio J, defined as the ratio between the volume of the sample at a given time and its initial dry volume. From the trends observed in figs. 6.2(**a**)-(**b**), it can be inferred that, except for the hydrogel sample, the higher the swelling capability, the lower the volumetric ratio.

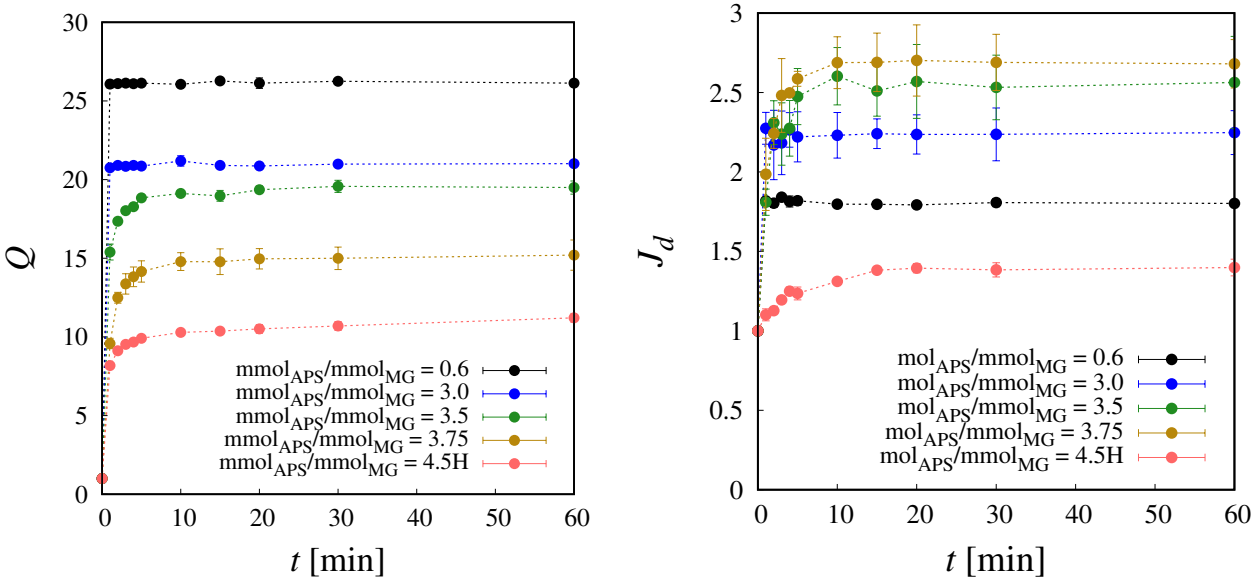


Figure 6.2: Swelling capability (**a**) and volumetric ratio (b) of $DEX_{40}MA$ cryogels prepared from polymer solutions containing 0.035 $mmoles_{MG}$, with $mmoles_{APS}/mmoles_{MG}$ = 0.4, 0.6, 3.0, 3.5, 3.75, and hydrogel samples with $mmoles_{APS}/mmoles_{MG}$ = 4.5.

Mechanical uniaxial tests were performed on freeze-dried systems in order to evaluate their compressive properties. The Young moduli, displayed in fig. 6.3, were extrapolated

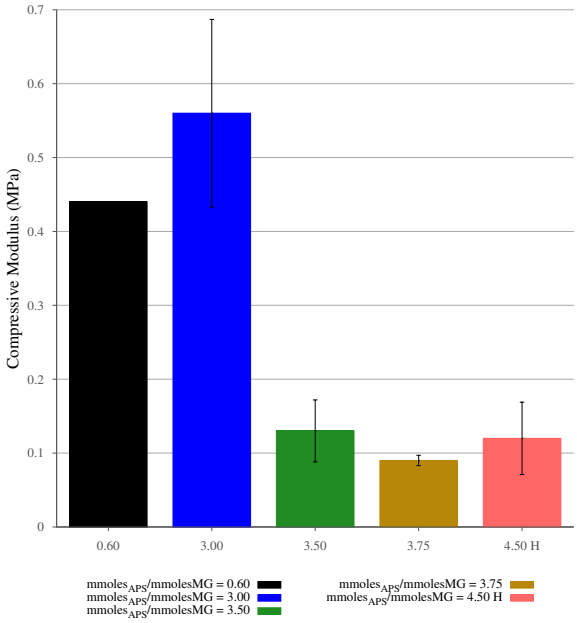


Figure 6.3: Bar plot with the compressive Young modulus of lyophilized samples.

from the compression curve adopting the same strategy described in Section 3.2.

6.2 The Mechano–Diffusion Model

The swelling of polymer gels represents a paradigmatic example of coupled multiphysical behavior, in which solvent transport and mechanical deformation are mutually dependent. The *Mechano–Diffusion* (MD) model provides a thermodynamically consistent framework that integrates these two phenomena within the continuum mechanics of deformable bodies. It extends classical diffusion theory by explicitly incorporating the effects of stress and deformation on solvent mobility, as well as the feedback of solvent absorption on the material strain and stress fields. In this sense, the MD theory bridges the gap between purely mechanical models of elasticity and purely diffusive models of mass transport.

Following Lucantonio *et al.* [85], the MD model treats the polymer gel as a single, homogenized, continuous medium. The microscopic structure—composed of a cross-linked polymer network permeated by a solvent—is represented macroscopically by averaged continuum fields. At each point of the body, the configuration is characterized by a deformation gradient $\mathbf{F}$, a local solvent concentration c, and the associated chemical potential μ. These quantities are not independent: solvent uptake increases the gel volume, while the resulting mechanical stress influences the local solvent activity. Hence, swelling is the macroscopic manifestation of a complex feedback between diffusion and elasticity.

The model is particularly suited to non-porous polymer gels, where the solvent does not flow through an explicit pore structure but rather diffuses through the molecular network.

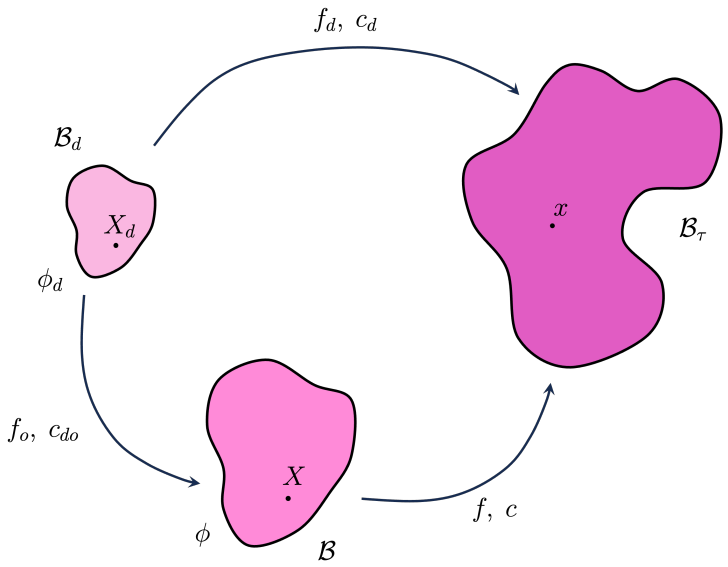


Figure 6.4: Mappings between the discrete reference configuration B_d, the continuous reference configuration B, and the current configuration B_τ. The maps ϕ_d, f_o, f, and f_d relate the corresponding material points X_d, X, and x across the three configurations.

The diffusion process is driven by gradients of chemical potential, not concentration alone, since the latter are altered by mechanical stress. This coupling is the essence of the MD formulation.

Kinematics of Swelling

To describe deformation and swelling, three configurations of the gel are introduced:

1. The dry configuration B_d, corresponding to the undeformed polymer network with no solvent;
2. The reference configuration B, representing the stress-free swollen state at equilibrium with an external solvent bath;
3. The current configuration B_τ, describing the deformed and swollen state of the gel at time τ.

Each configuration occupies a bounded region of the Euclidean space, with boundaries ∂B and ∂B_τ, and unit outward normals $\mathbf{m}$ and $\mathbf{n}$, respectively.

The motion of the body is described by a smooth mapping

$$\mathbf{x} = f(\mathbf{X}, \tau), \qquad \mathbf{X} \in B,\ \mathbf{x} \in B_\tau, \tag{6.1}$$

which assigns to each material point $\mathbf{X}$ of the reference configuration its spatial position $\mathbf{x}$ in the current one. The deformation gradient, determinant, and cofactor are defined as:

$$\mathbf{F} = \nabla f, \qquad J = \det \mathbf{F}, \qquad \mathbf{F}^* = J\,\mathbf{F}^{-T}. \tag{6.2}$$

Here, J represents the local change in volume between configurations. A value $J > 1$ indicates local swelling due to solvent absorption. The transformation laws for differential measures of volume and area read:

$$dv = J\,dV, \qquad da = |\mathbf{F}^{*}\mathbf{m}|\,dA. \tag{6.3}$$

Thus, the geometry of the body continuously evolves in response to solvent uptake, establishing the first level of coupling between diffusion and mechanics.

Balance of Solvent Mass

Let $c_s(\mathbf{x}, \tau)$ denote the solvent concentration per unit current volume. The total number of moles of solvent contained in a part $P_\tau \subset B_\tau$ is:

$$M(\tau) = \int_{P_\tau} c_s(\mathbf{x}, \tau)\,dv. \tag{6.4}$$

Assuming no chemical reactions or internal sources, the only mechanism that alters M is the diffusion of solvent through the boundary:

$$\frac{dM}{d\tau} = \int_{\partial P_\tau} q_s(\mathbf{x}, \tau)\,da, \qquad q_s = -\,\mathbf{h}_s \cdot \mathbf{n}, \tag{6.5}$$

where $\mathbf{h}_s$ is the spatial solvent flux and q_s the inflow per unit area.

To express this relation in the reference configuration, the referential solvent concentration $c = Jc_s$ is introduced. The local form of the solvent mass balance then becomes:

$$\dot{c} = -\,\nabla \cdot \mathbf{h} \quad \text{in } B \times I, \qquad -\,\mathbf{h} \cdot \mathbf{m} = q \quad \text{on } \partial B \times I. \tag{6.6}$$

Equation (6.6) expresses that temporal changes in solvent concentration within any material region are fully determined by the net flux of solvent across its boundary.

This diffusion equation is not Fickian in the classical sense: the flux $\mathbf{h}$ is not simply proportional to concentration gradients, but to gradients of the chemical potential μ, which is itself stress-dependent.

Mechanical Equilibrium

Mechanical equilibrium is described in the reference configuration through the balance of linear momentum:

$$\nabla \cdot \mathbf{S} + \mathbf{b} = \mathbf{0} \quad \text{in } B \times I, \tag{6.7}$$

$$\mathbf{S}\mathbf{m} = \mathbf{t} \quad \text{on } \partial_\tau B \times I, \tag{6.8}$$

where $\mathbf{S}$ denotes the first Piola–Kirchhoff stress tensor, $\mathbf{b}$ the body force, and $\mathbf{t}$ the prescribed traction on the boundary. Since the time scales of diffusion are much larger than those

associated with elastic wave propagation, inertial effects are negligible, and the mechanical problem is quasi-static.

The equivalence between internal and external mechanical power provides the variational form of equilibrium:

$$\int_B \mathbf{S} : \dot{\mathbf{F}}\, dV = \int_B \mathbf{b} \cdot \dot{f}\, dV + \int_{\partial B} \mathbf{t} \cdot \dot{f}\, dA. \tag{6.9}$$

This relation is fundamental to defining the constitutive behavior of the gel in energy terms. It should be emphasized that a general theoretical treatment is presented here. The case that will be examined, necessary to model the experimental tests of cryogel swelling, refers to a stress-free state, namely $\mathbf{b} = \mathbf{0}$ and $\mathbf{t} = \mathbf{0}$.

Thermodynamic Framework

Thermodynamic consistency requires that the constitutive relations satisfy the Clausius–Duhem inequality, which enforces the second law of thermodynamics at the local level. The inequality ensures that the rate of increase of Helmholtz free energy, ψ, does not exceed the external power supplied by mechanical and diffusive processes:

$$\dot{\psi} - \mathbf{S} : \dot{\mathbf{F}} - \mu\dot{c} + \mathbf{h} \cdot \nabla\mu \leq 0. \tag{6.10}$$

Each term in (6.10) has a clear physical interpretation:

- $\mathbf{S} : \dot{\mathbf{F}}$ is the mechanical power density;
- $\mu\dot{c}$ is the chemical power associated with solvent transfer;
- $\mathbf{h} \cdot \nabla\mu \geq 0$ represents the rate of energy dissipation due to diffusion.

Equation (6.10) thus provides the thermodynamic constraint that determines the admissible forms of stress, chemical potential, and flux in the material.

Constitutive Modeling: The Flory–Rehner Framework

To specify the constitutive response of the gel, the Helmholtz free energy is decomposed into an elastic and a mixing contribution, according to the classical *Flory–Rehner theory* [16, 17]:

$$\psi_d(\mathbf{F}_d, c_d) = \frac{1}{2} G\big(\mathrm{tr}(\mathbf{F}_d^T \mathbf{F}_d) - 3\big) + \frac{RT}{\Omega}\, h(c_d), \qquad J_d = 1 + \Omega c_d. \tag{6.11}$$

The first term represents the elastic energy of the cross-linked polymer network, governed by the shear modulus $G = Nk_BT$, where N is the number of polymer chains per unit dry volume. The second term, the mixing energy, accounts for the entropic and enthalpic interactions between polymer and solvent:

$$h(c_d) = \Omega c_d \ln\left(\frac{\Omega c_d}{1 + \Omega c_d}\right) + \chi(T)\frac{\Omega c_d}{1 + \Omega c_d}. \tag{6.12}$$

Here, Ω is the solvent molar volume, $\chi(T)$ is the temperature-dependent Flory–Huggins parameter, and RT is the thermal energy. The interplay between elastic and mixing contributions defines the equilibrium swelling degree of the gel.

Since the stress-free swollen state B is chosen as the reference configuration, the local swelling constraint linking solvent concentration c and volume ratio J reads:

$$J = \frac{1 + \Omega J_0 c}{J_0}, \tag{6.13}$$

where J_0 is the volume ratio between dry and reference states.

Constitutive Equations and Dissipation Mechanism

The constraint (6.13) is enforced by a Lagrange multiplier p, interpreted as a pressure-like internal variable. The relaxed free energy is defined as:

$$\psi_r(\mathbf{F}, c) = \hat{\psi}(\mathbf{F}, c) - p\left(J - \frac{1 + \Omega J_0 c}{J_0}\right). \tag{6.14}$$

From the Clausius–Duhem inequality (6.10), assuming that dissipation occurs only through solvent fluxes, the constitutive equations follow as:

$$\mathbf{S} = \frac{\partial \hat{\psi}}{\partial \mathbf{F}} - p\,\mathbf{F}^{-T}, \qquad \mu = \frac{\partial \hat{\psi}}{\partial c} + p\,\Omega, \qquad \mathbf{h} = -\,\hat{\mathbf{D}}(\mathbf{F}, c)\,\nabla\mu. \tag{6.15}$$

The first equation gives the stress in terms of deformation and pressure; the second relates the chemical potential to solvent content and pressure; the third defines the diffusion flux driven by chemical potential gradients, where $\hat{\mathbf{D}}$ is the mobility tensor. The positive semi-definiteness of $\hat{\mathbf{D}}$ ensures that dissipation $\mathbf{h}\cdot\nabla\mu$ is non-negative, thereby satisfying the second law.

Boundary and Reference Conditions

Boundary conditions for solvent transport can be specified as:

- **Neumann (flux) condition:**

$$q = -\,\mathbf{h}\cdot\mathbf{m} \quad \text{on } \partial_q B, \tag{6.16}$$

  for example $q = 0$ on impermeable boundaries;

- **Dirichlet (chemical potential) condition:**

$$\mu = \mu_{\text{ext}} = \hat{\mu}(c) + p\Omega \quad \text{on } \partial_c B, \tag{6.17}$$

  where $\partial_c B$ is the boundary in contact with a solvent bath of prescribed chemical potential.

In the free-swollen reference state, the gel is stress-free ($\mathbf{b} = \mathbf{0}$ and $\mathbf{t} = \mathbf{0}$) and chemically homogeneous. Assuming $\mathbf{F} = \mathbf{I}$ and no external loads:

$$J_0 = 1 + \Omega c_{d0}, \qquad c_0 = \frac{c_{d0}}{J_0}, \qquad p_0 = \frac{G}{J_0}, \qquad \mu_0 = \hat{\mu}(c_0) + p_0\Omega. \tag{6.18}$$

Under these conditions, $\dot{c} = 0$ and the gel remains in thermodynamic equilibrium with its environment.

6.2.1 Review of the basic model: the case of cryogels

Before modifying the MD theory, it is necessary to make evaluations and comparisons between non-porous (hydrogel) and porous (cryogel) systems. Firstly, there are evidences in some references about the swelling behaviour of macroporous gels which are said *to have a lower equilibrium swelling ratio compared to microporous hydrogels* [119]. The swelling of a hydrogel is a complex process driven by two main forces:

- thermodynamic mixing: water molecules diffuse into the polymer network to mix with the hydrophilic polymer chains, which is a thermodynamically favorable process;
- elastic retractive force: as the network swells, the cross-linked polymer chains stretch, creating an elastic force that resists further swelling.

In microporous hydrogels, the polymer network is dense, and the cross-links are close together. This means the polymer chains between cross-links are shorter. When these chains swell, they reach their maximum stretch relatively quickly, leading to a high degree of swelling before the elastic force overcomes the mixing force. In contrast, macroporous hydrogels have typically a higher degree of crosslinking as polymerization occurs in the volume not occupied by the large pores and contributes to create the rigid, open-pore structure which also characterizes cryogels. This means the polymer chains between the cross-links are shorter and less flexible than in a microporous gel. The elastic force of these shorter, more numerous chains quickly opposes the mixing force, limiting the overall swelling capacity.
The large, interconnected pores are the defining feature of macroporous cryogels. These pores are essentially empty spaces that are filled with water, but they do not contribute to the swelling of the polymer network itself. The polymer walls surrounding these pores are relatively thin and highly cross-linked, which gives the gel its mechanical stability but limits its capacity to swell further. Consequently, the overall swelling ratio is lower because the gel's volume is already dominated by its rigid, pre-formed pores.
Thus, let us start by trying to explain the differences in the swelling capacity $Q = m/m_d$ versus time curves for hydrogels and cryogels, and between them. The main observations from the experimental side which mark the difference between equilibrium swelling for hydrogels and cryogels are listed below.
First, the elasticity of the network. Fixed the volume V_d of a gel sample in the initial dry state and the number N of the cross links which occur in the volume, the crosslinking density

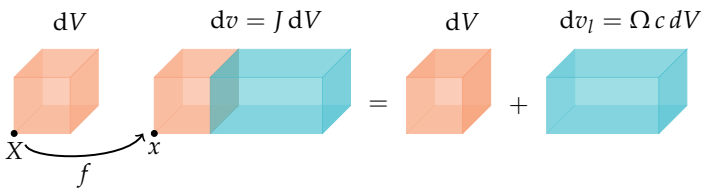


Figure 6.5: The final elementary volume $\mathrm{d}v$ of the gel consists of the initial dry volume $\mathrm{d}V_d$ (coral cube) plus the volume $\mathrm{d}v_l$ of the liquid absorbed (azure cube).

is higher for cryogels as they take place in a volume which is reduced by the pores. Denoted by V_p the volume occupied by pores in the sample, we define the effective volume

$$V_n = V_d - V_p \,, \tag{6.19}$$

which is the volume available for crosslinking and forming the network. Thus, the crosslinking density δ is higher for cryogels as

$$\delta = \frac{N}{V_n} \,. \tag{6.20}$$

Second, the relationship between volumes and the Jacobian of the deformation map. Given a gel sample of dry mass m_d (weighted) and denoted by m_l the mass of the liquid absorbed at the equilibrium state, it holds

$$m_l = m_\infty - m_d \,, \tag{6.21}$$

where m_∞ is the gel mass at the equilibrium state (weighted). In cryogels, the mass m_l includes both liquid in the network and liquid in the pores and, denoted by v_l the corresponding volume, it holds $\varrho_l \, v_l = m_l$. The following relationship is true

$$\frac{V_d + v_l}{V_d} = \frac{V_d + m_l/\varrho_l}{V_d} = 1 + \frac{m_\infty - m_d}{\varrho_l \, V_d} \,. \tag{6.22}$$

Typically, for a hydrogel, we write

$$v = V_d + v_l \,, \tag{6.23}$$

that is, we assume that the final volume v of the gel is given by the dry volume plus the liquid volume (Fig. 6.5). Thus, equation (6.22) can be written as

$$\frac{v}{V_d} = 1 + \frac{m_\infty - m_d}{\varrho_l \, V_d} \quad \text{or} \quad v = V_d + \frac{m_l}{\varrho_l \, V_d} \tag{6.24}$$

Apparently, measuring m_d and m_∞ as well as V_d and v, eq. (6.24) can be tested against the swelling samples: it holds for hydrogels and does not hold for cryogels.

Introduced the deformation map f_d from the dry configuration to the final equilibrium

configuration and its Jacobian J_d, we write

$$J_d = \frac{v}{V_d}\,, \tag{6.25}$$

and using (6.22) and (6.23), we find

$$J_d = \frac{v}{V_d} = 1 + \frac{m_\infty - m_d}{\varrho_l\, V_d}\,, \tag{6.26}$$

that is the equation typically used in a Lab to measure the Jacobian J_d for hydrogel samples.

For cryogels eq. (6.23) is not any longer true as part of the liquid absorbed fill the pores and does not contribute to increase the volume. The first question one may have is: is it possible to describe cryogel mechanics by using the Mechano-Diffusion theory and by introducing some corrections to account for the macroporous presence?
It is possible to answer just looking at the equilibrium state.
Assuming that the porosity at the dry state can be measured, then

$$V_p = \beta\, V_d \quad \text{or, equivalently,} \quad V_n = V_d - V_p = (1-\beta)\, V_d = \alpha\, V_d\,. \tag{6.27}$$

The parameter α is our key parameter: $\alpha = 1$ identifies hydrogels, $\alpha < 0.5$ identifies cryogels and we can say that $0.5 < \alpha < 1$ identifies gels between the two even if it says nothing about the inner structure.
We denoted (v_∞, m_∞) the pair volume-mass at the equilibrium state, and we know that for hydrogels

$$v_\infty = J_d\, V_d \quad \text{and} \quad m_\infty = m_d + m_l = \varrho_p\, V_d + \varrho_l \Omega c_d\, V_d\,. \tag{6.28}$$

Thus the swelling capacity

$$Q = \frac{m_\infty}{m_d} = 1 + \frac{m_l}{m_d} = 1 + \frac{\varrho_l \Omega c_d\, V_d}{\varrho_p\, V_d} = 1 + A\Omega\, c_d = (1-A) + A(1+\Omega\, c_d) = (1-A) + A J_d\,, \tag{6.29}$$

where $A = \varrho_l/\varrho_p$, as usually assumed. Thus, swelling capacity Q is measured by swelling ratio J_d.
For cryogels, we write:

$$v_\infty = J_d\, V_n + v_p \quad \text{and} \quad m_\infty = m_d + m_l = \varrho_p\, \alpha\, V_d + \varrho_l\, v_p + \varrho_l \Omega c_d\, \alpha\, V_d\,. \tag{6.30}$$

Consequently, the swelling capacity

$$Q = \frac{m_\infty}{m_d} = 1 + \frac{m_l}{m_d} = 1 + \frac{\varrho_l \Omega c_d\, \alpha\, V_d}{\varrho_p\, \alpha\, V_d} + \frac{\varrho_l\, v_p}{\varrho_p\, \alpha\, V_d} = 1 + A\Omega\, c_d + A\frac{v_p}{\alpha\, V_d}\,, \tag{6.31}$$

which needs a further specification of the current pore volume v_p to be evaluated.

Volumetric constraint

We assume that *pores deform as network does*, thus

$$v_p = J_d\, V_p = J_d(1-\alpha)\, V_d\,. \tag{6.32}$$

With this, the volumetric constraint takes the form

$$v = v_n + v_p + v_l = V_n + J_d\, V_p + \Omega c_d V_n = \alpha(1+\Omega c_d)V_d + J_d(1-\alpha)\, V_d\,. \tag{6.33}$$

Introduced the Jacobian J_d such that $v = J_d\, V_d$, we find

$$J_d\, V_d = \alpha(1+\Omega c_d)V_d + J_d(1-\alpha)\, V_d \quad \Rightarrow \quad J_d = 1 + \Omega\, c_d\,. \tag{6.34}$$

The volumetric constraint is unchanged. Using (6.32) and (6.34) in (6.31), we get

$$\begin{aligned} Q &= 1 + A\Omega\, c_d + A\frac{(1-\alpha)}{\alpha}\, J_d \\ &= (1-A) + A(1+\Omega\, c_d) + A\frac{1-\alpha}{\alpha}\, J_d \\ &= (1-A) + AJ_d + A\frac{J_d}{\alpha} - AJ_d \\ &= (1-A) + A\frac{J_d}{\alpha} \end{aligned} \tag{6.35}$$

Thus this equation holds true for cryogel systems

$$Q = (1-A) + A\frac{J_d}{\alpha} \tag{6.36}$$

meaning that swelling capacity is different from swelling ratio and smaller is α, that is, more is porous the gel, higher is the difference between Q and J_d.

Polymer fraction

Polymer fraction ϕ is the basic ingredient of the Flory-Huggins mixing energy; it is formulated as a function of ϕ and then rewritten as a function of c or J by using some straightforward relations between the three quantities, which must be reviewed. Polymer fraction ϕ is defined as the ratio between the current network volume and the current volume of polymer filled with water and says how much polymer is in an elementary volume swollen with water (the *lattice* of Flory-Huggins theory is identified with the current volume of polymer filled with water). For hydrogels, we write:

$$\phi = \frac{v_n}{v} = \frac{V_n}{v} = \frac{V_d}{J_d\, V_d} = \frac{1}{J_d} \quad \& \quad J_d = 1 + \Omega\, c_d \quad \Rightarrow \quad \phi = \frac{1}{1+\Omega c_d}\,. \tag{6.37}$$

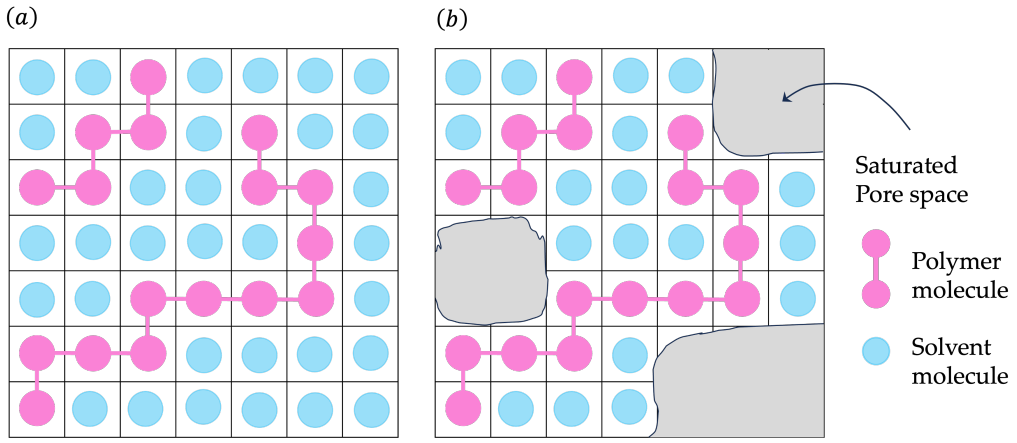


Figure 6.6: Graphical representation of the lattice in which the polymer fraction is evaluated.

For cryogels, we write

$$\phi = \frac{v_n}{v - v_p} = \frac{(1-\beta)\,V_d}{J_d\,V_d - J_d\,\beta\,V_d} = \frac{1}{J_d} \quad \& \quad J_d = 1 + \Omega\, c_d \quad \Rightarrow \quad \phi = \frac{1}{1+\Omega c_d}\,. \tag{6.38}$$

Thus, relations stay inchanged. Fig. 6.6 gives a representation of the lattice in the case of hydrogel(**a**) and cryogels (**b**).

Thermodynamics

Mixing energy is stored in the effective volume V_n only; on the contrary, in the homogenized Mechano-Diffusion model and coherently with the assumption about pore deformability, elastic energy is stored in all the volume. Thus, the free energy density per unit dry volume is

$$\psi = \psi_{\text{els}} + \alpha\psi_{\text{mix}} - p(J_d - \hat{J}(c_d))\,. \tag{6.39}$$

The constitutive equations for stress and chemical potential μ are:

$$\mathbf{S}_d = G\mathbf{F}_d - p_d\,\mathbf{F}_d^\star \quad \text{and} \quad \mu = \alpha\frac{RT}{\Omega}\,h'(c_d) + p_d\Omega\,. \tag{6.40}$$

At equilibrium, for $\mathbf{F} = \lambda\mathbf{I}$, it holds

$$\mathbf{S}_d = \mathbf{0} \quad \text{and} \quad \mu = \mu_{\text{ext}} = 0\,, \tag{6.41}$$

and we get

$$p_d = \frac{G}{\lambda} \quad \text{and} \quad \alpha\frac{RT}{\Omega}\,h'(c_d) = -\frac{G\Omega}{\lambda}\,. \tag{6.42}$$

Thus the final equilibrium equation delivering c at equilibrium is:

$$\frac{RT}{\Omega}\,h'(c_d) = -\frac{1}{\alpha}\,\frac{G}{(1+\Omega c_d)^{1/3}}\,. \tag{6.43}$$

It is observed that during swelling, liquid fill almost instantaneously the pores of the cryogel, which are connected with the external environment by channels. We can suppose that, at time $t = 0^+$, before diffusion in the polymeric network starts, cryogels's pores are already filled with liquid, which there remain due to the extra crosslinking density around the pores. Thus, free swelling processes in hydrogels and cryogels start under different conditions:

- in hydrogels, swelling process starts from the boundary surface and moves towards the core of the gel;
- in cryogels, swelling process starts from the boundary surface, moves towards the core of the gel where there are parts of the bulk which already stay at the chemical equilibrium.

As a prototype example, we can consider a sphere of radius R. We can assume that the diffusivity in the network is the same for hydrogels and cryogels. Thus, the characteristic swelling time is about $\tau_h = R^2/D$. If the same sphere includes a pore of radius R_p, the characteristic time is about $\tau_c = (R - R_p)^2/D < \tau_h$.

Thus, we would expect a faster swelling dynamics in cryogels. It has been observed that cryogels swell faster (read above) and swell more. This extra swelling shown by cryogels apparently is in contrast with our first item as the standard free swelling equation of the Mechano-Diffusion theory delivers a higher swelling volume if the shear modulus is smaller, and it is not our case (see Fig. 6.3).

FEM simulations

In the numerical implementation, the coupled balance equations governing swelling are expressed in their weak form. The weak form is obtained by multiplying each governing equation by a suitable test function and integrating over the domain B. This approach transforms the system of nonlinear partial differential equations into a set of integral equations that can be discretized and solved numerically by the *finite element method* (FEM).

The weak formulation is necessary because:

- it naturally incorporates boundary conditions (both mechanical and chemical);
- it allows the use of approximate trial functions for the unknown fields ($\mathbf{u}_d$, p_d, μ) that do not need to satisfy the strong form locally;
- it ensures numerical stability and consistency when dealing with nonlinear large deformations and diffusion problems.

At steady state, the time derivative of the solvent concentration vanishes ($\dot{c} = 0$), and the swelling process is described by the coupled equilibrium equations for the displacement field $\mathbf{u}_d$, the Lagrange multiplier p_d, and the chemical potential μ. The strong form of the problem can be written as:

$$\begin{cases} \nabla \cdot \left[\hat{\mathbf{S}}_d(\mathbf{F}_d) - p_d \, \mathbf{F}_d^* \right] = \mathbf{0}, & \text{in } B, \\ \nabla \cdot \left[\hat{\boldsymbol{h}}_d(\mathbf{F}_d, p_d, \mu) \right] = 0, & \text{in } B, \\ J_d = \dfrac{1 + \Omega J_0 c_d}{J_0}, & \text{in } B, \end{cases} \tag{6.44}$$

where the solvent flux is expressed in terms of the chemical potential as

$$\hat{\boldsymbol{h}}_d(\mathbf{F}_d, p_d, \mu) = - \, \mathbf{D}_d(\mathbf{F}_d) \, \nabla \mu, \tag{6.45}$$

with $\mathbf{D}_d(\mathbf{F}_d)$ the symmetric, positive-definite mobility tensor.

The equilibrium equations are complemented by the boundary conditions:

$$\begin{cases} (\hat{\mathbf{S}}_d - p_d \, \mathbf{F}_d^*) \, \mathbf{m} = \mathbf{t}, & \text{on } \partial_t B, \\ \mathbf{u}_d = \bar{\mathbf{u}}, & \text{on } \partial_u B, \\ -\hat{\boldsymbol{h}}_d \cdot \mathbf{m} = \bar{q}_d, & \text{on } \partial_q B, \\ \mu = \mu_{\text{ext}}, & \text{on } \partial_\mu B. \end{cases} \tag{6.46}$$

These equations describe the steady-state coupling between mechanical equilibrium and diffusive equilibrium in the gel. The deformation gradient $\mathbf{F}_d = \nabla \mathbf{u}_d + \mathbf{I}$ and the Jacobian $J_d = \det \mathbf{F}_d$ link the mechanical and chemical fields through the swelling constraint. The use of the chemical potential μ as the primary variable ensures thermodynamic consistency and allows one to impose physically meaningful boundary conditions for solvent transport.

The weak form of the steady-state problem, obtained by multiplying the balance equations by the admissible test functions $\tilde{\mathbf{u}}_d$, $\tilde{p}_d$, and $\tilde{\mu}$ and integrating over the domain B, reads as:

$$\begin{cases} \displaystyle\int_B \left(\hat{\mathbf{S}}_d(\mathbf{F}_d) - p_d \, \mathbf{F}_d^* \right) : \nabla \tilde{\mathbf{u}}_d \, dV - \int_{\partial_t B} \mathbf{t} \cdot \tilde{\mathbf{u}}_d \, dA = 0, \\ \displaystyle\int_B \left[J_d - \frac{1 + \Omega J_0 c_d}{J_0} \right] \tilde{p_d} \, dV = 0, \\ \displaystyle\int_B \mathbf{D}_d(\mathbf{F}_d) \, \nabla \mu \cdot \nabla \tilde{\mu} \, dV - \int_{\partial_q B} \bar{q}_d \, \tilde{\mu} \, dA - \int_{\partial_\mu B} (\mu - \mu_{\text{ext}}) \, \tilde{\mu} \, dA = 0. \end{cases} \tag{6.47}$$

In this formulation, the first equation represents the weak form of the mechanical equilibrium, the second enforces the swelling constraint, and the third expresses the diffusive equilibrium in terms of the chemical potential μ. The integrals over $\partial_t B$, $\partial_q B$, and $\partial_\mu B$ account respectively for the prescribed traction, solvent flux, and chemical potential boundary

conditions.

Assuming the swelling constraint is directly enforced in the free energy, the weak form of the steady-state problem involves only the displacement $\mathbf{u}$ and the chemical potential μ:

$$\begin{cases} \displaystyle\int_B \hat{\mathbf{S}}_d(\mathbf{F}_d, \mu) : \nabla \tilde{\mathbf{u}}_d \, dV - \int_{\partial_t B} \mathbf{t} \cdot \tilde{\mathbf{u}}_d \, dA = 0, \\ \displaystyle\int_B \mathbf{D}_d(\mathbf{F}_d) \, \nabla \mu \cdot \nabla \tilde{\mu} \, dV - \int_{\partial_q B} \bar{q_d} \, \tilde{\mu} \, dA - \int_{\partial_\mu B} (\mu - \mu_{\text{ext}}) \, \tilde{\mu} \, dA = 0. \end{cases} \tag{6.48}$$

The first integral equation represents the weak form of mechanical equilibrium, while the second ensures the diffusive equilibrium. The swelling constraint is implicitly satisfied through the constitutive dependence of $\hat{\mathbf{S}_d}$ on μ via the deformation gradient $\mathbf{F}_d$ and the incompressibility relation $J_d = 1 + \Omega c_d$.

Cryogel and hydrogel samples are put in a liquid bath and are not subject to any external force (usually, the weight force is neglected in these circumstances). Thus, since $\boldsymbol{b} = 0$ and $\boldsymbol{t} = 0$, the problem is addressed to as a free-swelling problem.

6.3 Analysis of the experimental data

Following the description explained in 6.2.1, at each instant of time the relationship between the volume of the current swollen configuration and the volume of the dry network is:

$$v(t) = (1 - \beta) \, V_d + \frac{m_l}{\varrho_l} \tag{6.49}$$

From eq. 6.49 it is possible to derive the porosity β of the dry system, and, as a consequence, the fraction α of polymer.

$$\beta = 1 - \frac{1}{V_d} \left(v(t) - \frac{m_l}{\varrho_l} \right) \tag{6.50}$$

$$\alpha = 1 - \beta \tag{6.51}$$

The evaluated values for β and α are listed in table 6.1. Based on the value of the initial porosity of the system, the density ϱ_p of the dry network was calculated for every investigated $\text{mmoles}_{APS}/\text{mmoles}_{MG}$ ratio, along with the ratio A between ϱ_p and the solvent density ϱ_l. The solvent molar volume is assumed equal to $\Omega = 1.8 \times 10^{-5} \, \text{m}^3/\text{mol}$.

The values of the porosity derived from the experimental data show a decreasing trend as the APS/MG molar ratio increases. This behavior is consistent with the fact that, as the concentration of cross-linkers increases, the reticulation kinetics dominate over that of crystal formation during the cryogelation process, leading to a morphology characterized by smaller and less interconnected pores.

According to the eq. 6.36, it can be observed that the the swelling capabilities and the volumetric ratios of the analyzed samples are related through α and A, as shown in picture

mmoles$_{\text{APS}}$/mmoles$_{\text{MG}}$	**0.6**	**3.0**	**3.5**	**3.75**	**4.5 H**
β	0.893 $\pm$0.015	0.835 $\pm$0.030	0.822 $\pm$0.044	0.779 $\pm$0.070	0.852 $\pm$0.029
α	0.107 $\pm$0.015	0.165 $\pm$0.030	0.178 $\pm$0.044	0.221 $\pm$0.070	0.148 $\pm$0.029
ϱ_p	0.624	0.620	0.710	0.798	0.854
A	1.603	1.613	1.408	1.253	1.171

Table 6.1: Values of the initial porosity β and the volumetric fraction of polymer network α derived from eqts. 6.50-6.51, the polymer density ρ_p and the ratio A for different mmoles$_{APS}$/mmoles$_{MG}$ ratios.

6.7, in which the lighter points correspond to the swelling capability derived from eqt. 6.36. Moreover, the hydrogel behaves as a porous structure, since the relationship $Q = J_d$ does not hold.

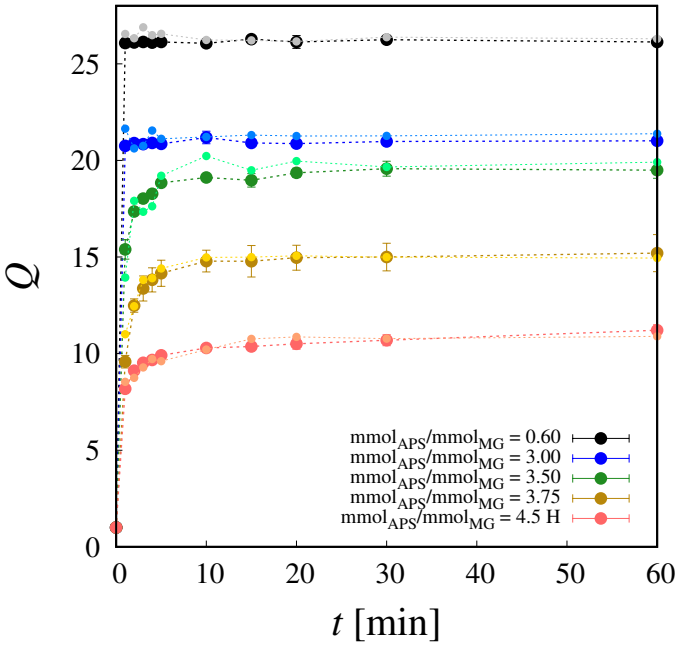


Figure 6.7: Comparison between the experimental swelling capabilities Q and the ones evaluated starting from J_d and α (in a lighter color).

The reviewed version of the MD approach illustrated in 6.2.1 is a part of a preliminary study with the aim of characterizing the swelling behavior of porous polymer systems. Thus, in order to validate it, the modeling work was focused on the steady-state conditions. The steady-state analysis was performed by considering different system configurations leading to equilibrium, starting from highly negative chemical potentials (far from equilibrium) up to zero chemical potential, which corresponds to the equilibrium hydration state.

It is important to emphasize that the analysis was conducted startting from the Young's modulus E obtained from the compression tests instead of the shear modulus G. These will be evaluated at a later time with the appropriate tests.

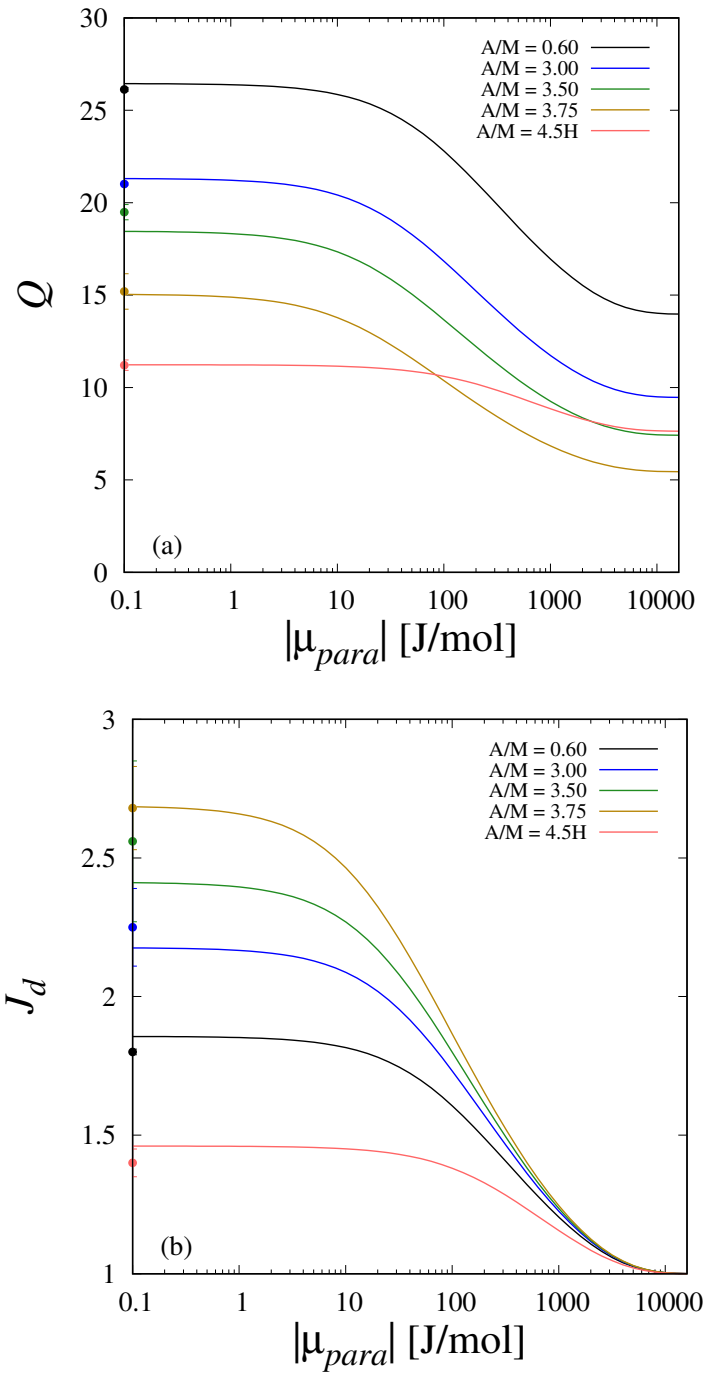


Figure 6.8: Swelling capability (**a**) and volumetric ratio (**b**) in steady state conditions. Solid lines reprent the computational result, while points with errorbar stand for the experimantal value. A/M indicates the APS/MG molar ratio.

To be more specific, under the hypothesis of an isotropic and linear behavior of the samples in the dry state, the values of G were evaluated following the relation

$$G = \frac{E}{2(1+\nu)} \tag{6.52}$$

ν being the Poisson's ratio. According to the literature [120–122], Poisson's ratio for

$\mathbf{mmoles_{APS}/mmoles_{MG}}$	**0.60**	**3.00**	**3.50**	**3.75**	**4.5H**
Q	26.13 ± 0.10	21.01 ± 0.06	19.49 ± 0.41	15.20 ± 0.96	11.21 ± 0.28
J_d	1.80 ± 0.01	2.25 ± 0.14	2.56 ± 0.29	2.68 ± 0.15	1.40 ± 0.05
G (MPa)	0.44	0.56	0.13	0.09	0.12
χ	0.825	0.73	0.69	0.67	1.00
Q_{comp}	26.45	21.32	18.46	15.06	11.23
$J_{d,comp}$	1.86	2.18	2.41	2.69	1.46
λ_r	1.28	1.28	1.28	1.19	1.16
λ_h	1.11	1.34	1.53	1.57	1.14
λ_r/λ_h	1.16	0.95	0.84	0.76	1.02

Table 6.2: Values of the swelling ratio Q, the volumetric ratio J, the shear modulus G, the Flory–Huggins interaction parameter χ, and the radial and axial stretches λ_r, λ_h, and the ratio λ_d/λ_h for different $\mathrm{mmol_{APS}/mmol_{MG}}$ ratios.

this class of materials typically ranges between 0 and 0.5, thus G should vary from $E/3$ to $E/2$. The results indicate that the model response is only weakly dependent on the shear modulus; instead, the polymer volume fraction appears to play a much more significant role in determining the overall mechanical behavior. For this reason, and given the preliminary nature of the study, simulations were performed by assuming $G = E$ as a simplifying numerical approximation, without significantly affecting the qualitative trends of the results.

The analysis was carried out on systems with high reagent concentrations to assess how this condition influences the swelling behavior, including a hydrogel sample. It is possible to observe, from the experimental data, that all systems, even hydrogel, are porous and for all of them the relation 6.36 holds true. It should be highlighted that the hydrogel system, despite having a high porosity and exceeding some cryogel samples, nevertheless shows a lower Q swelling capacity than all other samples and it goes to the equilibrium following a different trend from cryogel sample.

In addition, analysis of the experimental data shows that the value of the Flory–Huggins interaction parameter χ deviates from those typically reported in the literature for dextran-based solutions [123–125]. Specifically, the higher the porosity — that is, the lower the APS/MG molar ratio and the lower the swelling capacity — the larger the deviation of χ from the reference literature values. An exceptional case is represented by the hydrogel system, for which the deviation is even more pronounced.

This behavior can be attributed to the processing history of the hydrogel. The sample was subjected to freezing after formation and then lyophilized prior to hydration. According to several studies [104, 126], freezing of hydrogels can induce cryosuction and dehydration

phenomena within the polymer matrix. These effects occur because the water confined inside nanopores is unable to crystallize, and consequently migrates toward internal freezing fronts, leading to structural damage of the polymer network. As a result, the material exhibits a microstructure enriched in microcracks and overall mechanical weakening.

Although the preliminary model results are promising, further developments are required. In particular, the polymeric systems under investigation exhibit anisotropic characteristics, as suggested by the fact that the ratio between radial and axial stretches deviates from unity (see Table 6.2). Consequently, the scalar field alpha, representing the local porosity or pore volume fraction, cannot capture the anisotropic features of the microstructure. This limitation highlights the need for a more comprehensive modeling framework that incorporates anisotropy in future work.

Chapter 7

Cryogels as promising stationary phases for liquid chromatography: a literature review

The peculiar morphology of cryogels, characterized by large and highly interconnected pores, makes them very suitable for a wide variety of applications. Among them, cryogenic scaffolds can effectively serve as monolithic stationary phases in liquid chromatography (LC) applications. In fact, their microarchitecture enables the separation of molecules ranging from small organics to large biomacromolecus and even entire cells. One of the main aspects in the field of chromatography, is the optimization of the column through an optimal stationary phase. Historically, in this context, a great effort has been done starting from randomly packed beds to continuous monoliths, which can improve significantly the performance of the chromatographic column. To be more specific, the structure of a chromatographic stationary phase plays a crucial role in determining the operational efficiency of the system [127]. For many years, packed beds of spheres have served as a standard in separation technology due to their ease of production and effective performance at a low cost. However, it is now recognized that the theoretical performance of randomly packed beds is inherently restricted by the irregularities within the flow channels and an increasing number of computational studies reveal that ordered stationary phases can reduce band broadening compared to random packing by mitigating eddy dispersion and mass transfer resistance [21–26]. Ordered geometries for the stationary phase effectively address issues of eddy dispersion and mass transfer resistance by standardizing the internal channel structure of a porous medium. Previous investigations have shown that ordered arrangements of pillars [27, 28], spheres and other regular polygons [23, 29–32] can theoretically outperform randomly packed beds. This chapter is organized as follows. Firstly, the transition from randomly packed beds to monoliths is presented. Then, the discussion is addressed more specifically to cryogels as stationary phases and their specific applications. Subsequently, a brief overview of the approaches used to model the performance of this columns is shown. Finally, an analysis of possible future development is pointed out.

7.1 Monolithic structures in LC

In recent years, the use of monolithic structures (MS) as stationary phases for liquid chromatography (LC) has gained increasing attention due to their permeability, mechanical integrity, and ease of fabrication. The first attempts to employ monolithic supports date back to the early 1950s [128], although these early systems did not meet the expected performance standards. It was not until the late 1980s that a significant breakthrough was reported, marking the effective introduction of monolithic materials into chromatographic practice [129]. Monolithic supports consist of single, continuous porous blocks—representing the fourth generation of chromatographic stationary phases—distinguished by their highly interconnected pore network. Two main families can be identified: organic and inorganic monoliths. The former are typically synthesized through the polymerization of organic monomers in the presence of an initiator, crosslinker, and porogenic solvents. Common monomeric systems include methacrylates, acrylamides, and styrene derivatives. In contrast, inorganic monoliths are fabricated from materials such as alumina, hydroxyapatite, or silica, which offer enhanced rigidity and chemical stability. Monolithic structures offer several advantages over conventional packed-bed columns. First, they can be fabricated in a variety of shapes and directly formed within glass or polymeric housings, simplifying column preparation. Second, their low backpressure allows operation at higher flow rates, enabling faster separations and shorter analysis times. Third, the interconnected macropores promote convective mass transfer, minimizing band broadening and significantly reducing diffusion-related limitations. Although some degree of diffusive transport persists within the pore network, the predominance of convective flow accounts for the superior efficiency of monolithic systems. Finally, the wide range of available surface chemistries and functionalization strategies allows monolithic columns to be tailored for diverse chromatographic modes, including affinity, ion-exchange, and hydrophobic interaction chromatography [18]. These characteristics have established monolithic materials as a cornerstone of modern LC stationary phase design and provide the conceptual and structural foundation for the development of cryogel-based stationary phases, which further extend the advantages of monoliths by introducing tunable macroporosity and improved permeability for large biomolecular separations.

7.2 Cryogels as stationary phases and transport principles

Cryopolymerized matrices represent an exemplary form of monolithic structure. In contrast to traditional hydrogels, cryogels exhibit a distinctive sponge-like morphology composed of an open, interconnected network of supermacropores. The typical pore diameters range between 10 and 200 µm [86, 130]. This unique architecture allows unhindered convective flow and results in exceptionally low backpressure, even at high flow rates. As a direct consequence, cryogel columns can handle complex and particulate-containing feedstocks—such as

milk, whey, egg white, or cell broths—without requiring prefiltration or clarification steps. Across the literature, the defining advantage of cryogels lies in their fully interconnected macroporous network, which enables the direct passage of particle-laden fluids while maintaining efficient mass transfer [86, 131–133]. The convective transport regime dominates over diffusion within the continuous pore channels, minimizing resistance and enhancing throughput. This feature distinguishes cryogels from both traditional packed-bed and rigid monolithic columns, whose performance is often constrained by slow intraparticle diffusion or high pressure drops. The synthesis process itself—cryopolymerization—contributes to the superior structural features of these matrices. During polymerization at sub-zero temperatures, the solvent partially freezes, and the ice crystals act as porogens. Upon thawing, these crystals leave behind a continuous network of large flow-through pores. The resulting structure exhibits high porosity, low tortuosity, and strong mechanical integrity, allowing reproducible flow behavior and facile regeneration after multiple chromatographic cycles. From a functional standpoint, the combination of convective transport and structural flexibility makes cryogels an attractive platform for liquid chromatography. Their open-pore configuration supports high volumetric throughput and efficient binding of biomacromolecules, while the robust mechanical framework withstands repeated use and cleaning procedures. These features make cryogel-based stationary phases particularly valuable for integrated bioprocessing and continuous downstream operations, where speed, scalability, and tolerance to complex feed streams are critical performance factors [86, 130–133].

7.3 Applications of cryogels as monolithic columns

Cryogel-based matrices have been successfully applied across a wide range of chromatographic techniques. The most common among these are ion-exchange chromatography (IEX), affinity chromatography (AC), hydrophobic interaction chromatography (HIC), size-exclusion chromatography (SEC), and high-performance liquid chromatography (HPLC). Their unique macroporous architecture and convective mass-transfer properties enable fast separations and efficient processing of complex biological samples, setting them apart from conventional particulate or rigid monolithic supports.

7.3.1 Ion-Exchange Chromatography

Ion-exchange chromatography (IEX) is one of the most versatile and widely adopted techniques in liquid chromatography, relying on charge-based interactions between the analyte and the functional groups of the stationary phase. Its high resolving power, scalability, and cost-effectiveness have made it a fundamental tool in protein and enzyme purification. In this context, poly(acrylamide) (PAAm)-based cryogels have been extensively studied as ion-exchange matrices due to their hydrophilic nature, biocompatibility, chemical stability, and ease of functionalization [86, 130, 134–138]. Early studies demonstrated that acrylamide-based cryogels incorporating ionizable comonomers such as N,N-dimethylaminoethyl methacry-

late (DMAEMA) could efficiently capture charged biomolecules under convective flow conditions [86, 130]. These pioneering works established the fundamental principles of convective ion-exchange chromatography using supermacroporous monolithic matrices, showing that separation occurs throughout the entire column volume and that bound species interact directly with the accessible pore walls. A notable example was the use of PAAm-based anion-exchange cryogels for the binding of Escherichia coli cells, where the negatively charged bacterial surface interacted with positively charged tertiary amino ligands [86, 130]. The results confirmed that the process was volumetric—cells attached to the pore walls without clogging or forming aggregates in dead zones—while maintaining high cell viability. The exceptionally low backpressure enabled operation at flow rates comparable to those of HPLC, highlighting the potential of cryogel columns for handling large biological entities. Subsequent research sought to improve the functional-group density and ion-exchange capacity without compromising the advantageous flow properties. Studies by [134] and [135] introduced grafting strategies to increase ligand density, enhancing binding capacity while preserving pore accessibility. These improvements allowed cryogels to process large biomolecules efficiently and significantly reduced mass-transfer limitations. Parallel efforts extended their use to the separation of viable microbial cells via in-column cryopolymerization, which yielded elastic and reproducible monoliths functionalized with DMAEMA or Cu^{2+}–IDA ligands. Such systems achieved 70–80% recovery for ion exchange and around 80% for immobilized metal affinity chromatography (IMAC), while maintaining both cell integrity and column robustness [135]. The versatility of cryogels has also been demonstrated in food-related separations. Billakanti et al. [139] developed cation-exchange cryogel monoliths for the direct extraction of minor milk proteins, achieving over 90% purity and 85% recovery of lactoferrin and lactoperoxidase, together with excellent regeneration performance under conditions relevant to industrial scale-up. More recently, hybrid and composite cryogel systems have been introduced to enhance selectivity, stability, and reusability. Multiscale architectures combining micro- and macroporosity—such as poly(HEMA)–cellulose composites—enable selective separations of serum proteins (e.g., albumin and IgG) at high purity and throughput [140–142]. Charged-nanoparticle PEGDA and epoxy-bearing cryogels have demonstrated high-efficiency purification and industrial cleanability [143, 144], while natural-polymer systems such as cellulose–alginate and chitosan–nanogel composites offer renewable, mechanically robust matrices with high uptake and reusability [145–147]. Overall, the development of ion-exchange cryogels—from early acrylamide-based supports to modern hybrid and bio-based composites—demonstrates their adaptability and continuous improvement. Their inherent permeability, tunable functionality, and structural resilience make them suitable for large-scale bioprocessing and purification of complex biological systems, offering a viable alternative to conventional packed or rigid monolithic ion-exchange columns.

7.3.2 Affinity Chromatography

Affinity chromatography (AC) exploits specific and reversible interactions between a ligand immobilized on a stationary phase and its complementary target. Typical affinity pairs include antigen–antibody, enzyme–substrate, or receptor–hormone systems. Ligands may be biological (enzymes, lectins, antibodies) or synthetic (aptamers, dyes, metal ion chelates, molecularly imprinted polymers, boronate groups). Affinity cryogels combine the molecular selectivity of these systems with the convective transport typical of macroporous monoliths. Poly(acrylamide) and poly(2-hydroxyethyl methacrylate) matrices have been widely used due to their mechanical stability and ease of in situ functionalization with metal ions, dyes, peptides, or bioaffine ligands. IDA-functionalized cryogels efficiently capture histidine-tagged proteins [148], while cibacron blue– and triazine-modified supports show high selectivity for enzymes such as albumin and dehydrogenases [149, 150]. Ligands can be introduced post-polymerization or by co-polymerization and entrapment. Entrapped antibodies within polyacrylamide cryogels retained activity and enabled selective antigen recovery without loss of function after regeneration [151]. Similar immobilization of enzymes such as peroxidase and lipase preserved more than 80% activity after repeated cycles [152, 153]. Subsequent developments expanded the approach to protein A/G–based immunoaffinity cryogels capable of purifying antibodies directly from serum or hybridoma cultures with high recovery and durability [87, 154, 155]. Peptide-functionalized systems achieved comparable selectivity with enhanced chemical stability [156, 157]. Poly(HEMA)-based supports and hybrid composites further improved mechanical strength and reusability under continuous operation [158]. The resulting cryogels sustain flow rates up to 600–800 cm/h with negligible pressure drop, enabling high productivity and easy regeneration by pH or salt cycling. Dynamic binding capacities (10–30 mg/mL) are comparable to commercial resins but achieved under convective flow [87, 154]. Recent efforts have integrated affinity cryogels into modular and continuous systems, with composite matrices directly molded into disposable LC cartridges [157]. These advances confirm the transition of affinity cryogels from laboratory-scale prototypes to robust, reusable, and scalable stationary phases for bioseparation and purification [158, 159].

Immobilized Metal Affinity Chromatography Immobilized metal affinity chromatography (IMAC) cryogels represent a specific branch of affinity chromatography that combines the selectivity of metal–chelate interactions with the convective transport and mechanical resilience typical of macroporous monoliths. As in other chromatographic applications, the two main polymer systems used are polyacrylamide [86, 131, 133, 160–162] and poly(2-hydroxyethyl methacrylate) (pHEMA) [163, 164], often modified to enhance functionality and stability. Arvidsson et al. [86, 131] were among the first to introduce cryogel-type supports for IMAC. Their polyacrylamide-based matrices, functionalized with iminodiacetic acid (IDA) and loaded with Cu^{2+} ions, enabled efficient separation of proteins and larger bioparticles under convective flow. The open supermacroporous structure (10–100 µm pores)

prevented clogging and extended IMAC applicability beyond protein purification to whole-cell separations and direct processing of crude homogenates. Following these results, Dainiak et al. [132] demonstrated direct capture of His-tagged antibody fragments from undiluted microbial cultures using Cu^{2+}–IDA cryogels, successfully scaling the system from 5 mL analytical columns to 500 mL modular pilot units. Although Cu(II)–IDA complexes are widely used, their strong coordination can occasionally hinder elution or promote protein oxidation. To mitigate this, Wang et al. [160] proposed substituting Cu(II) with Zn(II) or Ni(II), achieving efficient protein recovery with milder elution and lower denaturation risk. Enhancements in ligand design have also been pursued: incorporation of rigid natural polymers such as sporopollenin improved mechanical stability [165], while in situ integration of metal-chelating groups during polymerization—such as in PHEMAGA/Fe^{3+} cryogels—simplified column preparation and eliminated post-synthesis activation steps [163]. More recent advances reflect the shift toward sustainability. Fioravante et al. [161] developed a composite polyacrylamide–alginate (PAAm–Alg) cryogel functionalized with IDA for IgG purification, combining the robustness of PAAm with the biocompatibility and hydrophilicity of alginate. The hybrid matrix efficiently bound bovine IgG through metal–ligand interactions, exemplifying the move toward eco-friendly bioseparation materials. Similarly, Porfirio et al. [162] reported a chlorophyll-activated PAAm cryogel that uses the natural porphyrin ring of chlorophyll to chelate Cu^{2+} ions. This green, low-cost system achieved up to sixfold purification of bromelain from pineapple extracts, demonstrating high performance with minimal environmental impact. Overall, IMAC cryogels have evolved from early Cu(II)–IDA polyacrylamide supports to multifunctional and sustainable composite systems. Their ability to integrate efficient metal–ligand binding with convective flow, scalability, and mechanical stability positions them as a promising class of stationary phases for next-generation bioseparations.

Molecularly Imprinted Chromatography Among affinity-based chromatographic methods, molecularly imprinted polymers (MIPs) offer an artificial route to molecular recognition by generating selective binding sites complementary to a target molecule. The process typically involves two stages: first, the pre-polymerization complexation between a functional monomer and a template molecule; and second, polymerization and crosslinking to fix this configuration within the matrix. After removal of the template, specific cavities remain that mirror the target's size, shape, and chemical functionality, allowing selective rebinding. Baydemir et al. were among the first to demonstrate the suitability of cryogels as matrices for MIP chromatography. They prepared supermacroporous poly(2-hydroxyethyl methacrylate) (pHEMA) cryogels using N-methacryloyl-(L)-tyrosine methyl ester (MAT) as a functional monomer for the selective recognition of bilirubin (BR) from human serum albumin (HSA) [166]. To overcome the intrinsic low surface area of cryogels, they later embedded BR-imprinted particles within the cryogel matrix, enhancing specific surface and adsorption capacity . The resulting BR-MIP cryogels exhibited high selectivity toward bilirubin com-

pared to structurally similar molecules such as cholesterol and testosterone. Following these studies, Andaç et al. [167] designed composite cryogels containing imprinted particles for selective depletion of albumin from HSA, achieving efficient separation even in the presence of competing proteins such as transferrin and myoglobin. The integration of these composites into fast protein liquid chromatography (FPLC) systems confirmed their compatibility with standard chromatographic setups. Similarly, Asliyüce et al. [168] produced membrane-type cryogels embedded with imprinted particles, achieving rapid, uniform flow and high selectivity due to the combined convective transport and molecular recognition features. Further contributions by Bereli et al. [169] demonstrated the successful imprinting of L-histidine for lysozyme purification, highlighting that supermacroporous cryogel monoliths can efficiently host imprinted sites for protein recognition. Their work confirmed that cryopolymerized systems maintain high binding capacity, structural reproducibility, and performance over multiple cycles, establishing molecularly imprinted cryogels as a robust platform for selective biomolecule purification.

Dye-Affinity Chromatography Dye-affinity cryogels exhibit the utility of the macroporous architecture of cryogenic polymer networks in selective, stable, and scalable bioseparations based on artificial ligand–protein interactions. They combine convective mass transfer in cryogel matrices with specificity and reversibility of dye–protein interactions and offer a low-cost and chemically stable platform for substituting biological ligands in affinity chromatography.

Two model studies report complementary design strategies. [170] fabricated composite cryogel discs with dye-functionalized PHEMA beads (20–71 µm) that carried Reactive Red 120 or Reactive Green HE 4BD ligands. Incorporation increased the specific surface area to 192 from 26 m^2/g without affecting convective flow, with up to 240 mg IgG/g adsorption capacity and recoveries of more than 90% and stable reuse for ten cycles. Discular modular arrangement facilitated subclass-specific IgG purification and demonstrated scalability for continuous or semicontinuous operation.

On the other hand, [171] prepared a monolithic poly(acrylamide–allyl glycidyl ether) [poly(AAm–AGE)] cryogel with covalent immobilization of Cibacron Blue F3GA dye via epoxy groups. The matrix was of uniform macroporosity (10–100 µm), free from leaching of the dye, and stable to alkaline cleaning. It yielded adsorption capacities of 74 mg HSA/g in plasma and maintained activity over ten regeneration cycles. Chemisorptive kinetics and strong selectivity towards human serum albumin of the system further testified its suitability for plasma protein purification.

These systems work together in the form of contrasting but complementary engineering philosophies: the monolithic structure maximizes operability and toughness for industrial strength, whereas the composite architecture prioritizes modularity and surface area for high-capacity separations. They both utilize convective flow, high reusability, and low backpressure, demonstrating that dye-affinity cryogels integrate synthetic chemistry with advanced polymer architectures to deliver selective, reusable, and industrially viable platforms

for next-generation protein purification.

Lectin Affinity Chromatography Lectin affinity cryogels correspond to an improved branch of affinity chromatography. Affinity chromatography utilizes carbohydrate-protein interactions for purification of lectins as well as glycoproteins. The hybrid of lectin chemistry and cryogels corresponds to an integration of molecular recognition properties with high mechanical strength. This helps in creating high selectivity at a low-pressure flow.

The column's performances, as it has been emphasized in several research works [172–174], largely rely on immobilization technique, accessibility of the ligand and matrix design. These three factors altogether define the selectivity, kinetic capabiliti es, as well as the reusability of

All three works noted the supermacroporous structure of the matrix with pore sizes of up to 100 µm as well as high chemical stability and consequently long-term reusability.

In both researches [172] and [173], the concanavalin A (Con A) was imobilized via covalent binding on the cryogel. The objective of both researches being to bind human immunoglobulin-G (IgG) and glycoproteins. The proposed structure by Hajizadeh *et al.*, consisting of pAAm beads dispersed within poly(vinyl alcohol), contributed towards an increase in the availability of the ligand without altering the dimension of the macroporosity. Gonçalves *et al.* proposed a new approach for overcoming the steric hindrance problem by immobilizing the carbohydrylates on the matrix surface via the glutaraldehyde technique. This had the advantage of forming spacer arms.

Immunoaffinity Chromatography Immunoaffinity cryogels incorporate the molecular precision of antibody–antigen recognition with the convective mass-transfer and robustness of cryogenic polymer networks, representing one of the most versatile and translationally relevant branches of cryogel-based separations. The activity of the ligands and overall durability of immunoaffinity cryogels remain unaltered during repeated cycles [175–178]. Second, an important step comes from the oriented immobilization of antibodies. As demonstrated by Bereli et al. in anti-LDL PHEMA cryogels [175], orientation via the Fc part using protein A promoted correct orientation of the antibodies with higher binding capacity of LDL (129 mg of LDL per g of matrix as opposed to 111 mg of LDL per g of matrix for randomly attached antibodies) and reduced nonspecific interactions. The 67 % macroscale porosity allowed for convective transport of the solution, enabling quick binding equilibrium attainment within 30 min and 80 % activity retention after six cycles of reuse. Then came improvements for large biomolecule purification. In these applications, cryogels excel by overcoming the diffusion limitations found in bead resins. Highly porous PHEMA cryogels with 95% porosity and 20 µm pore size and conjugated with anti-IgM antibodies were developed by Bakhshpour et al. [176]. These supports had a capacity of 11.1 mg/g and were long-lasting for ten cycles. Furthermore, they were resistant to NaOH cleaning without compromising functionality. The flexibility of cryogel preparation made it easy to miniaturize and apply it as an analyzer. Cetin et al. designed microcryogels of 400–500 µm size for transferrin

purification. These microcryogels showed both stability and 9.82 mg/g capacity with 80% binding capacity retention in ten cycles [177]. Zinggeler et al. designed another approach by combining photopatterned cryogel portions within transparent capillaries for IL-6 sensing [178]. The latter technique utilizes the photochemical technique for multiplex analysis without a pump. Sensitivity of 30 pg/mL concentration and optical detection were In aggregate, these investigations highlight the rapid kinetic rates of immunoaffinity cryogels with high selectivity and an unparalleled level of reusability within mild aqueous processing conditions. The design-enabled advantages of convective transport and robust antibody immobilization via protein-A or epoxy and cyanamide chemistry afford reproducible outcomes of 95% recoverability. From large-scale processing monoliths designed for industrious needs to laboratory microarrays for single-patient use, these immunoaffinity cryogels integrate well within the needs of existing biological manufacturing for therapy and within forthcoming analysis needs. The convergent power of immunoaffinity and structural/functional cryogel advantages offers mature solutions within existing chromatographic separations, therapeutic processing, and analysis needs.

7.3.3 Hydrophobic Interaction Chromatography

Hydrophobic chromatography (HIC) turns the hydrophobic interactions between hydrophobic ligands and non polar regions on the surface of the proteins to account. Besides, the properties of the stationary phase (matrix-ligand interactions), the mobile phase (pH, salt type and concentration) and temperature influence the success of the separation [179],[180]. Typically, the employed ligands are hydrophobic molecules with non-polar amino acid side chains on their surface. For example, alanine, methionine, tryptophan, and phenylalanine are used to isolate proteins like lysozime [180–184], albumin [185], and lipase [186]. Early designs included pHEMA cryogels functionalized with N-methacryloyl-L-tryptophan that showed moderate capacity of around 50 mg/g [181], but hybrid and composite ones improved that considerably. Incorporation of hydrophobic beads into the matrix of pHEMA improved the surface area and convective transport to as high as 332.7 mg/g [187], [182], though purification yields remained suboptimal for industrial application. The others attempted either chemical or structural advancements over and above simple ligand loading. Abdullah et al. [184] maximized lysozyme capacity based on imidazole functions that combined both hydrophobic and pseudoaffinity principles with outstanding reusability (>10 cycles), as Avcibacsi et al. [185] synthesized monolithic cryogels based on imidazole functions by using hydrophobic co-pollymers that were successful in retaining both elasticity and high flux at the same time. Oliveira et al. [188] synthesized a new system based on a single-step approach based on the use of MAPA ligands that released 199 mg/g capacity of binding of lipase with better ease as Erzengin et al. [183] released an outstandingly stable system (>30 cycles) that used 1-naphthylamine function on supports. More recently, the focus has been on moving beyond protein purification via cryogels. Molecularly imprinted cryogels were designed to selectively bind cholesterol from milk [189], and functionalized cryogels of amino

acids successfully separated proteins from plants on an ÄKTA platform [180]. Capillary and nanocomposite versions of cryogels successfully applied the underlying principles of cryogels to analytical separations [190], retaining both permeability and stability.

7.4 Modeling approaches for Cryogel Stationary Phases

In the last years a variety of attempts have been made in order to develop a model to describe properly chromatographic phenomenon in cryogels serving as stationary phases. The first works, suggested approaches which were based on the finite difference method.
In [191] monolithic cryogenic columns were characterized through a capillary-based model. According to this, some physical properties of the solid matrix - i.e. the pore size distribution, the tortuosity and the solid matrix thickness etc. - were taken into account.
A lately work, [192], proposed a simplified version in which the thickness of the capillaries is proportional to their inner-diameter, the pore size distribution is continuous and linearly proportional to that of the dry skeleton (through a swelling coefficient to consider morphological changes due to swelling) and all capillaries have the same tortuosity. Thus, Liu *et al.* found out an effective model which relies on fewer fitting parameters, simplifying the calculations. However, both the approaches were formulated in the case of non-adsorbing media.
Capillary-based description of cryoreticulated monoliths was extend in [193], where the influence of the channel architecture on transport phenomena was meticulously investigated in terms of tortuosity. The 3D computational model allowed an effective description of fluid dynamics and mass transfer in the case of adsorbing solid skeleton.
Even though the previously examined models displayed a good predictive capacity, they do not really describe the heterogeneous microscopic structure of a cryogel matrix. In fact, the main feature of this kind of monoliths is the high degree of interconnectivity among the pores, which affect the transport phenomena. Conversely, works [191–193] model the skeleton as a group of parallel non-interacting tortuous open tubes. To overcome the limitations arising from these geometric frameworks, recently works focused on three-dimensional reconstructions of internal morphology. To this end, cross-sectional imaging data have been exploited [194–196]. Despite the fact that in this way it is possible to conduct a precise analysis of the transport phenomena, which accounts for the real morphology of the medium, however, the computation costs are extremely high and very robust platforms are required.

Collectively, these works illustrate how progressive geometrical and CFD-based modeling has improved our understanding of cryogel transport phenomena. However, they also highlight the persisting challenge of reproducing experimentally the same morphology predicted numerically - owing to the stochastic nature of cryo-polimerization. Thus, the possibility to fabricate designed porous matrices with controllable and reproducible architectures through additive manufacturing (AM) represents a major conceptual and technological breaktrough.

7.5 Towards new highly ordered stationary phases: 3D-Printed Structures

Structural models based on Triply Periodic Minimal Surfaces (TPMS) - and particularly the gyroid - have been proposed as representative architectures capable of emulating the internal structure of cryogels. The gyroid provides a continuous, three-dimensional, and fully interconnected channel network with zero mean curvature, closely resembling the labyrinthine morphology of supermacroporous gels. Computational Fluid Dynamics studies based on gyroidal geometries have shown excellent agreement with experimental flows profiles, pressure drops, and breakthrough behaviors, confirming their effectiveness as models of convective-diffusive transport within cryogel matrices. In addition, the deterministic nature of the gyroid geometry enables reproducible design and parameter control, qualities that are inherently lacking in cryo-polymerized materials. Thus conceptual transition - from a randomly structured cryogels to mathematically defined TPMS architectures - coincides with the rapid development of additive manufacturing (AM) technologies. High-resolution 3D printing now allows for the physical realization of periodic, continuous, and customizable porous structures that can function as chromatographic stationary phases. By exploiting computationally designed geometries, it becomes possible to decouple structural design from synthesis randomness, ensuring reproducibility, scalability, and targeted optimization of mass transfer and hydrodynamics. While cryoreticulated gels typically exhibit porosities above 85 % and permeabilities in the range of 10^{-11}-10^{-9} m^2, gyroid-based TPMS lattices can be tunes across a comparable range, with the additional advantage of structural predictability and controlled tortuosity. Unlike cryogel synthesis, where pore formation is indirectly governed by the freezing kinetics, AM-based design allows direct control over pore shape, size, and interconnectivity. This designability enables parametric optimization of chromatographic efficiency through computational models prior to fabrication.

The structure of a chromatographic stationary phase plays a crucial role in determining the operational efficiency of the system [127]. For many years, packed beds of spheres have served as a standard in separation technology due to their ease of production and effective performance at a low cost. However, it is now recognized that the theoretical performance of randomly packed beds is inherently restricted by the irregularities within the flow channels and an increasing number of computational studies reveal that ordered stationary phases can reduce band broadening compared to random packing by mitigating eddy dispersion and mass transfer resistance [21–26]. Ordered geometries for the stationary phase effectively address issues of eddy dispersion and mass transfer resistance by standardizing the internal channel structure of a porous medium. Previous investigations have shown that ordered arrangements of pillars [27, 28], spheres and other regular polygons [23, 29–32] can theoretically outperform randomly packed beds.

The emergence of additive manufacturing, especially two-photon polymerization printers [197] with minimum feature size order of few hundreds of nanometers [198], represents a

significant transformation in our capacity to physically fabricate complex ordered structures that were once nearly impossible to produce. However, ordered packed beds are not optimal for 3D printing, because particles need to be fused and particle-particle contact points, necessary to form a monolithic matrix, are critical points for the structure [32]. 3D printing of porous beds offers the opportunity to design and create ordered monolithic structures optimized to maximize separation performance because it is possible to supersede particle-based structures and produce novel sets of combined solid- and mobile-phase geometries [199].

Literature studies aimed at characterizing new 3D printable stationary phases basically fall into three categories: (1) purely hydrodynamic studies in which the stationary phase is impermeable [30–32, 200, 201]; (2) studies in which the stationary phase is superficially activated/porous and thus only superficially adsorbent [28, 29, 202]; (3) studies in which the stationary phase is microporous and retentive [203–206] .

7.6 Surface Properties and Fluid-Solid Interactions

A critical arduous aspect of cryogel-based columns concerns the stochastic nature of the formation process. In fact, even if it is possible to tune the physical characteristics by manipulating the parameters affecting the balance between the freezing and the reticulation kinetics, however it is practically impossible to control precisely the surface properties and, hence, their impact on fluid-solid interactions. As a matter of fact, the conformation and the chemical properties of the internal pore surfaces determine the local distribution of ligands, the adsorption/desorption kinetics, and, as an effect, the selectivity and reproducibility of the entire separation process.

In point of fact, as already mentioned, the morphological feature of conventionally produced gels are determined by spontaneous, diffusion-limited, and thermodynamically driver phase separation events. Since the freezing and polymerization fronts generate randomly, the resulting ice-crystals or polymer-rich domains follow unpredictable growth kinetics. As a consequence, traditional cryogels present broad and multimodal pore size distributions, anisotropic channels, and chemically heterogeneous functional surfaces. In the latter, the densities of the functional densities can vary across the matrix [207]. The main effect of this intristinsic stochasticity can be found in non-uniform flow paths and heterogeneous mass transfer coefficients, which lead to band broadening, poor resolution, and, hence, limited scalability in separation applications.

Recently, Mancino *et al.* proposed a predictive model of the cryogelation process, capable of simulating the temperature field, the freezing kinetics, and ice crystals growth during agarose cryogel formation [208]. This mathematical approach gives a prediction of the local freezing rate and estimates the resulting pore dimensions relying on empirical correlations between the cooling velocity and the size of ice crystals. The results, validated by optical microscopy, demonstrated that the pore diameters decreases with decreasing process tem-

perature (from about 97 μm at -12°C to approximately 69 μm at -12 °C) and that spatial gradient in pore size exists within the matrix. This work represents a significant advancement toward a quantitative understanding of cryogel formation and introduces an initial level of predictability into a process previously considered entirely stochastic. Nevertheless, the resulting structures remain inherently constrained by the thermodynamics of phase separation, and the model cannot impose deterministic control over pore geometry or surface chemistry. On the contrary, through additive manufacturing structures can be created in a direct and deterministic manner, overcoming the limitations of traditional cryotemplating.

In fact, thanks to modern techniques, such as digital light projection (DLP) or vat photopolymerization especially when coupled with polymerization-induced phase separation (PIPS), it is feasible to fabricate monolithic structures with controlled pore geometry, uniform surface chemistry, and high reproducibility [209].

More precisely, the mechanism of this technologies, which can induce local polymerization and phase separation through light exposure, allows to control reaction kinetics, heat dissipation, and porogen distribution at the voxel scale. As demonstrated by Dimartino *et al.*, the resulting porous monoliths have a narrow pore size distribution (0.5–2 µm), homogeneous curing, and predictable permeability, eliminating the structural gradients typically observed in bulk polymerization.

The ability to digitally encode structural parameters transforms the Additive manufacturing (AM), by contrast, provides a direct and deterministic route to structure design, effectively overcoming the limitations of traditional cryogelation. e fabrication process from stochastic self-assembly into deterministic material design.

Moreover, the integration of Computer-Aided Design and Manufacturing (CAD/CAM) tools enables the generation of structures with precisely defined porosity, tortuosity, and surface-to-volume ratio—parameters directly influencing mass transfer and hydrodynamic behavior [210]. Conti and Dimartino emphasized that AM can decouple geometric design from chemical composition, allowing post-printing modification (e.g., via plasma or UV photoactivation) to selectively tailor the solid–liquid interfacial chemistry. Such control improves reproducibility and enables fine tuning of ligand density, adsorption selectivity, and surface energetics—features difficult or impossible to achieve in cryogels formed by uncontrolled freezing.

Further advances in graded-porosity printing extend the flexibility of AM even more. Balakrishnan et al. demonstrated that grayscale DLP printing can spatially modulate local curing energy, enabling the fabrication of functionally graded porous materials in a single step [211]. This method allows the seamless integration of dense and porous regions within the same structure, providing architectures that combine mechanical robustness with efficient convective flow and enhanced mass transfer. Such deterministic, design-driven control of porosity and surface topology sharply contrasts with the non-equilibrium, diffusion-limited nature of conventional cryogelation.

In summary, while predictive modeling of cryogelation (as in [208]) offers valuable insights and partial predictability, additive manufacturing introduces true structural determinism.

By enabling digital control over both morphology and surface functionality, AM bridges the gap between modeling and realization, allowing the fabrication of reproducible, chemically uniform, and geometrically optimized porous materials. This transition from stochastic formation to fully designed microarchitecture marks a fundamental evolution in the engineering of soft porous media for separation, adsorption, and biointeraction applications [207–211].

Part II

Computational modeling of liquid chromatography: Dispersion properties of triply periodic minimal surface stationary phases

Chapter 8

Dispersion properties of triply periodic minimal surface stationary phases for Liquid Chromatography

The transition from stochastic cryogel formation to digitally designed porous architectures represents a fundamental conceptual shift; yet, translating this structural determinism into functional chromatographic devices still entails substantial technological challenges. The integration of 3D printing technology into the field of chromatography offers promising potential, yet also presents significant challenges that must be overcome to make it a viable method for producing chromatographic media [199]. Chromatographic materials must be porous, with pore sizes in the tens of nanometers range, to facilitate high surface area interactions with analytes, thereby ensuring high separation efficiency. Moreover, they must possess excellent mechanical strength to withstand the high pressures associated with modern chromatography techniques, such as High-Performance Liquid Chromatography (HPLC) and Ultra High-Performance Liquid Chromatography (UHPLC). As a result, the development of 3D printable materials with both high porosity and robust mechanical properties remains a critical challenge. Despite these hurdles, 3D printing technologies have made considerable strides, enabling the creation of complex geometries using a variety of materials, including metals, ceramics, polymers, and hydrogels [203, 212–214]. Some of these materials, such as silica, hydroxyapatite, and cellulose, are already used in chromatography columns [215]. Moreover, new 3D printing materials that incorporate porogens [216–220] or bifunctional monomers [206, 221–224] and new techniques such as *wax templating* [205, 225] can be employed to obtain 3D printed porous stationary phases.

In this context, triply periodic minimal surface (TPMS) architectures, and in particular gyroid-based structures, provide a natural conceptual and technological bridge between stochastic cryogel media and fully deterministic porous materials. On the one hand, TPMS geometries are ordered, periodic, and inherently compatible with additive manufacturing, making them ideal candidates for the design of reproducible and high-performance chromatographic stationary phases. On the other hand, the possibility of functionalizing 3D-printed

TPMS scaffolds with cryogel-like materials enables a controlled multiscale description of transport phenomena, allowing the pore-scale mechanisms governing mass transfer in cryogels to be investigated within a well-defined and tunable geometric framework. This dual role motivates the present theoretical and numerical investigation of TPMS-based stationary phases as model systems for chromatographic transport in hierarchical porous media.

This chapter is organized as follows. Section 8.1 gives a brief overview of the Exact Moment Analysis, a robust and computationally efficient homogenization technique derived from Brenner's Moment Theory [226]. In Section 8.2, the exact moment method for the determination of the dispersion tensor in retentive porous media has been adopted to compute the dispersion coefficients, the plate height curves and the kinetic performance factors of eight different 3D printable stationary phases based on triply periodic minimal surfaces (TPMS). The two cases in which the stationary phase is impermeable (hydrodynamic dispersion) or superficially retentive have been analyzed in detail. The Carman-Kozeny relationship between permeability K_v, hydraulic diameter d_h and hydrodynamic tortuosity τ holds true for all the geometries investigated with a unique shape coefficient K_0. The analysis of plate height curves indicates that best performing geometries are associated with lower values of the effective diameter d_{eff}, and thus lower values of permeability. When compared in terms of kinetic performance factor, the best performing geometries are those characterized by lower tortuosity and higher coefficient of uniformity δ of the axial velocity field. Among all the geometries investigated, sheet-based Gyroid and Primitive are the best performing, both in terms of maximum kinetic performance factor $e_{c,max} \in (1, 1.4)$ and in terms of column void time $t_0 \in (0.4s, 1.6s)$ for $\Delta P = 500$ bar. Section 8.3 investigates TPMS serving as mesoporous stationary phases. Their separation performances, for different values of the zone retention factor k'', are analyzed in terms of plate height curves and kinetic performance factors. The two-zone moment analysis method (TZMA) for the determination of the dispersion tensor in hierarchical retentive porous media has been adopted to compute the dispersion coefficients under retentive conditions. The contribution of the internal porosity of the stationary zone drastically change the chromatographic performance of TPMS structures with respect to the non-retentive (hydrodynamic) and superficially retentive cases. Sheet-based TPMS structures are best performing geometries because the analysis of kinetic plots reveals that optimal functioning conditions are associated with optimal dimensions of the unit cell compatible with printing resolution of cutting-edge 3D printers.

8.1 The exact moment analysis: overview

The Exact Moment Analysis (EMA) [227] is a robust and computationally efficient homogenization technique derived from Brenner's Moment Theory [226]. It relies on the formulation of exact local and integral moments, enabling the accurate estimation of both the transient and asymptotic behavior of effective dispersion properties, i.e. effective velocity and dispersion tensor, in any system composed of 2D or 3D periodic unit cells. In substance, it reduces

the solution of time-dependent advection–diffusion equations from an unbounded propagation problem in $\mathbb{R}^n$ to a cell problem defined over a bounded domain $\Omega \subset \mathbb{R}^n$, on whose walls, periodic boundary conditions are imposed. Contrariwise, Brenner's original approach employs quantized moments referred to the lattice indices of the periodic cells, thereby capturing only the asymptotic behavior of the system. EMA can be applied to any steady or time-periodic velocity field, whether solenoidal, irrotational, or a superposition thereof.

The band broadening in chromatographic beds is governed by analyte advection and diffusion, which occur at different rates inside and outside the solid zones of the bed. The presence of the retentive zone creates a micro-environment affecting diffusion rates and consequently all three terms (A, B, C) of the plate height equation, generally referred as Van Deemter equation, and in general affecting the chromatogram. The effective velocity represents the average rate at which the solute front travels through the column, and it is directly linked to the mean residence time of the solute band. A higher effective velocity corresponds to a shorter mean residence time, indicating that the solute moves more rapidly through the column. The dispersion coefficient, on the other hand, quantifies the spreading of the solute band as it migrates. It is associated with the variance of the elution peak in the chromatogram: a larger dispersion coefficient leads to greater band broadening and thus a higher variance. Together, these two parameters describe the transport behavior of solutes within the column — the effective velocity determining the average elution time, and the dispersion coefficient characterizing the extent of peak spreading. The homogenization approach able to estimate the effective transport parameters, taking into account both the mobile and the stationary phases, is the two-zone moment analysis (TZMA). The TZMA approach is a novel homogenization strategy, alternative to volume averaging techniques aimed at significantly enhancing the speed and precision in addressing the general advection–diffusion equation within hierarchical porous media featuring diffusion and adsorption–desorption processes. This approach is grounded on EMA, so its shares with it the capability of estimating the exact effective transport parameters in the asymptotic and in the transient behavior. In this chapter, the TZMA is used to analyze bi-continuous media to model monolithic columns, in the case of both superficial retentive and fully retentive stationary phase.
Before discussing the case studies investigated in this thesis, a brief overview of the Exact Moment Approach is provided in this section. For the sake of simplicity, the theoretical discussion of the EMA in this paragraph will be restricted to two-dimensional systems, but it can be expandend to higher-order problems. The current theoretical analysis concerns the modeling of the convective/diffusion transport of a single solute in a two-dimensional fluid domain, referred to as the mobile phase, denoted by Ω_m, in the presence of a solid non-retentive phase - the stationary phase Ω_s - comprising some obstacles.

Let consider the evolution of the scalar field $p(\mathbf{x}, t)$, representing the normalized concentration field of the analyte, satisfies the advection–diffusion equation

$$\partial_t p(\mathbf{x}, t) = -\partial_i\big(v^i(\mathbf{x}) p(\mathbf{x}, t)\big) + \partial_i\big(D_m^{i,j}(\mathbf{x}) \partial_j p(\mathbf{x}, t)\big), \tag{8.1}$$

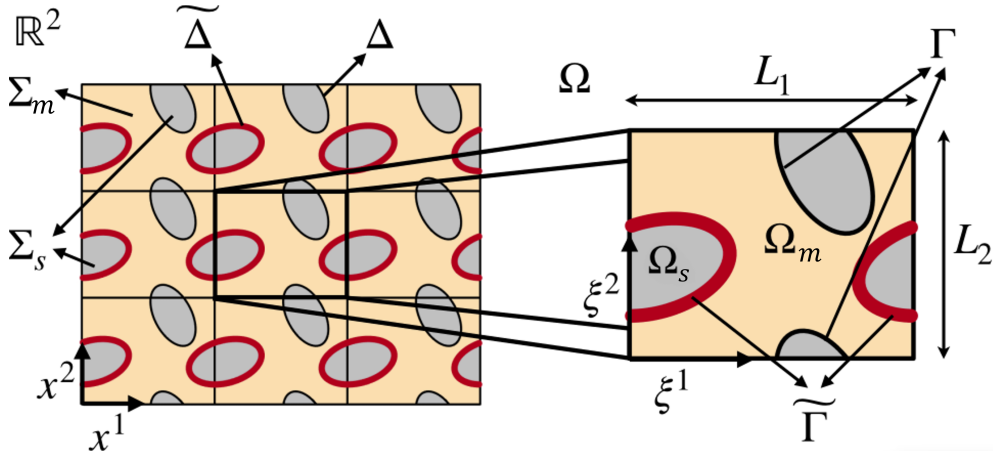


Figure 8.1: Schematic representation of the infinite domain and of the orthogonal Cartesian unit cell.

where $\mathbf{v}(\mathbf{x})$ is the spatially periodic flow field on a unit lattice cell Ω of a solvent (compressible or incompressible) laden with the analyte, satisfying the following periodic condition

$$\mathbf{v}(\mathbf{x} + m_1 L_1 \mathbf{e}_1 + m_2 L_2 \mathbf{e}_2) = \mathbf{v}(\mathbf{x}), \quad m_i \in \mathbb{Z} \tag{8.2}$$

where $\mathbf{e}_1$ and $\mathbf{e}_2$ are the two orthogonal lattice vectors characterizing Ω, and L_1 and L_2 are the periodicity lengths, and $D_m^{i,j} = D_m \delta_{i,j}$ is the uniform isotropic diffusion tensor of the analyte in the mobile phase, spatially periodic with the same periodicity of the velocity field, i.e.,

$$D_m^{i,j}(\mathbf{x} + m^1 L_1 \mathbf{e}_1 + m^2 L_2 \mathbf{e}_2) = D_m^{i,j}(\mathbf{x}), \qquad i,j = 1,2. \tag{8.3}$$

The purpose of this homogenization approach is to determine the effective transport parameters, $\mathscr{V}_\infty^i$ and $\mathscr{D}_\infty^{i,j}$, appearing in the long-time, large-distance limit equation (8.4), related to the properties of the periodic fields $v^i(\mathbf{x})$ and $D_m^{i,j}(\mathbf{x})$.

$$\partial_t \bar{p} = -\mathscr{V}_\infty^i \partial_i \bar{p} + \mathscr{D}_\infty^{i,j} \partial_i \partial_j \bar{p}. \tag{8.4}$$

This goal can be achieved, firstly, through the following procedure:

1. identifying $p(\mathbf{x}, t)$ as a probability density function (pdf) governed by a Fokker–Planck equation,
2. decoupling the spatial variables into local and global coordinates, and
3. employing the spatial moments of $p(\mathbf{x}, t)$ as estimators of the macrotransport parameters $\mathscr{V}_\infty^i$ and $\mathscr{D}_\infty^{i,j}$.

Let $\boldsymbol{\xi} = (\xi^1, \xi^2)$ denote the local coordinates within the unit lattice cell Ω, where $0 \leq \xi^1 \leq L_1$ and $0 \leq \xi^2 \leq L_2$. Any point $\mathbf{x} \in \mathbb{R}^2$ can then be uniquely expressed as

$$\mathbf{x} = (\xi^1 + m^1 L_1)\mathbf{e}_1 + (\xi^2 + m^2 L_2)\mathbf{e}_2 = \boldsymbol{\xi} + \mathbf{x}_\mathbf{m}, \tag{8.5}$$

where the compact notation $\boldsymbol{\xi} = (\xi^1, \xi^2)$ and $\mathbf{x}_\mathbf{m} = m^1 L_1 \mathbf{e}_1 + m^2 L_2 \mathbf{e}_2$ is adopted, with the

subscript "$\mathbf{m}$" denoting the multi-index $\mathbf{m} = (m^1, m^2)$.

At this point, it is necessary to introduce the moments. It must be pointed out that, differently from Brenner's theory, since in EMA a rigorous setting is adopted, the integral moments should be *exactly* the moments of the scalar field $p(\mathbf{x}, \mathrm{t})$ with respect to the global coordinate $\mathbf{x}$ evaluated over $\mathbb{R}^2$, namely:

$$M^{(q)}_{q_1,q_2}(t) = \int_{\mathbb{R}^2} (x^1)^{q_1} (x^2)^{q_2}\, p(\mathbf{x}, t)\, d\mathbf{x}, \qquad \text{with } q_1 + q_2 = q \tag{8.6}$$

By starting from this equation (8.6), using the equation (8.5), the following formulation of the local moments $P^{(q)}_{q_1,q_2}(\boldsymbol{\xi}, t)$ is derived, in agreement with their probabilistic interpretation and referenced to the global mean of the scalar field $p(\mathbf{x}, t)$:

$$\begin{aligned} M^{(q)}_{q_1,q_2}(t) &= \sum_{\mathbf{m}} \int_{\Omega} (\xi^1 + m^1 L_1)^{q_1} (\xi^2 + m^2 L_2)^{q_2}\, p(\boldsymbol{\xi} + \mathbf{x}_{\mathbf{m}}, t)\, d\boldsymbol{\xi} \\ &= \int_{\Omega} P^{(q)}_{q_1,q_2}(\boldsymbol{\xi}, t)\, d\boldsymbol{\xi}, \end{aligned} \tag{8.7}$$

where the exact local moments $P^{(q)}_{q_1,q_2}(\boldsymbol{\xi}, t)$ are defined as

$$P^{(q)}_{q_1,q_2}(\boldsymbol{\xi}, t) = \sum_{\mathbf{m}} (\xi^1 + m^1 L_1)^{q_1} (\xi^2 + m^2 L_2)^{q_2}\, p(\boldsymbol{\xi} + \mathbf{x}_{\mathbf{m}}, t). \tag{8.8}$$

Introducing integral and local moments permits the equations resolution to be transferred from $\mathbb{R}^2$ into the single unit cell of periodicity Ω. Thus, the local moments are defined in the Cartesian product. In order to evaluate the effective convective and dispersive parameter, the first- and second-order global moments - i.e. $\mathrm{M}^{(1)}_{q_1,q_2}(\mathrm{t})$ and $\mathrm{M}^{(2)}_{q_1,q_2}(\mathrm{t})$ - must be taken into account. In great detail, their time derivatives lead to:

$$\frac{dM^{(1)}_{1,0}(t)}{dt} = \mathscr{V}^1 \qquad \frac{dM^{(1)}_{0,1}(t)}{dt} = \mathscr{V}^2 \tag{8.9}$$

$$\begin{aligned} \frac{dM^{(2)}_{2,0}(t)}{dt} &= 2M^{(1)}_{1,0}(t)\mathscr{V}^1 + 2\mathscr{D}^{1,1}, \\ \frac{dM^{(2)}_{0,2}(t)}{dt} &= 2M^{(1)}_{0,1}(t)\mathscr{V}^2 + 2\mathscr{D}^{2,2}, \\ \frac{dM^{(2)}_{1,1}(t)}{dt} &= M^{(1)}_{1,0}(t)\mathscr{V}^2 + M^{(1)}_{0,1}(t)\mathscr{V}^1 + \mathscr{D}^{1,2} + \mathscr{D}^{2,1}. \end{aligned} \tag{8.10}$$

Therefore, the first-order moments $M^{(1)}_{1,0}(t)$ and $M^{(1)}_{0,1}(t)$ provide direct approximations of the components $\mathscr{V}^i$ $(i = 1, 2)$ of the effective velocity field. The dynamics of the second-order moments $M^{(2)}_{2,0}(t)$, $M^{(2)}_{1,1}(t)$, and $M^{(2)}_{0,2}(t)$ allow us to determine the independent entries of the symmetric dispersion tensor $\mathscr{D}^{i,j}$, which model the spreading process associated with the effective transport dynamics. $\mathscr{V}^i$ asymptotically converges toward the effective velocity

component $\mathscr{V}^i_\infty$ and each component of $\mathscr{D}^{i,j}$ converges toward $\mathscr{D}^{i,j}_\infty$, entering equation (8.4).

From (8.1), by enforcing the definition (8.8) for the local moments $P^{(q)}_{q_1,q_2}(\boldsymbol{\xi},t)$, one obtains the transport equation for the hierarchy of the local moments

$$\begin{aligned}\partial_t P^{(q)}_{q_1,q_2}(\boldsymbol{\xi},t) =& -\nabla\cdot\boldsymbol{J}[P^{(q)}_{q_1,q_2}] + q_1\big[v^1 P^{(q-1)}_{q_1-1,q_2} - \partial_{\xi,j}(D^{1,j}_m P^{(q-1)}_{q_1-1,q_2}) - D^{1,j}_m\partial_{\xi,j}(P^{(q-1)}_{q_1-1,q_2})\big]\\ &+ q_2\big[v^2 P^{(q-1)}_{q_1,q_2-1} - \partial_{\xi,j}(D^{2,j}_m P^{(q-1)}_{q_1,q_2-1}) - D^{2,j}_m\partial_{\xi,j}(P^{(q-1)}_{q_1,q_2-1})\big]\\ &+ 2q_1q_2D^{1,2}_m P^{(q-2)}_{q_1-1,q_2-1} + q_1(q_1-1)D^{1,1}P^{(q-2)}_{q_1-2,q_2} + q_2(q_2-1)D^{2,2}_m P^{(q-2)}_{q_1,q_2-2}\end{aligned} \tag{8.11}$$

where

$$J[\cdot] = v^i\,\cdot - D^{i,j}_m\partial_{\xi,j}\cdot \tag{8.12}$$

$$-\nabla\cdot\boldsymbol{J}[P^{(q)}_{q_1,q_2}] = -\partial_{\xi,i}\big(v^i(\xi)P^{(q)}_{q_1,q_2}\big) + \partial_{\xi,i}\big(D^{i,j}_m(\xi)\partial_{\xi,j}P^{(q)}_{q_1,q_2}\big), \tag{8.13}$$

equipped with the following boundary conditions of Γ

$$\boldsymbol{J}[P^{(q)}_{q_1,q_2}]\cdot\boldsymbol{n}|_\Gamma = -(q_1D^{1,j}_m P^{(q-1)}_{q_1-1,q_2} + q_2D^{2,j}_m P^{(q-1)}_{q_1,q_2-1})(\boldsymbol{e}_i\cdot\boldsymbol{n})|_\Gamma \tag{8.14}$$

and with periodic boundary conditions. It is necessary to solve only the first- and the second-order integral moments for the complete characterization of the effective transport properties, as follows

$$\begin{aligned}\mathscr{V}^i(t) &= \int_{\Omega_m}(v^iP^{(0)}_{0,0} - D^{i,j}_m\partial_{\xi,j}P^{(0)}_{0,0})d\boldsymbol{\xi}, \qquad i,j=1,2\\ \mathscr{D}^{1,1}(t) &= \int_{\Omega_m}D^{1,1}_m P^{(0)}_{0,0}d\boldsymbol{\xi} + \int_{\Omega_m}((v^1-\mathscr{V}^1)P^{(1)}_{1,0} - D^{1,j}_m\partial_{\xi,j}P^{(1)}_{1,0})d\boldsymbol{\xi}\\ \mathscr{D}^{2,2}(t) &= \int_{\Omega_m}D^{2,2}_m P^{(0)}_{0,0}d\boldsymbol{\xi} + \int_{\Omega_m}((v^2-\mathscr{V}^2)P^{(1)}_{0,1} - D^{2,j}_m\partial_{\xi,j}P^{(1)}_{0,1})d\boldsymbol{\xi}\\ \mathscr{D}^{1,2}(t) = \mathscr{D}^{2,1}(t) &= \int_{\Omega_m}D^{1,2}_m P^{(0)}_{0,0}d\boldsymbol{\xi} + \frac{1}{2}\int_{\Omega_m}((v^1-\mathscr{V}^1)P^{(1)}_{0,1} - D^{1,j}_m\partial_{\xi,j}P^{(1)}_{0,1})d\boldsymbol{\xi}\\ &\quad + \frac{1}{2}\int_{\Omega_m}((v^2-\mathscr{V}^2)P^{(1)}_{1,0} - D^{2,j}_m\partial_{\xi,j}P^{(1)}_{1,0})d\boldsymbol{\xi}\end{aligned} \tag{8.15}$$

When the macro-trasport conditions are reached, the asymptotic effective velocity $\mathscr{V}^i_\infty$ and the asymptotic dispersion tensor $\mathscr{D}^{i,j}_\infty$ can be determine replacing $P^{(0)}_{0,0}$ with its asymptotic stationary function $w_0(\boldsymbol{\xi})$, and the first local moments with $P^{(1)}_{1,0}$ with $w_0\mathscr{V}^1t\,b_{1,0}$ and $P^{(1)}_{0,1}$ with $w_0\mathscr{V}^2t\,b_{0,1}$ in equations (8.15) obtaining

$$\mathscr{V}^i_\infty = \int_{\Omega_m}(v^iw_0 - D^{i,j}_m\partial_{\xi,j}w_0)d\boldsymbol{\xi}, \qquad i,j=1,2, \tag{8.16}$$

where w_0 satisfies the transport equation

$$-\partial_i\big(v^i(\mathbf{x})w_0\big) + \partial_i\big(D^{i,j}_m(\mathbf{x})\partial_j w_0\big) = 0, \tag{8.17}$$

equipped with no-flux boundary conditions at the solid wall Γ and periodic conditions ad

the unit cell boundaries, and

$$\mathscr{D}_{\infty}^{1,1} = \int_{\Omega_m} D_m^{1,1} w_0 d\boldsymbol{\xi} + \int_{\Omega_m} ((v^i - \mathscr{V}_{\infty}^i) w_0 b_{1,0} - D_m^{1,j} \partial_{\xi,j}(w_0 b_{1,0})) d\boldsymbol{\xi}, \tag{8.18}$$

where $w_0 b_{1,0}$ is the stationary cell field satisfying the following transport equation and boundary conditions

$$-\partial_i\big(v^i(\mathbf{x}) w_0 b_{1,0}\big) + \partial_i\big(D_m^{i,j}(\mathbf{x}) \partial_j(w_0 b_{1,0})\big) = w_0(\mathscr{V}_{\infty}^i - v^i) + D_m^{1,j} \partial_j w_0 + \partial_j(D_m^{1,j} w_0), \tag{8.19}$$

$$\boldsymbol{J}[w_0 b_{1,0}] \cdot \boldsymbol{n}|_{\Gamma} = -D_m^{1,j} w_0 (\boldsymbol{e}_i \cdot \boldsymbol{n})|_{\Gamma} \tag{8.20}$$

and periodic boundary conditions at the edges of the periodicity cell, and analogously for the other entries of the dispersion tensor.

In the following sections, the moment analysis previously described—and extended to account for both the mobile and stationary phases within a system that also involves adsorption/desorption phenomena (TZMA)—is employed for the determination of the effective macrotransport parameters in three-dimensional, triply periodic bicontinuous systems.

8.2 The case of Superficial Adsorption

In this section, the separation performances of eight different ordered monolithic stationary phases based on Triply Periodic Minimal Surfaces (TPMS) are analyzed by addressing not only hydrodynamic dispersion (impermeable stationary phase) but also dispersion features in the wall-retentive case. Stationary phases based on TPMS have been already proposed as very promising geometries [200, 201]. Indeed, Dolamore et al. [201] investigated chromatographic performance of Schwarz Diamond, Schoën Gyroid and Schwarz Primitive stationary phases exclusively in the no-retentive case. We not only extended the analysis to five more TPMS geometries but also investigated how the presence of the stationary phase, assumed superficially retentive, modifies the separation performance of TPMS structures. The exact moment analysis method [228–231] for the determination of the dispersion tensor in retentive porous media has been adopted to compute the dispersion coefficients, the plate height curves and the kinetic performance factors of all the geometries. Furthermore, a critical analysis of the effective possibility of 3D printing TPMS stationary phases has been performed, based on the comparison between the optimal unit cell dimension and the resolution that can be recently attained with 3D printing advanced techniques. This section is organized as follows. Subsection 8.2.1 briefly reviews the transport equations that have been solved, via the Finite Element Method implemented by Comsol Multiphysics, to estimate the axial dispersion coefficient with the exact moment method. In Subsection 8.2.2 the eight different TPMS-based geometries are introduced. Their geometric and fluid dynamical characteristic parameters are presented in Subsection 8.2.3. Subsection 8.2.4 focuses of hydrodynamic dispersion data (no retention) while Subsection 8.2.5 analyses dispersion properties in the case

of surface retention. The analysis of the kinetic performance factors and kinetic plots, for all the TPMS-based geometries, is addressed in Subsection 8.2.6.

8.2.1 Theoretical framework

The exact moment method [230–232] has been adopted to estimate the asymptotic axial dispersion coefficient D^x of a single solute in the presence of a solid non-porous stationary phase Ω_s whose global surface $\partial\Omega_s$ is coated with a thin layer, acting as a retentive layer (providing either adsorptive or partitioning-based specific retention). We assume this layer has a thickness that is negligible with respect to the thickness of the support structure, such that the material behaves as if the retention occurs only on the outer surface of the material, a situation we refer to using the term "superficially retentive". A typical application of such material would be the separation of intact proteins [233]. Adsorption onto and desorption from $\partial\Omega_s$ allow linear and reversible mass transfer between the solid surface $\partial\Omega_s$ and the fluid (mobile) phase Ω_m. Analyte concentrations are assumed low enough to remain in the linear part of the retention isotherm. No drift or surface diffusion of the analyte are allowed. It must be underlined that small concentrations of the analyte, as occurs in biological chromatography, the amount adsorbed at equilibrium is proportional to the amount within the sample phase, as described by the linear adsorption isotherm. This occurs because at lower concentrations, the sample does not reach the saturation level of the adsorbent. Such an approximation is often made when modeling chromatography [234, 235]. Let $\mathbf{v}$ be the pressure driven flow field of a solvent laden with analyte, v_x the axial main component, D_m the bare diffusion coefficient of the analyte in the mobile phase Ω_m, k_a [m/s] and k_d [1/s] the adsorption and desorption kinetic constants, corresponding to an equilibrium adsorption constant $K_{eq} = k_a/k_d$ [m]. This constant allows to express the effect of changes in the elution strength of the mobile phase.
The asymptotic axial dispersion coefficient D^x, in the limiting case of negligible mass transfer resistance at the interface $\partial\Omega_s$, can be evaluated as [230]

$$D^x = \frac{D_m}{1+k''} + \frac{1}{1+k''}\Big\langle (v_x - U^x)\, b_m - D_m \partial_x b_m \Big\rangle_{\Omega_m} - U^x \frac{k''}{1+k''}\Big\langle b_m \Big\rangle_{\partial\Omega_s} \tag{8.21}$$

or equivalently

$$D^x = \frac{D_m}{1+k''}\Big\langle ||\nabla b_m - \mathbf{e}_x||^2 \Big\rangle_{\Omega_m} \tag{8.22}$$

where b_m is the b-field in the mobile phase, the symbol $\langle\cdot\rangle$ indicates the spatial average, $\mathbf{e}_x$ the unit vector along the x axis, U^x is the effective axial velocity, U_i the axial interstitial velocity, k'' the retention factor, V_m the volume of the mobile fluid phase and S the area of the adsorbent surface $\partial\Omega_s$

$$U^x = \frac{U_i}{1+k''}, \quad U_i = \langle v_x \rangle_{\Omega_m}, \quad k'' = K_{eq}\frac{S}{V_m} \tag{8.23}$$

According with Eq. (8.21), the estimate of D^x requires the determination of the velocity field $\mathbf{v}$ (via the solution of the Stokes equation with no-slip boundary conditions on $\partial\Omega_s$) and the b-field b_m in the mobile phase Ω_m, which satisfies the following advection/diffusion equation and boundary conditions on the periodic unit cell (see Section 8.2.2)

$$-\mathbf{v}\cdot\nabla b_m + D_m\nabla^2 b_m = (U^x - v_x) \tag{8.24}$$

$$-D_m(\nabla b_m - \mathbf{e}_x)\cdot\mathbf{n}\big|_{\partial\Omega_s} = U^x K_{eq} \tag{8.25}$$

and periodic boundary conditions at the edges of the unit cell. The physical parameters D_m, U_i and K_{eq} controlling dispersion features are grouped into the two dimensionless parameters $Pe = U_i L/D_m \in [0.1, 10^3]$ and $k'' \in [0, 16]$, L being the characteristic length of the unit periodic cell.

The equations for determining D^x in the non-retentive case [228, 229] (hydrodynamic dispersion) can be obtained from Eqs. (8.21) and Eqs. (8.24-8.25) by simple setting $K_{eq} = 0$ that implies $k'' = 0$ and $U^x = U_i$. The equations for determining the obstruction factor $\gamma_m^0 = \lim_{\mathbf{v}\to\mathbf{0}} D^x/D_m$ are obtained by further simplifying the hydrodynamic dispersion setting and enforcing $\mathbf{v} = \mathbf{0}$ that implies $v_x = 0$ and $U_i = U^x = 0$.

A detailed analysis and derivation of Eqs (8.21-8.25) can be found in [230] and their direct application to chromatographic systems, such as open tubular liquid chromatography and retentive pillar array columns, can be found in [231, 232]. It must be observed that Eqs. (8.21-8.25), obtained from the exact moment approach, permit to determine the asymptotic axial dispersion coefficient D^x, i.e. the axial dispersion coefficient when macro-transport conditions are attained. The latter imply that a sharply delimited injected plug of solute moves at constant effective velocity U^x along the main fluid-flow direction x, and it has attained a symmetric Gaussian shape with a variance $\sigma^2(t)$ growing linearly in time as $\sigma^2 = 2\mathscr{D}^x t$. The exact moment method differs from the classical Brenner moment approach [236, 237] because it allows us to estimate not only the asymptotic values but also the temporal evolution of dispersion properties of solute particles in periodic media possessing absorbing/desorbing walls. However, the two methods provide the same results for asymptotic quantities U^x and D^x. Indeed, Eqs. (8.21-8.25), coincide with those obtained via Brenner's macro-transport theory and also with those derived by Yan et al. [238] through the volume averaging approach.

The exact moment approach shares with Brenner's theory and the volume averaging approach [29, 238, 239] the key advantage, over Direct Numerical Simulation (DNS) and Lattice Boltzmann (LB) approaches [23, 31, 32], of requiring the solution of (i) a steady-state transport problem and (ii) only on the unit cell, instead of solving the time-dependent advection-diffusion equation for the analyte from the initial time instant until a final time large enough to ensure that asymptotic conditions are reached, which requires a large number of unit cells.

Numerical results for the velocity field $\mathbf{v}$ and the b-field b_m have been obtained through the solution of their respective partial differential equations using Comsol Multiphysics 5.5 that employs the Finite Element Method. The incompressible Navier–Stokes package (Stokes

flow) was adopted under stationary conditions, utilizing P2 + P1 Lagrange elements for velocity and pressure, respectively. No slip boundary conditions are enforced on $\partial\Omega_s$. For the numerical integration of the transport equation of b_m, the Coefficient Form Partial Differential Equation (PDE) package was utilized with Lagrangian quadratic elements. The MUltifrontal Massively Parallel Sparse direct Solver (MUMPS) was employed with a relative tolerance of 10^{-6}.

8.2.2 Geometries

Eight different geometries have been investigated: three strut-based TPMS, namely Schoen Gyroid (G), Schwarz Diamond (D), Schwarz Primitive (P) and five sheet-based TPMS, i.e. two Sheet Gyroids SGa and SGb, two Sheet Diamonds SDa and SDb, and one Sheet Primitive SPb [240–243]. The structures of the stationary phase Ω_s and the complementary mobile phase Ω_m for all the geometries investigated are shown in Figure 8.25 for Gyroids, Figure 8.3 for Diamonds and Figure 8.4 for Primitives. For all these structures, the void fraction occupied by the fluid, i.e. the external porosity $\varepsilon{=}V_m/L^3$, is set to $\varepsilon = 0.4$, L being the side length of the cubic unit cell.

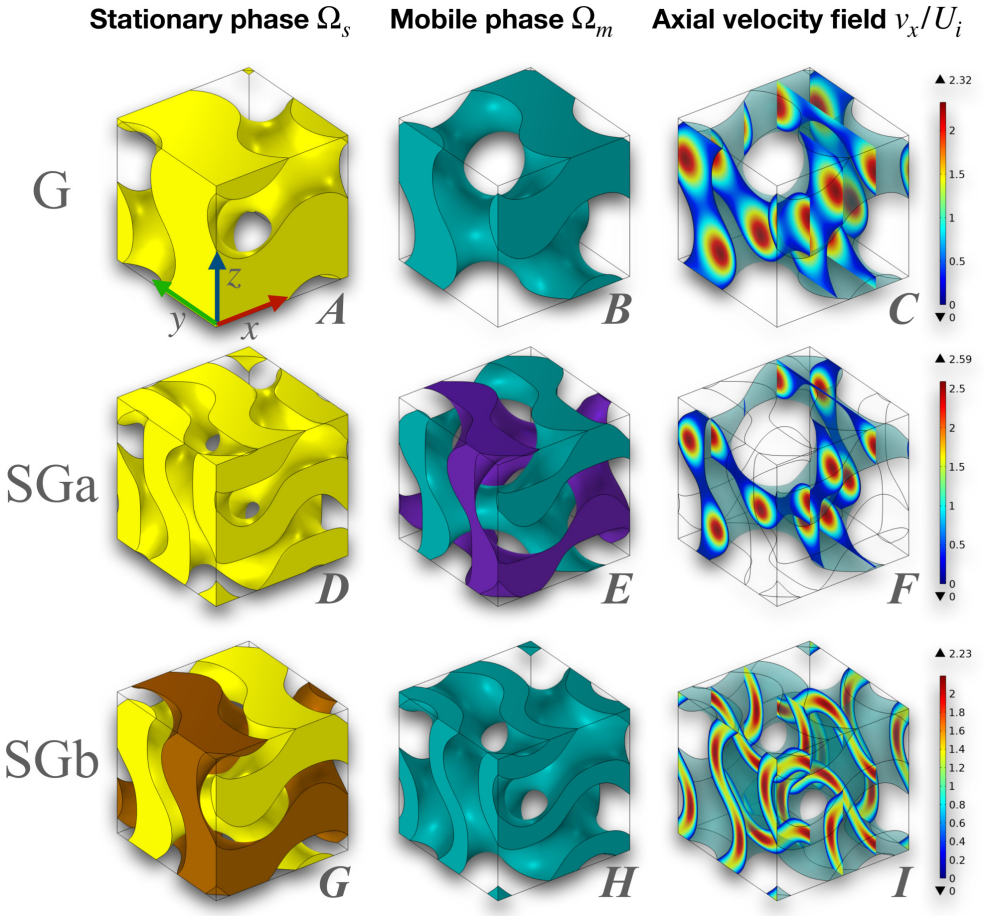


Figure 8.2: Strut-based Gyroid (G) and sheet-based Gyroids (SGa and SGb): stationary phase Ω_s (A,D,G), mobile phase Ω_m (B,E,H) and normalized axial component v_x/U_i of the fluid velocity field (C,F,I), U_i being the seepage (interstitial) velocity along x.

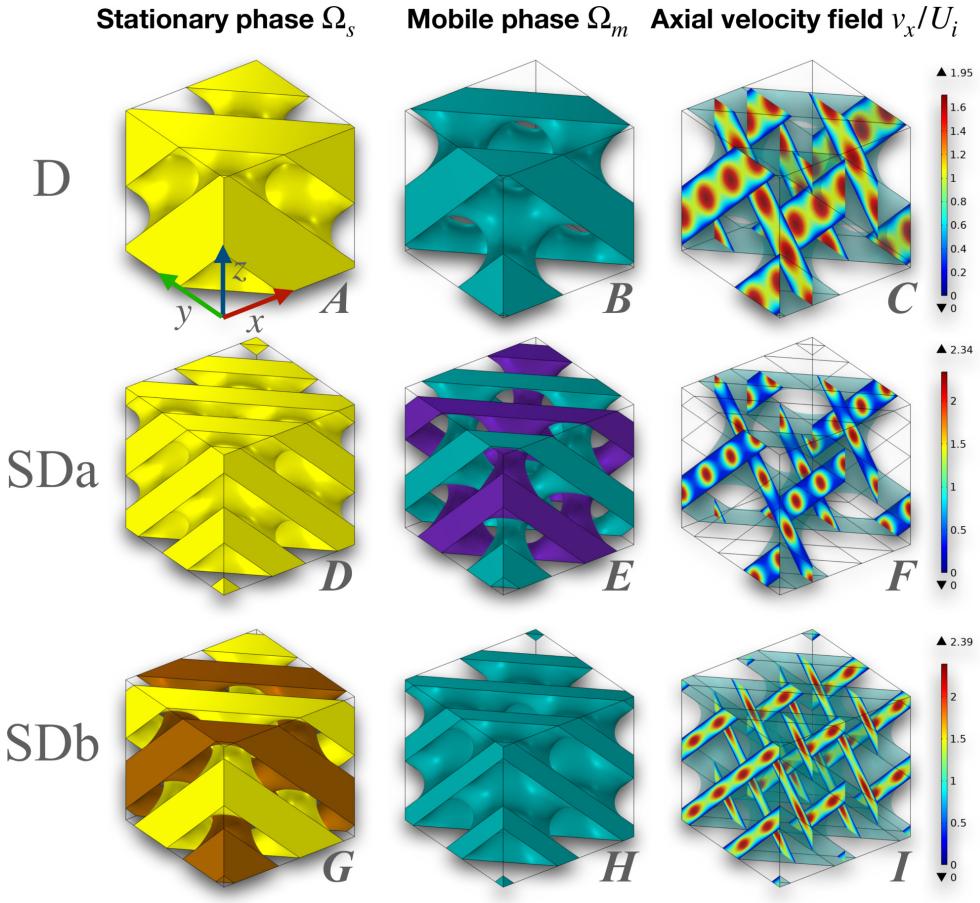


Figure 8.3: Strut-based Diamond (D) and sheet-based Diamonds (SDa and SDb): stationary phase Ω_s (A,D,G), mobile phase Ω_m (B,E,H) and normalized axial component v_x/U_i of the fluid velocity field (C,F,I), U_i being the seepage (interstitial) velocity along x.

The stationary phase Ω_s of the strut-based unit cells (G, D and P) is obtained by identifying the set of points satisfying the inequality constraint [242] $f(x,y,z) \leq \zeta$ where ζ is the parameter controlling the external porosity ε and

$$f(x,y,z) = \begin{cases} \sin\left(\frac{x}{l}\right)\cos\left(\frac{y}{l}\right) + \sin\left(\frac{y}{l}\right)\cos\left(\frac{z}{l}\right) + \sin\left(\frac{z}{l}\right)\cos\left(\frac{x}{l}\right), & \text{Gyroid} \\ \sin\left(\frac{x}{l}\right)\sin\left(\frac{y}{l}\right)\sin\left(\frac{z}{l}\right) + \sin\left(\frac{x}{l}\right)\cos\left(\frac{y}{l}\right)\cos\left(\frac{z}{l}\right) + \cos\left(\frac{x}{l}\right)\sin\left(\frac{y}{l}\right)\cos\left(\frac{z}{l}\right) + \cos\left(\frac{x}{l}\right)\cos\left(\frac{y}{l}\right)\sin\left(\frac{z}{l}\right), & \text{Diamond} \\ \cos\left(\frac{x}{l}\right) + \cos\left(\frac{y}{l}\right) + \cos\left(\frac{z}{l}\right), & \text{Primitive} \end{cases}$$

with $l = L/(2\pi)$ for a cubic periodic cell of side length L. Indeed, the boundary $\partial\Omega_s$ between the mobile and the stationary phase within the unit cell is the isosurface $f(x,y,z) = \zeta$. By changing the value of ζ, the isosurface is shifted along its normal direction within the unit periodic cell $L \times L \times L$, and this allows changing the fraction of unit-cell points belonging to Ω_s and consequently modulating the void fraction (external porosity) ε of the periodicity cell.

For sheet-based unit cells, the boundary $\partial\Omega_s$ between Ω_m and Ω_s is the isosurface $f(x,y,z)^2 = \zeta^2$. The stationary phase Ω_s of the sheet-based unit cells of type a (SGa and

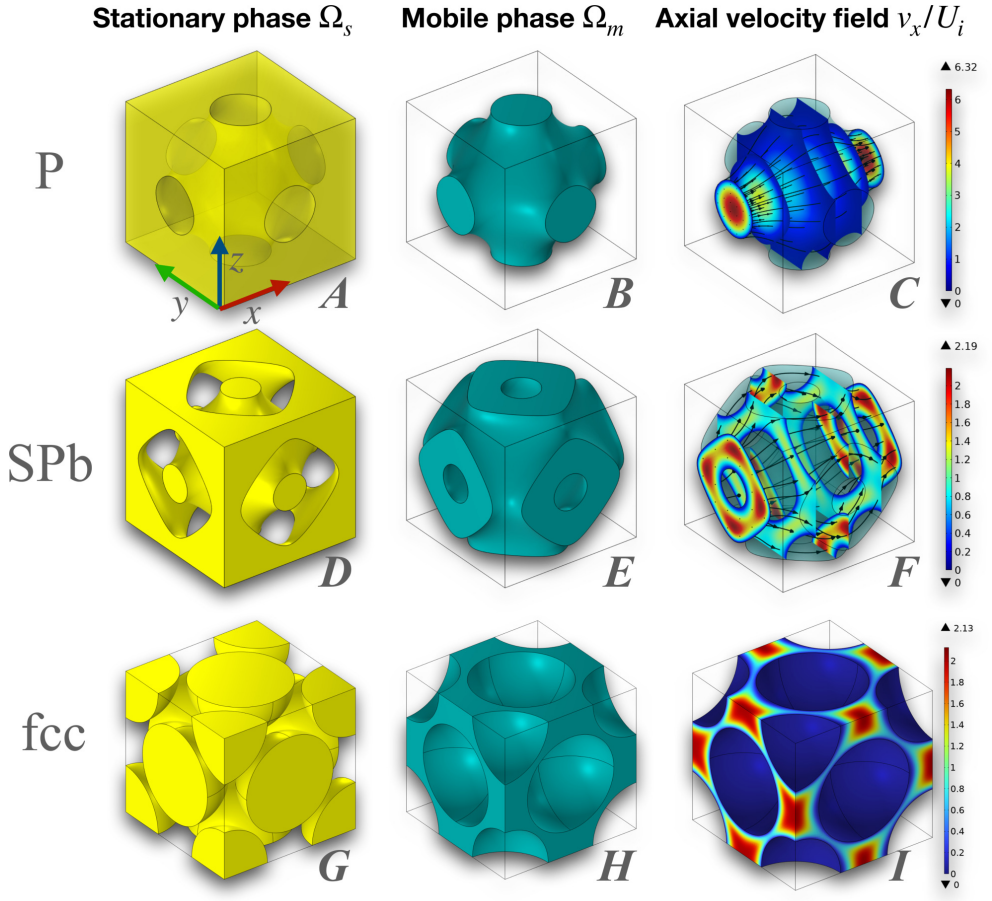


Figure 8.4: Strut-based Primitive (P), sheet-based Primitive (SPb) and face centered cubic array of spheres (fcc): stationary phase Ω_s (A,D,G), mobile phase Ω_m (B,E,H) and normalized axial component v_x/U_i of the fluid velocity field (C,F,I), U_i being the seepage (interstitial) velocity along x.

SDa) is obtained by enforcing the inequality constraint $f(x,y,z)^2 \leq \zeta^2$ while, for the sheet-based unit cells of type b (SGb, SDb and SPb) the inequality constraint is $f(x,y,z)^2 \geq \zeta^2$. The values of ζ adopted to obtain the same external porosity $\varepsilon = 0.4$ are (-0.32,-0.25,-0.35,-0.91,-0.72,-0.62,-0.49,-0.70) for G, D, P, SGa, SDa, SGb, SDb, SPb, respectively.

All the geometries are bicontinuous, meaning that both the mobile and the stationary phases allow end-to-end connected paths along x, y and z. Both Primitives P and SPb possess the peculiar feature that the velocity components v_y and v_z vanishes at $y = 0, L$ and $z = 0, L$, respectively, due to the symmetries of the geometry. As a consequence the streamlines are confined within the unit cell and a fluid element, entering the unit cell at $x = 0$, will never be able to enter and explore any of the four adjacent cells (adjacent in $y = 0, L$ and $z = 0, L$). The sheet-based Diamond and Gyroid of type a, namely SDa and SGa, possess a unique end-to-end connected stationary phase, but the the mobile phase consists of two distinct and unconnected volumes, although each of the two volumes allows an end-to-end path along all three directions x, y, and z. The structure of each of the two components of the mobile phase resembles that of the corresponding strut-based mobile phase, in terms of curvature and connectivity, but with an average surface to surface distance

almost halved. On the other hand, the sheet-based Diamond and Gyroid of type b, namely SDb and SGb, possess a unique end-to-end connected mobile phase, but the stationary phase consists of two distinct and unconnected volumes, although each of the two volumes allows an end-to-end path along all three directions x, y, and z. We also analyzed the separation performances of a face centered cubic (fcc) array of spheres (Figure 8.4 G-I) at the same external porosity $\varepsilon = 0.4$, as a prototype of an ordered array of spheres.

Numerical results have been obtained using a tetrahedral mesh spanning the mobile phase Ω_m. The complete mesh consists of approximately 10^6 domain elements, 10^5 boundary elements, and 10^3 edge elements for all the geometries. As an example, the meshes adopted for the SDa and SDb geometries are shown in Figures 8.5(**A**)–(**B**). Results are verified to be mesh independent in the whole range of Pe values investigated, $Pe \in (10^{-1}, 10^3)$.

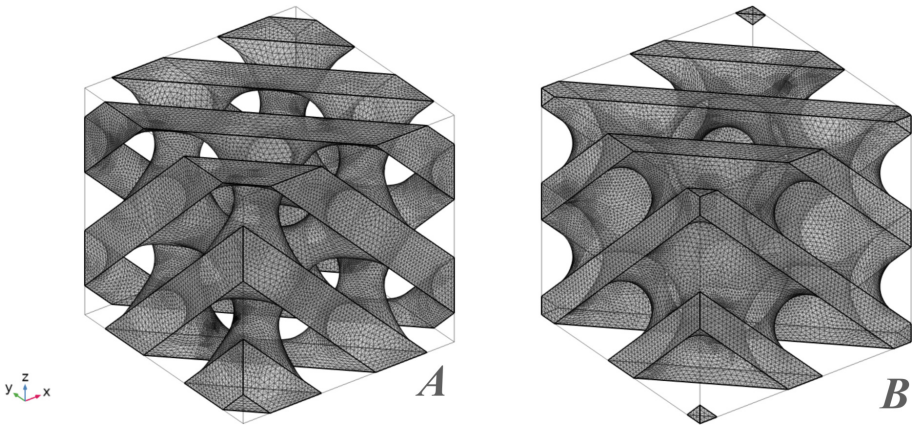


Figure 8.5: Meshes adopted for the Sheet-based Diamond of type a (SGa, panel A) and type b (SGb, panel B)

8.2.3 Fluid dynamic properties

Table 8.1 reviews, for all the geometries investigated, the interstitial permeability K_v [244, 245]

$$K_v = \frac{\eta L U_i}{P|_{x=0} - P|_{x=L}}, \quad U_i = \langle v_x \rangle_{\Omega_m} \tag{8.26}$$

the equivalent effective diameter d_{eff} [246]

$$d_{\text{eff}} = \sqrt{32 K_v} \tag{8.27}$$

the hydraulic diameter d_h

$$d_h = 4 \frac{\text{fluid volume}}{\text{wetted area}} = 4 \frac{V_m}{S} \tag{8.28}$$

the hydrodynamic tortuosity τ [31]

$$\tau = \frac{\left\langle \sqrt{v_x^2 + v_y^2 + v_z^2} \right\rangle_{\Omega_m}}{U_i} \tag{8.29}$$

the x component of the dimensionless vorticity σ [247], averaged over the fluid domain Ω_m

$$\sigma = \frac{\left\langle |\partial v_z/\partial y - \partial v_y/\partial z| \right\rangle_{\Omega_m}}{U_i/L} \tag{8.30}$$

and the coefficient of uniformity δ of the axial velocity field [29, 32]

$$\delta = 1 - \frac{\langle |v_x - U_i| \rangle_{\Omega_m}}{U_i} \tag{8.31}$$

with $\delta = 1$ in case of perfect uniformity (flat profile, no dispersion). The excellent agreement between the values of K_v and d_h reported in Table 8.1 and that obtained by Dolamore et al. [201] for the strut-based TPMS geometries D, G and P is shown in Figure 8.6.

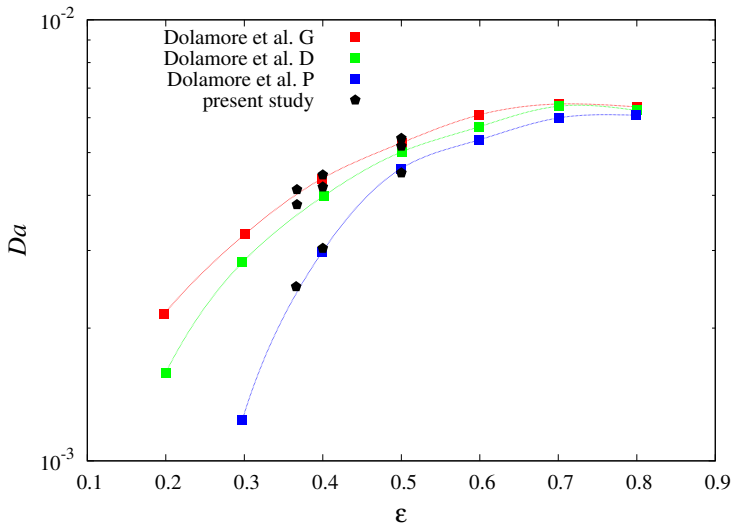


Figure 8.6: Darcy number $Da = K_v\varepsilon/d_h^2$ vs ε for the three strut-based geometries G, D and P. Squares are numerical results by Dolamore et. al. (2022). Black pentagons are numerical results of the present study.

Figure 8.7 A clearly shows that the effective diameter d_{eff} is a monotonically increasing (almost linear) function of the hydraulic diameter d_h because the smaller the hydraulic diameter, the larger the wetted area (for the same volume of fluid), and the smaller the permeability.

The Carman-Kozeny relationship between the permeability K_v and the hydraulic diameter d_h holds true for all the structures

$$K_v = \frac{d_h^2}{16K''}, \quad K'' = K_0\tau^2 \tag{8.32}$$

where, according to Carman [244, 245], the Kozeny constant K'' is related to the square of the tortuosity by a shape coefficient K_0 whose best-fit value, estimated in the present study, is $K_0 = 3.46$ for all the geometries investigated, as shown in Figure 8.7B. Only the permeability data of the Primitive (P) deviate significantly from the Carman-Kozeny

Table 8.1: Review of geometrical/fluid dynamical properties of all the structures for $\varepsilon = 0.4$

	$K_v/L^2 \times 10^3$	d_{eff}/L	d_h/L	τ	σ	δ
G	3.04	0.31	0.52	1.28	5.96	0.44
D	1.85	0.24	0.42	1.34	9.52	0.53
P	3.65	0.34	0.69	1.04	0.22	0.14
SGa	1.12	0.19	0.32	1.34	9.70	0.35
SDa	0.56	0.13	0.25	1.46	17.2	0.49
SGb	0.99	0.18	0.28	1.17	2.90	0.49
SDb	0.64	0.14	0.23	1.15	3.81	0.47
SPb	1.68	0.23	0.37	1.19	2.25	0.58
fcc	0.94	0.17	0.29	1.25	7.60	0.54

equation Eq. (8.32), but this is easily explained considering that underlying the Carman-Kozeny relationship there is the assumption that the ratio of the fluid volume V_m to the wetted surface is equal to the ratio of the cross-sectional area accessible to the fluid to the wetted perimeter at each section. This property is not satisfied by the Primitive geometry which has a huge section enlargement in the central part of the domain.

These geometric and fluid dynamic parameters play an important role in the subsequent analysis of the dispersion properties and separation efficiency of the geometries under investigation.

8.2.4 Hydrodynamic dispersion (no retention $k'' = 0$)

Figures 8.8 A-D show the reduced plate height curves $h = H/L = 2D^x/(U_i L) = 2(D^x/D_m)/Pe$ vs $Pe = U_i L/D_m$ for the strut-based geometries G, D, and P (Figure 8.8A), for the Diamonds D,SDa and SDb (Figure 8.8B), the Gyroids G, SGa and SGb (Figure 8.8C) and the Primitives P and SPb (Figure 8.8D). The reduced hetp curve for the fcc array of spheres is also reported for direct comparison with TPMS structures. Numerical results of h_{min} for strut-based TPMS geometries D, G and P are in excellent agreement with the numerical results by Dolamore et al. [201] as shown in Figure 8.9.

Among the strut-based geometries, the Diamond (D) provides the best result, comparable with that of the fcc array of spheres, as it reaches a minimum value $h_{min,D} = 0.057$ about 1/3 of that of the Gyroid ($h_{min,G} = 0.172$) and about 1/8 of that of the Primitive ($h_{min,P} = 0.483$). Correspondingly, $Pe_{min,D} = 51.75$ is about 2.5 times the value of $Pe_{min,G} = 20.24$ and more than 5 times larger than $Pe_{min,P} = 9.25$. Indeed, also Dolamore et al. [201] observed that the performance hierarchy between the strut-based TPMS structures D, G

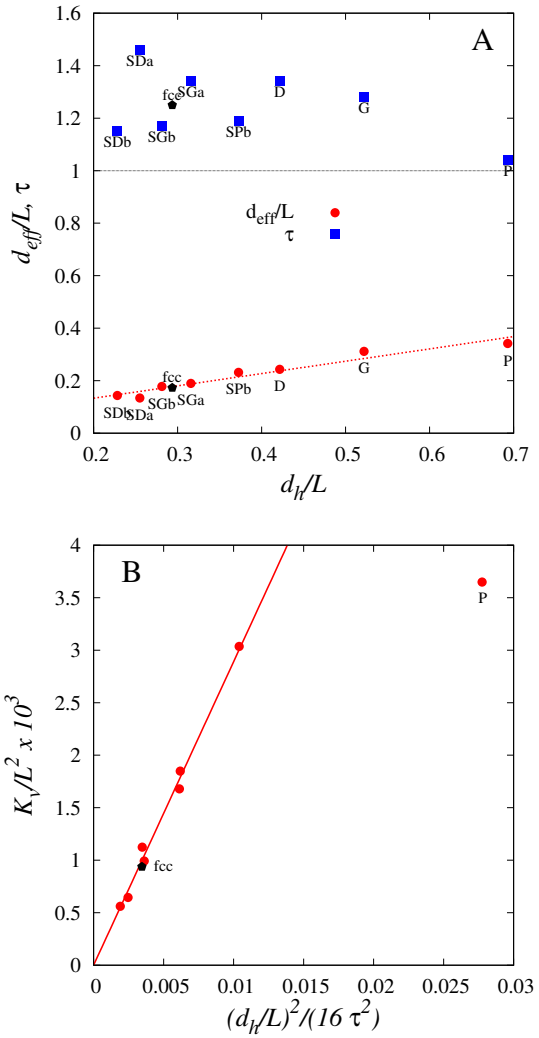


Figure 8.7: A) d_{eff}/L and τ vs d_h/L for alle the geometries investigated, including the fcc array of spheres (black pentagon). B) Validity of the Carman-Kozeny equation Eq. (8.32). The slope of the straight line is $1/K_0$ with $K_0 = 3.46$.

and P, in the non-retentive case, may be determined by their respective flow tortuosity (and hence extent of transverse flow), with higher tortuosity correlated with lower reduced plate height. However, this hypothesis, preliminarily confirmed by the analysis limited to the strut-based TPMS structures, is instead contradicted by the overall analysis of all the geometries considered, including the fcc array of spheres. Indeed, an increase in tortuosity does not necessarily imply a decrease in h_{min}. Two examples are illustrative: the Diamond (D) and Sheet-Gyroid of type a (SGa) are characterized by very close values of tortuosity , but $h_{min,SGa}$ is almost three times larger than $h_{min,D}$; the tortuosity of the fcc array of spheres is very close to that of the Gyroid, but $h_{min,fcc}$ is almost four times smaller than $h_{min,G}$. A review of all the minimum values h_{min} as a function of the tortuosity τ for all the geometries investigated is reported in Figure 8.10(**A**).

Indeed, also Dolamore at al. [201] observed the contradictory results that an increase of the porosity, and henceforth a decrease of the tortuosity, led to a lower reduced plate height

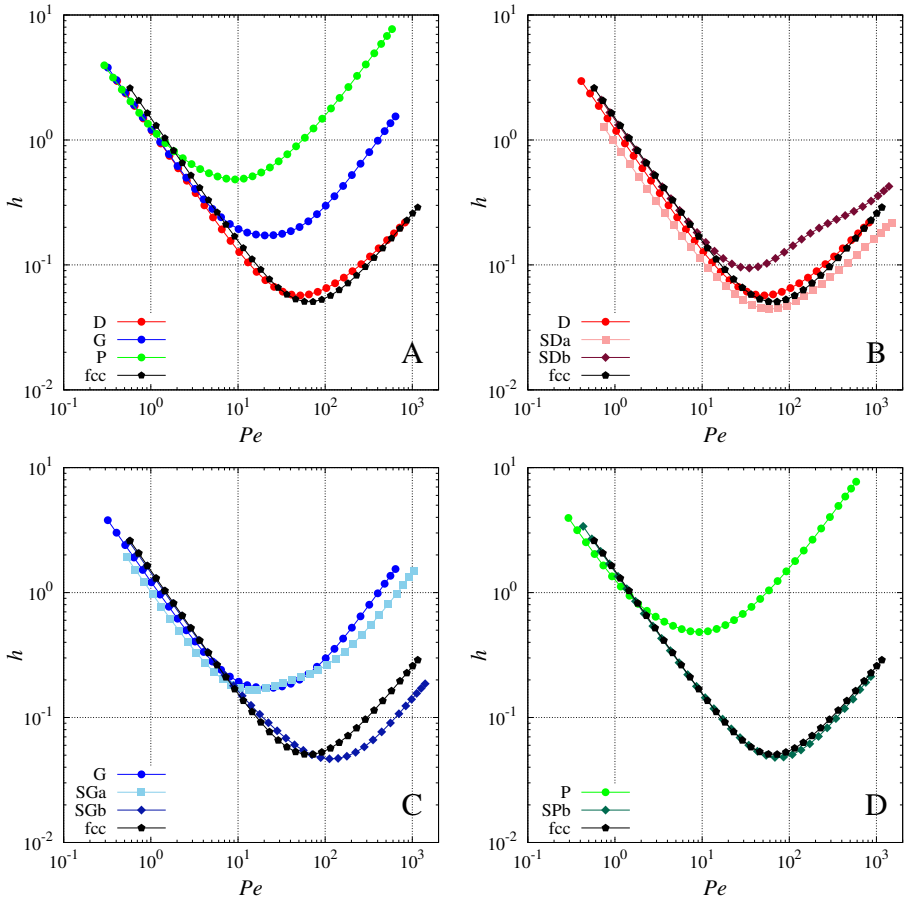


Figure 8.8: Numerical results for the reduced plate height curves $h = H/L$ vs $Pe = U_i L/D_m$ for all the geometries investigated in the non retentive case. A) Strut-based geometries G,D,P; B) Diamond based geometries D, SDa, SDb; C) Gyroid based geometries G, SGa, SGb; D) Primitive based geometries P, SPb. Black points refer to the fcc array of spheres (fcc).

and concluded that there is a complex interplay between geometry, tortuosity and porosity that is yet to be determined for ordered monolithic structures.

Another more specific measure of the transverse flow is the x component of the vorticity σ as defined in Eq. (8.30), but even the data of h_{min} vs σ, reported in Figure 8.10(**B**), do not show a well-defined trend that can confirm an exclusive dependence of h_{min} on the intensity of the transverse velocity field, if we assume that σ can be a reasonable measure of it.

Schure et al. [23], while investigating ordered and random packed beds of spheres at the close-packing limit, suggested that one possible factor contributing to the hydrodynamic separation performance is the distribution of axial velocities. Indeed they observed that the normalized axial velocity probability densities $pdf(v_x/U_i)$ in the low velocity region are inversely related to the efficiencies. They concluded that the random packing (RP) is more efficient than sc (simple cubic) and bcc (body centered cubic) ordered packings because it has fewer small velocities. The fcc packing is more efficient than the RP because it has a smaller range of velocities and lower velocity probability densities in the low velocity region.

We tried to apply the same kind of reasoning to our geometries, with results that support the validity of the approach, while not confirming its generality. In fact, the approach

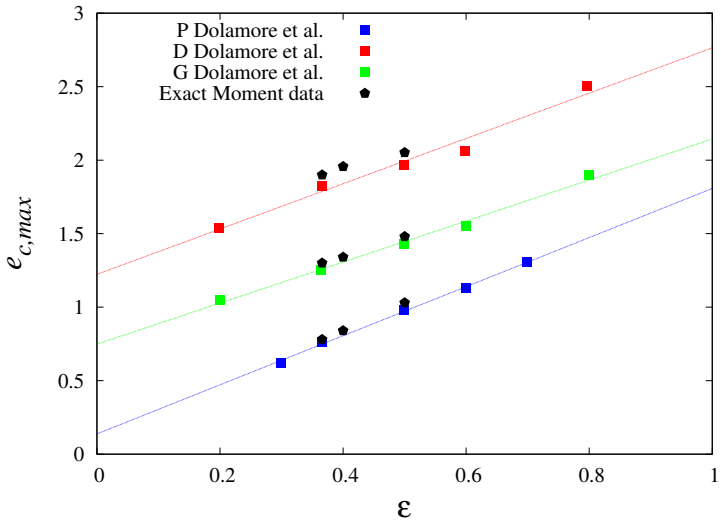


Figure 8.9: Maximum kinetic performance factor $e_{c,max}$ vs ε for the three strut-based geometries G, D and P in the non-retentive case $k'' = 0$. Squares are numerical results by Dolamore et. al. (2022). Black pentagons are numerical results of the present study.

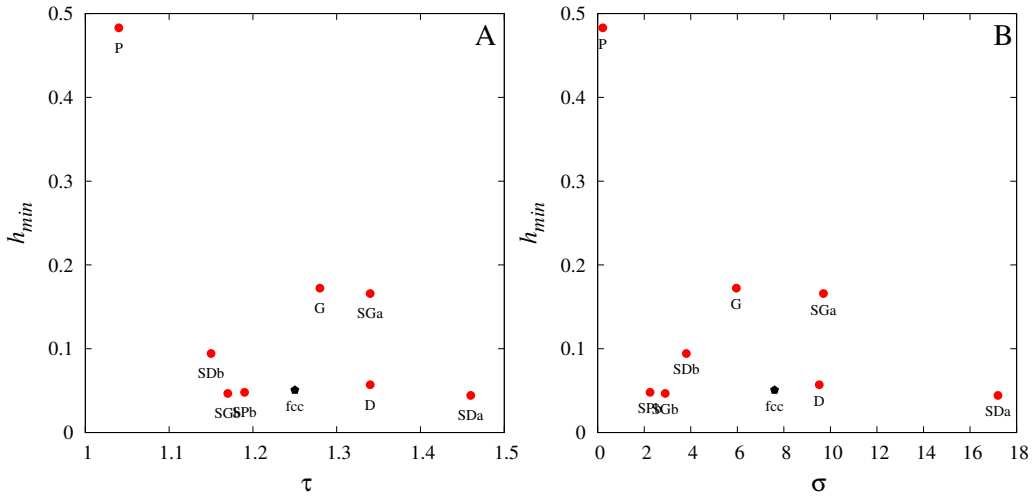


Figure 8.10: h_{min} vs τ (Figure A) and h_{min} vs σ (Figure B) for all the geometries investigated in the non-retentive case, $k'' = 0$, $\varepsilon = 0.4$.

proposed by Shure et al. is able to explain why Diamond, for the same tortuosity, is more efficient than SGa. In fact, the Diamond's axial velocity pdf covers a narrower range of velocities than SGa with a smaller fraction of low velocities, as shown in Figure 8.11A. The comparative analysis of the velocity pdfs of G, SGb and fcc (shown in Figure 8.11 B) suggests that fcc is more efficient than SGb, which in turn is more efficient than G. i.e. fcc>SGb>G. This approach thus explains why the fcc array of spheres, for the same tortuosity, is more efficient than G, but it does not explain why fcc is less efficient than SGb, especially for high values of Pe (see Figure 8.8 C)[1].

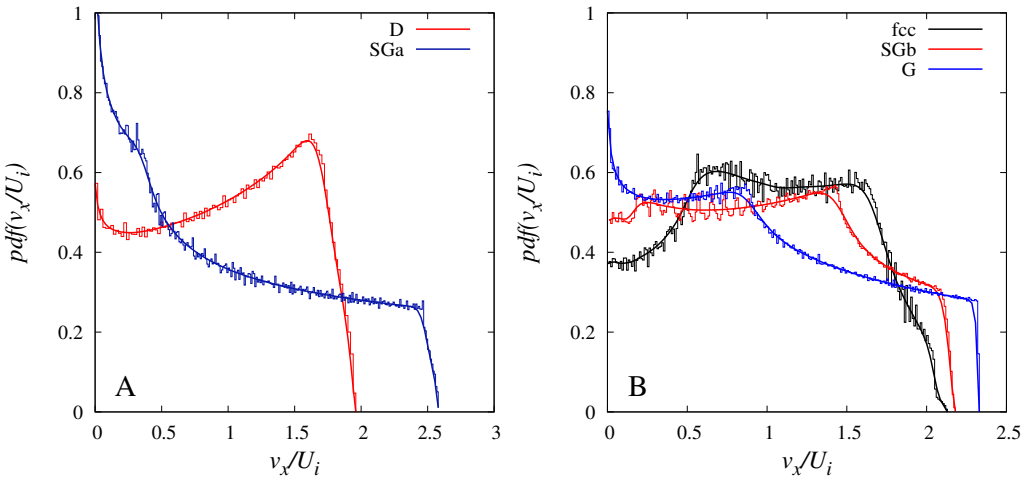


Figure 8.11: Probability density function $pdf(v_x/U_i)$ of the normalized axial velocity field v_x/U_i. A) D vs SGa; B) fcc array of spheres vs SGb and G

Another approach, adopted by both Li et al. [29] and Dolamore et al. [32] in the analysis of bicontinuous ordered packings of different particles (sphere, ellipsoid, octagon), is based on the uniformity factor δ of the axial velocity field and its direct correlation with the separation efficiency. Indeed, dispersion is undoubtedly a phenomenon induced by the spatial variation of the velocity field. Highly non-uniform velocity fields contribute to greater band broadening and inefficient separation. Of all the fluid dynamic quantities, the uniformity factor δ is certainly one of the best suited to rank the minimum height data h_{min} of TPMS geometries. From Table 8.1 it can be observed that the uniformity factor δ spans a wide range of values, from the minimum value $\delta = 0.14$ for the Primitive (P) to the maximum value $\delta = 0.58$ for the Sheet-based Primitive of type b (SPb). All the structures characterised by a sufficiently large value of the uniformity factor, $\delta \geq 0.48$, (e.g. D, fcc, SDa, SGb, Spb) exhibit close and low values of h_{min}, while h_{min} rapidly increases for $\delta < 0.5$, as shown in Figure 8.12. Unfortunately, even this analysis fails to explain why SGa and G have very close values of h_{min} while having very different values of the uniformity factor, namely $\delta_G = 0.44$ and $\delta_{SGa} = 0.35$.

[1]The normalized axial velocity pdfs are obtained by sampling the velocity field on an equally spaced grid of 3200000 points belonging to the mobile phase Ω_m. In this way, the resulting probability density curves are unaffected by the non-uniformity of the tetrahedral mesh used for the numerical solution of the velocity field and b-fields.

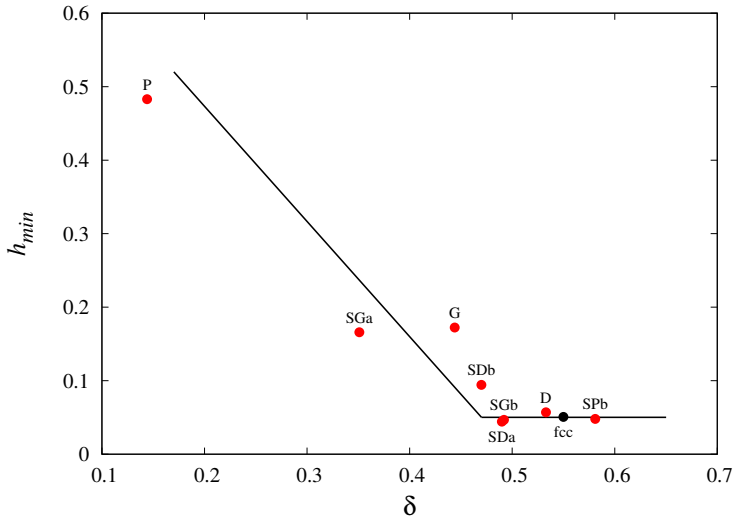


Figure 8.12: h_{min} vs δ for all the geometries investigated in the non-retentive case, $k'' = 0$, $\varepsilon = 0.4$.

We think that it is not possible to identify a single geometric or fluid-dynamic parameter (or a combination of them) that can explain, with no exceptions, the ordering of hydrodynamic dispersion data because the dispersion coefficient depends on the complex structure of the velocity field and of the resulting b-field in the mobile phase which must be analyzed on a case-by-case basis. One strategy that can be pursued consists in analyzing in detail the structure of the velocity field, keeping in mind that (i) large gradients of the velocity field correspond to large gradients of the b_m field and that (ii) the dispersion coefficient D^x, according to Eq. (2), is proportional to the square of the norm of the b-field gradient. Figures 8.13 A-B show the velocity fields of the Gyroid (G) and Diamond (D) in some representative yz sections. The colours indicate the normalized velocity magnitude $I = \sqrt{v_x^2 + v_y^2 + v_z^2}/U_i$, while the surfaces are proportional to the normalized velocity vector $(v_x, v_y, v_z)/U_i$. Figures 8.13 C-D show the b-field b_m at $Pe = 100$ in the same yz sections where the velocity field is plotted. It can be observed that the regions characterized by large velocity gradients correspond to the regions with large gradients of the b-field. Unlike the Gyroid, the Diamond (D) works like a split-and-recombine device with large regions characterized by a flat velocity profile, and in these same regions the b-field b_m also shows a flat profile with small gradients. This explains why the axial dispersion coefficient D^x of the Diamond is significantly lower than that of the Gyroid.

Proceeding in the same way and analyzing the structure of the velocity profiles of the SDb, SGb and SPb geometries (shown in Figure 8.14A-C), we can predict that the axial dispersion coefficient D^x of SDb will certainly be larger than that of SPb and SGb. In fact, the velocity profile of SDb (Figure 8.14A) presents a wavy trend that is reflected in the strongly wavy behavior of the b-field (Figure 8.14D), which in turn involves large gradients. On the contrary, both SGb and SPb present a much more regular shape of the velocity field (Figure 8.14 B-C) which corresponds to much flatter profiles of the b_m field (Figure 8.14E-F), with a consequent decrease of the dispersion coefficient and therefore of the hetp curves.

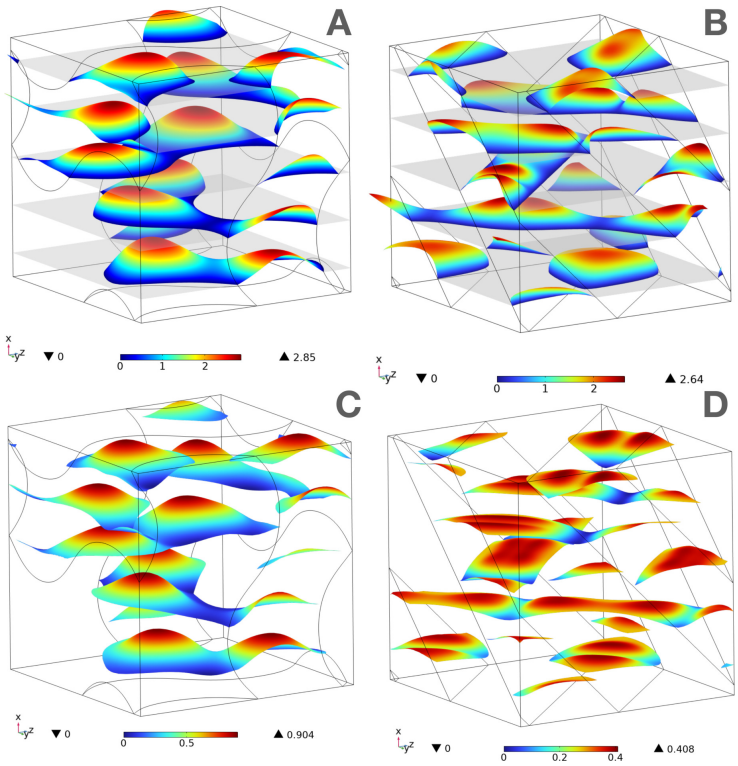


Figure 8.13: Velocity magnitude I (A-B) and b_m field at $Pe = 100$ (C-D) of Gyroid (A,C) and Diamond (B,D) in few representative yz cross-sections. The surface of the velocity field is obtained by applying a deformation along (x, y, z) proportional to $(v_x/U_i, v_y/U_i, v_z/U_i)$, respectively. The scaling factor is the same for all the geometries, in order to make the figures corresponding to different geometries quantitatively comparable. The surface of the b_m field is obtained by applying a deformation along (x, y, z) proportional to $(b, 0, 0)$, respectively. The scaling factor is the same for all the geometries, in order to make the figures corresponding to different geometries quantitatively comparable.

Analyzing the structure of velocity fields in detail, it can be observed that some geometries, namely G, SGa and SDb, despite the complex structure of the stationary phase, exhibit the peculiar feature of having high velocity flow tubes connecting the mobile phase in the axial direction from side to side ($x = 0, L$). The presence of these flow tubes is highlighted in the figures 8.15 A-C in which the gray surface identifies the set of points characterized by an axial velocity $v_x \geq 0.85\, v_{x,max}$ and the arrows show the velocity field on the surface, essentially tangent to the surface itself, supporting the fact that high axial velocity flow tubes exist. In the case of the SDb geometry, there is also evidence of straight streamlines connecting the moving phase from side to side.

The resulting channeling phenomenon, which certainly also and especially characterizes the Primitive (P) as clearly shown in Figure 8.4 C, is undoubtedly responsible for the low separation efficiency that characterizes these geometries compared with the other TPMS structures analyzed. Indeed, all geometries characterized by a low value of d_{eff}/L, and thus characterized by small cross-sectional (transverse) diffusional lengths, exhibit very low values of both h_{min} and h_{500}, i.e. h at $Pe = 500$, this value taken as representative of the behavior on the convection-controlled branch of the hetp curve, as shown in Figure 8.16

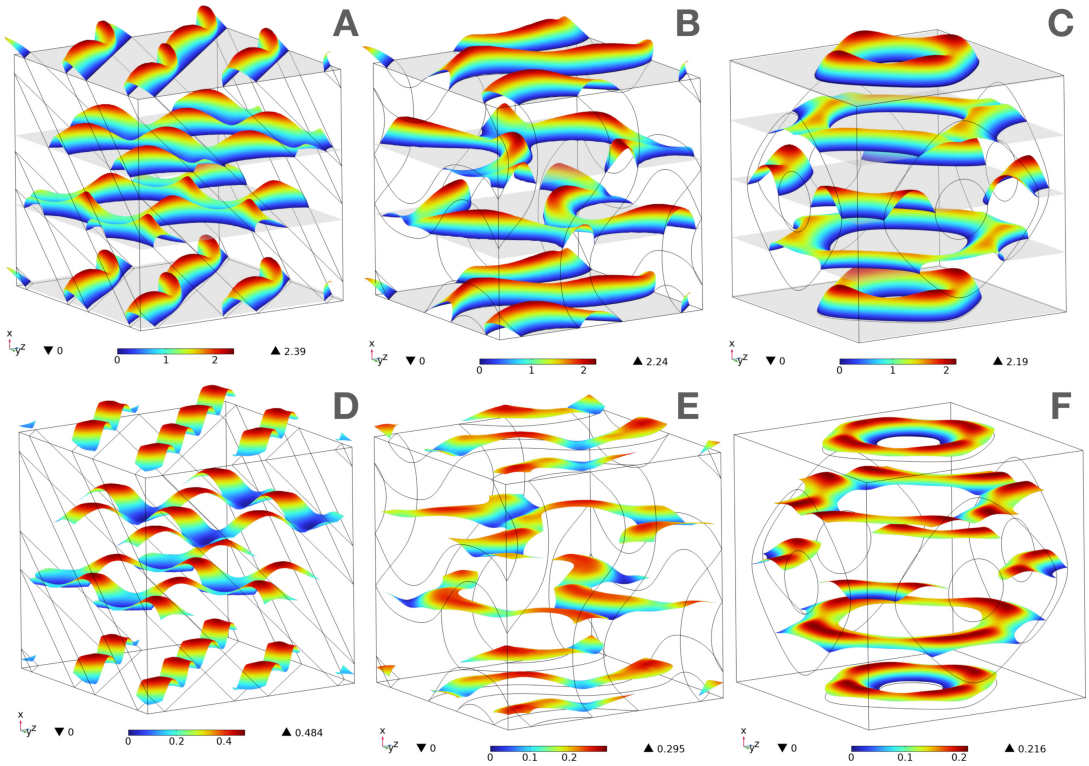


Figure 8.14: Velocity magnitude I (A-C) and b_m field at $Pe = 100$ (C-E) of SDb (A,D), SGb (B,E) and SPb (C,F) in few representative yz cross-sections.

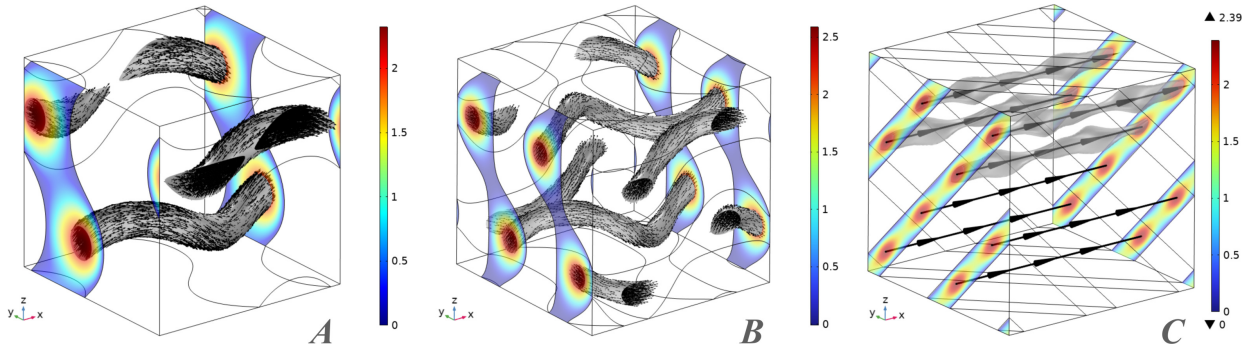


Figure 8.15: High velocity flow tubes $v_x \geq 0.85\, v_{x,max}$ for G (panel A), SGa (panel B) and SDb (panel C). The color plot shows the normalized axial velocity field v_x/U_i at the inlet/outlet cross-sections of the unit cell.

A-B. Exceptions are SGa and SDb geometries due to the channeling phenomenon. G and P structures are the worst in terms of separation efficiency both because they are characterized by a high value of the effective diameter d_{eff}/L and because they exhibit the phenomenon of channeling.

8.2.5 Dispersion with superficial retention

In the retentive case, analyte molecules are adsorbed on the surface $\partial\Omega_s$ of the stationary phase Ω_s. A practical example would be the case of a non-porous silica backbone grafted with a monolayer of C18 molecules acting as the stationary phase (RPLC), or grafted with

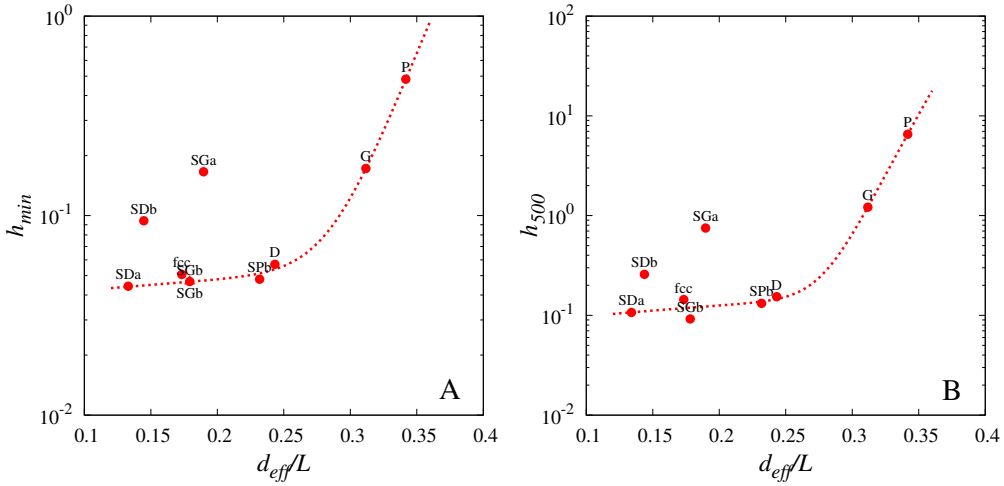


Figure 8.16: h_{min} vs d_{eff}/L (panel A) and h_{500} vs d_{eff}/L (panel B) for all the geometries investigated. The dashed fitting curve has been added to make a better link with the results in the retained case, Figure 8.27.

a monolayer of amino moieties (HILIC) or even the naked silica material itself (unbonded HILIC).

Figures 8.26 A-D show the reduced plate height curves h vs $Pe = U_i L/D_m$ (also referred to as reduced velocity)

$$h = \frac{H}{L} = \frac{2D^x(1+k'')}{U_i L} = \frac{2(D^x/D_m)(1+k'')}{Pe} \tag{8.33}$$

in the retentive case ($k'' > 0$) for the strut-based geometries G,D, and P (Figure 8.26A), for the Diamonds D, SDa and SDb (Figure 8.26B), the Gyroids G, SGa and SGb (Figure 8.26C) and the Primitives P and SPb (Figure 8.26D). Different curves correspond to different values of the retention factor $k'' = 1, 4, 16$, and therefore to a different effective velocity $U^x = U_i/(1+k'')$ and distribution of the solute between the mobile and stationary phase. In fact, the fraction of particles in the mobile phase m_m is $m_m = 1/(1+k'')$, while $m_s = 1 - m_m = k''/(1+k'')$ represents the fraction of solute in the adsorbed phase.

From the hetp curves shown in Figure 8.26, it is possible to estimate the minimum value h_{min}, the corresponding value Pe_{min} and the value h_{100} of h at $Pe = 100$. These three data can be used to characterize the hetp curve of each of the considered geometries. Numerical data for h_{min} and h_{100} of all the geometries are reviewed in Figures 8.27 A-B where they are plotted as a function of the dimensionless effective diameter d_{eff}/L for the three k'' values investigated.

The h_{min} and h_{100} data in the retentive case exhibit a well defined linear behaviour as a function of d_{eff} for all the geometries characterized by a low/intermediate value of d_{eff}, with the exception of SGa geometry for which the channeling effect plays a dominant role even in the presence of surface retention. The results shown in Figures 8.27 A-B can be explained by considering that the role of the adsorptive boundary condition Eq. (8.25) is to increase

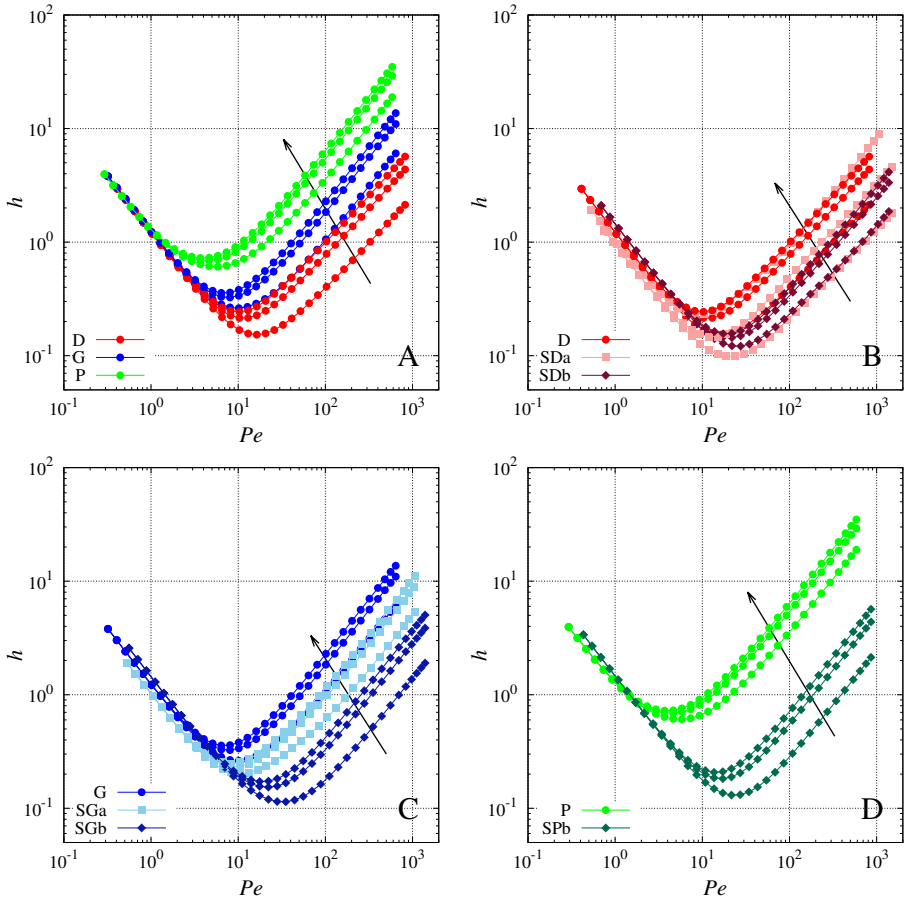


Figure 8.17: Numerical results for the reduced plate height curves $h = H/L$ vs $Pe = U_i L/D_m$ for all the geometries investigated in the retentive case. A) Strut-based geometries G,D,P; B) Diamond based geometries D, SDa, SDb; C) Gyroid based geometries G, SGa, SGb; D) Diamond based geometries P, SPb. Arrows indicate increasing values of the zone retention factor $k'' = 1, 4, 16$.

dispersion. By observing that the boundary condition Eq. (8.25) can be rewritten as

$$-D_m(\nabla b - \mathbf{e}_x) \cdot \mathbf{n}\Big|_{\partial\Omega_s} = U_i \frac{k''}{1+k''} \frac{d_h}{4} \tag{8.34}$$

we can understand that the axial dispersion coefficient increases with k'' and with the hydraulic diameter, which in turn increases with the effective diameter d_{eff}. In the retentive case, the best performing geometries are SDb, SDa and SGb, having the lowest values of d_{eff}.

Another interesting observation is that lower values of h_{min} correspond to higher values of Pe_{min}, as highlighted in Figure 8.28 showing the behaviour h_{min} vs Pe_{min}. More precisely, it can be observed that h_{min} is inversely proportional to Pe_{min}, i.e. $h_{min} = \beta/Pe_{min}$, with a prefactor β that depends on the geometry and is independent of k''. This finding is not surprising if one considers that the behaviour of the rescaled hetp curve h vs Pe can be approximated, for low-intermediate values of Pe including the minimum region, as

$$h = \frac{2}{Pe}\frac{\gamma_{eff}}{\widetilde{U}^x} + 2Pe\frac{\delta}{\widetilde{U}^x}, \quad \widetilde{U}^x = \frac{U^x}{U_i} = \frac{1}{1+k''} \tag{8.35}$$

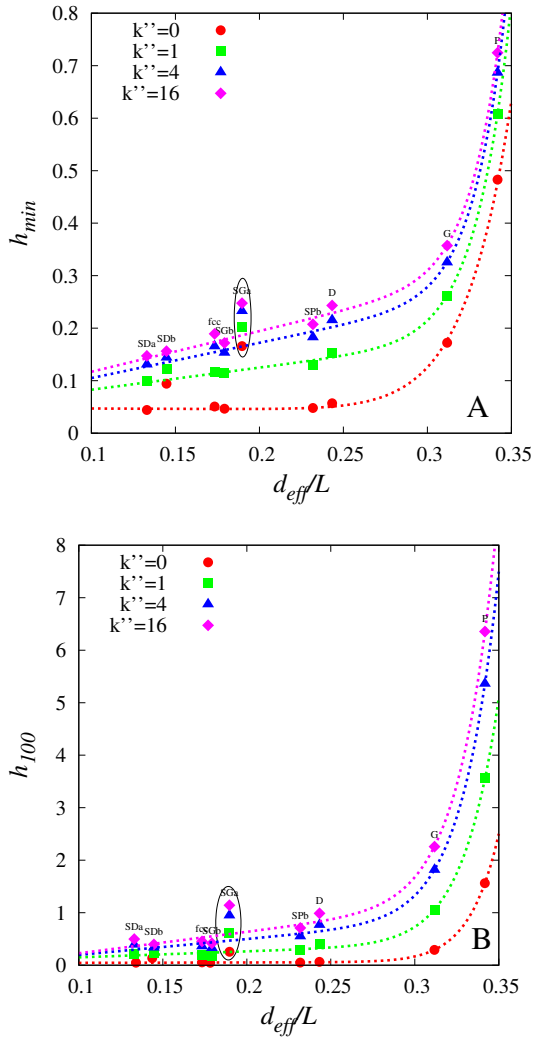


Figure 8.18: h_{min} vs d_{eff}/L (panel A) and h_{100} vs vs d_{eff}/L (panel B) for alle the geometries investigated.

where γ_{eff} (the effective axial diffusion coefficient, i.e. D^x/D_m at $Pe = 0$) and δ are quantities that depend on the geometry and the retention factor k''. By enforcing the minimum condition $dh/dPe = 0$ at $Pe = Pe_{min}$, one obtains $Pe_{min} = \sqrt{\gamma_{eff}/\delta}$ and the product $(h \times Pe)$ at the minimum (h_{min}, Pe_{min}) attains the form

$$h_{min}Pe_{min} = 2\frac{\gamma_{eff}}{\widetilde{U}^x} + 2Pe_{min}^2\frac{\delta}{\widetilde{U}^x} = 4\frac{\gamma_{eff}}{\widetilde{U}^x} = 4\gamma_{eff}(1 + k'') \tag{8.36}$$

By further observing that, in the presence of superficial adsorpion (and no surface diffusion)

$$\gamma_{eff} = \frac{\gamma_m^0}{1 + k''} \tag{8.37}$$

where γ_m^0 is the obstruction factor for longitudinal diffusion in the mobile phase, one obtains

$$h_{min}Pe_{min} = 4\gamma_m^0 \tag{8.38}$$

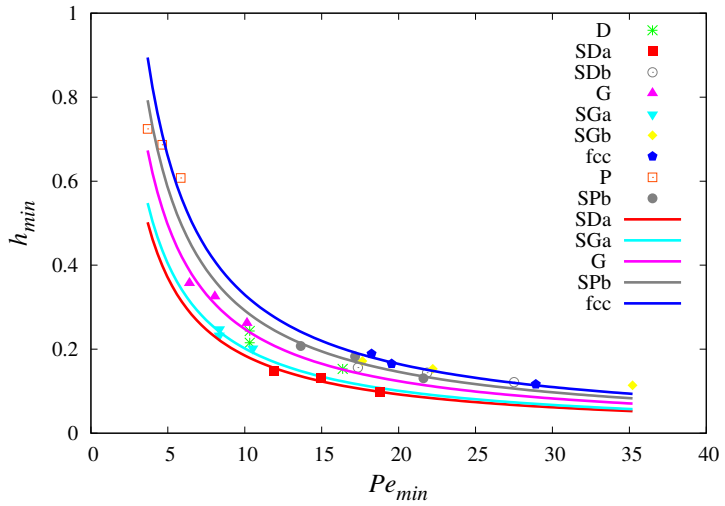


Figure 8.19: h_{min} vs Pe_{min} for all the geometries and for the three values $k'' = 1, 4, 16$ of the retention factor. Continuous lines show the predictions for SDa, SGa, G, fcc, SPb based on Eq. (8.38) with γ_m^0 values reported in Table 8.2

Figure 8.28 shows the behaviour of h_{min} vs Pe_{min} for the three values of k'' and for all the geometries investigated. Continuous lines shows the predictions for SDa, SGa, G, fcc, SPb based on Eq. (8.38). The value of the obstruction factor γ_m^0 for all geometries is reported in Table 8.2.

Table 8.2: Obstruction factor γ_m^0 for all the geometries.

	G	**D**	**P**	**SGa**	**SDa**	**SGb**	**SDb**	**SPb**	**fcc**
γ_m^0	0.609	0.606	0.572	0.502	0.471	0.716	0.720	0.728	0.750

8.2.6 Kinetic performance of TPMS structures

Separation impedance SI is a dimensionless parameter [248] used to characterize the efficiency of a chromatographic media in terms of its resistance to fluid flow and the time required for separation. It is defined as the inverse of the time and pressure drop across a single theoretical plate during a separation, normalized by the viscosity of the mobile phase and the retention time of the analyte. Written in terms of the plate height h and equivalent diameter d_{eff}, SI attains the form

$$SI = 32h_c^2, \quad h_c = H/d_{eff} \tag{8.39}$$

where h_c is referred to as *universal plate height* [246]. The separation impedance provides insight into the overall performance of a chromatographic system, with lower values indicating a more efficient medium that offers lower resistance to flow, faster separation times, and

potentially higher resolution.
Strictly related to SI, the kinetic performance factor e_c

$$e_c = 1/\sqrt{h_c} \tag{8.40}$$

was introduced by Blumberg and Desmet [246] in order to compare different chromatographic system on a linear scale. Indeed, e_c is a more practical, rescaled version of separation impedance that is easier to apply for comparing real-world chromatographic systems. It is proportional to the peak capacity of a system, allowing a straightforward comparison of chromatographic performance. Figures 8.20show the universal plate height curves h_c vs $Pe_m = U_i d_{eff}/D_m$ for all the geometries and for the three k'' values analyzed. The analysis of

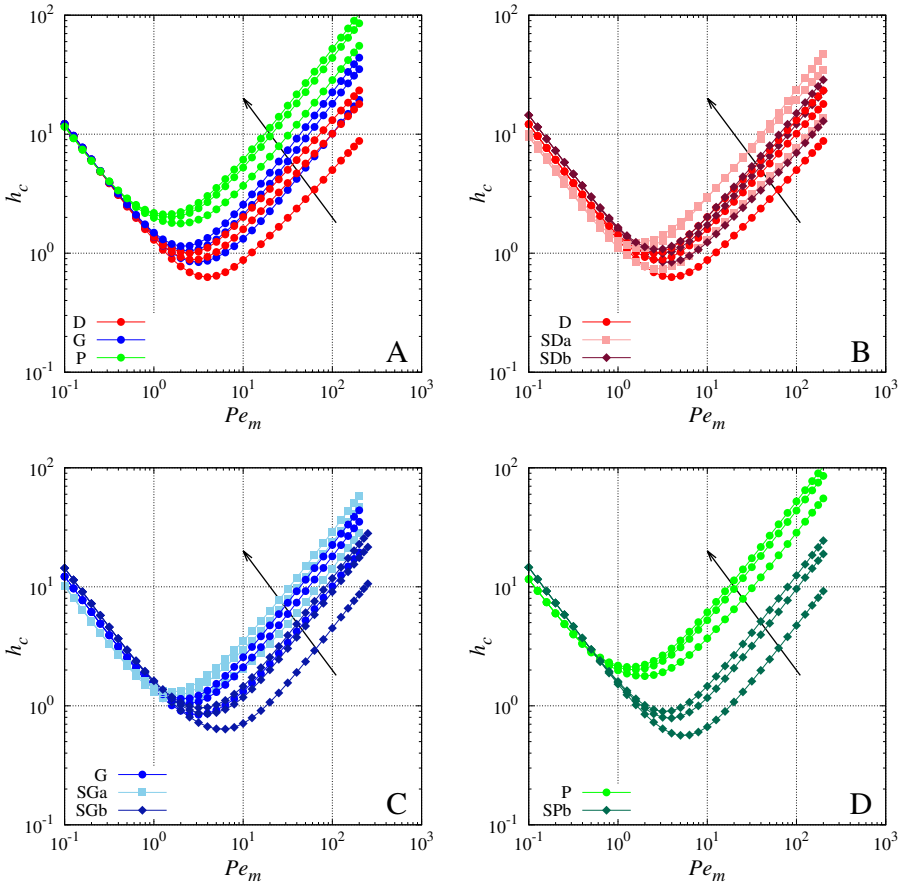


Figure 8.20: Universal plate height curves $h_c = H/d_{eff}$ vs $Pe_m = U_i d_{eff}/D_m$ for all the geometries investigated in the retentive case. Arrows indicate increasing values of $k'' = 1, 4, 16$. A) Strut-based geometries G,D,P; B) Diamond based geometries D, SDa, SDb; C) Gyroid based geometries G, SGa, SGb; D) Primitive based geometries P, SPb.

the universal plate height curves is summarized in Figure 8.29 A, which reports the maximum value of the kinetic performance factor $e_{c,max} = 1/\sqrt{h_{c,min}}$ for $k'' = 1, 4, 16$ for all geometries.

The best performing geometries in terms of $e_{c,max}$ are SPb, D and SGb for all the three k'' values. We come to the same result if we compare the different geometries at the same

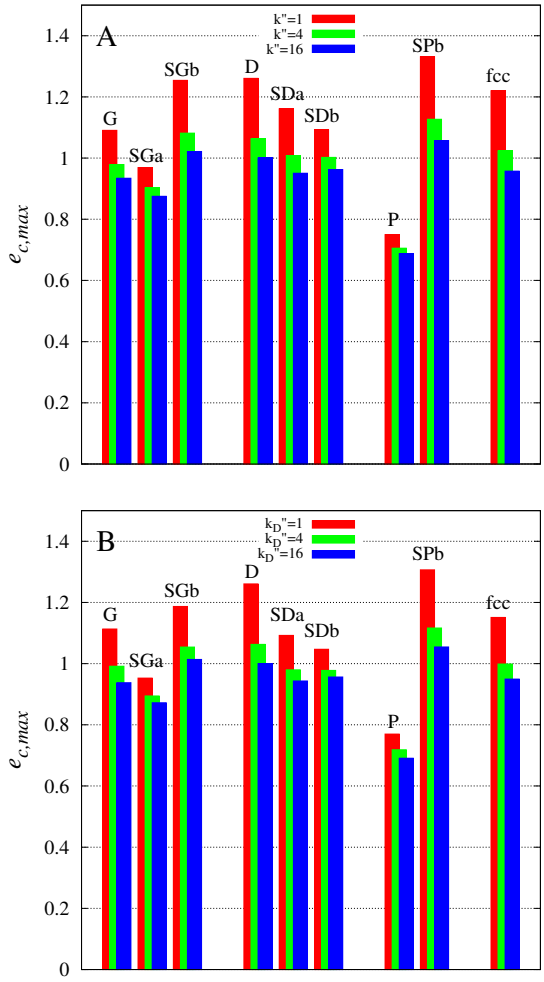


Figure 8.21: $e_{c,max}$ for different geometries investigated. (A) $k'' = 1, 4, 16$. (B) $k''_D = 1, 4, 16$.

equilibrium constant K_{eq} instead of at the same retention factor k'', as shown in Figure 8.29 B. The two analyses might differ in that different geometries have different surface areas[2]. The three K_{eq} values considered are $K_{eq}/L = 0.105, 0.422, 1.686$, to which correspond $k''_D = 1, 4, 16$ for the strut Diamond taken as reference. The SPb and SGb geometries are characterized by lower tortuosity τ (promoting a high permeability) and a high value of the homogeneity factor δ (promoting a low h_{min}). Diamond D also has a high value of δ and a significant contribution of transversal mixing associated with a very high value of the parameter σ. It must be further observed that also the fcc array of sphere, although is not 3D printable at the investigated porosity $\varepsilon = 0.4$, is overall performing very well (only D, SGb and SPb are better).

The analysis based on the kinetic performance factor $e_{c,max}$ can be complemented by the analysis of the kinetic plots [249–251] t_0/N^2 vs N

$$\frac{t_0}{N^2} = \frac{\eta}{\Delta P_{max}} \frac{h^2}{K_v}, \quad N = \frac{\Delta P_{max}}{\eta} \frac{K_v}{U_i H} \tag{8.41}$$

[2]Please note that the case of a constant K_{eq} corresponds to the relative retention experienced when all structures would be coated with the same stationary phase and used with the same mobile phase.

where t_0 is the column void time and N the plate number. Kinetic plots play a key role in the analysis/comparison of the separation performance of TPMS structures because they explicitly account for the length L of the unit cell. The length L cannot be less than a minimum size L_{min} controlled by the resolution of 3D printers currently available on the market. Even the most cutting-edge 3D printers, based on the two-photon polymerization technique, having minimum feature size order of hundreds of nanometers [198], allow to 3D print TPMS geometries with a sufficient level of accuracy only if $L \geq L_{min} \simeq 2\mu m$ [197]. Figure 8.32 shows the kinetic plots for $k'' = 4$ for all the geometries with the same length $L = L_{min} = 2\mu m$ and fixed values of $\eta = 5 \times 10^{-4}$ [Pa s], $D_m = 1 \times 10^{-9}$ [m^2/s] and $\Delta P_{max} = 500$ [bar]. Kinetic plots for $k'' = 1$ and $k'' = 16$ are shown in Figure 8.23 A-B.

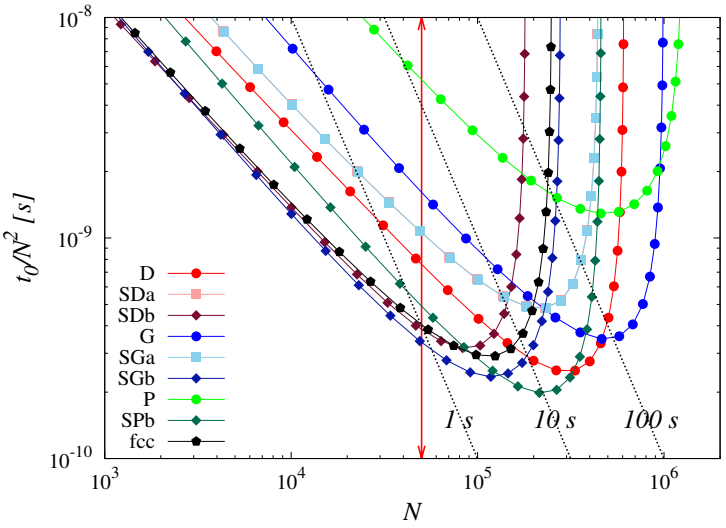


Figure 8.22: t_0/N^2 vs N of all the TPMS geometries and the fcc array of spheres for the same unit cell dimension $L = 2$ [μm] and $k'' = 4$. $\Delta P_{max} = 500$ [bar], $\eta = 5 \times 10^{-4}$ [Pa s], $D_m = 1 \times 10^{-9}$ [m^2/s]. The vertical red line indicates $N = N_{req}$

The red vertical line indicates, as an example, a given required plate number N_{req}. set to $N_{req} = 50000$. It can be observed that the minimum of all the curves lies on the right of the vertical line $N = N_{req}$. This implies that it would be necessary, for all geometries, to decrease the dimension L below L_{min} in order to operate in optimal conditions which are achieved when the minimum of the curve t_0/N^2 vs N is positioned exactly in $N = N_{req}$. Indeed, the optimal value of N for each geometry, that is, the value N_{opt} at which the kinetic plot exhibits the minimum, can be predicted by observing that N_{opt} can be rewritten as

$$N_{opt} = \frac{\Delta P_{max}}{\eta D_m} \frac{K_v}{Pe_{min} h_{min}} \tag{8.42}$$

By further enforcing Eq. (8.38) one obtains

$$N_{opt} = \frac{\Delta P_{max}}{\eta D_m} \left(\frac{K_v / L^2}{4\gamma_m^0} \right) L^2 = \frac{\Delta P_{max}}{\eta D_m} \theta L^2 \tag{8.43}$$

Equation (8.55) clearly indicates that N_{opt} is (i) independent of the retention factor k'', (ii)

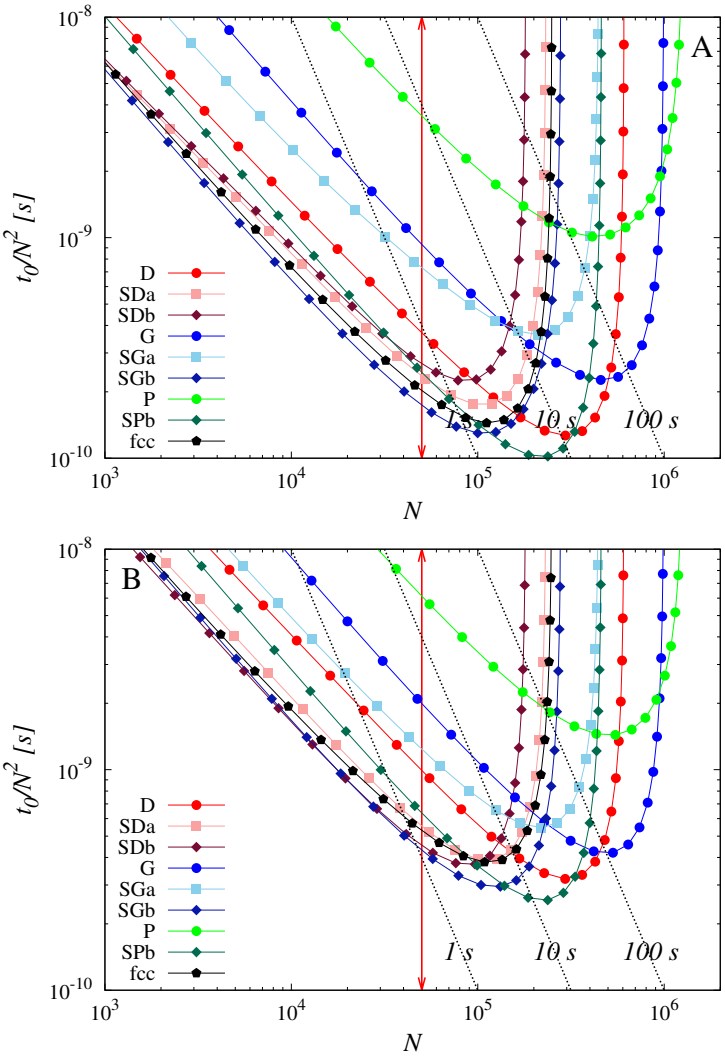


Figure 8.23: t_0/N^2 vs N of all the TPMS geometries and the fcc array of spheres for the same unit-cell dimension $L = 2$ μm and $k'' = 1$ (panel A) and $k'' = 16$ (panel B). $\Delta P_{max} = 500$ bar, $\eta = 5 \times 10^{-4}$ Pa s, $D_m = 1 \times 10^{-9}$ m^2/s. The vertical red line indicates $N = N_{req} = 50000$.

directly proportional to the dimensionless parameter $\theta = K_v/(4L^2\gamma_m^0)$ characterizing each geometry and (iii) proportional to the square of the length L of the unit cell. Among all geometries, the one with the minimum value of θ is SDb, to which corresponds a minimum value of $N_{opt} \simeq 10^5$ for $L = 2\mu m$. Since the lower value of N_{opt} is significantly higher than N_{req} for $L = L_{min}$ but it is not possible to decrease the size L below L_{min}, we set $L = L_{min}$ for all structures, and estimate the column void time t_0 [s] for $N = N_{req}$. Results for t_0 at N_{req} are reported in Table 8.3 and Figure 8.24.

The geometries characterized by the lowest void time t_0 are SGb, SDb and SPb. Also the fcc array of sphere is performing about as well as SGb and SDb. We can conclude that, among all the geometries, SGb and SPb are the ones with the best performance, both in terms of maximum kinetic performance factor $e_{c,max}$ and in terms of void time t_0.

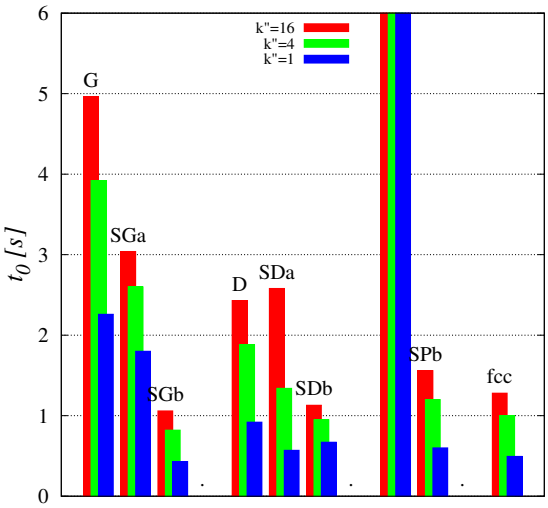


Figure 8.24: t_0 [s] for $N = N_{req} = 50000$ for all the TPMS geometries and the fcc array of spheres for $L = L_{min} = 2\mu m$. $\Delta P_{max} = 500$ [bar], $\eta = 5 \times 10^{-4}$ [Pa s], $D_m = 1 \times 10^{-9}$ [m^2/s]. Results for the Primitive (P) are out of range.

Table 8.3: Column void time t_0 [s] for $N = N_{req} = 50000$, $L = L_{min} = 2$ μm, $\Delta P_{max} = 500$ [bar], $\eta = 5 \times 10^{-4}$ [Pa·s], $D_m = 1 \times 10^{-9}$ [m^2/s], for all the geometries and three values of k''.

t_0[s]	**G**	**D**	**P**	**SGa**	**SDa**	**SGb**	**SDb**	**SPb**	**fcc**
$k'' = 1$	2.26	0.92	8.87	1.81	0.57	0.43	0.67	0.62	0.49
$k'' = 4$	3.92	1.88	12.4	2.61	1.34	0.82	0.95	1.21	1.05
$k'' = 16$	4.96	2.43	14.9	3.04	2.58	1.06	1.13	1.56	1.28

8.3 The mesoporous case

This Section reports a numerical study of the separation performance of eight different 3D printable mesoporous stationary phases based on triply periodic minimal surfaces. TPMS-based stationary phases have already been proposed as very promising geometries [200, 201]. However, the analysis by Dolamore et al. [201] was limited to the study of chromatographic performance under purely hydrodynamic conditions, i.e., in the non-retentive case. The previous Section 8.2 presents an investigation, conducted as part of the present thesis, of the separation performance of the same eight TPMS geometries analyzed in this paper, but limited to the non-retentive and superficially retentive case. Results can be summarized as follows: (1) the Carman-Kozeny relationship between permeability K_v, hydraulic diameter d_h and hydrodynamic tortuosity τ holds true for all the geometries with a unique shape coefficient K_0; (2) the analysis of plate height curves reveals that the best-performing geometries, in both non-retentive and superficially retentive conditions, are associated with smaller effective diameters $d_{eff} = \sqrt{32K_v}$, leading to lower permeability values—except in cases where significant channeling effects occur; (3) when comparing kinetic performances,

the best geometries are characterized by lower tortuosity and a higher coefficient of uniformity in the axial velocity field; (4) the kinetic plot analysis shows that none of the geometries investigated can operate at optimal conditions, as achieving this goal would require reducing the unit cell dimension L below the limits imposed by the minimum feature size of current 3D printing technologies.

A completely different scenario appears when the stationary phase is assumed mesoporous, so that solute particles have access to the stationary phase where they are free to diffuse with an effective intraparticle diffusivity D_s accounting for hindered diffusion and superficial adsorption, according to a general rate model [232, 238, 252, 253]. The Two Zone Moment Analysis (TZMA) method [202, 254–256] for the determination of the dispersion tensor in hierarchical retentive porous media has been adopted to compute the axial dispersion coefficients, the plate height curves, the kinetic performance factors and the kinetic plots for all the geometries. A comprehensive analysis is presented to evaluate the feasibility of 3D printing TPMS stationary phases, by comparing the ideal unit-cell dimensions with the resolution achievable using the latest 3D printing technologies. The results are encouraging because, unlike what was observed in the superficial retentive case, the analysis of kinetic plots reveals that optimal functioning conditions for mesoporous sheet-based TPMS structures are associated with optimal dimensions of the unit cell compatible with printing resolution of cutting-edge 3D printers.

8.3.1 Theoretical framework

We model the convection-diffusion transport of a single solute within a fluid domain Ω_m in the presence of a mesoporous adsorbing solid phase Ω_s. Let ε represent the external porosity, and ε_{int}, a [m^2/m^3], K_{eq} [m] denote the internal porosity, specific surface area, and equilibrium adsorption constant of the mesoporous stationary zone, respectively. Analyte concentrations are assumed low enough to remain in the linear part of the retention isotherm. In typical biomolecular chromatography experiments, this hypothesis is satisfied because analyte concentrations are mantained sufficiently low relative to the binding capacity of the stationary phase, ensuring operation within the linear adsorption regime. In the conventional biomolecular chromatography experiments, this is satisfied because the concentrations of the analytes are kept well below the binding capacity of the stationary phase [257, 258]. The pressure driven flow field $\mathbf{v}$ of the solvent, laden with the analyte, satisfies the Stokes equation and no-slip boundary conditions on the interface $\partial\Omega_s$ between the mobile and stationary zones. In the macroporous fluid zone, solute transport occurs through both advection and diffusion. The analyte can enter the mesoporous stationary zone, where fluid motion is absent, and transport occurs solely via hindered diffusion in the mesopores, subject to adsorptive boundary conditions.

Let D_m and D_s be the analyte diffusion coefficients in the mobile and stationary zones,

respectively, and k'' the zone retention factor

$$k'' = k_p \frac{V_s}{V_m} = \varepsilon_{\text{int}}(1 + K_{eq}a)\frac{V_s}{V_m} = \varepsilon_{\text{int}}(1 + K_{eq}a)\frac{1-\varepsilon}{\varepsilon} \tag{8.44}$$

where V_m is the volume occupied by the mobile fluid zone Ω_m, V_s the volume occupied by the stationary solid zome Ω_s (including the volume of the mesopores), and k_p the partition coefficient relating the concentrations c_m and c_s in the mobile and stationary zones at the interface $\partial\Omega_s$, i.e. $c_m|_{\partial\Omega_s} = k_p c_s|_{\partial\Omega_s}$.

By adopting the TZMA approach [202, 254–256], the axial dispersion coefficient D^x along the main fluid flow direction x can be estimated in a straightforward way from the b-fields b_m and b_s in the mobile and stationary zone of the periodic unit cell

$$D^x = \frac{D_m + k''\,D_s}{1+k''} + \frac{1}{1+k''}\Big\langle (v_x - U^x)\,b_m - D_m\,\partial_x b_m \Big\rangle_{\Omega_m} + \frac{k''}{1+k''}\Big\langle -U^x b_s - D_s\,\partial_x b_s \Big\rangle_{\Omega_s} \tag{8.45}$$

or equivalently

$$D^x = \frac{D_m}{1+k''}\Big\langle ||\nabla b_m - \mathbf{e}_x||^2 \Big\rangle_{\Omega_m} + \frac{D_s\,k''}{1+k''}\Big\langle ||\nabla b_s - \mathbf{e}_x||^2 \Big\rangle_{\Omega_s} \tag{8.46}$$

where the symbols $\big\langle\,\cdot\,\big\rangle_{\Omega_m}$ and $\big\langle\,\cdot\,\big\rangle_{\Omega_s}$ indicate the spatial average over the mobile and stationary domains, respectively, $||\cdot||$ indicates the vector norm, $\mathbf{e}_x$ the unit vector along along the x axis, and U^x is the effective axial velocity

$$U^x = \frac{U_i}{1+k''}, \quad U_i = \big\langle v_x \big\rangle_{\Omega_m} \tag{8.47}$$

where U_i is the axial interstitial velocity. The b-fields b_m and b_s satisfy the following stationary transport equations and boundary conditions in the unit cell

$$\begin{aligned}
D_m\nabla^2 b_m - \mathbf{v}\cdot\nabla b_m &= (U^x - v_x) && (8.48)\\
D_s\,\nabla^2 b_s &= U^x && (8.49)\\
b_m\big|_{\partial\Omega_s} &= b_s\big|_{\partial\Omega_s} && (8.50)\\
-D_m(\nabla b_m - \mathbf{e}_x)\cdot\mathbf{n}\big|_{\partial\Omega_s} &= k_p[-D_s(\nabla b_s - \mathbf{e}_x)\cdot\mathbf{n}]\big|_{\partial\Omega_s} && (8.51)
\end{aligned}$$

and periodic boundary conditions on the edges of the periodic cell.

It should be noted that the stationary transport equations (8.48)-(8.51) for the b-fields allow for the determination of the asymptotic axial dispersion coefficient D^x, which corresponds to the axial dispersion coefficient under macro-transport conditions that are attained when a sharply defined solute plug injected into the system has begun to move at a constant effective velocity U^x along the main fluid-flow direction x, and has developed a symmetric Gaussian shape with a variance $\sigma^2(t)$ that increases linearly with time as $\sigma^2 = 2\mathscr{D}^x t$. The TZMA method differs from the Brenner-Adler moment approach [236, 237] in that it al-

lows for the estimation of not only the asymptotic values but also the temporal evolution of dispersion properties in spatially periodic porous media. However, both methods yield the same results for the asymptotic quantities U^x and D^x. Indeed, Equations (8.48)-(8.51) coincide with those derived from Brenner and Adler [237], as well as those obtained by Yan et al. [253] using the volume averaging approach. These three approaches offers a key advantage, because they only require solving (i) a steady-state transport problem and (ii) within a single unit cell, rather than solving the time-dependent advection-diffusion equation for the analyte from the initial time to a final time that ensures asymptotic conditions are met, which would necessitate solving the analyte transport equation over many unit cells. Numerical results for the spatially periodic velocity field $\mathbf{v}$ and the spatially periodic b-fields b_m, b_s are obtained through the solution of their respective partial differential equations using Comsol Multiphysics 5.5 that employs the Finite Element Method. The incompressible Navier–Stokes package (Stokes flow) was adopted under stationary conditions, utilizing P2 + P1 Lagrange elements for velocity and pressure, respectively. For the numerical integration of the coupled stationary transport equations of b_m and b_s, the Coefficient Form Partial Differential Equation (PDE) package was utilized with Lagrangian quadratic elements. The MUltifrontal Massively Parallel Sparse direct Solver (MUMPS) linear solver was employed with a relative tolerance of 10^{-6}.

8.3.2 Geometries

Figures 8.25 A-I show the tetrahedral meshes spanning Ω_m and Ω_s in the unit periodic cell (side length L) for all the nine geometries investigated: three strut-based TPMS, namely Schoën Gyroid (G), Schwarz Diamond (D), Schwarz Primitive (P), five sheet-based TPMS, i.e. two Sheet Gyroids SGa and SGb, two Sheet Diamonds SDa and SDb, one Sheet Primitive SPb and the face centred cubic array of spheres (fcc) [240–243, 259]. The fcc array of spheres was chosen as one of the most efficient of all the ordered arrangements of spheres analyzed in the literature. Indeed, several papers [22, 23, 31, 239], although limited to analysis of the purely hydrodynamic non-retentive case, have shown that the fcc array of spheres performs better than the simple cubic (sc), the body centred cubic (bcc) and the random packing (rp) across a wide range of reduced velocities. For all the geometries, the external porosity ε has been set to $\varepsilon = 0.4$. Figure 8.25 also reports the geometric and fluid dynamic parameters, namely the effective diameter $d_{eff} = \sqrt{32K_v}$ (K_v is the interstitial permeability), the hydraulic diameter $d_h = 4V_m/S$ (S is the area of $\partial\Omega_s$) and the fluid dynamic tortuosity $\tau = \langle\sqrt{v_x^2 + v_y^2 + v_z^2}\rangle_{\Omega_m}/U_i$. For a detailed description of how to generate the TPMS geometries at a given porosity, the structure of Ω_m, Ω_s and the velocity field $\mathbf{v}$ in these geometries, the reader is referred to [259]. The complete mesh consists of approximately 2×10^6 domain elements, 2×10^5 boundary elements, and 2×10^3 edge elements for all the geometries. Results are verified to be mesh independent in the whole range of $Pe \in (10^{-1}, 10^3)$ and $k'' \in (0, 20)$ values investigated. Specifically, by halving the number of domain elements from $N1 = 2 \times 10^6$ to $N2 = 1 \times 10^6$, we observed that

$|D^x_{N1} - D^x_{N2}|/D^x_{N1} \leq 5\%\ \forall Pe,\ \forall k''$.

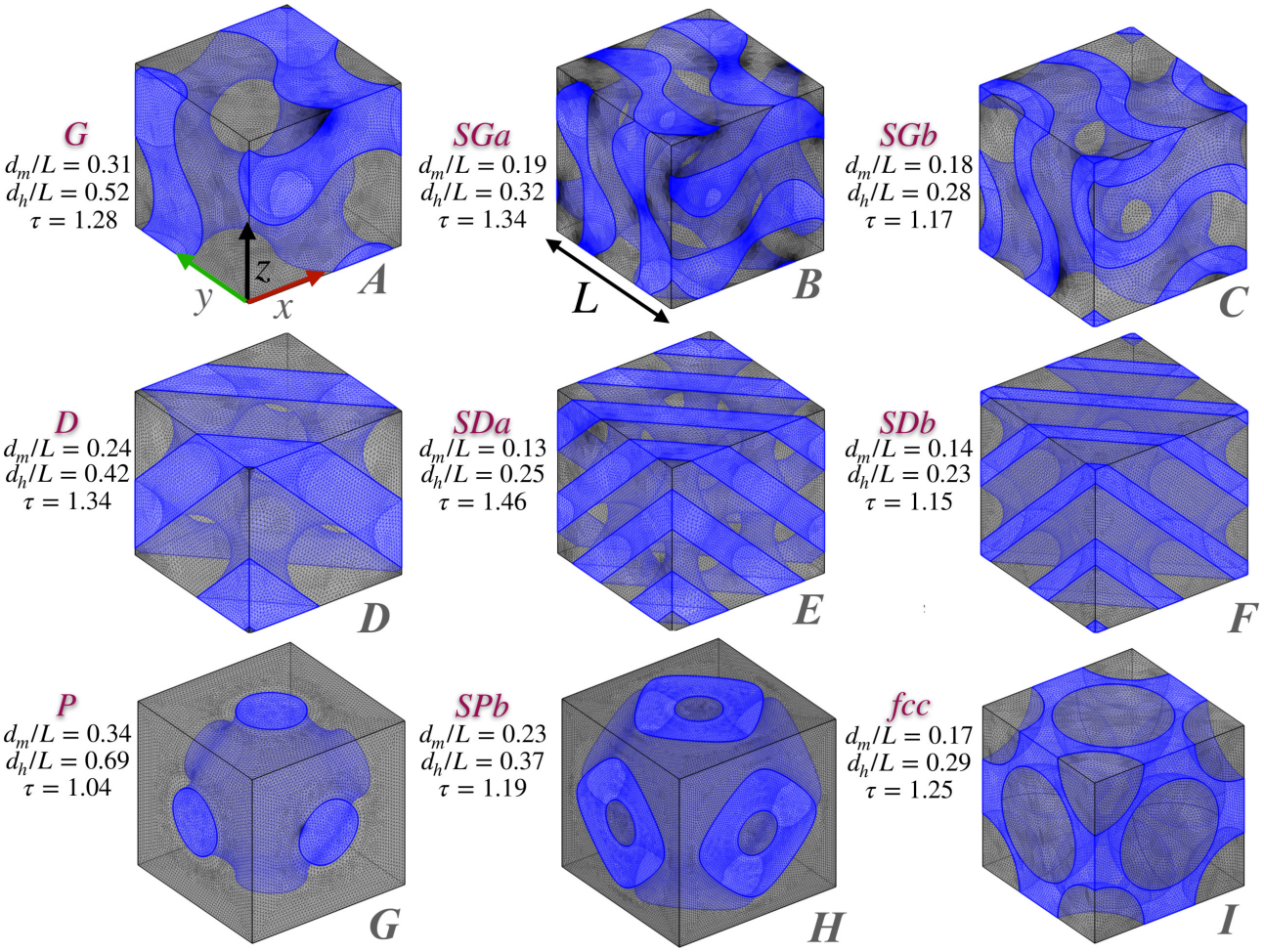


Figure 8.25: Tetrahedral meshes spanning Ω_m (blue) and Ω_s (grey) for all the nine geometries investigated. A) Strut-based Gyroid (G); B) Sheet-based Gyroid of type a (SGa); C) Sheet-based Gyroid of type b (SGb); D) Strut-based Diamond (D); E) Sheet-based Diamond of type a (SDa); F) Sheet-based Diamond of type b (SDb); G) Strut-based Primitive (P); H) Sheet-based Primitive of type b (SPb); I) face-centered cubic array of spheres (fcc).

8.3.3 Dispersion analysis

In the case of a mesoporous retentive stationary phase Ω_s, solute particles have access to Ω_s where they are free to diffuse with an effective diffusivity D_s set to $D_s = 0.3D_m$ as an intermediate value representative of the typical range $D_s/D_m \in [0.1, 0.5]$ of the intra-particle diffusion coefficient in silica columns [260]. Figures 8.26 A-D show the reduced plate height curves h vs the Peclet number Pe (also referred to as reduced velocity)

$$h = \frac{H}{L} = \frac{2D^x}{LU^x} = \frac{2\,(D^x/D_m)(1+k'')}{Pe}, \quad Pe = \frac{U_i L}{D_m} \tag{8.52}$$

for the strut-based geometries G,D, and P (Figure 8.26A), for the Diamonds D, SDa and SDb (Figure 8.26B), the Gyroids G, SGa and SGb (Figure 8.26C) and the Primitives P and

SPb (Figure 8.26D). Different curves correspond to different values of the zone retention factor $k'' = 1, 4, 16$, and therefore to a different effective velocity U^x and distribution of the analyte between the mobile and stationary zones.

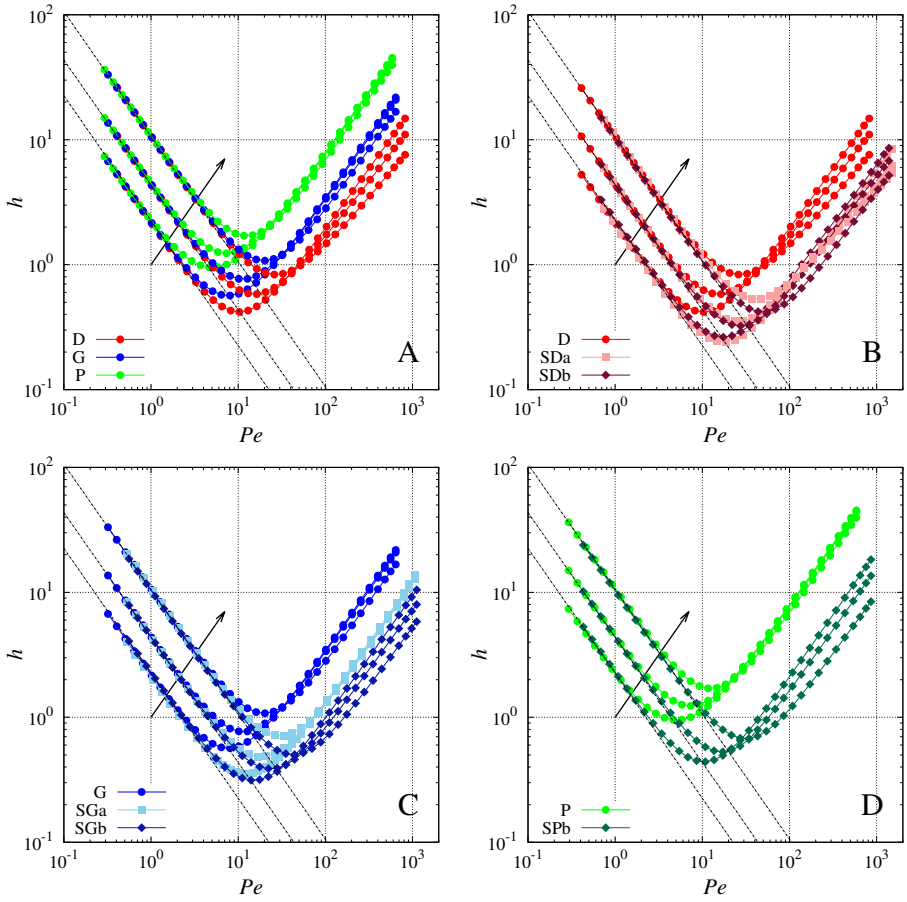


Figure 8.26: Reduced plate height curves h vs $Pe = U_i L/D_m$ for all the geometries investigated in the mesoporous retentive case. A) Strut-based geometries G,D,P; B) Diamond based geometries D, SDa, SDb; C) Gyroid based geometries G, SGa, SGb; D) Diamond based geometries P, SPb. Arrows indicate increasing values of the zone retention factor $k'' = 1, 4, 16$. Dot-dashed lines indicate the behavior $h = 2\gamma_{eff}(1 + k'')/Pe$ with $\gamma_{eff} = 0.562, 0.435, 0.312$ for $k'' = 1, 4, 16$, respectively. The same value of γ_{eff} is adopted for all the geometries.

From the plate height curves shown in Figure 8.26, it is possible to estimate the minimum value h_{min}, the corresponding Peclet value Pe_{min} and the value h_{100} of h at $Pe = 100$, the latter as a characteristic value of the hetp curve in the convection-controlled regime. These three data can be used to characterize the hetp curve of each of the considered geometries. Numerical results of h_{min} for all the geometries are reviewed in Figure 8.27 where they are plotted as a function of the dimensionless hydraulic diameter d_h/L for the three k'' values investigated. Unlike what was observed in the purely hydrodynamic case ($k'' = 0$) [259], the h_{min} data in the mesoporous retentive case, with an exception for the Primitive structure, exhibit a well defined linear behaviour as a function of d_h, for all the k'' values analyzed. This result can be explained by considering that the smaller the hydraulic diameter, the larger the contact surface between the mobile and the stationary zones, the more the solute particles have access to the stationary zone Ω_s. Moreover, lower values of d_h correspond to

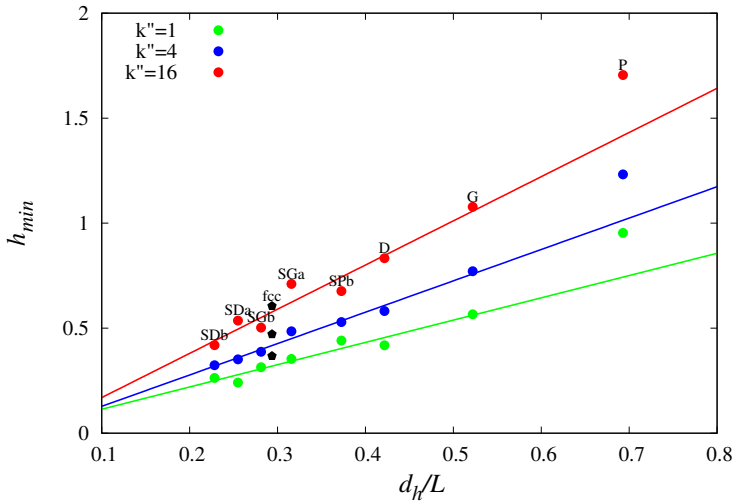


Figure 8.27: h_{min} vs d_h/L in the mesoporous retentive case, $k'' = 1, 4, 16$, $D_s/D_m = 0.3$. Black points indicate fcc data.

shorter distances between nearest solid surfaces, and henceforth shorter diffusional lengths, facilitating the transfer from Ω_m to Ω_s. Although Ω_s is a low diffusion zone because $D_s < D_m$, it still represents a shortcut for the motion of the analyte which no longer has to bypass the stationary zone by following the streamlines of the velocity field, but can penetrate and diffuse into the stationary zone [243]. Moreover, the "shortcut effect" is enhanced by the sorption equilibrium providing an additional driving force for the transport through the stationary zone.

These observations apply to both TPMS-based geometries and array of spheres, although the former are bicontinuous packings, while the latter are not. In bicontinuous beds, like monolithic columns, solutes experience a connected end-to-end pathway in both the mobile and stationary zones, as opposed to discontinuous packings, wherein the stationary adsorptive zone is distributed over a set of isolated elements.

Best performing geometries are SDb, SDa and SGb, having the lowest values of d_h. Lower values of h_{min} correspond to higher values of Pe_{min}, as highlighted in Figure 8.28 A showing the behaviour h_{min} vs Pe_{min}. It can be readily observed that h_{min} is inversely proportional to Pe_{min}, i.e. $h_{min} = \beta_{k''}/Pe_{min}$, with $\beta_{k''} = 4.5, 8.7, 21.2$ for $k'' = 1, 4, 16$, respectively. This implies that the product $h_{min} \times Pe_{min}$ attains a constant value, namely $\beta_{k''}$, for all the geometries investigated, and $\beta_{k''}$ depends exclusively on the zone retention factor k''. This

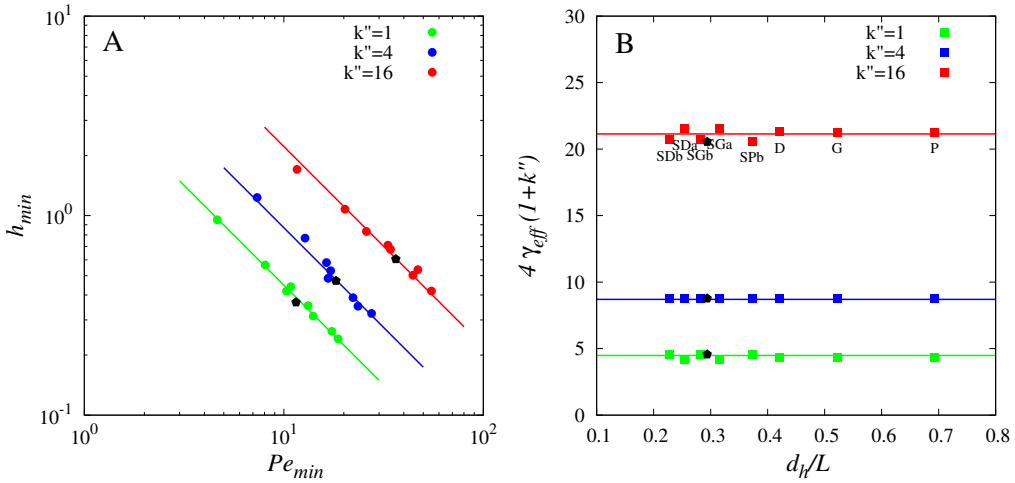


Figure 8.28: (A) Log-log plot of h_{min} vs Pe_{min} in the mesoporous retentive case, $k'' = 1, 4, 16$, $D_s/D_m = 0.3$. Straight lines show the behaviour $h_{min} = \beta_{k''}/Pe_{min}$ with $\beta_{k''} = 4.5, 8.7, 21.2$ for $k'' = 1, 4, 16$, respectively. (B) Comparison between $4\gamma_{eff}(1 + k'')$ for all the geometries (points) and the value of $\beta_{k''}$ (straight lines) for $k'' = 1, 4, 16$. Black pentagons indicate the fcc array of spheres.

finding is not surprising because it can be demonstrated that[3]

$$h_{min}Pe_{min} = \beta_{k''} = 4\,\gamma_{eff}(1 + k'') \tag{8.53}$$

where $\gamma_{eff} = D_{eff}/D_m$ is the dimensionless effective axial diffusion coefficient [243, 261], i.e. D^x/D_m at $Pe = 0$. The parameter γ_{eff} controls the initial $1/Pe$ behaviour of the rescaled hetp curve, i.e. $h \simeq 2\gamma_{eff}(1 + k'')/Pe$ for $Pe < Pe_{min}$, as shown in Figures 8.26 A-D (dot-dashed lines). It can be observed that all geometries, for the same value of k'', are characterized by very close values of γ_{eff}, since the dashed lines shown in Figures 8.26 A-D are the same for all geometries, being obtained using the same value of γ_{eff}, that is, $\gamma_{eff} = 0.562, 0.435, 0.312$, for $k'' = 1, 4, 16$, respectively. As a further confirmation, Figure 8.28 B shows the almost constant behaviour of $4\,\gamma_{eff}(1 + k'')$ vs d_h for all the geometries, in perfect agreement with the values of $\beta_{k''}$ estimated from the behaviour of h_{min} vs Pe_{min} shown in Figure 8.28 A.

Consistently with findings shown in Figure 8.27, also h_{100} (the rescaled plate height at

[3]The behaviour of the rescaled hetp curve h vs Pe can be approximated, for low-intermediate values of Pe including the minimum region, as

$$h = \frac{2}{Pe}\frac{\gamma_{eff}}{\widetilde{U}^x} + 2Pe\frac{\delta}{\widetilde{U}^x}, \quad \widetilde{U}^x = \frac{U^x}{U_i} = \frac{1}{1 + k''}$$

where γ_{eff}, $\widetilde{U}^x$ and δ are parameters which depend on the geometry and the k'' value. By enforcing the minimum condition $dh/dPe = 0$ at $Pe = Pe_{min}$, one obtains $Pe_{min} = \sqrt{\gamma_{eff}/\delta}$ and the product $h \times Pe$ at the minimum (h_{min}, Pe_{min}) attains the form

$$h_{min}Pe_{min} = 2\frac{\gamma_{eff}}{\widetilde{U}^x} + 2Pe^2_{min}\frac{\delta}{\widetilde{U}^x} = 4\frac{\gamma_{eff}}{\widetilde{U}^x} = 4\gamma_{eff}(1 + k'')$$

$Pe = 100$), increases with the hydraulic diameter d_h, as shown in Figure 8.29. In particular, h_{100} exhibits a well-defined quadratic behavior $h_{100} \sim d_h^2$ implying that the best performing structures, even at high Peclet values, are SDb, SDa and SGb, having the lowest values of d_h. The value of h_{100} decreases as k'' increases, that is, as the fraction of analyte particles trapped

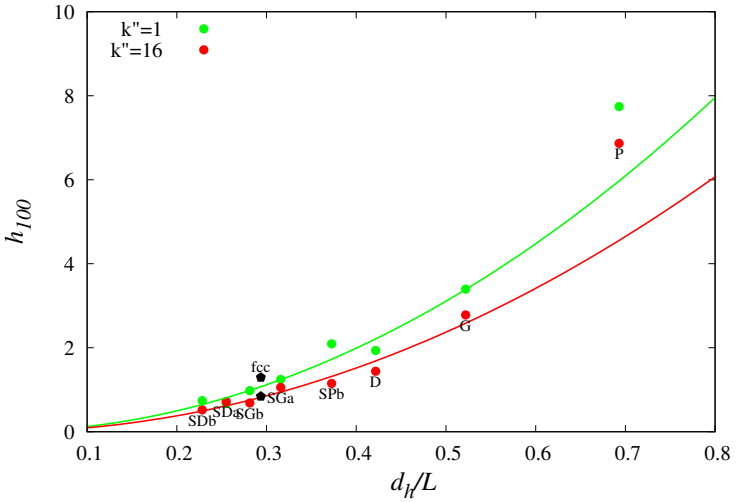


Figure 8.29: h_{100} vs d_h/L in the mesoporous retentive case, $k'' = 1, 16$, $D_s/D_m = 0.3$. Continuous lines show the behaviour $h_{100} = \gamma d_h^2$ with $\gamma = 12.43, 9.48$ for $k'' = 1, 16$, respectively. Black pentagons indicate the fcc array of spheres.

in the stationary zone increases. This marks a significant difference from what observed in the case of surface adsorption, where the value of h_{100} increases as k'' increases [259]. For sake of clarity, Figures 8.30 A-B show the comparison between rescaled plate height curves with equal zone retention factors $k'' = 1, 4, 16$ for D (Figure 8.30 A) and SPb (Figure 8.30 B) in the porous case (diffusion and adsorption within the stationary zone Ω_s) and the superficial case (adsorption on the surface of Ω_s). The significant differences observed in the hetp curves, both in the diffusive branch (low Pe) and in the convection controlled branch (high Pe), confirm that the transport mechanism changes dramatically when the analyte can penetrate and diffuse within the stationary zone instead of being adsorbed only superficially. Indeed, as k'' increases, the fraction $m_m = 1/(1 + k'')$ of solute particles in the mobile zone that are affected by the velocity gradients decreases and the larger fraction $m_s = k''/(1 + k'')$ of solute particles resides in the stazionary zone where it can diffuse (in the mesoporous case) and travel through the chromatographic bed.

Refocusing on the analysis of the porous case, it is worth noting that dispersion data for the fcc array of spheres also fit well into the overall picture, although the fcc array of spheres, for the porosity $\varepsilon = 0.4$, is not a bicontinuous medium, and therefore not 3D printable. Its separation performances, in terms of h_{min} and h_{100}, are comparable with that of SGa and SGb having close values of d_h. Dispersion data shown in Figure 8.27 and Figure 8.29 clearly indicates that the only geometry that deviates significantly from the highlighted behaviors is the Primitive (P) because the hydraulic diameter, evaluated as the ratio "fluid volume to wetted surface" is not representative of the ratio "cross-sectional area to wetted perimeter"

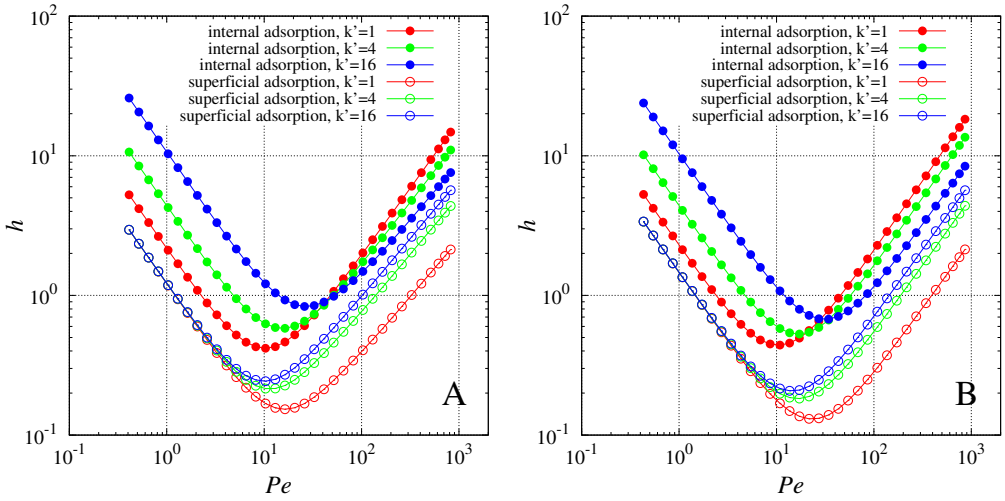


Figure 8.30: Log-log plot of h vs Pe in two different retentive cases, i.e., the mesoporous case (diffusion and adsorption within the stationary zone Ω_s) and the superficial case (adsorption on the surface of Ω_s). Porous case $k'' = 1, 4, 16$ (see Eq. (8.44)), $D_s/D_m = 0.3$. Superficial case $k'' = K_{eq}S/V_m = 1, 4, 16$, no surface diffusion of the analyte. A) Diamond (D); B) Sheet Primitive of type b (SPb).

in any cross-section of the domain [259].

Sensitivity to the intra-particle diffusivity ratio

To assess the sensitivity of the results to the choice of the intra-particle diffusivity, additional simulations were performed for the strut-based TPMS geometries at fixed zone retention factor $k'' = 4$, considering three values of the diffusivity ratio $\alpha = D_s/D_m = 0.1, 0.3$, and 0.5. The corresponding rescaled plate height curves are reported in Fig. 8.31.

The investigated range of α is experimentally relevant and spans different chromatographic application regimes. Lower values of α (e.g. $\alpha = 0.1$) are representative of small-molecule separations, as encountered in LC–MS metabolomics workflows, where analytes readily access the porous domain but experience strong surface interactions that significantly reduce the effective intraparticle diffusivity [262, 263]. Higher values of α (e.g. $\alpha = 0.5$) are instead characteristic of peptide and protein separations in proteomics, where wide-pore stationary phases are deliberately employed to mitigate confinement effects and enable more efficient diffusive transport within the stationary domain [264, 265].

For all geometries, the dispersion curves exhibit qualitatively analogous trends across the investigated range of α, preserving their characteristic shape and the relative ranking among different structures. Variations of α primarily induce a systematic shift of the curves, affecting the absolute values of the reduced plate height and the location of the minimum, without altering the underlying scaling behavior. This indicates that the choice $D_s/D_m = 0.3$ is representative of the entire experimentally relevant interval $\alpha \in [0.1, 0.5]$, and that the conclusions drawn in the following are robust with respect to variations of the intra-particle diffusivity ratio.

The observed shift of the dispersion curves with varying α (see Fig. 8.31 A) can be in-

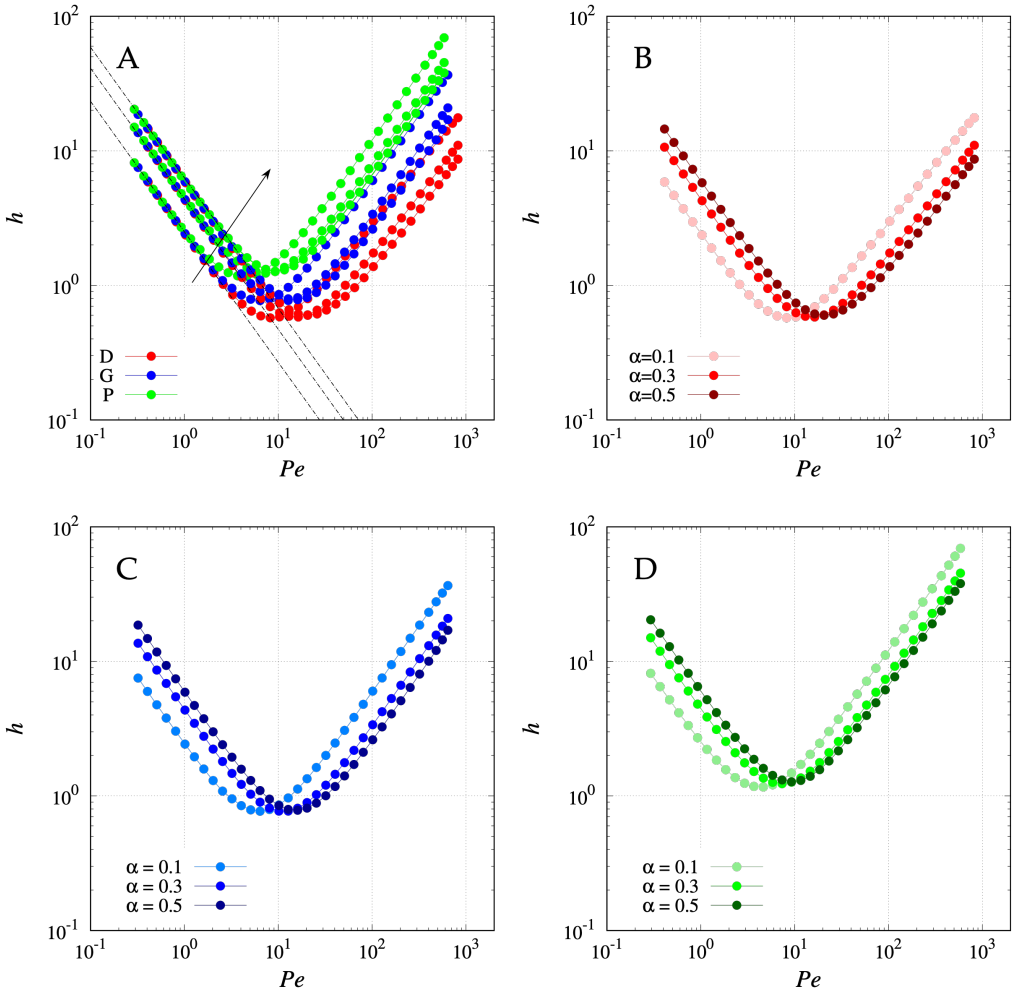


Figure 8.31: Log–log plot of the reduced plate height h versus the Peclet number Pe for three different values of the intra-particle diffusivity ratio $\alpha = D_s/D_m = 0.1, 0.3$, and 0.5, for the three strut-based TPMS geometries at fixed zone retention factor $k'' = 4$. (A) Comparison among all geometries and α values; the arrow indicates increasing α. (B) Diamond (D). (C) Gyroid (G). (D) Primitive (P).

terpreted in light of the non-additive nature of mass transport in retentive porous media. In particular, Adrover *et al.* [243] showed that, in retentive systems, changes in transport properties within the stationary phase do not simply superimpose to the hydrodynamic contribution, but modify the effective axial dispersion through a coupled mechanism involving phase exchange and diffusion.

While the structures analyzed by Adrover *et al.* are not bicontinuous, the same physical principle applies here. In the present TPMS-based architectures, both the mobile and stationary domains form connected end-to-end pathways, so that the stationary phase acts as a parallel transport route rather than a purely stagnant region. Variations of the intra-particle diffusivity ratio α therefore alter the efficiency of this parallel pathway, leading to a systematic shift of the dispersion curves without affecting their overall shape or scaling behavior. Geometry thus controls the dispersion morphology, whereas α acts as a tuning parameter for the absolute transport efficiency.

8.3.4 Kinetic performance of TPMS structures

Dispersion data shown in Figures 8.26, 8.27 and 8.29 allow a comparison of the separation performance of different geometries with the same characteristic length L of the unit cell, since the plate height has been rescaled to L. However, different geometries have different permeabilities K_v, and therefore different equivalent diameters d_{eff}. If a comparison between different geometries is desired, at the same pressure drop $\Delta P/L$, it is necessary to analyze the plate height curves rescaled with respect to the equivalent diameter d_{eff}, which corresponds to compare the separation performance of different geometries at the same d_{eff}. Figures 8.32 A-D show the rescaled hetp curves $h_c = H/d_{eff}$ vs $Pe_m = U_i d_{eff}/D_m$ for all the geometries and for the three k'' values analyzed. It is worth noting that comparing different geometries

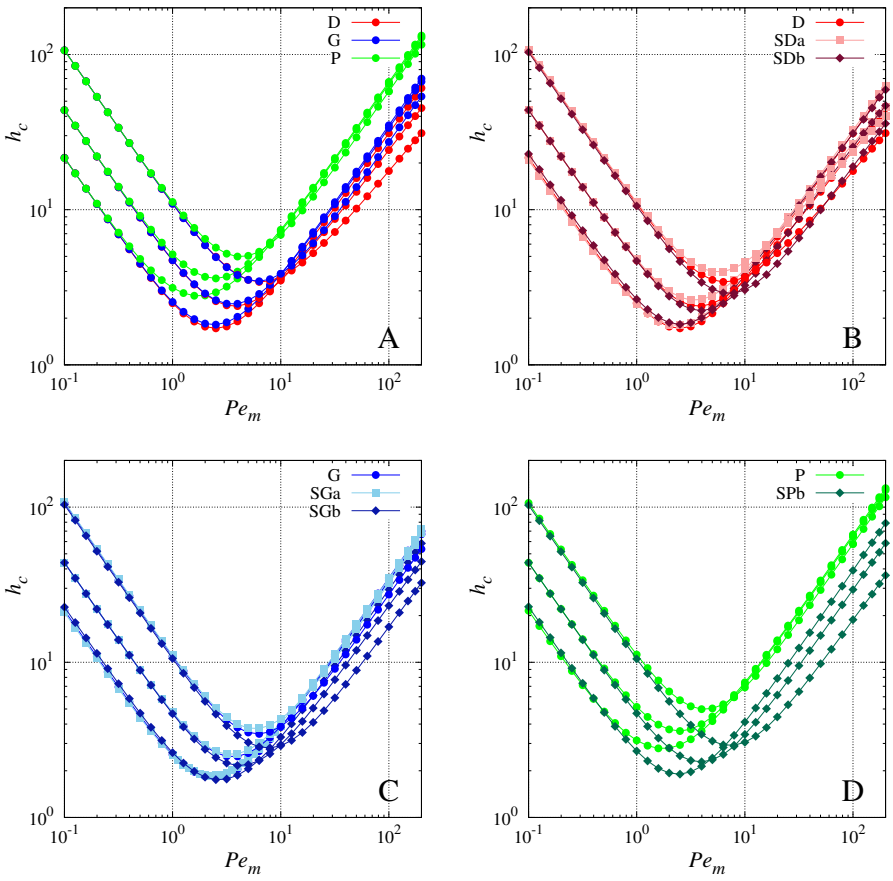


Figure 8.32: Reduced plate height curves $h_c = H/d_{eff}$ vs $Pe_m = U_i d_{eff}/D_m$ for all the geometries investigated in the mesoporous retentive case. A) Strut-based geometries G,D,P; B) Diamond based geometries D, SDa, SDb; C) Gyroid based geometries G, SGa, SGb; D) Diamond based geometries P, SPb. Arrows indicate increasing values of the zone retention factor $k'' = 1, 4, 16$.

in terms of h_c, also called *universal plate height* [246], corresponds to compare them in terms of *separation impedance* $SI = 32h_c^2$ [248] or *kinetic performance factor* $e_c = 1/\sqrt{h_c}$ [201, 246].

The hetp curves h_c vs Pe_m shown in Figures 8.32 A-D clearly show that, for the same pressure drop, the different geometries exhibit much more similar separation performance. The values of $h_{c,min} = H_{min}/d_{eff}$ of the different geometries, except for the Primitive, are very close to each other for $k'' = 1$ and show an appreciable linear dependence on the

tortuosity τ for larger values of k'', as shown in Figure 8.33 A. The same result can be viewed in terms of the maximum value of the kinetic performance factor, $e_{c,max} = 1/\sqrt{h_{c,min}}$, as shown in Figure 8.33B. Indeed, the lower the tortuosity, the higher the maximum kinetic performance factor, for $k'' = 4, 16$. Figures 8.33 A-B clearly show that (i) the best performing TPMS geometries are those with a lower tortuosity value, i.e. SDb, SGb and SPb, and (ii) the fcc array of spheres is significantly less efficient than all TPMS geometries, at least for low/intermediate values of k''.

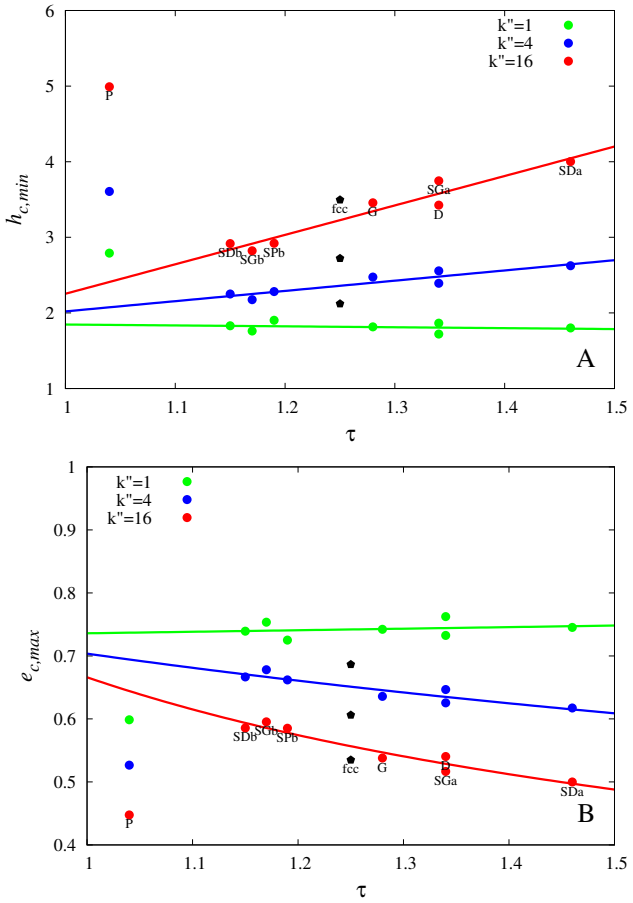


Figure 8.33: $h_{c,min} = H_{min}/d_{eff}$ vs τ (A) and $e_{c,max} = 1/\sqrt{h_{c,min}}$ vs τ (B) in the mesoporous retentive case, $k'' = 1, 4, 16$, $D_s/D_m = 0.3$

A lower value of $h_{c,min}$ also corresponds to a higher value of $Pe_{m,min}$. In fact, having previously shown that $h_{min} \times Pe_{min} = H_{min}U_{i,min}/D_m = \beta_{k''}$, we have also implicitly shown that $h_{c,min} \times Pe_{m,min} = H_{min}U_{i,min}/D_m = \beta_{k''}$, which implies $h_{c,min} = \beta_{k''}/Pe_{m,min}$. This finding has important consequences in the analysis of kinetic plots [249–251] t_0/N^2 vs N

$$\frac{t_0}{N^2} = \frac{\eta}{\Delta P_{max}}\frac{H^2}{K_v}, \quad N = \frac{\Delta P_{max}}{\eta}\frac{K_v}{U_i H} \tag{8.54}$$

where t_0 is the column void time and N the plate number. Kinetic plots (shown in Figure 8.34 for $k'' = 4$, $L = 2$ [μm], $\Delta P_{max} = 500$ [bar], $\eta = 5 \times 10^{-4}$ [Pa s], $D_m = 1 \times 10^{-9}$ [m^2/s]) play a key role in the analysis/comparison of the separation performance of TPMS structures because they explicitly account for the length L of the unit cell. The length

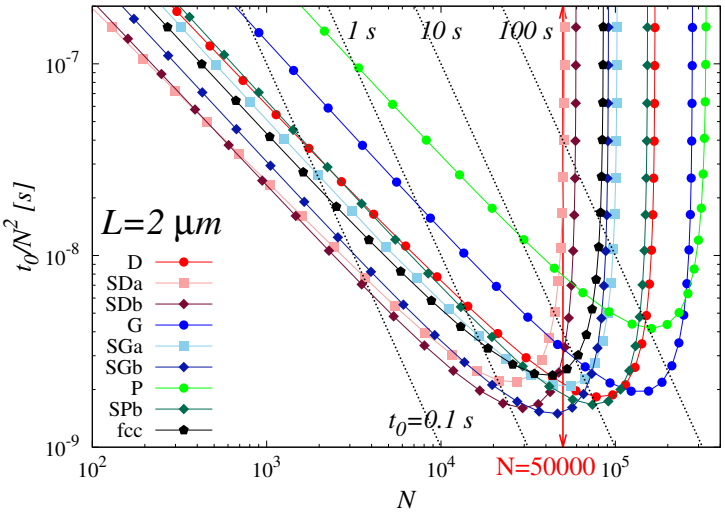


Figure 8.34: t_0/N^2 vs N for all the TPMS geometries and the fcc array of spheres for the same unit-cell dimension $L = 2$ [μm] and $k'' = 4$. $\Delta P_{max} = 500$ [bar], $\eta = 5 \times 10^{-4}$ [Pa s], $D_m = 1 \times 10^{-9}$ [m^2/s]. The vertical red line indicated $N = N_{req} = 50000$.

L cannot be smaller than a minimum size L_{min}, which is determined by the resolution of current 3D printers on the market. Even the most advanced 3D printers, which use the two-photon polymerization technique and achieve minimum feature sizes on the order of hundreds of nanometers [198], can only 3D print TPMS geometries with adequate accuracy if $L \geq L_{min} = 2\mu$m.
According to Eq. (8.53), the optimal number of plates N_{opt}, corresponding to the minimum of the kinetic plot, attains the form

$$N_{opt} = \frac{\Delta P_{max}}{\eta D_m} \frac{K_v}{Pe_{min} h_{min}} = \frac{\Delta P_{max}}{\eta D_m} \frac{K_v}{4\gamma_{eff}(1+k'')} = \frac{\Delta P_{max}}{\eta D_m} \frac{(d_{eff}/L)^2 L^2}{32\beta_{k''}} \tag{8.55}$$

Eq. (8.55) clearly indicates that N_{opt} (i) increases linearly with the permeability K_v (quadratically with d_{eff}/L), (ii) decreases with $\beta_{k''}$ and therefore with k'', and (iii) increases quadratically with the length L of the unit cell. Eq. (8.55) can be used to estimate the optimal unit-cell length L_{opt}, i.e. the value of L such that the minimum of the kinetic plot occurs for a required value of the number of plates $N = N_{req}$. Figure 8.35 shows L_{opt} vs d_{eff} for all the geometries and three k'' values, as estimated directly from the kinetic plots (points), and the predictions (continuous lines) obtained from Eq. (8.55) where N_{req} has been set to $N_{req} = 50000$.

Lower values of the column void time t_0 are associated to Sheet-based geometries of type b, namely SGb, SDb and SPb (see Figure 8.34). Best printable geometries are SDa and SDb, because characterized by higher values of $L_{opt} \geq L_{min}$, as shown in Figure 8.35. As a consequence, the SDb is the structure that is best suited for 3D printing as it combines a high L_{opt} value with an excellent separation performance.

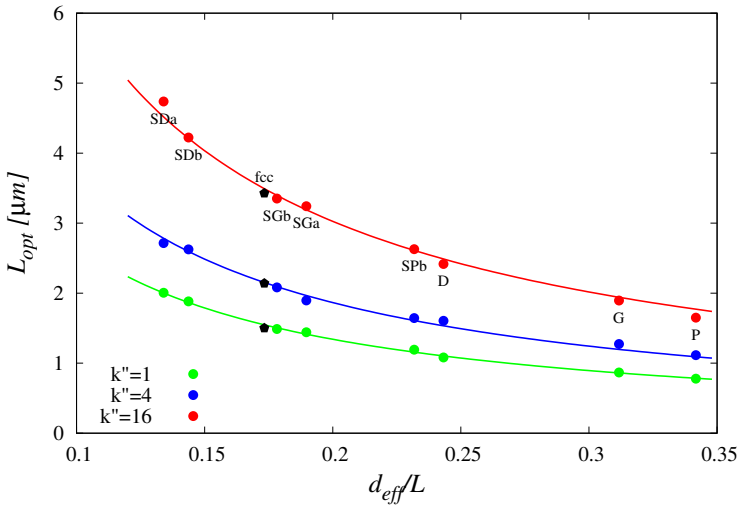


Figure 8.35: L_{opt} vs d_{eff}/L for $k'' = 1, 4, 16$. $N_{req} = 50000$, $\Delta P_{max} = 500$ [bar], $\eta = 5 \times 10^{-4}$ [Pa s], $D_m = 1 \times 10^{-9}$ [m^2/s]. Continuous lines show the predictions of L_{opt} by Eq. (8.55).

Printability constraints and manufacturability of strut-based TPMS geometries

The results reached within this work were mainly governed by transport properties and size scales rather than details of the interface between the solid and fluid phases. Specifically, the work has revealed that dispersion and kinetic separations can depend instead on hydraulic diameter, effective diameter, permeability, and tortuosity, which are all averages of the type described above. Previous literature studies regarding ordered and additively manufactured media suggests that geometric flaws do not significantly affect overall transport within the media [266–268]. In this respect, there exists a clearly definable reference class where the periodic morphologies are simpler and composed of straight channels and orthogonal unit cells, referred to as cuboid-like and channel-based morphologies. In fact, specific designs consisting of straight quadratic channels made by additive manufacturing have been theoretically and experimentally assessed in terms of dispersion, diffusion, and the effect of natural imperfections [269]. These cuboid-channel morphologies clearly provide a feasible compromise between permeability, dispersion, and geometric complexity. These types of channel architectures have also been employed successfully in real-world separation and sample preparation systems such as liquid chromatography, solid-phase extraction, and bio-separations, with efficient mass transfer and demonstrated robustness [270–275]. Their resilience to fabrication errors, which makes them less sensitive compared to others, makes them relevant for use as manufacturable benchmark geometries [276]. Conversely, from recent studies it has been highlighted that bicontinuous and TPMS-inspired stationary phases enhance transverse diffusion and isotropic transport properties, and reduce heterogeneities among the channels, which are not easily accessible through simple geometric models of straight-channel systems, for example. Furthermore, transverse diffusion in stationary phases represents a driving factor in suppressing polydispersity for cuboid channel geometries, thereby verifying the quality of intrachannel connectivity [269]. As evidence supporting this postulate, protein and vi-

ral separation on TPMS monolithic systems clearly reveals efficient separation performance with suitable permeability-versus-dispersion compromises achieved in current experimental work [272, 277]. Following this thinking, cuboids with similarities in their channel geometry provide a workable, highly stable system for comparative purposes. However, within this study, geometrical configurations of TPMS systems based on sheet geometry, including their SDb phase, provide a highly optimal current compromise with respect to separation efficiency, transverse mixing, and technological feasibility, taking into account demands for mesoporosities and resolution.

From a practical point of view, the choice of material represents the main implicating factor for the use of 3D-printed TPMS-based stationary phases. However, the geometric deductions presented in the current work are found mostly insensitive to the exact chemistry involved in the printing material, which instead depends mostly on structural properties such as bicontinuity, interconnectivity, and scales related to transport lengths. For these reasons, the concurrent performance behaviors noted for the tested TPMS geometries will likely prove relevant across a variety of material types, as long as a comparable geometric realism and accessibility can be realized [270, 278].

At the current stage, polymeric systems are the most advanced paradigm for 3D-printed chromatographic material with high geometric resolution and compatibility with conventional functionalization methods. Functional polymeric monoliths made using additive manufacturing have already shown comparable performance to conventional chromatography and sample preparation procedures [267, 271, 272]. On the other hand, the ceramic and silica counterparts, being very appealing due to their chemical and heat stability, are currently limited by the resolution, shrinkage upon post-processing, and inability to accurately tailor the mesoporous structure at the corresponding size scales [278].

In addition to chromatography, polymeric TPMS scaffolds generated using extrusion-based printing have been demonstrated to preserve mechanical strength and connectivity for a variety of material compositions, which suggests once again that TPMS microarchitecture is not necessarily tied to a given type of material. In sum, while issues specific to individual materials remain, especially for high-resolution inorganic embodiments, this analysis suggests that the current trends seen in TPMS performance can be transferred to polymeric, hybrid, and eventually inorganic materials [276, 279].

Chapter 9

Conclusions and Future developments

9.1 Summary of the research work

The research work under study in this thesis has been divided into two parts. The first part contains an integrated experimental and modeling approach aimed at optimizing cryogel-type systems with applications in the biomedical and pharmaceutical fields. Regarding the second part, this presents a modeling investigation in order to optimize the performance of chromatographic columns that can be modeled using triply periodic geometries.
In Chapter 2, the protocols followed for the synthesis of polymers and their characterization, the preparation procedures and physical, mechanical and morphological characterization of the polymer gels under study were described.
In Chapter 3, an experimental analysis is carried out aimed at understanding the parameters that influence the final structure and the mechanical properties of the cryoreticulated samples. Therefore, all the steps performed are described to be able to discern when a sample produced according to the methodology used for cryogels can actually be considered as such. In this regard, the window of formation of cryogel systems was identified recurring to $DEX_{40}HEMA$, a methacrylic derivative of dextran with excellent biodegradability and biocompatibility properties, as a polymer. The following parameters were kept unchanged:

- the volume of polymer solution (2 mL)
- the temperature of the cryostatic bath (-12°C)
- the degree of derivatization of the polymer (5% ± 0.5%)
- the molar ratio between the two reagents APS and TEMED (0.9)

The study was therefore reduced to the analysis of the effects of the polymer concentration - i.e. the number of mmoles of methacrylic groups MG - and the concentration of reagents, expressed in terms of the APS/MG molar ratio. The range of $mmoles_{MG}$ values has been reduced to [0.015;0.055] $mmoles_{MG}$. In fact, systems below the lower limit did not crosslink and once hydrated they dissolved. Instead, above the right limit of the range they exhibited

a structure too massive to be applied in the biomedical field. After establishing the polymer concentrations, the investigation focused on the concentrations of reagents which, for each selected polymer concentration, allow the formation of a cryogel-like system. Such a study was carried out for the following systems: 0.015 $mmoles_{MG}$, 0025 $mmoles_{MG}$, 0.035 $mmoles_{MG}$, 0.045 $mmoles_{MG}$ and 0.055 $mmoles_{MG}$, corresponding to 2.5 %w/v, 4.2 %w/v, 6.0 %w/v, 7.6%w/v and 9.4 %w/v.

Below there is a description of the steps followed in order to locate the lower and upper bound of the $mmolesl_{APS}/mmoles_{MG}$ ratio. For the lower limit, given that the quantity of reagents is very low, the gel fraction was evaluated, i.e. the fraction of polymer that cross-linked. Systems with GF greater than 0.75 were classified as cryogel. Therefore, from the determination of the gel fraction of the analyzed samples, it was possible to ascertain that, as expected, by slowing down the crosslinking kinetics, the polymer is unable to cross-link completely, thus resulting in a progressive decrease in the gel fraction values. The lower the mass of polymer, the higher the cross-linker concentration must be for this value of GF to be reached. These systems were also subjected to swing tests. Regarding the upper limit, the distinction parameter was chosen between a cryogel-type system and one that does not respect this definition, the weight degree of swelling Q. The analysis of the swelling curves has, in fact, made it possible to highlight the close relationship between reagent concentration, polymer concentration and degree of swelling Q. Specifically, by increasing the concentration of the APS/TEMED reactants, the rate of crosslinking of the polymer progressively increases and, as a result, the swelling kinetics become increasingly slower and then decrease to match that of the corresponding hydrogel, while greatly decreasing the equilibrium absorption distinction occurring in the upper limit has also been confirmed by FE-SEM images, from which it emerges that the degree of interconnection of the pores is lowered as the APS/MG molar ratio increases, tending towards a morphology closer to that of the hydrogel. An initial analysis was also carried out on the role of air oxygen as a radical quencher. A polymer solution containing 0.035 $mmol_{MG}$ was selected and reactive were introduced according to two ratios $mmol_{APS}/mmol_{MG}$, 0.6 and 0.8. The preparation procedures were carried out according to the original protocol, in which the solutions are in contact with oxygen in the air, and in an inert nitrogen atmosphere, after eliminating the dissolved oxygen by blowing N_2 into the solution. The morphology of the samples prepared according to the two different procedures is highly different: the samples prepared in a nitrogen atmosphere are more anisotropic and inhomogeneous, furthermore they are more massive.

The optimization of dextran-based cryogel systems has evolved to broaden the range of dextran-based polymers, as set out in Chapter 4. Then, the effect of the molecular weight of the polymer chain of DEX and the length of the spacers were analyzed, which differ in the number of oxyethylene units that exist between the main dextran chain and the methacrylic group. The analysis of the swelling and degradation tests showed that the change in molecular weight and spacer length of the methacrylic derivative of DEX has a more marked influence than the change in molecular weight of the starting DEX chain. These systems have also been characterized through release tests. More precisely, the study demonstrates

the potential of dextran-based cryogels for controlled drug release applications, using Vitamin B_{12} as a model drug for in vitro release tests. It is pointed out how different drug loading procedures significantly influence the release kinetics. Specifically, freeze-dried samples infused with the drug after cryogel formation exhibit a fast Fickian release. In contrast, when the drug is loaded before the low-temperature crosslinking step that leads to cryogel formation, a retarded, highly non-Fickian release behavior is observed. This non-Fickian release is attributed to the cryoconcentration phenomenon and is accurately modeled using a two-step release process. The mechanistic model proposed in this study successfully explains the anomalous non-Fickian release trends, distinguishing it from other diffusion processes such as Case II diffusion. This study highlights the importance of the drug loading procedure in tailoring drug release profiles from cryogels, offering valuable insights for the development of controlled-release therapies. The cryogels proposed in this work may also be suitable for drug molecules of higher molecular weight. Indeed, we already reported on the possibility of applying these dextran derivatives for the development of injectable and in situ gelling drug delivery systems, specifically designed for the controlled release of large molecules [98]. Certainly, the carbonate ester makes these polymer networks easily degradable in vivo. Therefore, these dextran derivatives can certainly also be proposed also for the delivery of high molecular weight drugs with cryogel systems.The macroporous microarchitecture of cryogel systems makes them suitable for applications in the tissue and regenerative medicine fields. In fact, cellular scaffolds must have high mechanical resistance to promote cell adhesion but at the same time they must guarantee that exchanges of nutrients, oxygen and waste with the external environment take place. Compared to older two-dimensional, in vitro cultivation technologies, 3D cultures better reflect natural conditions in vivo. Therefore, the 3D scaffold must act as a temporary extracellular matrix that promotes tissue development. However, dextran-based cryogels do not allow tissue growth, despite having the required mechanical and structural characteristics. This is a direct consequence of the composition of the polymero itself, which is unable to provide the right nutrients to cellular metabolism.

For this reason, in Chapter 5, blended systems were developed based on the methacrylic derivatives of dextran and methacrylated gelatin, containing the amino acids needed by the cells. Starting from a previous study in which GelMA-DEX_{40}MA systems were processed, polymer solutions containing 0.050 $mmoles_{MG}$ with $mmoles_{APS}/mmoles_{MG}$ ratio were formulated = 0.45 and were characterized from a mechanical point of view. The interaction of two different polymer systems led to better structural properties. In addition, the systems were subjected to preliminary cell adhesion analyses.

One of the most relevant aspects in the biomedical and drug delivery fields is represented by swelling phenomena. In order to appropriately describe the swelling mechanics of cryogel-type systems, a preliminary study was carried out in which modifications were made to the Mechano-Diffusion theory, originally applied for the description of swelling phenomena in hydrogel, polymeric systems in which the pores are very small and negligible, since these are isolated structures that do not communicate and which can be considered as an integral

part of the polymeric matrix. There are several reasons why it was chosen to modify this theory and not to resort to Mixture Theory or Poromechanics. For one thing, these last two theories do not resort to a homogenized treatment of the phenomenon. The deformation induced by sqwelling is described in a Lagrangian framework, that is, the evolution of the deformation that takes place on the solid body is followed. Such an approach, for a. highly porous system such as cryogel (porosity greater than 70%) could lead to an incorrect description considering that a large portion of the domain is liquid and only a small fraction is occupied by the solid. Moreover, the mixing effect between the polymer chains and the solvent molecules is not taken into consideration Conversely, Mechano-Diffusion is based on the statistical mechanics of polymer systems formulated by Flory and Rehner, which leads to a more rigorous and robust treatment. The application to cryogel systems the introduction of a α scalar field, corresponding to the volume fraction of polymer in the dry sample. This parameter led to a different version of the chemical potential constitutive equation. Furthermore, the swelling capability Q and the volumetric variation J_d were related, with good preliminary results. At this stage of the study, however, systems under steady-state conditions were modeled.

Chapter 7 provides a review regarding the use, very widespread in the literature, of cryogel systems such as chromatographic columns. In the century it has been established that the applications are truly numerous and this is a direct consequence of the architectural structure of the system, characterized by interconnected channels and highly resistant walls. Therefore, no phenomena of hindered diffusion or high pressure drops occur. One of the most appreciated aspects is certainly the possibility of not having to pre-treat the feed. Numerous scientific studies have shown that monolithic structures order enhance significantly the performance of the column. However, in the case of cryogel, since such systems are formed as a result of intrinsically stochastic phenomena, they lack predictability and order. This aspect, however, can be overcome through 3D printing of polymer constructs. An example of this is the triple periodic minimal surfaces, widely studied lately, also as a possible geometric model for cryogel.

Starting from these considerations, in Chapter 8 a modeling and computational study was carried out relying on the Two Zone Moment Analysis. Specifically, firstly, the chromatographic performance of eight different 3D printable non-porous stationary phases based on triply periodic minimal surfaces have been investigated in both no-retentive and superficially retentive cases. A detailed analysis of hydrodynamic dispersion data indicates that it is not possible to identify a single geometric or fluid-dynamic parameter that can explain, with no exceptions, the ordering of hydrodynamic performances. The analysis of plate height curves indicates that best performing geometries, nanely SDa and SGb, in both the non-retentive and the retentive case, are associated with lower values of the effective diameter, and thus lower values of permeability, except for geometries affected by significant channeling phenomena. When compared in terms of kinetic performance factor, the best performing geometries are SPb, D and SGb, characterized by ower tortuosity and higher coefficient of uniformity of the axial velocity field. The analysis of the kinetic plot reveals that none of the geome-

tries investigated can operate in optimal conditions (minimum of the kinetic plot) because this would require to diminish the dimension L of the unit cell below the limits dictated by the minimum feature size of the currently available 3D printing techniques. However, this finding should not suggest that TPMS geometries are not promising candidates for practical efficient chromatography. In fact, several studies [203–205] have already shown the possibility of 3D printing microporous stationary phases. The contribution of the internal porosity of the stationary phase to the separation properties is of fundamental importance and can drastically change the chromatographic performance of novel stationary phases based on triply periodic minimal surfaces [280]. In a second moment, the same geometric models were used to investigate the case of 3D printable porous stationary phases. The analysis of plate height curves indicates that best performing geometries, in terms of h_{min} and h_{100}, are SDb, SGa and SDb, associated with lower values of the hydraulic diameter d_h. Hetp curves differ significantly from that obtained in the superficial retentive case, both in the diffusive branch (low Pe) and in the convection controlled branch (high Pe), because the transport mechanism changes dramatically when the analyte can penetrate and diffuse within the stationary zone instead of being adsorbed only superficially. A net relationship between h_{min} and Pe_{min} is established, namely $h_{min} \times Pe_{min} = \beta_{k''}$ where $\beta_{k''} = 4\gamma_{eff}(1 + k'')$ is independent of the geometry because all the structures, for the same external porosity, exhibit very close values of effective longitudinal diffusion coefficient γ_{eff} at the same k'' value. When compared in terms of the maximum kinetic performance factor $e_{c,max}$, best performing geometries are SDb, SGb and SPb associated to lower values of the tortuosity τ. These same sheet-based geometries are also characterized by lower values of column void time t_0. Not all geometries are actually 3D printable, as the optimal unit cell size L_{opt} turns out to be smaller than the minimum size $L_{min} \simeq 2\mu$m that can be achieved through the most advanced 3D printing techniques. The sheet diamond of type b (SDb) is the structure that is best suited for 3D printing as it combines a high L_{opt} with an excellent separation performance.

9.2 Future developments

In the previous section, a brief overview of the study carried out during the Doctorate was outlined. However, as highlighted, some aspects offer promising directions for future investigation, while others are still in an early stage of development, reflecting the most recent advances in this research.

First, regarding the window of formation of cryogel-type structures, it is interesting to carry out further studies regarding the effect of oxygen. From the preliminary results, it was understood that the absence of oxygen, as expected, speeds up the crosslinking reaction, impacting the properties of the final system, making it denser. Furthermore, the dynamics of the swelling of systems obtained in an inert atmosphere highlights a strong anisotropic character of the system itself, which deserves further analysis. It would be interesting to carry out an internal evaluation of the quantity of dissolved oxygen within the starting

polymer solutions and, to demonstrate the antagonistic effect of oxygen, system preparation procedures could be followed in an oxygen atmosphere alone.
Secondly, future work will focus on completing cellular studies on blended systems through detailed biocompatibility analyses, building upon the promising preliminary findings. In fact, although fluorescence microscope images provide hope, however more rigorous studies are foundational. In parallel, advanced non-destructive characterization of the hydrated microstructure will be pursued using techniques such as low-field NMR [281–283] and Environmental SEM [284, 285], in order to better correlate cell response with network heterogeneity, pore architecture, and swelling state. Obviously, the development of 3D bioprinting must be taken into consideration, through which it is possible to directly print the bioink, i.e. the polymer gel not yet cross-linked and containing the cells, giving the shape of the desired organ([286]). However, various critical parameters must be evaluated, first of all the stress to which the cells are subjected during the molding phase ([287, 288]).
Thirdly, as already pointed out, future developments envisage describing the dynamics of swelling with the modified Mechano-Diffusion model. Preliminary analyses of the samples showed an anistropic behaviour which was not taken into account. Furthermore, despite having introduced the scalar field α which takes into account the body fraction actually occupied by polymer, however this does not provide details regarding the anisotropic structure of the pores. In correlation with a future torpedo of this model, there is the possibility of reinterpreting the swelling kinetics by coupling them with the force balance equations. Finally, it is in our interests to proceed with the printing of TPMS-type chromatographic columns in which the stationary phase consists of functionalized hydrogel or cryogel systems in order to verify the good agreement between experimental and computational data and to optimize the choice of printing materials.

Bibliography

[1] Isiaka Oluwole Oladele, Taiwo Fisayo Omotosho, and Adeolu Adesoji Adediran. Polymer-based composites: an indispensable material for present and future applications. *International Journal of Polymer Science*, 2020(1):8834518, 2020.

[2] Anna Bratek-Skicki. Towards a new class of stimuli-responsive polymer-based materials–recent advances and challenges. *Applied Surface Science Advances*, 4:100068, 2021.

[3] Daniel Crístian Ferreira Soares, Stephanie Calazans Domingues, Daniel Bragança Viana, and Marli Luiza Tebaldi. Polymer-hybrid nanoparticles: Current advances in biomedical applications. *Biomedicine & Pharmacotherapy*, 131:110695, 2020.

[4] Adina-Elena Segneanu, Ludovic Everard Bejenaru, Cornelia Bejenaru, Antonia Blendea, George Dan Mogoşanu, Andrei Biţă, and Eugen Radu Boia. Advancements in hydrogels: a comprehensive review of natural and synthetic innovations for biomedical applications. *Polymers*, 17(15):2026, 2025.

[5] Wei Hong, Zishun Liu, and Zhigang Suo. Inhomogeneous swelling of a gel in equilibrium with a solvent and mechanical load. *International Journal of Solids and Structures*, 46(17):3282–3289, 2009. ISSN 0020-7683. doi: https://doi.org/10.1016/j.ijsolstr.2009.04.022. URL `https://www.sciencedirect.com/science/article/pii/S0020768309001899`.

[6] Yulin Li, João Rodrigues, and Helena Tomás. Injectable and biodegradable hydrogels: gelation, biodegradation and biomedical applications. *Chemical Society Reviews*, 41 (6):2193–2221, 2012.

[7] Hao-xuan Li, Kun-chi Zhao, Jia-jia Jiang, and Qing-san Zhu. Research progress on black phosphorus hybrids hydrogel platforms for biomedical applications. *Journal of Biological Engineering*, 17(1):8, 2023.

[8] Nguyen Hoc Thang, Truong Bach Chien, and Dang Xuan Cuong. Polymer-based hydrogels applied in drug delivery: An overview. *Gels*, 9(7):523, 2023.

[9] Ana M.S. Costa and João F. Mano. Extremely strong and tough hydrogels as prospective candidates for tissue repair – a review. *European Polymer Journal*, 72:344–364,

2015. ISSN 0014-3057. doi: https://doi.org/10.1016/j.eurpolymj.2015.07.053. URL https://www.sciencedirect.com/science/article/pii/S0014305715004012.

[10] Caroline SA de Lima, Tatiana S Balogh, Justine PRO Varca, Gustavo HC Varca, Ademar B Lugão, Luis A. Camacho-Cruz, Emilio Bucio, and Slawomir S Kadlubowski. An updated review of macro, micro, and nanostructured hydrogels for biomedical and pharmaceutical applications. *Pharmaceutics*, 12(10):970, 2020.

[11] Irina N Savina, Ganesh C Ingavle, Andrew B Cundy, and Sergey V Mikhalovsky. A simple method for the production of large volume 3d macroporous hydrogels for advanced biotechnological, medical and environmental applications. *Scientific reports*, 6(1):21154, 2016.

[12] Anca Roxana Petrovici, Mariana Pinteala, and Natalia Simionescu. Dextran formulations as effective delivery systems of therapeutic agents. *Molecules*, 28(3):1086, 2023.

[13] Stéphane G. Lévesque, Ryan M. Lim, and Molly S. Shoichet. Macroporous interconnected dextran scaffolds of controlled porosity for tissue-engineering applications. *Biomaterials*, 26(35):7436–7446, 2005. ISSN 0142-9612. doi: https://doi.org/10.1016/j.biomaterials.2005.05.054. URL https://www.sciencedirect.com/science/article/pii/S0142961205004679. Dedicated to Canadian Biomaterials Research.

[14] Stephanie Möller, Jürgen Weisser, Sabine Bischoff, and Matthias Schnabelrauch. Dextran and hyaluronan methacrylate based hydrogels as matrices for soft tissue reconstruction. *Biomolecular Engineering*, 24(5):496–504, 2007. ISSN 1389-0344. doi: https://doi.org/10.1016/j.bioeng.2007.08.014. URL https://www.sciencedirect.com/science/article/pii/S1389034407000858. Proceedings on Symposium J Surface Functionalization of Biomaterials.

[15] Laura Di Muzio, Claudia Sergi, Vito Cosimo Carriero, Jacopo Tirillò, Alessandra Adrover, Elisa Messina, Roberto Gaetani, Stefania Petralito, Maria Antonietta Casadei, and Patrizia Paolicelli. Gelatin-based spongy and compressive resistant cryogels with shape recovery ability as ideal scaffolds to support cell adhesion for tissue regeneration. *Reactive and Functional Polymers*, 189:105607, 2023. ISSN 1381-5148. doi: https://doi.org/10.1016/j.reactfunctpolym.2023.105607. URL https://www.sciencedirect.com/science/article/pii/S1381514823001104.

[16] Paul J. Flory and John Rehner. Statistical mechanics of cross-linked polymer networks. i. rubberlike elasticity. *Journal of Chemical Physics*, 11:512–520, 1943.

[17] Paul J. Flory and John Rehner. Statistical mechanics of cross-linked polymer networks. ii. swelling. *Journal of Chemical Physics*, 11:521–526, 1943.

[18] Rangan Mallik and David S Hage. Affinity monolith chromatography. *Journal of separation science*, 29(12):1686–1704, 2006.

[19] Gizem Ertürk and Bo Mattiasson. Cryogels-versatile tools in bioseparation. *Journal of Chromatography A*, 1357:24–35, 2014. ISSN 0021-9673. doi: https://doi.org/10.1016/j.chroma.2014.05.055. URL https://www.sciencedirect.com/science/article/pii/S0021967314008218. Advanced Materials for Separation Science.

[20] Niloofar Babanejad, Kwadwo Mfoafo, Ershuai Zhang, Yadollah Omidi, Reza Razeghifard, and Hossein Omidian. Applications of cryostructures in the chromatographic separation of biomacromolecules. *Journal of Chromatography A*, 1683:463546, 2022. ISSN 0021-9673. doi: https://doi.org/10.1016/j.chroma.2022.463546. URL https://www.sciencedirect.com/science/article/pii/S0021967322007373.

[21] John H Knox. Band dispersion in chromatography – a new view of a-term dispersion. *Journal of Chromatography A*, 831(1):3–15, 1999. ISSN 0021-9673. doi: https://doi.org/10.1016/S0021-9673(98)00497-X. URL https://www.sciencedirect.com/science/article/pii/S002196739800497X.

[22] Mark R. Schure, Robert S. Maier, Daniel M. Kroll, and H. Ted Davis. Simulation of packed-bed chromatography utilizing high-resolution flow fields: Comparison with models. *Analytical Chemistry*, 74(23):6006–6016, 2002. doi: 10.1021/ac0204101. URL https://doi.org/10.1021/ac0204101. PMID: 12498196.

[23] Mark R. Schure, Robert S. Maier, Daniel M. Kroll, and H. Ted Davis. Simulation of ordered packed beds in chromatography. *Journal of Chromatography A*, 1031(1):79–86, 2004. ISSN 0021-9673. doi: https://doi.org/10.1016/j.chroma.2003.12.030. URL https://www.sciencedirect.com/science/article/pii/S0021967303023239. 27th International Symposium on High-Performance Liquid-Phase Separations and Related Techniques. Part II.

[24] Conan Fee, Suhas Nawada, and Simone Dimartino. 3d printed porous media columns with fine control of column packing morphology. *Journal of Chromatography A*, 1333:18–24, 2014. ISSN 0021-9673. doi: https://doi.org/10.1016/j.chroma.2014.01.043. URL https://www.sciencedirect.com/science/article/pii/S0021967314001253.

[25] Conan Fee. 3d-printed porous bed structures. *Current Opinion in Chemical Engineering*, 18:10–15, 2017. ISSN 2211-3398. doi: https://doi.org/10.1016/j.coche.2017.07.003. URL https://www.sciencedirect.com/science/article/pii/S2211339817300370. Biotechnology and bioprocess engineering / Process systems engineering.

[26] K. Broeckhoven and G. Desmet. Advances and innovations in liquid chromatography stationary phase supports. *Analytical Chemistry*, 93(1):257–272, 2021. doi: 10.1021/acs.analchem.0c04466. URL https://doi.org/10.1021/acs.analchem.0c04466. PMID: 33300336.

[27] P. Gzil, N. Vervoort, G. V. Baron, and G. Desmet. Advantages of perfectly ordered 2d porous pillar arrays over packed bed columns for lc separations: A theoretical analysis. *Analytical Chemistry*, 75(22):6244–6250, 2003. doi: 10.1021/ac034345m. URL https://doi.org/10.1021/ac034345m. PMID: 14616008.

[28] Wim De Malsche, Han Gardeniers, and Gert Desmet. Experimental study of porous silicon shell pillars under retentive conditions. *Analytical Chemistry*, 80(14):5391–5400, 2008. doi: 10.1021/ac800424q. URL https://doi.org/10.1021/ac800424q. PMID: 18558724.

[29] Long Li, Xiaohong Yan, Jian Yang, and Qiuwang Wang. Numerical investigation on band-broadening characteristics of an ordered packed bed with novel particles. *Applied Energy*, 185:2168–2180, 2017. ISSN 0306-2619. doi: https://doi.org/10.1016/j.apenergy.2016.03.045. URL https://www.sciencedirect.com/science/article/pii/S0306261916303658. Clean, Efficient and Affordable Energy for a Sustainable Future.

[30] Suhas Nawada, Simone Dimartino, and Conan Fee. Dispersion behavior of 3d-printed columns with homogeneous microstructures comprising differing element shapes. *Chemical Engineering Science*, 164:90–98, 2017. ISSN 0009-2509. doi: https://doi.org/10.1016/j.ces.2017.02.012. URL https://www.sciencedirect.com/science/article/pii/S0009250917301100.

[31] Fabian Dolamore, Conan Fee, and Simone Dimartino. Modelling ordered packed beds of spheres: The importance of bed orientation and the influence of tortuosity on dispersion. *Journal of Chromatography A*, 1532:150–160, 2018. ISSN 0021-9673. doi: https://doi.org/10.1016/j.chroma.2017.12.004. URL https://www.sciencedirect.com/science/article/pii/S0021967317317648.

[32] Fabian Dolamore, Simone Dimartino, and Conan J. Fee. Numerical elucidation of flow and dispersion in ordered packed beds: Nonspherical polygons and the effect of particle overlap on chromatographic performance. *Analytical Chemistry*, 91(23):15009–15016, 2019. doi: 10.1021/acs.analchem.9b03598. URL https://doi.org/10.1021/acs.analchem.9b03598. PMID: 31684719.

[33] Ghodsiehsadat Jahanmir and Ying Chau. Chapter 9 - mathematical models of drug release from degradable hydrogels. In Alexandru Mihai Grumezescu, editor, *Biomedical Applications of Nanoparticles*, pages 233–269. William Andrew Publishing, 2019. ISBN 978-0-12-816506-5. doi: https://doi.org/10.1016/B978-0-12-816506-5.00002-4. URL https://www.sciencedirect.com/science/article/pii/B9780128165065000024.

[34] Yong Kiel Sung and Sung Wan Kim. Recent advances in polymeric drug delivery systems. *Biomaterials Research*, 24(1):12, 2020.

[35] Aydin Bordbar-Khiabani and Michael Gasik. Smart hydrogels for advanced drug delivery systems. *International Journal of Molecular Sciences*, 23(7), 2022. ISSN 1422-0067. doi: 10.3390/ijms23073665. URL `https://www.mdpi.com/1422-0067/23/7/3665`.

[36] Boya Liu and Kuo Chen. Advances in hydrogel-based drug delivery systems. *Gels*, 10(4), 2024. ISSN 2310-2861. doi: 10.3390/gels10040262. URL `https://www.mdpi.com/2310-2861/10/4/262`.

[37] Vladimir I Lozinsky. Cryogels on the basis of natural and synthetic polymers: preparation, properties and application. *Russian Chemical Reviews*, 71(6):489–511, 2002.

[38] Vladimir I Lozinsky, Igor Yu Galaev, Fatima M Plieva, Irina N Savina, Hans Jungvid, and Bo Mattiasson. Polymeric cryogels as promising materials of biotechnological interest. *TRENDS in Biotechnology*, 21(10):445–451, 2003.

[39] Enrique Seoane-Vazquez, Rosa Rodriguez-Monguio, and Richard Hansen. Interchangeability, safety and efficacy of modified-release drug formulations in the usa: the case of opioid and other nervous system drugs. *Clinical drug investigation*, 36(4):281–292, 2016.

[40] Luke O Jones, Leah Williams, Tasmin Boam, Martin Kalmet, Chidubem Oguike, and Fiona L Hatton. Cryogels: recent applications in 3d-bioprinting, injectable cryogels, drug delivery, and wound healing. *Beilstein Journal of Organic Chemistry*, 17(1): 2553–2569, 2021.

[41] Settimio Pacelli, Laura Di Muzio, Patrizia Paolicelli, Valeria Fortunati, Stefania Petralito, Jordan Trilli, and Maria Antonietta Casadei. Dextran-polyethylene glycol cryogels as spongy scaffolds for drug delivery. *International Journal of Biological Macromolecules*, 166:1292–1300, 2021. ISSN 0141-8130. doi: https://doi.org/10.1016/j.ijbiomac.2020.10.273. URL `https://www.sciencedirect.com/science/article/pii/S0141813020349102`.

[42] O. Franssen, L. Vandervennet, P. Roders, and W.E. Hennink. Degradable dextran hydrogels: controlled release of a model protein from cylinders and microspheres. *Journal of Controlled Release*, 60(2):211–221, 1999. ISSN 0168-3659. doi: https://doi.org/10.1016/S0168-3659(99)00074-7. URL `https://www.sciencedirect.com/science/article/pii/S0168365999000747`.

[43] Jianyu Li and David J Mooney. Designing hydrogels for controlled drug delivery. *Nature Reviews Materials*, 1(12):1–17, 2016.

[44] Jiaen Wu, Zixin Zhang, Jin'ge Gu, Weixian Zhou, Xiaoyu Liang, Guoqiang Zhou, Charles C. Han, Shanshan Xu, and Ying Liu. Mechanism of a long-term controlled drug release system based on simple blended electrospun fibers. *Journal of Controlled Release*, 320:337–346, 2020. ISSN 0168-3659. doi: https://doi.org/10.1016/j.

jconrel.2020.01.020. URL https://www.sciencedirect.com/science/article/pii/S0168365920300286.

[45] Annika Wartenberg, Jürgen Weisser, and Matthias Schnabelrauch. Glycosaminoglycan-based cryogels as scaffolds for cell cultivation and tissue regeneration. *Molecules*, 26(18), 2021. ISSN 1420-3049. doi: 10.3390/molecules26185597. URL https://www.mdpi.com/1420-3049/26/18/5597.

[46] Ping I Lee. Kinetics of drug release from hydrogel matrices. *Journal of Controlled Release*, 2:277–288, 1985.

[47] Manish Singh, Janice A Lumpkin, and Joel Rosenblatt. Mathematical modeling of drug release from hydrogel matrices via a diffusion coupled with desorption mechanism. *Journal of controlled release*, 32(1):17–25, 1994.

[48] Diego Caccavo, Sara Cascone, Gaetano Lamberti, and Anna Angela Barba. Controlled drug release from hydrogel-based matrices: Experiments and modeling. *International journal of pharmaceutics*, 486(1-2):144–152, 2015.

[49] Settimio Pacelli, Patrizia Paolicelli, Michele Avitabile, Gabriele Varani, Laura Di Muzio, Stefania Cesa, Jacopo Tirillò, Cecilia Bartuli, Martina Nardoni, Stefania Petralito, et al. Design of a tunable nanocomposite double network hydrogel based on gellan gum for drug delivery applications. *European Polymer Journal*, 104:184–193, 2018.

[50] Diego Caccavo, Gaetano Lamberti, and Anna Angela Barba. Mechanics and drug release from poroviscoelastic hydrogels: Experiments and modeling. *European Journal of Pharmaceutics and Biopharmaceutics*, 152:299–306, 2020.

[51] Pınar Öncel, Kemal Çetin, Aykut Arif Topçu, Handan Yavuz, and Adil Denizli. Molecularly imprinted cryogel membranes for mitomycin c delivery. *Journal of Biomaterials Science, Polymer Edition*, 28(6):519–531, 2017.

[52] Ecaterina Stela Dragan, Maria Valentina Dinu, Claudiu Augustin Ghiorghita, Maria Marinela Lazar, and Florica Doroftei. Preparation and characterization of semi-ipn cryogels based on polyacrylamide and poly (n, n-dimethylaminoethyl methacrylate); functionalization of carrier with monochlorotriazinyl-β-cyclodextrin and release kinetics of curcumin. *Molecules*, 26(22):6975, 2021.

[53] Sophie Groult, Sytze Buwalda, and Tatiana Budtova. Pectin hydrogels, aerogels, cryogels and xerogels: Influence of drying on structural and release properties. *European Polymer Journal*, 149:110386, 2021.

[54] Ali Akbari, Hessam Jafari, Gholamreza Gohari, Gader Kheiri, and Gholam Reza Mahdavinia. Fulvic acid-embedded poly (vinyl alcohol)–zinc oxide hydrogel nanocomposite:

synthesis, characterization, swelling and release kinetic. *International Nano Letters*, 11(4):347–354, 2021.

[55] Marta Szekalska, Katarzyna Sosnowska, Magdalena Wróblewska, Anna Basa, and Katarzyna Winnicka. Does the freeze–thaw technique affect the properties of the alginate/chitosan glutamate gels with posaconazole as a model antifungal drug? *International Journal of Molecular Sciences*, 23(12):6775, 2022.

[56] Chiara Zagni, Alessandro Coco, Tommaso Mecca, Giusy Curcuruto, Vincenzo Patamia, Katia Mangano, Antonio Rescifina, and Sabrina Carola Carroccio. Sponge-like macroporous cyclodextrin-based cryogels for controlled drug delivery. *Materials Chemistry Frontiers*, 7(13):2693–2705, 2023.

[57] T. Higuchi. Mechanism of sustained-action medication. theoretical analysis of rate of release of solid drugs dispersed in solid matrices. *Journal of Pharmaceutical Sciences*, 52(12):1145–1149, 1963. doi: https://doi.org/10.1002/jps.2600521210. URL `https://onlinelibrary.wiley.com/doi/abs/10.1002/jps.2600521210`.

[58] Richard W. Korsmeyer, Robert Gurny, Eric Doelker, Pierre Buri, and Nikolaos A. Peppas. Mechanisms of solute release from porous hydrophilic polymers. *International Journal of Pharmaceutics*, 15(1):25–35, 1983. ISSN 0378-5173. doi: https://doi.org/10.1016/0378-5173(83)90064-9. URL `https://www.sciencedirect.com/science/article/pii/0378517383900649`.

[59] Philip L. Ritger and Nikolaos A. Peppas. A simple equation for description of solute release i. fickian and non-fickian release from non-swellable devices in the form of slabs, spheres, cylinders or discs. *Journal of Controlled Release*, 5(1):23–36, 1987. ISSN 0168-3659. doi: https://doi.org/10.1016/0168-3659(87)90034-4. URL `https://www.sciencedirect.com/science/article/pii/0168365987900344`.

[60] Philip L Ritger and Nikolaos A Peppas. A simple equation for description of solute release ii. fickian and anomalous release from swellable devices. *Journal of controlled release*, 5(1):37–42, 1987.

[61] Settimio Pacelli, Laura Di Muzio, Patrizia Paolicelli, Valeria Fortunati, Stefania Petralito, Jordan Trilli, and Maria Antonietta Casadei. Dextran-polyethylene glycol cryogels as spongy scaffolds for drug delivery. *International Journal of Biological Macromolecules*, 166:1292–1300, 2021. ISSN 0141-8130. doi: https://doi.org/10.1016/j.ijbiomac.2020.10.273. URL `https://www.sciencedirect.com/science/article/pii/S0141813020349102`.

[62] Georgy L Georgiev, Barbara Trzebicka, Bistra Kostova, and Petar D Petrov. Super-macroporous dextran cryogels via uv-induced crosslinking: synthesis and characterization. *Polymer International*, 66(9):1306–1311, 2017. doi: https://doi.org/10.1002/pi.

5386. URL https://scijournals.onlinelibrary.wiley.com/doi/abs/10.1002/pi.5386.

[63] Haifeng Ni, Sunxiang Qian, Jie Lu, Jie Feng, Xiao-zhou Mou, and Jing Zhang. Natural polysaccharide delivery platforms with multiscale structure used for cancer chemoimmunotherapy. *Molecular Pharmaceutics*, 20(11):5778–5789, 2023. doi: 10.1021/acs.molpharmaceut.3c00633. URL https://doi.org/10.1021/acs.molpharmaceut.3c00633. PMID: 37752866.

[64] Parvaiz Ahmad Shiekh, Syed Muntazir Andrabi, Anamika Singh, S. Majumder, and Ashok Kumar. Designing cryogels through cryostructuring of polymeric matrices for biomedical applications. *European Polymer Journal*, 144:110234, 2021. ISSN 0014-3057. doi: https://doi.org/10.1016/j.eurpolymj.2020.110234. URL https://www.sciencedirect.com/science/article/pii/S0014305720319510.

[65] Maria del Mar Fernández Sandra Gonzalo-Flores Silvia Villar-Rodil Julio San Román Nimet Bölgen, Maria Rosa Aguilar and Erhan Pişkin. Thermoresponsive biodegradable hema–lactate–dextran-co-nipa cryogels for controlled release of simvastatin. *Artificial Cells, Nanomedicine, and Biotechnology*, 43(1):40–49, 2015. doi: 10.3109/21691401.2013.837475. URL https://doi.org/10.3109/21691401.2013.837475.

[66] M Iv Slavkova, DB Momekova, BD Kostova, G Tz Momekov, and PD Petrov. Novel dextran/β-cyclodextrin and dextran macroporous cryogels for topical delivery of curcumin in the treatment of cutaneous t-cell lymphoma. *Bulg. Chem. Commun*, 49(4): 792–799, 2017.

[67] Dong Lei, Jing Zhao, Chenhui Zhu, Min Jiang, Pei Ma, Yu Mi, and Daidi Fan. Multifunctional oxidized dextran cross-linked alkylated chitosan/drug-loaded and silver-doped mesoporous bioactive glass cryogel for hemostasis of noncompressible wounds. *Gels*, 9(6), 2023. ISSN 2310-2861. doi: 10.3390/gels9060455. URL https://www.mdpi.com/2310-2861/9/6/455.

[68] Laurent Simon. A computational procedure for assessing the dynamic performance of diffusion-controlled transdermal delivery devices. *Pharmaceutics*, 3(3):485–496, 2011.

[69] Margarethe Hauck, Jan Dittmann, Berit Zeller-Plumhoff, Roshani Madurawala, Dana Hellmold, Carolin Kubelt, Michael Synowitz, Janka Held-Feindt, Rainer Adelung, Stephan Wulfinghoff, et al. Fabrication and modelling of a reservoir-based drug delivery system for customizable release. *Pharmaceutics*, 14(4):777, 2022.

[70] George Kalosakas and Eleni Panagopoulou. Lag time in diffusion-controlled release formulations containing a drug-free outer layer. *Processes*, 10(12):2592, 2022.

[71] P Volpi, L De Girolamo, et al. Rigenerazione tissutale: applicazioni cliniche nel trattamento della cartilagine articolare. *Giornale Italiano di Ortopedia e Traumatologia*, 36:200–205, 2010.

[72] Alondra Escudero-Castellanos, Blanca E Ocampo-García, Ma Victoria Domínguez-García, Jaime Flores-Estrada, and Miriam V Flores-Merino. Hydrogels based on poly (ethylene glycol) as scaffolds for tissue engineering application: biocompatibility assessment and effect of the sterilization process. *Journal of Materials Science: Materials in Medicine*, 27(12):176, 2016.

[73] Qiu Li Loh and Cleo Choong. Three-dimensional scaffolds for tissue engineering applications: role of porosity and pore size. *Tissue Engineering Part B: Reviews*, 19(6), 2013.

[74] Yongsung Hwang, Nivedita Sangaj, and Shyni Varghese. Interconnected macroporous poly (ethylene glycol) cryogels as a cell scaffold for cartilage tissue engineering. *Tissue Engineering Part A*, 16(10):3033–3041, 2010.

[75] Laura J Bray, Constanze Secker, Berline Murekatete, Jana Sievers, Marcus Binner, Petra B Welzel, and Carsten Werner. Three-dimensional in vitro hydro-and cryogel-based cell-culture models for the study of breast-cancer metastasis to bone. *Cancers*, 10(9):292, 2018.

[76] Yongsung Hwang, Chao Zhang, and Shyni Varghese. Poly (ethylene glycol) cryogels as potential cell scaffolds: effect of polymerization conditions on cryogel microstructure and properties. *Journal of Materials Chemistry*, 20(2):345–351, 2010.

[77] Masao Doi. *Introduction to polymer physics*. Oxford university press, 1996.

[78] P. Colombo, R. Bettini, P. Santi, A. De Ascentiis, and N.A. Peppas. Analysis of the swelling and release mechanisms from drug delivery systems with emphasis on drug solubility and water transport. *Journal of Controlled Release*, 39(2):231–237, 1996. ISSN 0168-3659. doi: https://doi.org/10.1016/0168-3659(95)00158-1. URL `https://www.sciencedirect.com/science/article/pii/0168365995001581`. Proceedings of the Seventh International Symposium on Recent Advances in Drug Delivery Systems.

[79] José Augusto Ferreira, Paula de Oliveira, Mario Grassi, and Giuseppe Romanazzi. Drug release from viscoelastic swelling polymeric platforms. *SIAM Journal on Applied Mathematics*, 78(3):1378–1401, 2018.

[80] Fahimeh Farshi Azhar, Ali Olad, and Roya Salehi. Fabrication and characterization of chitosan–gelatin/nanohydroxyapatite–polyaniline composite with potential application in tissue engineering scaffolds. *Designed Monomers and Polymers*, 17(7):654–667, 2014.

[81] Pedro J Díaz-Payno, Maria Kalogeropoulou, Iain Muntz, Esther Kingma, Nicole Kops, Matteo D'Este, Gijsje H Koenderink, Lidy E Fratila-Apachitei, Gerjo JVM van Osch, and Amir A Zadpoor. Swelling-dependent shape-based transformation of a human mesenchymal stromal cells-laden 4d bioprinted construct for cartilage tissue engineering. *Advanced healthcare materials*, 12(2):2201891, 2023.

[82] D. Ambrosi. Infiltration through deformable porous media. *ZAMM - Journal of Applied Mathematics and Mechanics / Zeitschrift für Angewandte Mathematik und Mechanik*, 82(2):115–124, 2002. doi: https://doi.org/10.1002/1521-4001(200202)82:2<115::AID-ZAMM115>3.0.CO;2-4. URL https://onlinelibrary.wiley.com/doi/abs/10.1002/1521-4001%28200202%2982%3A2%3C115%3A%3AAID-ZAMM115%3E3.0.CO%3B2-4.

[83] Christopher W. MacMinn, Eric R. Dufresne, and John S. Wettlaufer. Large deformations of a soft porous material. *Phys. Rev. Appl.*, 5:044020, Apr 2016. doi: 10.1103/PhysRevApplied.5.044020. URL https://link.aps.org/doi/10.1103/PhysRevApplied.5.044020.

[84] Olivier Coussy. *Poromechanics*. John Wiley & Sons, 2004.

[85] A. Lucantonio, P. Nardinocchi, and L. Teresi. Transient analysis of swelling-induced large deformations in polymer gels. *Journal of the Mechanics and Physics of Solids*, 61(1):205–218, 2013. ISSN 0022-5096. doi: https://doi.org/10.1016/j.jmps.2012.07.010. URL https://www.sciencedirect.com/science/article/pii/S0022509612001548.

[86] Pär Arvidsson, Fatima M. Plieva, Irina N. Savina, Vladimir I. Lozinsky, Sara Fexby, Leif Bülow, Igor Yu. Galaev, and Bo Mattiasson. Chromatography of microbial cells using continuous supermacroporous affinity and ion-exchange columns. *Journal of Chromatography A*, 977(1):27–38, 2002. ISSN 0021-9673. doi: https://doi.org/10.1016/S0021-9673(02)01114-7. URL https://www.sciencedirect.com/science/article/pii/S0021967302011147.

[87] Ashok Kumar and Akshay Srivastava. Cell separation using cryogel-based affinity chromatography. *Nature protocols*, 5(11):1737–1747, 2010.

[88] Roberto Mauri. Dispersion, convection, and reaction in porous media. *Physics of Fluids A: Fluid Dynamics*, 3(5):743–756, 1991.

[89] J Salles, J-F Thovert, Renaud Delannay, L Prevors, J-L Auriault, and PM Adler. Taylor dispersion in porous media. determination of the dispersion tensor. *Physics of Fluids A: Fluid Dynamics*, 5(10):2348–2376, 1993.

[90] OA Plumb and S Whitaker. Dispersion in heterogeneous porous media: 1. local volume averaging and large-scale averaging. *Water Resources Research*, 24(7):913–926, 1988.

[91] Xiaohong Yan, Qiuwang Wang, and Haim H Bau. Dispersion in retentive pillar array columns. *Journal of Chromatography A*, 1217(8):1332–1342, 2010.

[92] Howard Brenner and Lawrence J Gaydos. The constrained brownian movement of spherical particles in cylindrical pores of comparable radius: Models of the diffusive and convective transport of solute molecules in membranes and porous media. *Journal of Colloid and Interface Science*, 58(2):312–356, 1977.

[93] Shimon Haber and Roberto Mauri. Lagrangian approach to time-dependent laminar dispersion in rectangular conduits. part 1. two-dimensional flows. *Journal of Fluid Mechanics*, 190:201–215, 1988.

[94] Gianluca Boccardo, Igor M Sokolov, and Amir Paster. An improved scheme for a robin boundary condition in discrete-time random walk algorithms. *Journal of Computational Physics*, 374:1152–1165, 2018.

[95] Frederick Matheuse, Sander Deridder, and Gert Desmet. An explicit expression for the retention factor and velocity dependency of the mobile zone mass transfer band broadening in packed spheres beds used in liquid chromatography. *Journal of Chromatography A*, 1634:461710, 2020.

[96] Jan De Smet, Piotr Gzil, Nico Vervoort, H Verelst, GV Baron, and G Desmet. Influence of the pillar shape on the band broadening and the separation impedance of perfectly ordered 2-d porous chromatographic media. *Analytical chemistry*, 76(13):3716–3726, 2004.

[97] WNE van Dijk-Wolthuis, O Franssen, H Talsma, MJ Van Steenbergen, JJ Kettenes-Van Den Bosch, and WE Hennink. Synthesis, characterization, and polymerization of glycidyl methacrylate derivatized dextran. *Macromolecules*, 28(18):6317–6322, 1995.

[98] Laura Di Muzio, Patrizia Paolicelli, Chiara Brandelli, Stefania Cesa, Jordan Trilli, Stefania Petralito, and Maria Antonietta Casadei. Injectable and in situ gelling dextran derivatives containing hydrolyzable groups for the delivery of large molecules. *Gels*, 7 (4):150, 2021.

[99] W.N.E. van Dijk-Wolthuls, S.K.Y. Tsang, and J.J. Kettenes-van den BoschW.E. Hennink. A new class of polymerizable dextrans with hydrolyzable groups: hydroxyethyl methacrylated dextran with and without oligolactate spacer. *Polymer*, 38(25):6235–6242, 1997. ISSN 0032-3861. doi: https://doi.org/10.1016/S0032-3861(97)00189-4. URL `https://www.sciencedirect.com/science/article/pii/S0032386197001894`.

[100] Sabyasachi Maiti, Biswajit Maji, and Harsh Yadav. Progress on green crosslinking of polysaccharide hydrogels for drug delivery and tissue engineering applications. *Carbohydrate Polymers*, page 121584, 2023.

[101] Alex Carvalho Alavarse, Emilli Caroline Garcia Frachini, Rafael Leonardo Cruz Gomes da Silva, Vitoria Hashimoto Lima, Amin Shavandi, and Denise Freitas Siqueira Petri. Crosslinkers for polysaccharides and proteins: Synthesis conditions, mechanisms, and crosslinking efficiency, a review. *International journal of biological macromolecules*, 202:558–596, 2022.

[102] Elizabeth A Pumford, Brooke A Jackson Hoffman, and Andrea M Kasko. Nontoxic initiator alternatives to temed for redox hydrogel polymerization. *ACS Applied Bio Materials*, 7(4):2264–2271, 2024.

[103] Elaine Halligan, Billy Shu Hieng Tie, Declan Mary Colbert, Mohamad Alsaadi, Shuo Zhuo, Gavin Keane, and Luke M Geever. Synthesis and characterisation of hydrogels based on poly (n-vinylcaprolactam) with diethylene glycol diacrylate. *Gels*, 9(6):439, 2023.

[104] Joseph J Webber and M Grae Worster. Cryosuction and freezing hydrogels. 481(2310): 20240721, 2025.

[105] M. Avalle, G. Belingardi, and R. Montanini. Characterization of polymeric structural foams under compressive impact loading by means of energy-absorption diagram. *International Journal of Impact Engineering*, 25(5):455–472, 2001. ISSN 0734-743X. doi: https://doi.org/10.1016/S0734-743X(00)00060-9. URL `https://www.sciencedirect.com/science/article/pii/S0734743X00000609`.

[106] Carolina Lauriola, Laura Di Muzio, Patrizia Paolicelli, Maria Antonietta Casadei, Claudia Sergi, Jacopo Tirillò, Vito Cosimo Carriero, and Alessandra Adrover. Experimental and modelling study of controlled release from dextran-based cryogels. *Pharmaceutics*, 16(10), 2024. ISSN 1999-4923. doi: 10.3390/pharmaceutics16101256. URL `https://www.mdpi.com/1999-4923/16/10/1256`.

[107] Martin C. Heller, John F. Carpenter, and Theodore W. Randolph. Application of a thermodynamic model to the prediction of phase separations in freeze-concentrated formulations for protein lyophilization. *Archives of Biochemistry and Biophysics*, 363 (2):191–201, 1999. ISSN 0003-9861. doi: https://doi.org/10.1006/abbi.1998.1078. URL `https://www.sciencedirect.com/science/article/pii/S0003986198910785`.

[108] Alessandra Adrover, Gabriele Varani, Patrizia Paolicelli, Stefania Petralito, Laura Di Muzio, Maria Antonietta Casadei, and Ingunn Tho. Experimental and modeling study of drug release from hpmc-based erodible oral thin films. *Pharmaceutics*, 10(4), 2018. ISSN 1999-4923. doi: 10.3390/pharmaceutics10040222. URL `https://www.mdpi.com/1999-4923/10/4/222`.

[109] Alessandra Adrover, Patrizia Paolicelli, Stefania Petralito, Laura Di Muzio, Jordan Trilli, Stefania Cesa, Ingunn Tho, and Maria Antonietta Casadei. Gellan gum/laponite

beads for the modified release of drugs: Experimental and modeling study of gastrointestinal release. *Pharmaceutics*, 11(4), 2019. ISSN 1999-4923. doi: 10.3390/pharmaceutics11040187. URL https://www.mdpi.com/1999-4923/11/4/187.

[110] U. Conte, P. Colombo, A. Gazzaniga, M.E. Sangalli, and A. La Manna. Swelling-activated drug delivery systems. *Biomaterials*, 9(6):489–493, 1988. ISSN 0142-9612. doi: https://doi.org/10.1016/0142-9612(88)90043-9. URL https://www.sciencedirect.com/science/article/pii/0142961288900439.

[111] Anna Gutowska, Jong Seok Bark, Ick Chan Kwon, You Han Bae, Younsik Cha, and Sung Wan Kim. Squeezing hydrogels for controlled oral drug delivery. *Journal of Controlled Release*, 48(2):141–148, 1997. ISSN 0168-3659. doi: https://doi.org/10.1016/S0168-3659(97)00041-2. URL https://www.sciencedirect.com/science/article/pii/S0168365997000412.

[112] Paolo Colombo, Ruggero Bettini, Patrizia Santi, and Nikolaos A. Peppas. Swellable matrices for controlled drug delivery: gel-layer behaviour, mechanisms and optimal performance. *Pharmaceutical Science Technology Today*, 3(6):198–204, 2000. ISSN 1461-5347. doi: https://doi.org/10.1016/S1461-5347(00)00269-8. URL https://www.sciencedirect.com/science/article/pii/S1461534700002698.

[113] H. Omidian and K. Park. Swelling agents and devices in oral drug delivery. *Journal of Drug Delivery Science and Technology*, 18(2):83–93, 2008. ISSN 1773-2247. doi: https://doi.org/10.1016/S1773-2247(08)50016-5. URL https://www.sciencedirect.com/science/article/pii/S1773224708500165.

[114] Muhammad Rizwan, Rosiyah Yahya, Aziz Hassan, Muhammad Yar, Ahmad Danial Azzahari, Vidhya Selvanathan, Faridah Sonsudin, and Cheyma Naceur Abouloula. ph sensitive hydrogels in drug delivery: Brief history, properties, swelling, and release mechanism, material selection and applications. *Polymers*, 9(4), 2017. ISSN 2073-4360. doi: 10.3390/polym9040137. URL https://www.mdpi.com/2073-4360/9/4/137.

[115] Rachel A. Hegab, Sibile Pardue, Xinggui Shen, Christopher Kevil, Nicholas A. Peppas, and Mary E. Caldorera-Moore. Effect of network mesh size and swelling to the drug delivery from ph responsive hydrogels. *Journal of Applied Polymer Science*, 137(25):48767, 2020. doi: https://doi.org/10.1002/app.48767. URL https://onlinelibrary.wiley.com/doi/abs/10.1002/app.48767.

[116] Amanina Setapa, Naveed Ahmad, Shalela Mohd Mahali, and Mohd Cairul Iqbal Mohd Amin. Mathematical model for estimating parameters of swelling drug delivery devices in a two-phase release. *Polymers*, 12(12), 2020. ISSN 2073-4360. doi: 10.3390/polym12122921. URL https://www.mdpi.com/2073-4360/12/12/2921.

[117] Fatma Zehra Kocak, Muhammad Yar, and Ihtesham U. Rehman. In vitro degradation, swelling, and bioactivity performances of in situ forming injectable chitosan-matrixed hydrogels for bone regeneration and drug delivery. *Biotechnology and Bioengineering*, 121(9):2767–2779, 2024. doi: https://doi.org/10.1002/bit.28755. URL https://analyticalsciencejournals.onlinelibrary.wiley.com/doi/abs/10.1002/bit.28755.

[118] Rong Wang, Chongling Cheng, Huiyun Wang, and Dayang Wang. Swollen hydrogel nanotechnology: Advanced applications of the rudimentary swelling properties of hydrogels. *ChemPhysMater*, 3(4):357–375, 2024. ISSN 2772-5715. doi: https://doi.org/10.1016/j.chphma.2024.07.006. URL https://www.sciencedirect.com/science/article/pii/S2772571524000445.

[119] Reza Foudazi, Ryan Zowada, Ica Manas-Zloczower, and Donald L Feke. Porous hydrogels: present challenges and future opportunities. *Langmuir*, 39(6):2092–2111, 2023.

[120] Jérémie Fromageau, Jean-Luc Gennisson, Cédric Schmitt, Roch L Maurice, Rosaire Mongrain, and Guy Cloutier. Estimation of polyvinyl alcohol cryogel mechanical properties with four ultrasound elastography methods and comparison with gold standard testings. *IEEE transactions on ultrasonics, ferroelectrics, and frequency control*, 54(3): 498–509, 2007.

[121] Nela Buchtová, Christophe Pradille, Jean-Luc Bouvard, and Tatiana Budtova. Mechanical properties of cellulose aerogels and cryogels. *Soft matter*, 15(39):7901–7908, 2019.

[122] Sujie Yu, Christophe Pradille, and Tatiana Budtova. Mechanical properties of carboxymethyl cellulose aerogels and cryogels. *Cellulose*, pages 1–14, 2025.

[123] Dilek Imren, Menemşe Gümüşderelioğlu, and Ali Güner. Synthesis and characterization of dextran hydrogels prepared with chlor-and nitrogen-containing crosslinkers. *Journal of applied polymer science*, 102(5):4213–4221, 2006.

[124] John Eckelt, Rei Sugaya, and Bernhard A Wolf. Pullulan and dextran: Uncommon composition dependent flory–huggins interaction parameters of their aqueous solutions. *Biomacromolecules*, 9(6):1691–1697, 2008.

[125] R.G.M. van der Sman. Scaling of flory-huggins interaction parameter for polyols with chain length and number of hydroxyl groups. *Food Hydrocolloids*, 96:396–401, 2019. ISSN 0268-005X. doi: https://doi.org/10.1016/j.foodhyd.2019.05.042. URL https://www.sciencedirect.com/science/article/pii/S0268005X19307714.

[126] Shaohua Yang, Dominic Gerber, Yanxia Feng, Nicolas Bain, Matthias Kuster, Laura de Lorenzis, Ye Xu, Eric R Dufresne, and Robert W Style. Dehydration drives damage in the freezing of brittle hydrogels. *Science Advances*, 10(34):eado7750, 2024.

[127] J. Billen and G. Desmet. Understanding and design of existing and future chromatographic support formats. *Journal of Chromatography A*, 1168(1):73–99, 2007. ISSN 0021-9673. doi: https://doi.org/10.1016/j.chroma.2007.07.069. URL https://www.sciencedirect.com/science/article/pii/S0021967307013222. Editors' Choice I.

[128] D. L. Mould and R. L. M. Synge. Electrokinetic ultrafiltration analysis of polysaccharides. a new approach to the chromatography of large molecules. *Analyst*, 77(921): 964–969, 1952. doi: 10.1039/AN9527700964. URL http://dx.doi.org/10.1039/AN9527700964.

[129] Stellan Hjertén, Jia-Li Liao, and Rong Zhang. High-performance liquid chromatography on continuous polymer beds. *Journal of Chromatography A*, 473:273–275, 1989. ISSN 0021-9673. doi: https://doi.org/10.1016/S0021-9673(00)91309-8. URL https://www.sciencedirect.com/science/article/pii/S0021967300913098.

[130] Fatima M Plieva, Irina N Savina, Sahar Deraz, Jonatan Andersson, Igor Yu Galaev, and Bo Mattiasson. Characterization of supermacroporous monolithic polyacrylamide based matrices designed for chromatography of bioparticles. *Journal of Chromatography B*, 807(1):129–137, 2004. ISSN 1570-0232. doi: https://doi.org/10.1016/j.jchromb.2004.01.050. URL https://www.sciencedirect.com/science/article/pii/S1570023204001126. 12th International Conference on Biopartitioning and Purification.

[131] Pär Arvidsson, Fatima M Plieva, Vladimir I Lozinsky, Igor Yu Galaev, and Bo Mattiasson. Direct chromatographic capture of enzyme from crude homogenate using immobilized metal affinity chromatography on a continuous supermacroporous adsorbent. *Journal of Chromatography A*, 986(2):275–290, 2003. ISSN 0021-9673. doi: https://doi.org/10.1016/S0021-9673(02)01871-X. URL https://www.sciencedirect.com/science/article/pii/S002196730201871X.

[132] Maria B Dainiak, Ashok Kumar, Fatima M Plieva, Igor Yu Galaev, and Bo Mattiasson. Integrated isolation of antibody fragments from microbial cell culture fluids using supermacroporous cryogels. *Journal of Chromatography A*, 1045(1):93–98, 2004. ISSN 0021-9673. doi: https://doi.org/10.1016/j.chroma.2004.06.029. URL https://www.sciencedirect.com/science/article/pii/S0021967304009409.

[133] Anuj Tripathi and Ashok Kumar. Integrated approach for -glucosidase purification from non-clarified crude homogenate using macroporous cryogel matrix. *Separation Science and Technology*, 48(16):2410–2417, 2013. doi: 10.1080/01496395.2013.807833. URL https://doi.org/10.1080/01496395.2013.807833.

[134] Irina N. Savina, Igor Yu. Galaev, and Bo Mattiasson. Anion-exchange supermacroporous monolithic matrices with grafted polymer brushes of n,n-dimethylaminoethylmethacrylate. *Journal of Chromatography A*, 1092(2):199–205, 2005. ISSN 0021-

9673. doi: https://doi.org/10.1016/j.chroma.2005.06.094. URL https://www.sciencedirect.com/science/article/pii/S0021967305014093.

[135] Fang Chen, Kejian Yao, Shaochuan Shen, and Junxian Yun. Influence of grafting conditions on the properties of polyacrylamide-based cation-exchange cryogels grafted with 2-acrylamido-2-methyl-1-propanesulfonic acid. *Chemical Engineering Science*, 63 (1):71–77, 2008. ISSN 0009-2509. doi: https://doi.org/10.1016/j.ces.2007.09.008. URL https://www.sciencedirect.com/science/article/pii/S0009250907007269.

[136] Shi-Peng Tao, Chuan Wang, and Yan Sun. Coating of nanoparticles on cryogel surface and subsequent double-modification for enhanced ion-exchange capacity of protein. *Journal of Chromatography A*, 1359:76–83, 2014. ISSN 0021-9673. doi: https://doi.org/10.1016/j.chroma.2014.07.019. URL https://www.sciencedirect.com/science/article/pii/S0021967314010887.

[137] Paula Chequer Gouveia Mól, Lizzy Ayra Alcântara Veríssimo, Luis Antonio Minim, Maurício Boscolo, Eleni Gomes, and Roberto da Silva. Production and capture of -glucosidase from thermoascus aurantiacus using a tailor made anionic cryogel. *Process Biochemistry*, 82:75–83, 2019. ISSN 1359-5113. doi: https://doi.org/10.1016/j.procbio.2019.03.029. URL https://www.sciencedirect.com/science/article/pii/S1359511318318841.

[138] Lucas Silva de Sousa, Flaviana S. Chaves, Rafael B. Ferraro, Adalberto Pessoa, and Luis Antonio Minim. A quaternary amine cryogel column for chromatographic capture of l-asparaginase. *Process Biochemistry*, 127:92–98, 2023. ISSN 1359-5113. doi: https://doi.org/10.1016/j.procbio.2023.01.016. URL https://www.sciencedirect.com/science/article/pii/S1359511323000223.

[139] Jagan M Billakanti and Conan J Fee. Characterization of cryogel monoliths for extraction of minor proteins from milk by cation exchange. *Biotechnology and bioengineering*, 103(6):1155–1163, 2009.

[140] Jialei Ye, Junxian Yun, Dong-Qiang Lin, Linhong Xu, Harald Kirsebom, Shaochuan Shen, Gensheng Yang, Kejian Yao, Yi-Xin Guan, and Shan-Jing Yao. Poly (hydroxyethyl methacrylate)-based composite cryogel with embedded macroporous cellulose beads for the separation of human serum immunoglobulin and albumin. *Journal of separation science*, 36(24):3813–3820, 2013.

[141] Junxian Yun, Xiuhong Cheng, Jialei Ye, Shaochuan Shen, Gensheng Yang, Kejian Yao, Harald Kirsebom, Dong-Qiang Lin, Yi-Xin Guan, and Shan-Jing Yao. Chromatographic adsorption of serum albumin and antibody proteins in cryogels with benzyl-quaternary amine ligands. *Journal of Chromatography A*, 1381:173–183, 2015. ISSN 0021-9673. doi: https://doi.org/10.1016/j.chroma.2014.11.081. URL https://www.sciencedirect.com/science/article/pii/S0021967314018792.

[142] Maomao Pan, Shaochuan Shen, Liang Chen, Bin Dai, Linhong Xu, Junxian Yun, Kejian Yao, Dong-Qiang Lin, and Shan-Jing Yao. Separation of lactoperoxidase from bovine whey milk by cation exchange composite cryogel embedded macroporous cellulose beads. *Separation and Purification Technology*, 147:132–138, 2015. ISSN 1383-5866. doi: https://doi.org/10.1016/j.seppur.2015.04.026. URL `https://www.sciencedirect.com/science/article/pii/S1383586615002506`.

[143] R. Dario Arrua, Paul R. Haddad, and Emily F. Hilder. Monolithic cryopolymers with embedded nanoparticles. ii. capillary liquid chromatography of proteins using charged embedded nanoparticles. *Journal of Chromatography A*, 1311:121–126, 2013. ISSN 0021-9673. doi: https://doi.org/10.1016/j.chroma.2013.08.077. URL `https://www.sciencedirect.com/science/article/pii/S0021967313013460`.

[144] Shasha Dong, Liang Chen, Bin Dai, Wilfred Johnson, Jialei Ye, Shaochuan Shen, Junxian Yun, Kejian Yao, Dong-Qiang Lin, and Shan-Jing Yao. Isolation of immunoglobulin g from bovine milk whey by poly (hydroxyethyl methacrylate)-based anion-exchange cryogel. *Journal of separation science*, 36(15):2387–2393, 2013.

[145] Yiran Tian, Xufeng Zhang, Xiyun Feng, Jinmeng Zhang, and Tianyi Zhong. Shapeable and underwater super-elastic cellulose nanofiber/alginate cryogels by freezing-induced oxa-michael reaction for efficient protein purification. *Carbohydrate Polymers*, 272:118498, 2021. ISSN 0144-8617. doi: https://doi.org/10.1016/j.carbpol.2021.118498. URL `https://www.sciencedirect.com/science/article/pii/S0144861721008857`.

[146] Songhong Zhang, Xinyu Gao, Mingyan Zhang, Yuye Wang, Weilong Cheng, Wenjing Zhang, Xiaoling Lou, and Junxian Yun. Chromatographic separation of ovalbumin by novel chitosan and poly(butyl methacrylate) nanogels-based anion-exchange cryogels. *Journal of Chromatography A*, 1758:466188, 2025. ISSN 0021-9673. doi: https://doi.org/10.1016/j.chroma.2025.466188. URL `https://www.sciencedirect.com/science/article/pii/S0021967325005345`.

[147] Mariana Oliveira Mendes, Ana Cristina Freitas de Oliveira Meira, Paula Chequer Gouveia Mól, Isabelle Cristina Oliveira Neves, Luis Antonio Minim, Jaime Vilela de Resende, and Lizzy Ayra Alcântara Veríssimo. Optimization of ion exchange cryogel functionalization via the epoxy method for protein adsorption from ora-pro-nobis (pereskia aculeata). *The Canadian Journal of Chemical Engineering*, 2025.

[148] Ashok Kumar, Fatima M Plieva, Igor Yu Galaev, and Bo Mattiasson. Affinity fractionation of lymphocytes using a monolithic cryogel. *Journal of Immunological Methods*, 283(1):185–194, 2003. ISSN 0022-1759. doi: https://doi.org/10.1016/j.jim.2003.09.017. URL `https://www.sciencedirect.com/science/article/pii/S0022175903003715`.

[149] Vibha Bansal, Pradip K Roychoudhury, Bo Mattiasson, and Ashok Kumar. Recovery of urokinase from integrated mammalian cell culture cryogel bioreactor and purification of the enzyme using p-aminobenzamidine affinity chromatography. *Journal of Molecular Recognition: An Interdisciplinary Journal*, 19(4):332–339, 2006.

[150] Josefin Ahlqvist, Ashok Kumar, Heléne Sundström, Erika Ledung, E. Gunnar Hörnsten, Sven-Olof Enfors, and Bo Mattiasson. Affinity binding of inclusion bodies on supermacroporous monolithic cryogels using labeling with specific antibodies. *Journal of Biotechnology*, 122(2):216–225, 2006. ISSN 0168-1656. doi: https://doi.org/10.1016/j.jbiotec.2005.09.007. URL https://www.sciencedirect.com/science/article/pii/S0168165605006097.

[151] Wim Noppe, Fatima M. Plieva, Igor Yu Galaev, Karen Vanhoorelbeke, Bo Mattiasson, and Hans Deckmyn. Immobilised peptide displaying phages as affinity ligands: Purification of lactoferrin from defatted milk. *Journal of Chromatography A*, 1101(1):79–85, 2006. ISSN 0021-9673. doi: https://doi.org/10.1016/j.chroma.2005.09.064. URL https://www.sciencedirect.com/science/article/pii/S0021967305018686.

[152] Amro Hanora, Fatima M. Plieva, Martin Hedström, Igor Yu. Galaev, and Bo Mattiasson. Capture of bacterial endotoxins using a supermacroporous monolithic matrix with immobilized polyethyleneimine, lysozyme or polymyxin b. *Journal of Biotechnology*, 118(4):421–433, 2005. ISSN 0168-1656. doi: https://doi.org/10.1016/j.jbiotec.2005.05.006. URL https://www.sciencedirect.com/science/article/pii/S0168165605002294.

[153] Kejian Yao, Junxian Yun, Shaochuan Shen, Lianghua Wang, Xingjiao He, and Xiaomei Yu. Characterization of a novel continuous supermacroporous monolithic cryogel embedded with nanoparticles for protein chromatography. *Journal of Chromatography A*, 1109(1):103–110, 2006. ISSN 0021-9673. doi: https://doi.org/10.1016/j.chroma.2006.01.014. URL https://www.sciencedirect.com/science/article/pii/S002196730600121X. Advances in Monoliths.

[154] Işık Perçin, Emel Sağlar, Handan Yavuz, Erol Aksöz, and Adil Denizli. Poly(hydroxyethyl methacrylate) based affinity cryogel for plasmid dna purification. *International Journal of Biological Macromolecules*, 48(4):577–582, 2011. ISSN 0141-8130. doi: https://doi.org/10.1016/j.ijbiomac.2011.01.022. URL https://www.sciencedirect.com/science/article/pii/S0141813011000286.

[155] Xiaoming Yu, Peng Zhao, Lihua Zhang, and Yukui Zhang. Screening of phage-displayed human liver cdna library against doxorubicin with drug-immobilized monolithic polyacrylamide cryogel. *Biomedical Chromatography*, 27(11):1574–1579, 2013.

[156] Gry Ravn Jespersen, Anders Laerke Nielsen, Finn Matthiesen, Henrik Sune Andersen, and Harald Kirsebom. Dual application of cryogel as solid support in peptide synthesis

and subsequent protein-capture. *Journal of Applied Polymer Science*, 130(6):4383–4391, 2013.

[157] Idris Guven, Orhan Gezici, Mevlut Bayrakci, and Massimo Morbidelli. Calixarene-immobilized monolithic cryogels for preparative protein chromatography. *Journal of Chromatography A*, 1558:59–68, 2018. ISSN 0021-9673. doi: https://doi.org/10.1016/j.chroma.2018.05.026. URL https://www.sciencedirect.com/science/article/pii/S0021967318306095.

[158] Paula Chequer Gouveia Mól, Lizzy Ayra Alcântara Veríssimo, Monique Renon Eller, Valéria Paula Rodrigues Minim, and Luis Antonio Minim. Development of an affinity cryogel for one step purification of lysozyme from chicken egg white. *Journal of Chromatography B*, 1044-1045:17–23, 2017. ISSN 1570-0232. doi: https://doi.org/10.1016/j.jchromb.2016.12.032. URL https://www.sciencedirect.com/science/article/pii/S1570023216310315.

[159] Jiasheng Shi, Henan Zhang, Qian Wang, Zhengyu Duan, Li Xu, Fenghao Guo, Yunfeng Xie, and Zhiyong Chen. Biomimetic rigid cryogels with aligned micro-sized tubular structures prepared by conventional redox-induced cryopolymerization in a freezer. *Chemical Engineering Journal*, 427:131903, 2022. ISSN 1385-8947. doi: https://doi.org/10.1016/j.cej.2021.131903. URL https://www.sciencedirect.com/science/article/pii/S1385894721034835.

[160] Lianghua Wang, Shaochuan Shen, Xingjiao He, Junxian Yun, Kejian Yao, and Shan-Jing Yao. Adsorption and elution behaviors of bovine serum albumin in metal-chelated affinity cryogel beds. *Biochemical Engineering Journal*, 42(3):237–242, 2008. ISSN 1369-703X. doi: https://doi.org/10.1016/j.bej.2008.07.002. URL https://www.sciencedirect.com/science/article/pii/S1369703X08002283.

[161] Igor Ferreira Fioravante and Sonia Maria Alves Bueno. Performance of polyacrylamide-alginate-based cryogel for igg purification from bovine serum by imac. *Process Biochemistry*, 118:413–424, 2022. ISSN 1359-5113. doi: https://doi.org/10.1016/j.procbio.2022.04.034. URL https://www.sciencedirect.com/science/article/pii/S1359511322001568.

[162] Márjorie Castro Pinto Porfirio, Jonathan Barbosa Santos, Annie Nolasco Alves, Leandro Soares Santos, Renata Cristina Ferreira Bonomo, and Rafael da Costa Ilhéu Fontan. Purification of pineapple bromelain by imac chromatography using chlorophyll-activated macroporous matrices. *Journal of Chromatography B*, 1234:124027, 2024. ISSN 1570-0232. doi: https://doi.org/10.1016/j.jchromb.2024.124027. URL https://www.sciencedirect.com/science/article/pii/S1570023224000357.

[163] Ilgım Göktürk, Işık Perçin, and Adil Denizli. Catalase purification from rat liver with iron-chelated poly(hydroxyethyl methacrylate-n-methacryloyl-(l)-glutamic acid)

cryogel discs. *Preparative Biochemistry & Biotechnology*, 46(6):602–609, 2016. doi: 10.1080/10826068.2015.1085400. URL https://doi.org/10.1080/10826068.2015.1085400. PMID: 26460882.

[164] Ayfer Menteş Ömür Acet and Mehmet Odabaşı. Cssessment of a new dual effective combo polymer structure for separation of lysozyme from hen egg white. *Polymer Bulletin*, 77(9):4679–4695, 2020. doi: 10.1007/s00289-019-02959-w. URL https://doi.org/10.1007/s00289-019-02959-w.

[165] Mahmut Erzengin, Nuri Ünlü, and Mehmet Odabaşı. A novel adsorbent for protein chromatography: Supermacroporous monolithic cryogel embedded with cu2+-attached sporopollenin particles. *Journal of Chromatography A*, 1218(3):484–490, 2011. ISSN 0021-9673. doi: https://doi.org/10.1016/j.chroma.2010.11.074. URL https://www.sciencedirect.com/science/article/pii/S0021967310016626.

[166] Okan Zenger and Gözde Baydemir Peşint. Preparation of molecularly imprinted bilayer cryogel columns for selective protein depletion. *Process Biochemistry*, 117:90–100, 2022. ISSN 1359-5113. doi: https://doi.org/10.1016/j.procbio.2022.03.018. URL https://www.sciencedirect.com/science/article/pii/S1359511322001003.

[167] Müge Andaç, Gözde Baydemir, Handan Yavuz, and Adil Denizli. Molecularly imprinted composite cryogel for albumin depletion from human serum. *Journal of Molecular Recognition*, 25(11):555–563, 2012. doi: https://doi.org/10.1002/jmr.2202. URL https://onlinelibrary.wiley.com/doi/abs/10.1002/jmr.2202.

[168] Sevgi Asliyuce, Lokman Uzun, Abbas Yousefi Rad, Serhat Unal, Ridvan Say, and Adil Denizli. Molecular imprinting based composite cryogel membranes for purification of anti-hepatitis b surface antibody by fast protein liquid chromatography. *Journal of Chromatography B*, 889-890:95–102, 2012. ISSN 1570-0232. doi: https://doi.org/10.1016/j.jchromb.2012.02.001. URL https://www.sciencedirect.com/science/article/pii/S1570023212000761.

[169] Nilay Bereli, Yeşeren Saylan, Lokman Uzun, Rıdvan Say, and Adil Denizli. l-histidine imprinted supermacroporous cryogels for protein recognition. *Separation and Purification Technology*, 82:28–35, 2011. ISSN 1383-5866. doi: https://doi.org/10.1016/j.seppur.2011.08.011. URL https://www.sciencedirect.com/science/article/pii/S1383586611004710.

[170] Nazan Demiryas, Nalan Tüzmen, Igor Yu Galaev, Erhan Pişkin, and Adil Denizli. Poly (acrylamide-allyl glycidyl ether) cryogel as a novel stationary phase in dye-affinity chromatography. *Journal of Applied Polymer Science*, 105(4):1808–1816, 2007.

[171] Sabina Huseynli, Gözde Baydemir, Esma Sarı, Assem Elkak, and Adil Denizli. Affinity composite cryogel discs functionalized with reactive red 120 and green he

4bd dye ligands: Application on the separation of human immunoglobulin g subclasses. *Materials Science and Engineering: C*, 46:77–85, 2015. ISSN 0928-4931. doi: https://doi.org/10.1016/j.msec.2014.10.007. URL https://www.sciencedirect.com/science/article/pii/S0928493114006262.

[172] Ceyhun Babac, Handan Yavuz, Igor Yu Galaev, Erhan Pişkin, and Adil Denizli. Binding of antibodies to concanavalin a-modified monolithic cryogel. *Reactive and Functional Polymers*, 66(11):1263–1271, 2006. ISSN 1381-5148. doi: https://doi.org/10.1016/j.reactfunctpolym.2006.03.007. URL https://www.sciencedirect.com/science/article/pii/S1381514806000678.

[173] Solmaz Hajizadeh, Harald Kirsebom, Andre Leistner, and Bo Mattiasson. Composite cryogel with immobilized concanavalin a for affinity chromatography of glycoproteins. *Journal of separation science*, 35(21):2978–2985, 2012.

[174] Gabriel Ramos Ferreira Gonçalves, Olga Reinert Ramos Gandolfi, Leandro Soares Santos, Renata Cristina Ferreira Bonomo, Cristiane Martins Veloso, Lizzy Ayra Alcântara Veríssimo, and Rafael da Costa Ilhéu Fontan. Immobilization of sugars in supermacroporous cryogels for the purification of lectins by affinity chromatography. *Journal of Chromatography B*, 1068-1069:71–77, 2017. ISSN 1570-0232. doi: https://doi.org/10.1016/j.jchromb.2017.10.019. URL https://www.sciencedirect.com/science/article/pii/S1570023217313193.

[175] Nilay Bereli, Gülsu Şener, Handan Yavuz, and Adil Denizli. Oriented immobilized anti-ldl antibody carrying poly(hydroxyethyl methacrylate) cryogel for cholesterol removal from human plasma. *Materials Science and Engineering: C*, 31(5):1078–1083, 2011. ISSN 0928-4931. doi: https://doi.org/10.1016/j.msec.2011.03.008. URL https://www.sciencedirect.com/science/article/pii/S0928493111001019.

[176] Monireh Bakhshpour, Aykut Arif Topcu, Nilay Bereli, Huseyin Alkan, and Adil Denizli. Poly (hydroxyethyl methacrylate) immunoaffinity cryogel column for the purification of human immunoglobulin m. *Gels*, 6(1):4, 2020.

[177] Kemal Çetin and Adil Denizli. Immunoaffinity microcryogels for purification of transferrin. *Journal of Chromatography B*, 1114-1115:5–12, 2019. ISSN 1570-0232. doi: https://doi.org/10.1016/j.jchromb.2019.03.017. URL https://www.sciencedirect.com/science/article/pii/S1570023218313783.

[178] Marc Zinggeler, Patrick L Fosso, Yan Hao, Thomas Brandstetter, and Jurgen Ruhe. Preparation of linear cryogel arrays as a microfluidic platform for immunochromatographic assays. *Analytical Chemistry*, 89(11):5697–5701, 2017.

[179] J.A. Queiroz, C.T. Tomaz, and J.M.S. Cabral. Hydrophobic interaction chromatography of proteins. *Journal of Biotechnology*, 87(2):143–159, 2001. ISSN 0168-

1656. doi: https://doi.org/10.1016/S0168-1656(01)00237-1. URL https://www.sciencedirect.com/science/article/pii/S0168165601002371.

[180] Ana Cristina Freitas de Oliveira, Isabelle Cristina Oliveira Neves, Jamile Alves Meireles Saraiva, Marcelle Flores Fernandes de Carvalho, Gioanni Aleixo Batista, Lizzy Ayra Alcântara Veríssimo, and Jaime Vilela de Resende. Capture of lysozyme on macroporous cryogels by hydrophobic affinity chromatography. *Separation Science and Technology*, 55(11):2012–2024, 2020. doi: 10.1080/01496395.2019.1617743. URL https://doi.org/10.1080/01496395.2019.1617743.

[181] Fatma Yılmaz, Nilay Bereli, Handan Yavuz, and Adil Denizli. Supermacroporous hydrophobic affinity cryogels for protein chromatography. *Biochemical Engineering Journal*, 43(3):272–279, 2009. ISSN 1369-703X. doi: https://doi.org/10.1016/j.bej.2008.10.009. URL https://www.sciencedirect.com/science/article/pii/S1369703X08003446.

[182] Deniz Türkmen and Adil Denizli. Phema based composite cryogels with loaded hydrophobic beads for lysozyme purification. *Colloids and Surfaces B: Biointerfaces*, 123:859–865, 2014. ISSN 0927-7765. doi: https://doi.org/10.1016/j.colsurfb.2014.10.034. URL https://www.sciencedirect.com/science/article/pii/S0927776514005839.

[183] Mahmut Erzengin, Gözde Baydemir Peşint, Okan Zenger, and Mehmet Odabaşı. Monolithic hydrophobic cryogel columns for protein separation. *Polymer Bulletin*, 79(3):1485–1499, 2022.

[184] Radwan Ahmed Tarish Abdullah and Koray Şarkaya. Interaction of lysozyme with solid supports cryogels containing imidazole functional group. *Journal of Chromatography B*, 1251:124405, 2025. ISSN 1570-0232. doi: https://doi.org/10.1016/j.jchromb.2024.124405. URL https://www.sciencedirect.com/science/article/pii/S1570023224004148.

[185] Nesibe Avcibaşi, Murat Uygun, M Emin Çorman, Sinan Akgöl, and Adil Denizli. Application of supermacroporous monolithic hydrophobic cryogel in capturing of albumin. *Applied biochemistry and biotechnology*, 162(8):2232–2243, 2010.

[186] Özlem Biçen Ünlüer, Ayça Özcan, and Lokman Uzun. Preparation of a novel hydrophobic affinity cryogel for adsorption of lipase and its utilization as a chromatographic adsorbent for fast protein liquid chromatography. *Biotechnology Progress*, 30 (2):376–382, 2014.

[187] Özlem Biçen Ünlüer, Ayça Özcan, and Lokman Uzun. Preparation of a novel hydrophobic affinity cryogel for adsorption of lipase and its utilization as a chromatographic adsorbent for fast protein liquid chromatography. *Biotechnology Progress*, 30 (2):376–382, 2014.

[188] Ana Cristina Freitas de Oliveira, Isabelle Cristina Oliveira Neves, Jamile Alves Meireles Saraiva, Marcelle Flores Fernandes de Carvalho, Gioanni Aleixo Batista, Lizzy Ayra Alcântara Veríssimo, and Jaime Vilela de Resende. Capture of lysozyme on macroporous cryogels by hydrophobic affinity chromatography. *Separation Science and Technology*, 55(11):2012–2024, 2020.

[189] Ilgım Göktürk, Yeşeren Saylan, Fatma Yılmaz, Fatma Kartal, and Adil Denizli. Phenylalanine functionalized cryogels for selective cholesterol removal from milk. *Chemical Papers*, 78(7):4307–4316, 2024.

[190] R. Dario Arrua, Anna Nordborg, Paul R. Haddad, and Emily. F. Hilder. Monolithic cryopolymers with embedded nanoparticles. i. capillary liquid chromatography of proteins using neutral embedded nanoparticles. *Journal of Chromatography A*, 1273:26–33, 2013. ISSN 0021-9673. doi: https://doi.org/10.1016/j.chroma.2012.10.068. URL `https://www.sciencedirect.com/science/article/pii/S0021967312016809`.

[191] Junxian Yun, Gry Ravn Jespersen, Harald Kirsebom, Per-Erik Gustavsson, Bo Mattiasson, and Igor Yu Galaev. An improved capillary model for describing the microstructure characteristics, fluid hydrodynamics and breakthrough performance of proteins in cryogel beds. *Journal of Chromatography A*, 1218(32):5487–5497, 2011. ISSN 0021-9673. doi: https://doi.org/10.1016/j.chroma.2011.06.056. URL `https://www.sciencedirect.com/science/article/pii/S0021967311008715`.

[192] Chunjie Liu, Haiyan Zhang, Liang Chen, and Bin Dai. A simplified capillary model for hydrodynamics simulation of cryogel continuous beds and particle packed beds. *Chemical Engineering Research and Design*, 145:203–212, 2019. ISSN 0263-8762. doi: https://doi.org/10.1016/j.cherd.2019.03.016. URL `https://www.sciencedirect.com/science/article/pii/S0263876219301157`.

[193] Jamille C Coimbra, Marcio A Martins, and Luis Antonio Minim. Analysis of flow profiles and mass transfer of monolithic chromatographic columns: the geometric influence of channels and tortuosity. *Brazilian Journal of Chemical Engineering*, 37(2): 425–438, 2020.

[194] S. Pawlowski, N. Nayak, M. Meireles, C.A.M. Portugal, S. Velizarov, and J.G. Crespo. Cfd modelling of flow patterns, tortuosity and residence time distribution in monolithic porous columns reconstructed from x-ray tomography data. *Chemical Engineering Journal*, 350:757–766, 2018. ISSN 1385-8947. doi: https://doi.org/10.1016/j.cej.2018.06.017. URL `https://www.sciencedirect.com/science/article/pii/S138589471831057X`.

[195] Dzmitry Hlushkou, Stefan Bruns, Andreas Seidel-Morgenstern, and Ulrich Tallarek. Morphology–transport relationships for silica monoliths: From physical reconstruction to pore-scale simulations. *Journal of separation science*, 34(16-17):2026–2037, 2011.

[196] Tibor Müllner, Klaus K Unger, and Ulrich Tallarek. Characterization of microscopic disorder in reconstructed porous materials and assessment of mass transport-relevant structural descriptors. *New Journal of Chemistry*, 40(5):3993–4015, 2016.

[197] Fréderick Matheuse, Koen Vanmol, Jürgen Van Erps, Wim De Malsche, Heidi Ottevaere, and Gert Desmet. On the potential use of two-photon polymerization to 3d print chromatographic packed bed supports. *Journal of Chromatography A*, 1663:462763, 2022. ISSN 0021-9673. doi: https://doi.org/10.1016/j.chroma.2021.462763. URL https://www.sciencedirect.com/science/article/pii/S0021967321008852.

[198] Federico Cantoni, Daniel Maher, Eugenia Bosler, Stefan Kühne, Laurent Barbe, Dirk Oberschmidt, Christophe Marquette, Rafael Taboryski, Maria Tenje, and Ada-Ioana Bunea. Round-robin testing of commercial two-photon polymerization 3d printers. *Additive Manufacturing*, 76:103761, 2023. ISSN 2214-8604. doi: https://doi.org/10.1016/j.addma.2023.103761. URL https://www.sciencedirect.com/science/article/pii/S2214860423003743.

[199] Christopher Salmean and Simone Dimartino. 3d-printed stationary phases with ordered morphology: state of the art and future development in liquid chromatography. *Chromatographia*, 82(1):443–463, 2019.

[200] Daniel A. Clarke, Fabian Dolamore, Conan J. Fee, Petrik Galvosas, and Daniel J. Holland. Investigation of flow through triply periodic minimal surface-structured porous media using mri and cfd. *Chemical Engineering Science*, 231:116264, 2021. ISSN 0009-2509. doi: https://doi.org/10.1016/j.ces.2020.116264. URL https://www.sciencedirect.com/science/article/pii/S000925092030796X.

[201] Fabian Dolamore, Benjamin Houlton, Conan J. Fee, Matthew J. Watson, and Daniel J. Holland. A numerical investigation of the hydrodynamic dispersion in triply periodic chromatographic stationary phases. *Journal of Chromatography A*, 1685:463637, 2022. ISSN 0021-9673. doi: https://doi.org/10.1016/j.chroma.2022.463637. URL https://www.sciencedirect.com/science/article/pii/S0021967322008287.

[202] A. Moussa, B. Huygens, C. Venditti, A. Adrover, and G. Desmet. On the contribution of the top and bottom walls in micro-pillar array columns and related high-aspect ratio chromatography systems. *Journal of Chromatography A*, 1720, 2024. doi: 10.1016/j.chroma.2024.464825. URL https://www.sciencedirect.com/science/article/pii/S0021967324001985.

[203] Anne Mary Gordon. Development, functionalisation, and characterisation of triply periodic minimum surface hydrogels for solid-tolerant chromatography. *PhD Thesis, University of Canterbury*, 2020.

[204] Sean Feast, Conan Fee, Tim Huber, and Daniel Clarke. Printed monolith adsorption as an alternative to expanded bed adsorption for purifying m13 bacteriophage. *Journal of Chromatography A*, 1652:462365, 2021. ISSN 0021-9673. doi: https://doi.org/10.1016/j.chroma.2021.462365. URL https://www.sciencedirect.com/science/article/pii/S0021967321004891.

[205] Mafalda G. Moleirinho, Sean Feast, Ana S. Moreira, Ricardo J.S. Silva, Paula M. Alves, Manuel J.T. Carrondo, Tim Huber, Conan Fee, and Cristina Peixoto. 3d-printed ordered bed structures for chromatographic purification of enveloped and non-enveloped viral particles. *Separation and Purification Technology*, 254:117681, 2021. ISSN 1383-5866. doi: https://doi.org/10.1016/j.seppur.2020.117681. URL https://www.sciencedirect.com/science/article/pii/S1383586620321559.

[206] Mariachiara Conti, Deirdre Boland, Carmen Heeran, Jodie A. Symington, James R. Pullen, and Simone Dimartino. Purification of monoclonal antibodies using novel 3d printed ordered stationary phases. *Journal of Chromatography A*, 1722:464873, 2024. ISSN 0021-9673. doi: https://doi.org/10.1016/j.chroma.2024.464873. URL https://www.sciencedirect.com/science/article/pii/S0021967324002474.

[207] Mariusz Belka and Tomasz Bączek. Additive manufacturing and related technologies – the source of chemically active materials in separation science. *TrAC Trends in Analytical Chemistry*, 142:116322, 2021. ISSN 0165-9936. doi: https://doi.org/10.1016/j.trac.2021.116322. URL https://www.sciencedirect.com/science/article/pii/S016599362100145X.

[208] Raffaele Mancino, Diego Caccavo, Anna Angela Barba, Gaetano Lamberti, Alice Biasin, Angelo Cortesi, Gabriele Grassi, Mario Grassi, and Michela Abrami. Agarose cryogels: Production process modeling and structural characterization. *Gels*, 9(9):765, 2023.

[209] Simone Dimartino, Mariachiara Conti, Rok Mravljak, Gabriele Picerni, and James R Pullen. Characterization of pore morphology and performance of 3d-printed porous polymers for chromatography. *Industrial & Engineering Chemistry Research*, 64(19): 9782–9793, 2025.

[210] Mariachiara Conti and Simone Dimartino. Materials for 3d printing of chromatographic stationary phases. *TrAC Trends in Analytical Chemistry*, 192:118301, 2025. ISSN 0165-9936. doi: https://doi.org/10.1016/j.trac.2025.118301. URL https://www.sciencedirect.com/science/article/pii/S0165993625001694.

[211] Hari Kalathil Balakrishnan, Ludovic F Dumée, Andrea Merenda, Cyril Aubry, Dan Yuan, Egan H Doeven, and Rosanne M Guijt. 3d printing functionally graded porous materials for simultaneous fabrication of dense and porous structures in membrane-integrated fluidic devices. *Small Structures*, 4(5):2200314, 2023.

[212] Huijun Li, Cavin Tan, and Lin Li. Review of 3d printable hydrogels and constructs. *Material & Design*, 159:20–38, 2018. ISSN 0264-1275. doi: https://doi.org/10.1016/j.matdes.2018.08.023. URL https://www.sciencedirect.com/science/article/pii/S0264127518306385.

[213] Saman Naghieh, MD Sarker, N. K. Sharma, Zohra Barhoumi, and Xiongbiao Chen. Printability of 3d printed hydrogel scaffolds: Influence of hydrogel composition and printing parameters. *Applied Sciences*, 10(1), 2020. ISSN 2076-3417. doi: 10.3390/app10010292. URL https://www.mdpi.com/2076-3417/10/1/292.

[214] Arpana Agrawal and Chaudhery Mustansar Hussain. 3d-printed hydrogel for diverse applications: A review. *Gels*, 9(12), 2023. ISSN 2310-2861. doi: 10.3390/gels9120960. URL https://www.mdpi.com/2310-2861/9/12/960.

[215] Lujun Wang, Weili Wei, Zhining Xia, Xu Jie, and Zeng Zilu Xia. Recent advances in materials for stationary phases of mixed-mode high-performance liquid chromatography. *TrAC Trends in Analytical Chemistry*, 80:495–506, 2016. ISSN 0165-9936. doi: https://doi.org/10.1016/j.trac.2016.04.001. URL https://www.sciencedirect.com/science/article/pii/S0165993615302004.

[216] Eric C Peters, Miroslav Petro, Frantisek Svec, and Jean MJ Fréchet. Molded rigid polymer monoliths as separation media for capillary electrochromatography. 1. fine control of porous properties and surface chemistry. *Analytical chemistry*, 70(11):2288–2295, 1998.

[217] Petrus Hemström, Anna Nordborg, Knut Irgum, Frantisek Svec, and Jean MJ Fréchet. Polymer-based monolithic microcolumns for hydrophobic interaction chromatography of proteins. *Journal of separation science*, 29(1):25–32, 2006.

[218] Yun Li, Binghe Gu, H Dennis Tolley, and Milton L Lee. Preparation of polymeric monoliths by copolymerization of acrylate monomers with amine functionalities for anion-exchange capillary liquid chromatography of proteins. *Journal of Chromatography A*, 1216(29):5525–5532, 2009.

[219] Xin Chen, H Dennis Tolley, and Milton L Lee. Polymeric cation-exchange monolithic columns containing phosphoric acid functional groups for capillary liquid chromatography of peptides and proteins. *Journal of Chromatography A*, 1217(24):3844–3854, 2010.

[220] Xin Chen, H Dennis Tolley, and Milton L Lee. Weak cation-exchange monolithic column for capillary liquid chromatography of peptides and proteins. *Journal of separation science*, 34(16-17):2063–2071, 2011.

[221] Ursula Simon and Simone Dimartino. Direct 3d printing of monolithic ion exchange adsorbers. *Journal of Chromatography A*, 1587:119–128, 2019. ISSN 0021-9673. doi:

https://doi.org/10.1016/j.chroma.2018.12.017. URL https://www.sciencedirect.com/science/article/pii/S0021967318315243.

[222] M. Sulaiman Sarwar, Ursula Simon, and Simone Dimartino. Experimental investigation and mass transfer modelling of 3d printed monolithic cation exchangers. *Journal of Chromatography A*, 1646:462125, 2021. ISSN 0021-9673. doi: https://doi.org/10.1016/j.chroma.2021.462125. URL https://www.sciencedirect.com/science/article/pii/S0021967321002491.

[223] Jiangtao Yu, Jie Zhu, Linlin Chen, Yanhong Chao, Wenshuai Zhu, and Zhichang Liu. A review of adsorption materials and their application of 3d printing technology in the separation process. *Chemical Engineering Journal*, 475:146247, 2023. ISSN 1385-8947. doi: https://doi.org/10.1016/j.cej.2023.146247. URL https://www.sciencedirect.com/science/article/pii/S1385894723049781.

[224] Sean Feast, James Titterington, Viet-Anh Hoang, Timothy M. Allison, Conan Fee, and Ali Reza Nazmi. Purification of his-tagged proteins using printed monolith adsorption columns. *Journal of Chromatography A*, 1733:465216, 2024. ISSN 0021-9673. doi: https://doi.org/10.1016/j.chroma.2024.465216. URL https://www.sciencedirect.com/science/article/pii/S0021967324005909.

[225] Tim Huber, Sean Feast, Simone Dimartino, Wanwen Cen, and Conan Fee. Analysis of the effect of processing conditions on physical properties of thermally set cellulose hydrogels. *Materials*, 12(7), 2019. ISSN 1996-1944. doi: 10.3390/ma12071066. URL https://www.mdpi.com/1996-1944/12/7/1066.

[226] Howard Brenner. *Macrotransport processes*. Elsevier, 2013.

[227] Claudia Venditti, Massimiliano Giona, and Alessandra Adrover. Exact moment analysis of transient/asymptotic dispersion properties in periodic media with adsorbing/desorbing walls. *Physics of Fluids*, 34(12), 2022.

[228] A. Adrover, C. Passaretti, C. Venditti, and M. Giona. Exact moment analysis of transient dispersion properties in periodic media. *Physics of Fluids*, 31(11), 2019. doi: 10.1063/1.5127278.

[229] V. Biagioni, C. Venditti, A. Adrover, M. Giona, and S. Cerbelli. Taming taylor-aris dispersion through chaotic advection. *Journal of Chromatography A*, 1673, 2022. doi: 10.1016/j.chroma.2022.463110.

[230] C. Venditti, M. Giona, and A. Adrover. Exact moment analysis of transient/asymptotic dispersion properties in periodic media with adsorbing/desorbing walls. *Physics of Fluids*, 34(12), 2022. doi: 10.1063/5.0130648.

[231] C. Venditti, V. Biagioni, A. Adrover, and S. Cerbelli. Impact of transversal vortices on the performance of open-tubular liquid chromatography. *Journal of Chromatography A*, 1685, 2022. doi: 10.1016/j.chroma.2022.463623.

[232] Claudia Venditti, Bram Huygens, Gert Desmet, and Alessandra Adrover. Moment analysis for predicting effective transport properties in hierarchical retentive porous media. *Journal of Chromatography A*, 1703:464099, 2023. ISSN 0021-9673. doi: https://doi.org/10.1016/j.chroma.2023.464099. URL https://www.sciencedirect.com/science/article/pii/S0021967323003254.

[233] T Issaeva, A Kourganov, and K Unger. Super-high-speed liquid chromatography of proteins and peptides on non-porous micra nps-rp packings. *Journal of Chromatography A*, 846(1):13–23, 1999. ISSN 0021-9673. doi: https://doi.org/10.1016/S0021-9673(99)00360-X. URL https://www.sciencedirect.com/science/article/pii/S002196739900360X.

[234] Arch Creasy, Gregory Barker, Yan Yao, and Giorgio Carta. Systematic interpolation method predicts protein chromatographic elution from batch isotherm data without a detailed mechanistic isotherm model. *Biotechnology Journal*, 10(9):1400–1411, 2015. doi: https://doi.org/10.1002/biot.201500089. URL https://analyticalsciencejournals.onlinelibrary.wiley.com/doi/abs/10.1002/biot.201500089.

[235] Orla P. Murphy, Mayank Vashishtha, Parimaladevi Palanisamy, and K. Vasanth Kumar. A review on the adsorption isotherms and design calculations for the optimization of adsorbent mass and contact time. *ACS Omega*, 8(20):17407–17430, 2023. doi: 10.1021/acsomega.2c08155. URL https://doi.org/10.1021/acsomega.2c08155.

[236] Howard Brenner and Davis A. Edwards. *Macrotransport processes*. Butterworth-Heinemann, 1993.

[237] H. Brenner, P. M. Adler, and Keith Stewartson. Dispersion resulting from flow through spatically periodic porous media ii. surface and intraparticle transport. *Philosophical Transactions of the Royal Society of London. Series A, Mathematical and Physical Sciences*, 307(1498):149–200, 1982. doi: 10.1098/rsta.1982.0108. URL https://royalsocietypublishing.org/doi/abs/10.1098/rsta.1982.0108.

[238] Xiaohong Yan, Qiuwang Wang, and Haim H. Bau. Dispersion in retentive pillar array columns. *Journal of Chromatography A*, 1217(8):1332–1342, 2010. ISSN 0021-9673. doi: https://doi.org/10.1016/j.chroma.2009.12.069. URL https://www.sciencedirect.com/science/article/pii/S0021967309019190.

[239] Xiaohong Yan and Qiuwang Wang. Numerical investigation into the effects of ordered particle packing and slip flow on the performance of chromatography. *Journal*

of Separation Science, 36(9-10):1524–1529, 2013. doi: https://doi.org/10.1002/jssc.201201109. URL `https://analyticalsciencejournals.onlinelibrary.wiley.com/doi/abs/10.1002/jssc.201201109`.

[240] Y. Jung and S. Torquato. Fluid permeabilities of triply periodic minimal surfaces. *Phys. Rev. E*, 72:056319, Nov 2005. doi: 10.1103/PhysRevE.72.056319. URL `https://link.aps.org/doi/10.1103/PhysRevE.72.056319`.

[241] Leonie Wallat, Michael Selzer, Uwe Wasmuth, Frank Poehler, and Britta Nestler. Energy absorption capability of graded and non-graded sheet-based gyroid structures fabricated by microcast processing. *Journal of Materials Research and Technology*, 21:1798–1810, 2022. ISSN 2238-7854. doi: https://doi.org/10.1016/j.jmrt.2022.09.093. URL `https://www.sciencedirect.com/science/article/pii/S2238785422015009`.

[242] David Downing, Alistair Jones, Milan Brandt, and Martin Leary. Increased efficiency gyroid structures by tailored material distribution. *Materials and Design*, 197:109096, 2021. ISSN 0264-1275. doi: https://doi.org/10.1016/j.matdes.2020.109096. URL `https://www.sciencedirect.com/science/article/pii/S0264127520306316`.

[243] Alessandra Adrover, Claudia Venditti, and Gert Desmet. On the modelling of the effective longitudinal diffusion in bi-continuous chromatographic beds. *Journal of Chromatography A*, 1721:464817, 2024. ISSN 0021-9673. doi: https://doi.org/10.1016/j.chroma.2024.464817. URL `https://www.sciencedirect.com/science/article/pii/S0021967324001900`.

[244] Philip Crosbie Carman. Fluid flow through granular beds. *Trans. Inst. Chem. Eng. London*, 15:150–156, 1937.

[245] Raj P Chhabra and Basavaraj Gurappa. *Coulson and Richardson's chemical engineering: volume 2A: particulate systems and particle technology*. Butterworth-Heinemann, 2019.

[246] Leonid M. Blumberg and Gert Desmet. Kinetic performance factor – a measurable metric of separation-time-pressure tradeoff in liquid and gas chromatography. *Journal of Chromatography A*, 1567:26–36, 2018. ISSN 0021-9673. doi: https://doi.org/10.1016/j.chroma.2018.06.048. URL `https://www.sciencedirect.com/science/article/pii/S0021967318308045`.

[247] Robert W Fox, Alan T McDonald, and Philip J Pritchard. Introduction to fluid mechanics, john wiley&sons. *Inc., New York*, 1994.

[248] Paul A Bristow and John H Knox. Standardization of test conditions for high performance liquid chromatography columns. *Chromatographia*, 10:279–289, 1977.

[249] Gert Desmet, David Clicq, and Piotr Gzil. Geometry-independent plate height representation methods for the direct comparison of the kinetic performance of lc supports with a different size or morphology. *Analytical Chemistry*, 77(13):4058–4070, 2005.

[250] K. Broeckhoven, D. Cabooter, F. Lynen, P. Sandra, and G. Desmet. The kinetic plot method applied to gradient chromatography: Theoretical framework and experimental validation. *Journal of Chromatography A*, 1217(17):2787–2795, 2010. ISSN 0021-9673. doi: https://doi.org/10.1016/j.chroma.2010.02.023. URL https://www.sciencedirect.com/science/article/pii/S0021967310002281.

[251] Axel Andrés, Ken Broeckhoven, and Gert Desmet. Methods for the experimental characterization and analysis of the efficiency and speed of chromatographic columns: A step-by-step tutorial. *Analytica Chimica Acta*, 894:20–34, 2015. ISSN 0003-2670. doi: https://doi.org/10.1016/j.aca.2015.08.030. URL https://www.sciencedirect.com/science/article/pii/S0003267015010089.

[252] OA Plumb and Stephen Whitaker. Diffusion, adsorption and dispersion in porous media: small-scale averaging and local volume averaging. *IN: Dynamics of Fluids in Hierarchical Porous Media. Academic Press, Inc., San Diego, California. 1990. p 97-148*, 1990.

[253] Xiaohong Yan, Qiuwang Wang, and Nan Li. Predictive model of solute transport with reversible adsorption in spatially periodic hierarchical porous media. *Journal of Chromatography A*, 1407:69–75, 2015.

[254] B. Huygens, C. Venditti, A. Adrover, and G. Desmet. Nonadditivity and nonlinearity of mobile and stationary zone mass transfer resistances in chromatography. *Analytical Chemistry*, 95(41):15199–15207, 2023. doi: 10.1021/acs.analchem.3c01971. URL https://doi.org/10.1021/acs.analchem.3c01971.

[255] C. Venditti, G. Desmet, and A. Adrover. Prediction of plate height curves of porous-shell pillar array columns micro-pillar array columns. *Separations*, 11(1), 2024. doi: 10.3390/separations11010022. URL https://www.mdpi.com/2297-8739/11/1/22.

[256] A. Moussa, B. Huygens, C. Venditti, A. Adrover, and G. Desmet. Theoretical computation of the band broadening in micro-pillar array columns. *Journal of Chromatography A*, 1715, 2024. doi: 10.1016/j.chroma.2023.464607. URL https://www.sciencedirect.com/science/article/pii/S0021967323008324.

[257] Hassan Y Aboul-Enein. *Analytical and preparative separation methods of biomacromolecules*. CRC Press, 1999.

[258] Georges Guiochon, Dean G Shirazi, and Attila Felinger. *Fundamentals of preparative and nonlinear chromatography*. Academic Press, 2006.

[259] Carolina Lauriola, Claudia Venditti, Gert Desmet, and Alessandra Adrover. Dispersion properties of triply periodic minimal surface stationary phases for lc: The case of superficial adsorption. *Journal of Chromatography A*, 1743:465676, 2025. ISSN 0021-9673. doi: https://doi.org/10.1016/j.chroma.2025.465676. URL `https://www.sciencedirect.com/science/article/pii/S0021967325000251`.

[260] Anuschka Liekens, Joeri Denayer, and Gert Desmet. Experimental investigation of the difference in b-term dominated band broadening between fully porous and porous-shell particles for liquid chromatography using the effective medium theory. *Journal of Chromatography A*, 1218(28):4406–4416, 2011. ISSN 0021-9673. doi: https://doi.org/10.1016/j.chroma.2011.05.018. URL `https://www.sciencedirect.com/science/article/pii/S0021967311006467`.

[261] A. Adrover, C. Venditti, and G. Desmet. An alternative general model for the effective longitudinal diffusion in chromatographic beds filled with ordered porous particles. *Journal of Chromatography A*, 1715, 2024. doi: 10.1016/j.chroma.2023.464598. URL `https://www.sciencedirect.com/science/article/pii/S0021967323008233`.

[262] Warwick B. Dunn and David. I. Ellis. Metabolomics: Current analytical platforms and methodologies. *TrAC Trends in Analytical Chemistry*, 24(4):285–294, 2005. ISSN 0165-9936. doi: https://doi.org/10.1016/j.trac.2004.11.021. URL `https://www.sciencedirect.com/science/article/pii/S0165993605000348`.

[263] Katja Dettmer, Pavel A. Aronov, and Bruce D. Hammock. Mass spectrometry-based metabolomics. *Mass Spectrometry Reviews*, 26(1):51–78, 2007. doi: https://doi.org/10.1002/mas.20108. URL `https://analyticalsciencejournals.onlinelibrary.wiley.com/doi/abs/10.1002/mas.20108`.

[264] Martin Gilar, Petra Olivova, Amy E Daly, and John C Gebler. Orthogonality of separation in two-dimensional liquid chromatography. *Analytical chemistry*, 77(19): 6426–6434, 2005.

[265] Timothy K Toby, Luca Fornelli, and Neil L Kelleher. Progress in top-down proteomics and the analysis of proteoforms. *Annual review of analytical chemistry*, 9(1):499–519, 2016.

[266] Suhas Nawada, Simone Dimartino, and Conan Fee. Dispersion behavior of 3d-printed columns with homogeneous microstructures comprising differing element shapes. *Chemical Engineering Science*, 164:90–98, 2017. ISSN 0009-2509. doi: https://doi.org/10.1016/j.ces.2017.02.012. URL `https://www.sciencedirect.com/science/article/pii/S0009250917301100`.

[267] M. Sulaiman Sarwar, Ursula Simon, and Simone Dimartino. Experimental investigation and mass transfer modelling of 3d printed monolithic cation exchangers.

Journal of Chromatography A, 1646:462125, 2021. ISSN 0021-9673. doi: https://doi.org/10.1016/j.chroma.2021.462125. URL https://www.sciencedirect.com/science/article/pii/S0021967321002491.

[268] Thomas F Johnson, Mariachiara Conti, Francesco Iacoviello, Paul R Shearing, James Pullen, Simone Dimartino, and Daniel G Bracewell. Evaluating 3d-printed bioseparation structures using multi-length scale tomography. *Analytical and Bioanalytical Chemistry*, 415(24):5961–5971, 2023.

[269] Fabrice Gritti, Dzmitry Hlushkou, and Ulrich Tallarek. Multiple-open-tubular column enabling transverse diffusion. part 3: Simulation of solute dispersion along a real three dimensional-printed column with quadratic channels. *Journal of Chromatography A*, 1693:463860, 2023. ISSN 0021-9673. doi: https://doi.org/10.1016/j.chroma.2023.463860. URL https://www.sciencedirect.com/science/article/pii/S0021967323000882.

[270] Christopher Salmean and Simone Dimartino. 3d-printed stationary phases with ordered morphology: state of the art and future development in liquid chromatography. *Chromatographia*, 82(1):443–463, 2019.

[271] Feng Li, Melisa Rodas Ceballos, Sepideh Keshan Balavandy, Jingxi Fan, Mohammad Mahdi Khataei, Yadollah Yamini, and Fernando Maya. 3d printing in analytical sample preparation. *Journal of Separation Science*, 43 (9-10):1854–1866, 2020. doi: https://doi.org/10.1002/jssc.202000035. URL https://analyticalsciencejournals.onlinelibrary.wiley.com/doi/abs/10.1002/jssc.202000035.

[272] Ursula Simon, Livia C T Scorza, Sarah Teworte, Alistair J McCormick, and Simone Dimartino. Demonstration of protein capture and separation using three-dimensional printed anion exchange monoliths fabricated in one-step. *Journal of Separation Science*, 44(6):1078–1088, 2021. doi: https://doi.org/10.1002/jssc.202000722. URL https://analyticalsciencejournals.onlinelibrary.wiley.com/doi/abs/10.1002/jssc.202000722.

[273] Cheng-Kuan Su, Pei-Jin Peng, and Yuh-Chang Sun. Fully 3d-printed preconcentrator for selective extraction of trace elements in seawater. *Analytical Chemistry*, 87(13): 6945–6950, 2015. doi: 10.1021/acs.analchem.5b01599. URL https://doi.org/10.1021/acs.analchem.5b01599. PMID: 26101898.

[274] Melisa Rodas Ceballos, Francisco González Serra, José Manuel Estela, Víctor Cerdà, and Laura Ferrer. 3d printed resin-coated device for uranium (vi) extraction. *Talanta*, 196:510–514, 2019. ISSN 0039-9140. doi: https://doi.org/10.1016/j.talanta.2018.12.055. URL https://www.sciencedirect.com/science/article/pii/S0039914018313225.

[275] Wen-Hsiu Tsai and Cheng-Kuan Su. 4d-printed elution-peak-guided dual-responsive monolithic packing for the solid-phase extraction of metal ions. *Analytical Chemistry*, 96(11):4469–4478, 2024. doi: 10.1021/acs.analchem.3c04961. URL https://doi.org/10.1021/acs.analchem.3c04961. PMID: 38380612.

[276] Cristian Y Chaparro-Garnica, Pepe Jorda-Faus, Esther Bailon-Garcia, Raul Ocampo-Perez, Carlos G Aguilar-Madera, Arantxa Davo-Quinonero, Dolores Lozano-Castello, and Agustin Bueno-Lopez. Customizable heterogeneous catalysts: nonchanneled advanced monolithic supports manufactured by 3d-printing for improved active phase coating performance. *ACS Applied Materials & Interfaces*, 12(49):54573–54584, 2020.

[277] Mafalda G. Moleirinho, Sean Feast, Ana S. Moreira, Ricardo J.S. Silva, Paula M. Alves, Manuel J.T. Carrondo, Tim Huber, Conan Fee, and Cristina Peixoto. 3d-printed ordered bed structures for chromatographic purification of enveloped and non-enveloped viral particles. *Separation and Purification Technology*, 254:117681, 2021. ISSN 1383-5866. doi: https://doi.org/10.1016/j.seppur.2020.117681. URL https://www.sciencedirect.com/science/article/pii/S1383586620321559.

[278] Mariachiara Conti and Simone Dimartino. Materials for 3d printing of chromatographic stationary phases. *TrAC Trends in Analytical Chemistry*, 192:118301, 2025. ISSN 0165-9936. doi: https://doi.org/10.1016/j.trac.2025.118301. URL https://www.sciencedirect.com/science/article/pii/S0165993625001694.

[279] Wang Guo, Yanjuan Yang, Chao Liu, Wenlang Bu, Feng Guo, Jiaqi Li, Enyu Wang, Ziying Peng, Huaming Mai, Hui You, and Yu Long. 3d printed tpms structural pla/go scaffold: Process parameter optimization, porous structure, mechanical and biological properties. *Journal of the Mechanical Behavior of Biomedical Materials*, 142:105848, 2023. ISSN 1751-6161. doi: https://doi.org/10.1016/j.jmbbm.2023.105848. URL https://www.sciencedirect.com/science/article/pii/S1751616123002011.

[280] C. Lauriola, A. Moussa, G. Desmet, and A. Adrover. Dispersion properties of tpms micro-porous stationary phases for lc. *in preparation*, 2025.

[281] N. Halib, M.C.I. Mohd Amin, I. Ahmad, M. Abrami, S. Fiorentino, R. Farra, G. Grassi, F. Musiani, R. Lapasin, and M. Grassi. Topological characterization of a bacterial cellulose–acrylic acid polymeric matrix. *European Journal of Pharmaceutical Sciences*, 62: 326–333, 2014. ISSN 0928-0987. doi: https://doi.org/10.1016/j.ejps.2014.06.004. URL https://www.sciencedirect.com/science/article/pii/S0928098714002644.

[282] Tilen Kopač, Michela Abrami, Mario Grassi, Aleš Ručigaj, and Matjaž Krajnc. Polysaccharide-based hydrogels crosslink density equation: A rheological and lf-nmr study of polymer-polymer interactions. *Carbohydrate Polymers*, 277:118895, 2022. ISSN 0144-8617. doi: https://doi.org/10.1016/j.carbpol.2021.118895. URL https://www.sciencedirect.com/science/article/pii/S0144861721012820.

[283] Michela Abrami, Fabio Bignotti, Francesco Baldi, Gloria Spagnoli, Alice Biasin, Lucia Grassi, Gabriele Grassi, and Mario Grassi. Rheological and low field nmr characterization of hydrophobically-modified peg hydrogels for drug delivery. *International Journal of Pharmaceutics*, 637:122882, 2023. ISSN 0378-5173. doi: https://doi.org/10.1016/j.ijpharm.2023.122882. URL `https://www.sciencedirect.com/science/article/pii/S0378517323003022`.

[284] Fatima M Plieva, Malin Karlsson, Maria-Rosa Aguilar, David Gomez, Sergey Mikhalovsky, and Igor Yu Galaev. Pore structure in supermacroporous polyacrylamide based cryogels. *Soft Matter*, 1(4):303–309, 2005.

[285] Zhansaya Kaberova, Evgeny Karpushkin, Martina Nevoralová, Miroslav Vetrík, Miroslav Šlouf, and Miroslava Dušková-Smrčková. Microscopic structure of swollen hydrogels by scanning electron and light microscopies: Artifacts and reality. *Polymers*, 12(3), 2020. ISSN 2073-4360. doi: 10.3390/polym12030578. URL `https://www.mdpi.com/2073-4360/12/3/578`.

[286] Mojdeh Mirshafiei, Hamid Rashedi, Fatemeh Yazdian, Abbas Rahdar, and Francesco Baino. Advancements in tissue and organ 3d bioprinting: Current techniques, applications, and future perspectives. *Materials Design*, 240:112853, 2024. ISSN 0264-1275. doi: https://doi.org/10.1016/j.matdes.2024.112853. URL `https://www.sciencedirect.com/science/article/pii/S0264127524002260`.

[287] Vidhi Mathur, Prachi Agarwal, Meghana Kasturi, Varadharajan Srinivasan, Raviraja N Seetharam, and Kirthanashri S Vasanthan. Innovative bioinks for 3d bioprinting: Exploring technological potential and regulatory challenges. *Journal of Tissue Engineering*, 16:20417314241308022, 2025.

[288] Scott Taylor, Eva Mueller, Lamont R Jones, Ashley V Makela, and Nureddin Ashammakhi. Translational aspects of 3d and 4d printing and bioprinting. *Advanced Healthcare Materials*, 13(27):2400463, 2024.